UNIVERSIDADE FEDERAL DO CEARÁ

CENTRO DE CIÊNCIAS

DEPARTAMENTO DE FÍSICA

PROGRAMA DE PÓS-GRADUAÇÃO EM FÍSICA

ENZO VICTORINO HERNÁNDEZ AGRESSOTT

RAMAN STUDY OF Ag NANOPARTICLES COATED WITH PROTEINS SYNTHESIZED BY FUNGI USING SURFACE-ENHANCED RAMAN SPECTROSCOPY AND TIP-ENHANCED RAMAN SPECTROSCOPY

Fortaleza

2020

ENZO VICTORINO HERNÁNDEZ AGRESSOTT

RAMAN STUDY OF Ag NANOPARTICLES COATED WITH PROTEINS SYNTHESIZED BY FUNGI USING SURFACE-ENHANCED RAMAN SPECTROSCOPY AND TIP-ENHANCED RAMAN SPECTROSCOPY

Tese de Doutorado submetida ao programa de Pós-Graduação em Física da Universidade Federal do Ceará, como parte dos requisitos para a obtenção do Título de Doutor em Física.

Orientador: Prof. Dr. Alexandre Rocha Paschoal
Coorientador: Prof. Dr. Antônio Gomes de Sousa Filho.

Universidade Federal do Ceará – CE

Departamento de Física

Programa de Pós-Graduação

Fortaleza

2020

ENZO VICTORINO HERNÁNDEZ AGRESSOTT

RAMAN STUDY OF Ag NANOPARTICLES COATED WITH PROTEINS SYNTHESIZED BY FUNGI USING SURFACE-ENHANCED RAMAN SPECTROSCOPY AND TIP-ENHANCED RAMAN SPECTROSCOPY

Tese de Doutorado submetida ao programa de Pós-Graduação em Física da Universidade Federal do Ceará, como parte dos requisitos para a obtenção do Título de Doutor em Física.

Aprovada em: 19/02/2020, Fortaleza-CE, Comissão julgadora:

BANCA EXAMINADORA

_____

Prof. Dr. Alexandre Rocha Paschoal
Universidade Federal do Ceará (UFC)
Orientador

_____

Prof. Dr. Antônio Gomes de Sousa Filho
Universidade Federal do Ceará (UFC)

_____

Prof. Dr. Carlos Lenz Cesar
Universidade Federal do Ceará (UFC)

_____

Prof. Dr. Francisco Afrânio Cunha
Universidade Federal do Ceará (UFC)

_____

Prof. Dr. Thiago de Lourenço e Vasconcelos
Pesquisador Tecnologista Instituto Nacional de Metrologia INMETRO

Fortaleza
2020

A Deus.

Aos meus pais, Victoria Elena Agressott Vargas
e Enzo Hernández Escorcia.

AGRADECIMENTOS

Não é a força, mas a perseverança é
A que realiza grandes coisas.
Samuel Johnson

RESUMO

As nanopartículas de Prata (AgNPs) têm um grande número de aplicações em tecnologia e ciências físicas e biológicas. Esses nanomateriais podem ser sintetizados por métodos químicos e biológicos. A síntese biológica que utiliza fungos representa uma abordagem ecológica para a produção de nanomateriais que possui a vantagem da biocompatibilidade. Este artigo estuda as nanopartículas de prata (AgNPs) produzidas pelos fungos Rhodotorula glutinis e Rhodotorula mucilaginosa encontrados no solo comum do campus da Universidade Federal do Ceará (Brasil). Os AgNPs biossintetizados possuem uma camada protetora de proteínas que envolve um núcleo de metal Ag. O objetivo deste trabalho é investigar o tamanho e a estrutura da camada protéica de cobertura, como ela interage com o núcleo Ag e a sensibilidade do sistema. (núcleo+proteína) à iluminação da luz visível, especificamente sua resposta Raman. Para isso, usamos SEM, AFM, espectroscopia de fotoluminescência, SERS, espectroscopia de campo escuro e TERS. Os AgNPs foram isolados e as medidas de MEV indicaram diâmetro médios entre 58 nm para R. glutinis e 30 nm para R. mucilaginous. Esses valores estão de acordo com as medições de AFM, que também forneceram o diâmetro médio de 85 nm para R. glutinis e 56 nm para R. mucilaginous, além de informações adicionais sobre o tamanho médio das camadas de proteção de proteínas, cujos valores foram 24 e 21 nm para as nanopartículas de R. mucilaginosa e R. glutinis, respectivamente. A estrutura da camada das proteínas que revestem os AgNPs parecia ser facilmente perturbada, e os espectros de SERS eram instáveis, mas em TERS eles mostraram-se estáveis. Foi possível identificar os picos de Raman que estão relacionados à hélice α, à folha (zig-zag) β e às estruturas proteicas mistas, além de diferenças na estrutura da formação. Finalmente, a microscopia de campo escuro mostrou que os núcleos de prata são muito estáveis, mas alguns são afetados pela energia do laser devido ao aquecimento ou à fusão.

Palavras-chave: Biogênica**.** Nano partículas de Prata. Espectroscopia Raman. SERS. TERS. AFM. Capa de proteínas.

ABSTRACT

Silver nanoparticles (AgNPs) have a large number of applications in technology and physical and biological sciences. These nanomaterials can be synthesized by chemical and biological methods. The biological synthesis that uses fungi represents an ecological approach to the production of nanomaterials that has the advantage of biocompatibility. This paper studies the silver nanoparticles (AgNPs) produced by the fungi Rhodotorula glutinis and Rhodotorula mucilaginosa found in the ordinary soil of the campus of the Federal University of Ceará (Brazil). Biosynthesized AgNPs have a protective layer of proteins that involves an Ag metal core. The objective of this work is to investigate the size and structure of the coverture protein layer, how it interacts with the Ag core and how sensitive the system is (core+protein) to visible light illumination, specifically your Raman response. For this, we use SEM, AFM, photoluminescence spectroscopy, SERS, dark field spectroscopy and TERS. AgNPs were isolated and SEM measurements showed the average size diameter between 58 nm for R. glutinis and 30 nm for R. mucilaginous. These values are in accordance with the AFM measurements, which also provided the average diameter of 85 nm for R. glutinis and 56 nm for R. mucilaginous, as well as additional information on the average size of the protein protection layers, whose values were 24 and 21 nm for R. mucilaginosa and R. glutinis nanoparticles, respectively. The layer structure of the proteins that coat the AgNPs seemed to be easily disturbed, and the SERS spectra were unstable but in TERS they were shown to be stable. It was possible to identify the Raman peaks that could be related to the α −helix, the β −sheet and the mixed protein structures, in addition to differences in formation structure. Finally, dark field microscopy showed that silver nuclei are very stable, but some are affected by laser energy due to heating or melting.

Keywords: Biogenic. Silver nanoparticle. Raman spectroscopy. SERS. TERS. AFM. Protein layers.

LIST OF FIGURES

LIST OF TABLES

LIST OF ABBREVIATIONS AND ACRONYMS

AFM	Atomic Force Microscopy
Ag	Silver
AgNPs	Ag nanoparticles
CS	Conformational Sub-state
DLS	Dynamic Light Scattering
DNA	DeoxyriboNucleic Acid
EF	Enhancement Factor
EM	Electromagnetic
ff	far field
FWHM	Full Width at Half Maximum
GP	Gap Plasmon
HOMO	Higthest Occupied Molecular Orbital
IR	Infra-Red
nf	near field
NA	Numerical Aperture
NPs	Nanoparticles
LPP	Localized Plasma Polaritons
LSPR	Localized Surface Plasmons Resonant
LSPP/R	Localized Surface Plasmon Polariton/Resonant
PSPP/R	Propagating Surface Plasmon Polariton/Resonant

LUMO	Lowest Unoccupied Molecular Orbital
LSP	Localized Surface Plasmons
RNA	RiboNucleic Acid
PL	Photoluminescence
PSPP	Propagating Surface Plasmons Polaritons
Rff	Raman far-field
Rnf	Raman near field
Rg	Rhodotorula glutinis
Rm	Rhodotorula mucilaginosa
SERS	Surface-Enhanced Raman Scattering
SHG	Second Harmonic Generation
SNOM	Scanning Near-Field Optical Microscopy
SPM	Scanning Probe Microscopy
SPP	Surface Plasmons Polaritons
SPR	Surface Plasmons Resonance
SPs	Surface Plasmons
STM	Scanning Tunnel Microscope
UV	UltraViolet
TERS	Tip-Enhanced Raman Scattering

LIST OF SYMBOLS

$\alpha-$Helix	Helix structure
$\beta-$Sheet	Lamina structure (zigzag)
λ	Wavelength
ν_0	Initial Frequency
I_0	Initial Intensity
Ω	Solid Angle
$\overleftrightarrow{\alpha}$	Polarizability Tensor
$\vec{\mu}$	Dipole-moment Induced
δ	Deformation Vibrations
ε	Dielectric Constants
ω	Angular Frequency
Å	Angstrom

SUMARY

1. INTRODUCTION

Characterizing biological systems with spectroscopic techniques today is common; In fact, one of the most commonly used techniques is Raman spectroscopy because it provides information on the chemical composition, molecular structure and molecular interactions between biomolecules in cells and tissues. Therefore, it can be obtained biochemical information related to proteins, lipids, carbohydrates, and nucleic acids. However, these techniques face difficulties when the size of the systems is very small. The size scale of biological systems ranges from the basic components of biopolymers (which are amino acids or lipids), or protein cofactors to sets of proteins, membranes or DNA-protein complexes, all with sizes on the nanometric scale. Solving these types of problems is today one of the objectives of nanoscience research. In this work, we are interested in the metal-based nanoparticles, such as silver nanoparticles, which have already been used successfully in sanitary, cosmetic and food products, as well as objects of study in environmental sciences, biomedical, chemical industries, space industries and catalysis **[1-3]**.

In this sense, many types of chemical routes and methods have been developed that use metal salts as sources for the development and synthesis of metallic nanoparticles (NPs). However, most of them include the use of toxic solvents that generate wastes that are harmful to health and the environment, resulting in high consumption of energy and resources on chemical routes that are generally complex, multi-step and economically expensive. Consequently, synthetic methods were sought that did not have those disadvantages; From there, the idea of developing biogenic synthesis systems (green synthesis) for the production of metallic NPs, especially those mediated by fungi, arose, since they have high efficiency, simplicity, economy, and respect for the environment. In this context, the use of fungi

for silver nanoparticle biosynthesis (AgNPs) is a biosynthesis that has been growing in recent years [4-7]. Fungi cultures, compared to bacteria, require simpler nutrients, produce a greater amount of biomass and are easily managed. Also, most of the fungi used to produce AgNPs are not pathogenic to humans, and the presence of a protective layer of proteins that surrounds coats the metal core makes these particles potentially biocompatible. The use of metallic NPs, in this case, Ag, turns out to be very advantageous compared to them made in bulk, due to the high surface/volume ratio that AgNps have, which provides better contact with microorganisms. Silver nanoparticles have been shown to restrict the growth of microorganisms that develop resistance [7-9].

The AgNPs produced by the fungi *Rhodotorula glutinis* and *Rhodotorula mucilaginosa* found in an ordinary soil of the Universidade Federal do Ceará, Campus do Pici. The biosynthesized AgNPs have a protein-capping layer involving the metallic Ag core. One the focus of this work is to investigate the size and structure of the capping layer, how it interacts with the Ag core and how sensitive the system (core+protein) is too visible light illumination. For this, we employed SEM, AFM, photoluminescence spectroscopy, SERS, dark-field spectroscopy, and TERS. The structure of the protective layer seems to be easily altered due to the laser incidence used for the Raman spectra. It was possible to identify Raman peaks that might be related to α−helix, β−sheet, and protein mixed structures. Dark-field microscopy showed that the silver cores are very stable, but some are affected by the laser energy due to heating or melting.

The study of proteins and their characterization by Raman spectroscopy is of vital importance because it allows the study in cells

(proteins represent more than half of the mass of a cell, excluding water). These macromolecules play a crucial role in the functioning of living beings. Knowledge of their native or non-native conformation or their interactions with the complex chemical and biological environment is important to understand their role in organisms and more precisely in cells. Since its implementation, Raman spectroscopy has been widely used by many research groups to analyze protein structures and their interactions with the environment. Taking Raman measurements on proteins and their assemblies is not an easy task. Although Raman spectroscopy is used successfully in organic and inorganic, natural and synthetic chemical compounds, usually in a crystalline state, things are a bit more complex in the case of proteins. This is not surprising considering that proteins are large and complex biological systems (from 10 kDa to 150 kDa, a Dalton (Da) is an alternative name for the unit of atomic mass, a kilodalton (kDa) is 1,000 daltons. therefore, a protein with a mass of 64 kDa has a molecular weight of 64,000 grams per mole) **[10-16]**.

The ability to identify and analyze ever-smaller structures and materials is one of the major challenges for nanoscience and nanotechnology. In optics, space-scale experiments of a few tens of nanometers are subject to the barrier imposed by the light diffraction limit. The resolution limit is a physical principle based on the diffraction of light which roughly restricts the smallest distance in which two light sources can be distinguished from each other, and that is half the wavelength of the excitation light ($\sim\boldsymbol{\lambda/2}$). This is valid in the case of transmission of information by means of propagating electromagnetic waves in the distant field regime that is the case of the techniques of conventional optical microscopy and the typical Raman microspectroscopy.

Over the last few years, enormous advances have been made in the technologies related to the development, synthesis and growth of nanomaterials that bring to light their characteristics and properties, clearly different from the same one's materials made in bulk. However, in contrast to the rapid growth of the techniques of elaboration, the advances in the techniques of analysis and characterization of these nanoscales (10^{-9} meters) have been slower. This work uses the techniques that are relatively new, that allow to capture, to detect, to measure optical signals (Raman) increasing the signal, enabling the characterization of low concentrations of the analyte, including single molecules as is the Surface-Enhanced Raman Scattering (SERS) technique and the Tip-Enhanced Raman Scattering (TERS) that allows to break the diffraction limit and to enable the material characterization in the nanometer scale. These experimental tools use the generation of localized surface plasmons resonant to amplify the Raman signal. Obtain Raman signal on the nanoscale, whether by SERS and TERS techniques it is vitally important because performing this type of measurement in the nano biological world will provide valuable information on the health and pathology of tissues.

The favorable properties of metallic-NPs to generate surface plasmons that enhance the local electric field using nanostructures as a support for other materials (molecules) which enhance the cross-sections of Raman scattering. One of the first works that can be cited using AgNPs are Melissa F. Mrozek et al. for the detection and identification of aqueous saccharides using silver colloids, Chanda Ranjit Yonzon et al. used AgNPs as sensors for metabolites, Karen E. Shafer-Peltier et al. used nanosphere as a glucose biosensor like Chanda Ranjit Yonzon et al and Olga Lyandres et al. used Raman enhanced surface dispersion (SERS) for the detection of glucose, lactate, and other plasma analytes. It can also refer to the use of

AgNPs as a very useful biological nanosensor on the publications TianhuiJiao et al., Angela Capocefalo et al., Vinay Bhardwaj et al. Another feature of Raman spectroscopy is that it allows the study of nanomaterials, providing a non-invasive and non-destructive environmental characterization for the nano samples of interest. This technique has high chemical sensitivity and provides structural and electronic information with the use of coherent monochromatic excitation sources in the visible and not visible of the electromagnetic spectrum. Unfortunately, Raman scattering has a very low dispersion efficiency that is proportional to the cross-section of illuminated sample volume (Raman signal is weak). Therefore, in the study of small amounts of samples in isolated nanomaterials, it is in many cases a great challenge. Then, as an alternative to solve this problem, methods were sought to intensify the Raman signal.

Amplification of the Raman signals originates mainly through the electromagnetic interaction of light with metals, which produces large amplification of the electro-optical laser field, $\vec{E}_{laser}$, through excitations generally known as plasmonic resonances. To benefit from this, the molecules must generally be adsorbed on the metal surface, or at least be very close to them (typically 10 nm distance maximum). The local optical electric field enhanced, $\vec{E}_{loc}$, generates an enhanced Raman scattering (Raman scattering transversal section increase) which can be obtained by two methods.

i) Using metal nanoparticles. When the light interaction with metal nanostructures a strong and spatially localized field amplitude enhancement is generated, due to resonant excitation of collective electron oscillations (plasma oscillations) in single or coupled nanoparticles (Grand et al. 2003, Mühlschlegel et al. 2005). The resonance frequencies associated with such

oscillations and thus the optical properties can be tuned in a broad spectral range according to the material and the shape of the nanostructure. Materials that possess a negative real and small positive imaginary dielectric constant are capable of supporting a Surface Plasmons Resonance (SPR). This resonance is a coherent oscillation of the surface conduction electrons excited by electromagnetic (EM) radiation, see Fig. 1.1 a) [17].
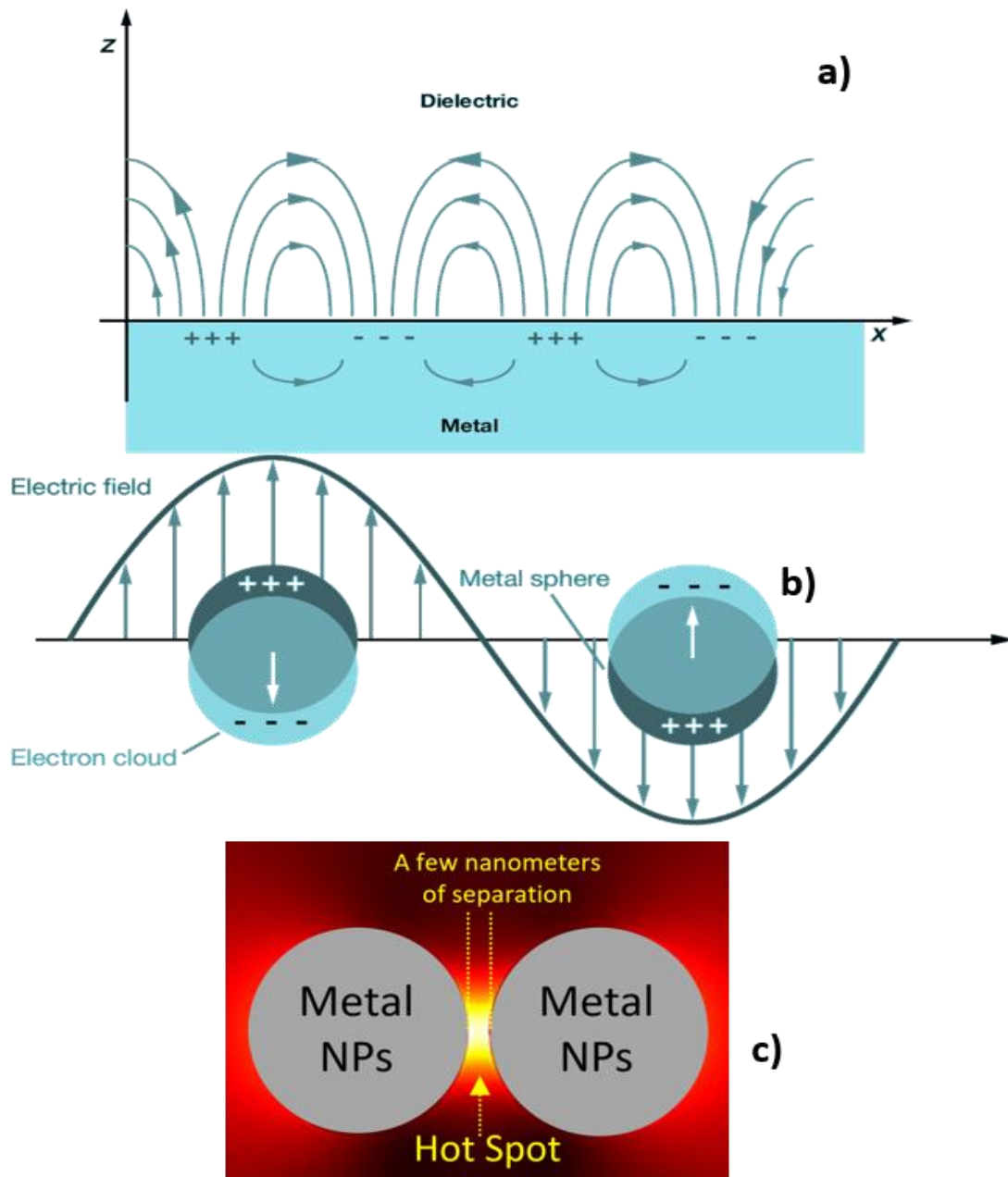
Figure 1.1. Schematic diagrams illustrating a) a Surface Plasmons (SPs) (or propagating plasmon on metal), b) a Localized Surface Plasmons Resonant (LSPR) and c) enhanced EM fields in the nano gaps where are generated the hot spot between the metal nanoparticles [17].

When light is incident on the surface of a roughened metal substrate, a local EM field with a strength much stronger than the incident light is generated in the vicinity of the substrate. The highly magnified local field significantly strengthens the Raman scattering process of molecules adsorbed on the substrate or very close to this, which works effectively as an antenna capable of collecting photons. Furthermore, the substrate also enhances the Raman scattering light emitted from the molecules, playing the role of an antenna for broadcasting. The EM effect from SPs excitation, which is the collective electronic excitation mode that is manifested as coherent electron density oscillation localized at the surface of conductive materials. The surface roughness enables the SPR to focus the light at the subwavelength scale, forming "hots pots" with strong enhancement of the EM field. The largest enhancements are obtained in the junction between two nanostructures, commonly referred to as "hot spots". The signal from hot spots is reported to dominate the observed Raman spectrum. An electromagnetic field of 10^8 is commonly obtained in a 1 nm gap between two silver nanoparticles **[18, 19, 20-29]**.

On the other hand, when the incident light is used to excite the SPs, energies of the photon and plasmons must match, as well as their momenta. These matching conditions may be simultaneously satisfied when the translational symmetry is broken, which renders surface roughness conducive to coupling light to SPRs. In the case of metal nanoparticle surfaces, see Fig 1,1 b), light interacts with particles much smaller than the incident wavelength. This leads to plasmons that oscillate locally around the nanoparticle with a frequency known as Localized Surface Plasmons Resonant (LSPR), collective excitation of conduction band electrons in a nanostructure. Similar to the SPR, the LSPR are sensitive to changes in the local dielectric environment. The plasmons coupling between adjacent

metal nanostructures can largely shift the LSPR frequencies and generate hugely enhanced EM fields in the nanogaps (hot spots) between the nanostructures, see Fig 1.1 c). The LSPR is an optical phenomenon generated by a light wave trapped within conductive nanoparticles (NPs) smaller than the wavelength of light. This interaction produces coherent localized plasmon oscillations with a resonant frequency that strongly depends on the composition, size, geometry, dielectric environment and particle–particle separation distance of NPs. The huge field enhancement is probably the most prominent property of SPs for a large variety of applications. LSPR is a particular type of SPR, in the case for instance of nanoparticles; the electromagnetic field remains localized in a nanoscale region around the nanoparticle-dielectric interface, and it cannot propagate. SPPs refer to a coupled electromagnetic-electron waves along the metal-dielectric interface can to propagate and exponentially decay perpendicular to it why they are evanescent waves (in either way, the wavenumber in the direction normal to the interface becomes imaginary and hence the waves do not propagate in this direction). SPR is a physical resonance state, which is established when the frequency of incident photons matches the natural frequency of surface electrons nevertheless it is not conditions necessary that frequency of incident photons to match with frequency of SPR.

Plasmon-enhanced spectroscopy based on this field enhancement effect is an important point for SERS techniques, see Fig. 1.2. Enhancement of the optical electric field as necessary to improve Raman signal levels can be achieved by utilizing localized plasmons resonances in noble metal nanoparticles. These resonances are the result from localized charge density oscillations, can yield a Raman enhancement of up to 10 orders of magnitude via scattering (SERS) effect. In conventional SERS, however, the enhancement can be difficult to control and remains spatially

confined to stationary nanoparticles or surface features. The correct transfer or deposition-adequacy of several molecules to a nano-metal is a recurring theme (and a problem is the molecule is not oddly added) in the practical implementations of SERS **[18, 19, 20-29]**.
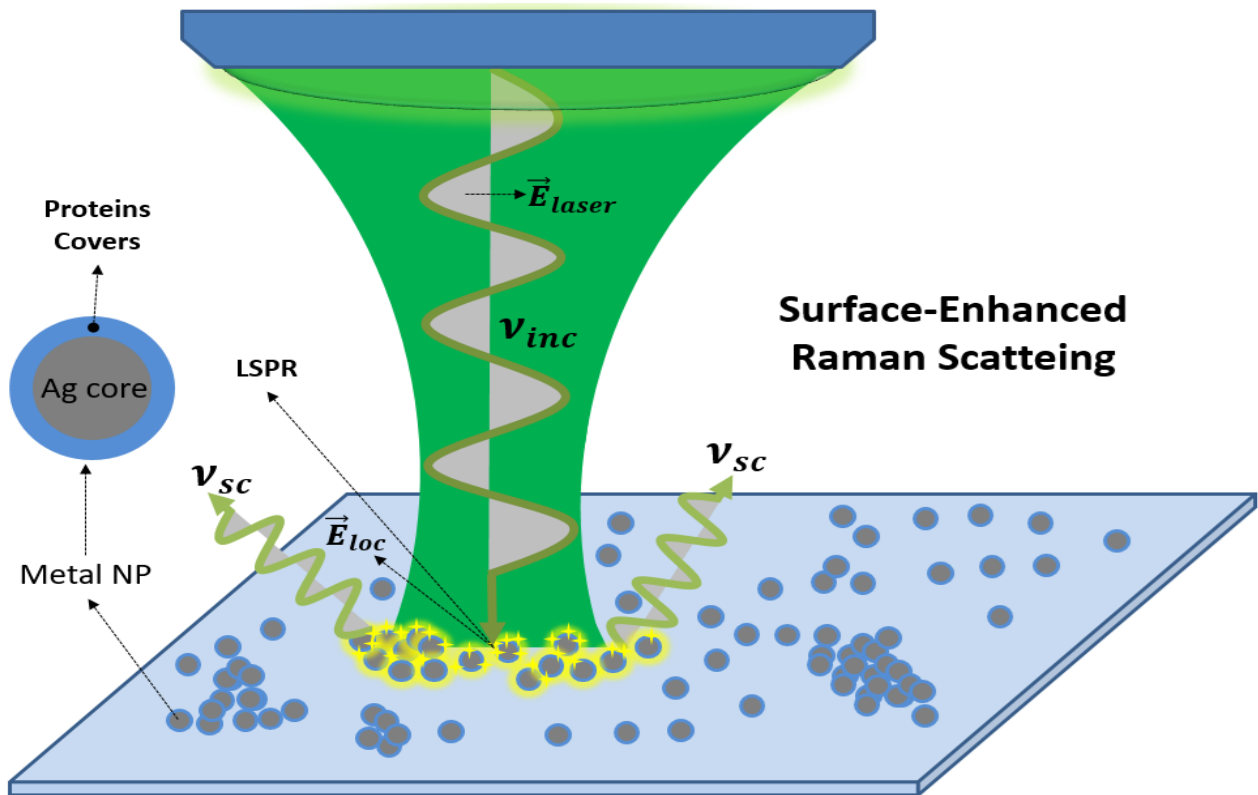
Figure 1.2. Surface-enhanced Raman Scattering (SERS). Illustrations of SERS experiment. The incident laser light ($\vec{E}_{loc}$) induces a local surface plasmons resonance. The resulting improvement in the intensity of the oscillatory electromagnetic field (shown in yellow) in the metal nano-surface intensifies the light-matter interaction and, consequently, increases the intensity of the light with Raman scattering.

ii) Using noble metal as nano-tip scanning proves of a scanning probe microscopy. TERS techniques see Fig. 1.3. Here, the enhanced Raman signal is due to lightning rod effects (see Fig. 1.4) induced by the sharp curvatures (Novotny and Hecht 2006) on the nano-tip apex. The incident beam with appropriate wavelength and polarization state is focused at the apex of the nano-scale metallic tip, these enhanced electric field is due to the oscillations of the localized charge densities generated in

the vicinity of metallic tip (see Fig 1.5 a)). It should be mentioned that the excitation wavelength has to coincide with the resonance energy of the metal surface plasmons, the LSPRs on the nano-tip are strongly dependent on structure geometries, size, and environments. In a vision more general, the mechanism of the enhancement can be attributed to the surface plasmon polariton (SPP) **[24]** or by the too call it localized plasma polaritons (LPP) (Zayats, 1999), or Localized surface plasma polaritons (LSPP) effect (Bohren & Huffman, 1998) and/or the lightning-rod effect (Novotny et al., 1999) where both mechanisms can act simultaneously, although the lightning-rod effect is assigned to be more predominating in the case of metal nano tip. The metallic tip can be regarded as a nano-scale light source with quite high power density. Consequently, Raman signal from the localized position of the specimen excited by the enhanced field very close to the tip is markedly enhanced **[21-29]**.

The sensitive response of the resonance frequency to environmental change is attractive for chemical and biological sensing applications. The TERS technique can be implemented as a scanning probe method, providing optical nanometer spatial resolution. Here, rather than relying on the enhancement of stationary nanoparticles, a plasmon resonance located at the apex of a noble metal scanning probe tip is utilized, with TERS will have control of the area where want to generate the plasmons resonance located with tip apex resolutions but this will depend on the qualities of the metal nano-tip.

Tip-enhanced Raman scattering (TERS) is based on the same phenomenon as surface-enhanced Raman scattering (SERS), which occurs on island structures consisting of metallic nanoparticles. Chemical enhancement effect, which occurs due to the formation of a complex of

sample molecules and metal atoms, as well as physical enhancement effect (e.g. SPP or LSPP) can be expected in TERS. The differences between TERS and SERS are as follows: (1) TERS occurs on a single metallic nano tip which specifies position for observation and analysis with nano metric accuracy, while SERS is induced on plenty of metallic nanostructures. (2) A metal nano tip is able to perturb molecules dynamically, electrically, or magnetically as the tip is controlled by another Scanning Probe Microscopy (SPM), e.g. Atomic Force Microscopy (AFM) or scanning tunneling microscopy. Hence, TERS provides special circumstances for Raman spectroscopy like high pressure, intense electric field, and so on [21-29].
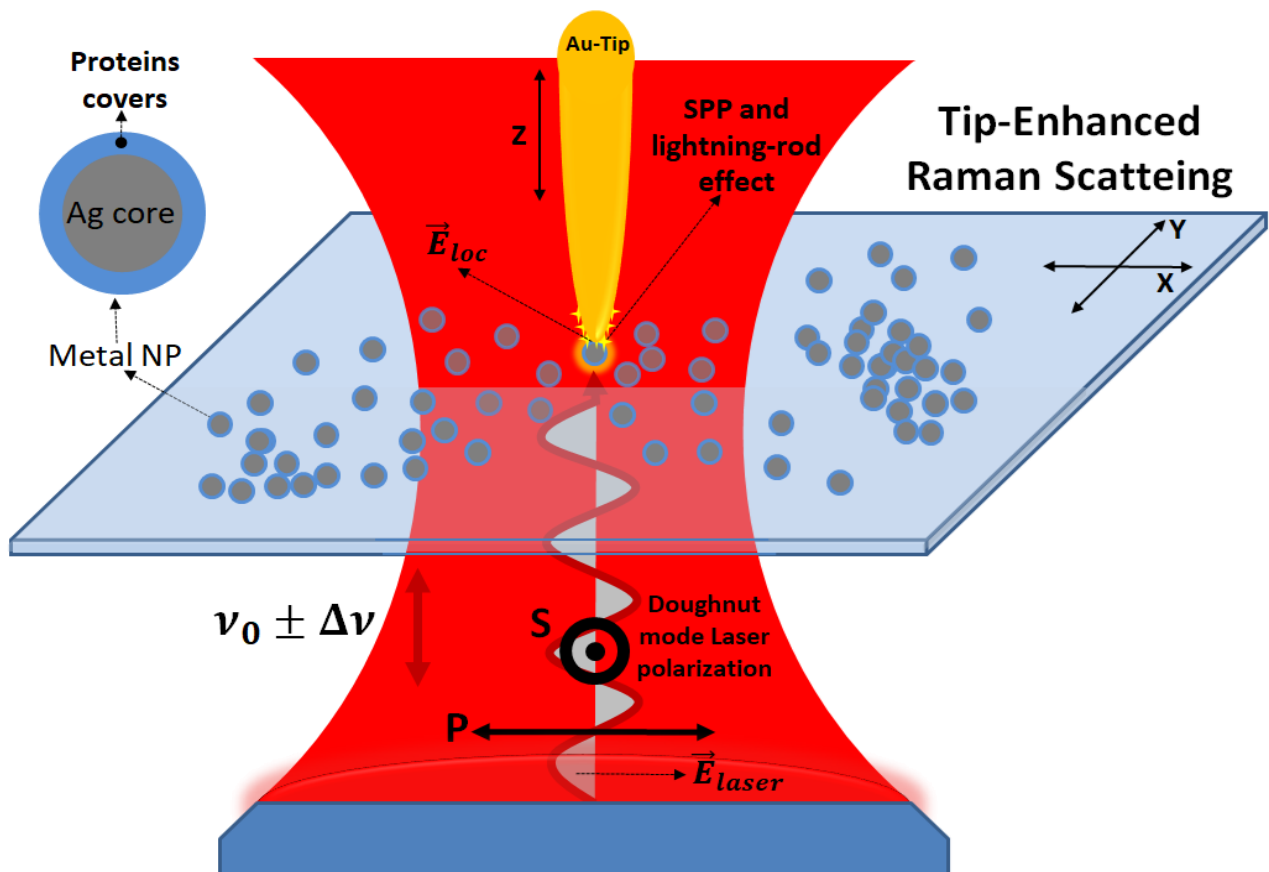
Figure 1.3. Illustration of a TERS experiment. The incident light (a laser) is concentrated in the space between the sample and a probe tip through an objective lens of an inverted microscope. The distance between the sample and the probe tip is achieved through AFM or SPM. The back-diffused light is collected through the same objective lens, spectrally filtered and taken up to a spectrometer.
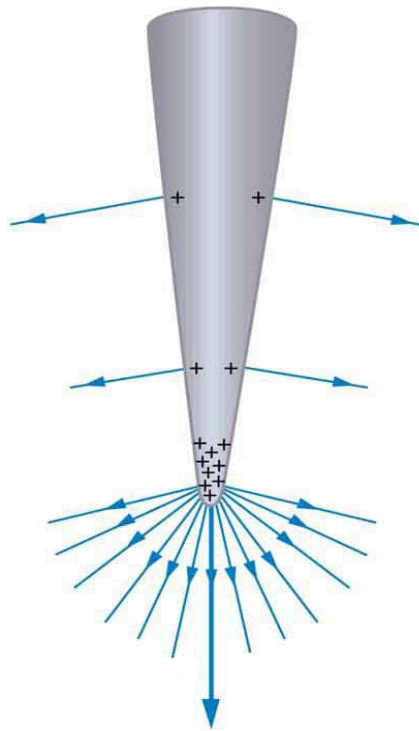
Figure 1.4. Lightning rod effects phenomenon. This occurs due to sharp curvatures on the metal nano-tip apex that induced charges concentration on the apex.

TERS is a variant of SERS (see Fig. 1.5). It may be imagined that the rough metallic surface excited and enhanced in SERS is scaled down to a nanometer "hot-spot" scattering Raman spectral signal enhanced from the tip apex. In this situation, the distance and relative position between the "hot-spot" and the specimen is precisely controllable. Thus, the irksome measurement uncertainty and non-repeatability in the former SERS detection caused by the random distributed enhancing "hot-spots" on the rough metal substrate is avoided (see Fig 1.5 b)). The inherent flexibility of a scanning probe system affords the freedom for spatially resolved spectroscopic probing and imaging of surface analytes. These techniques can produce an increase in Raman signal strength by up to 10 orders of magnitude. The term "plasma resonances" is, in fact, an abbreviation of a family of effects associated with the interaction of electromagnetic radiation with metals.
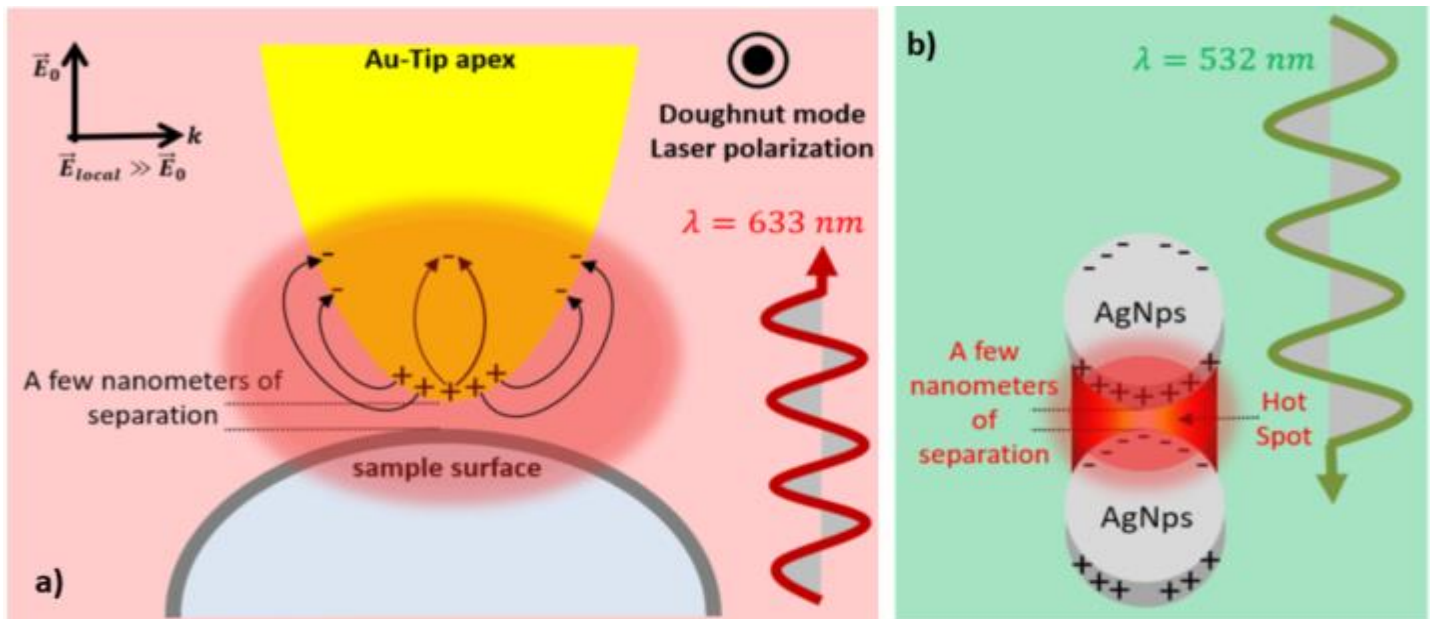
Figure 1.5. a) The conceptual illustration of tip-enhanced Raman spectroscopy (TERS) shows a strongly enhanced optical field generated at the apex of sharp metal tip of SPM by the external illumination. b) The conceptual illustration of SERS hot spot showing the parallels between SERS and TERS technique.

Common materials used for NPs production and scanning prove tip are noble metals as Ag and Au, which due to the energy levels of $d - d$ transitions exhibit LSPR in the visible range of the spectrum. Although, Ag exhibits the sharpest and strongest bands among all metals. The shape and size of a metallic nanoparticle dictate the spectral signature of its plasmons resonance, the ability to change these two parameters and study the effect on the LSPR is an important in these type experiment and challenge. LSPR response to the morphological changes to be directly correlated, these is due to the inherent heterogeneity among individual nanoparticles, each LSPR spectrum is different, revealing the true distribution of resonance wavelengths. To understand these phenomena, let's analyze the optical properties of spherical AgNPs, which depend in large measure on the diameter of nanoparticles. The extinction spectra for 10 different sizes are shown in Fig. 1.6. The smallest nano spheres of the Plate mainly absorb light around 420 nm, even though the larger spheres exhibit a greater

dispersion and have peaks that expand and exchange longer wavelengths passing through 530 nanometers **[17, 21-29, 56]**.
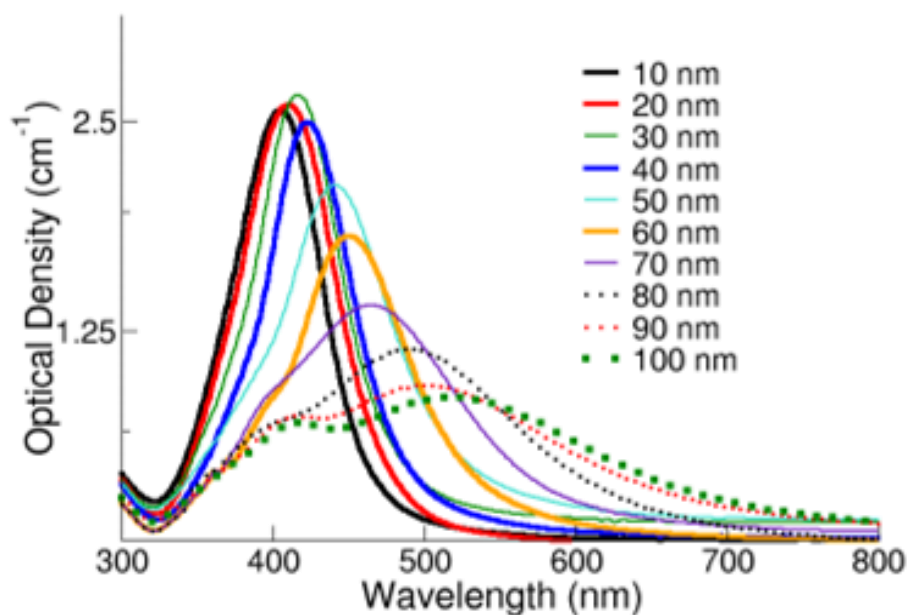
Figure 1.6. Extinction spectra to 10 different size of AgNPs **[17]**.

Owing to the high spatial optical resolution due to the spatial confinement of the plasmons in the optics near field at the apex of the tip combined with an intensified spectroscopic sensitivity, SERS and TERS have been used to study a wide variety of systems. Using dyes deposited on substrates, such systems demonstrated a sensitivity of studies even in individual molecules. Other systems include biologically relevant molecules and cells, in addition to materials of reduced sizes, such as graphene and carbon nanotubes. Besides, SERS and TERS have also been used to study crystalline systems ranging from semiconductors to ferroelectric crystals. It should be mentioned that the effectiveness of Raman intensification produced by TERS metal tips depends on the polarization of the monochromatic beam used to excite the sample, size, and tip qualities **[21-29, 56]**.

As a result of the dispersion of the electromagnetic radiation generated by an object, there are two regimes in the electromagnetic field, the near field (nf) and the far field (ff) regimes which carry all the information coming from the object. The conventional Raman and the SERS technique provide information on the regime ff of light, where due to the diffraction limit; spatial information is lost during the propagation of light from the sample to the detector. The topographic and optical variations of a sample may contain spatial information with dimensions below the wavelength of the exciting light source and this information is available due to the evanescent waves scattered throughout the sample in the nf regime of light. In the TERS experiment, the tip probe is used to collect or generate this information in the nf regime and the Raman signal is guided to the Raman spectroscope for analysis. The information in the nf regime decays very quickly so at a distance of a few tens of nanometers that information fades.

The intensification of the local electric field, $\vec{E}_{loc}$, on the nano-metal surface in SERS and spatial confinement in the near field around the apex of the TERS nano-tip-probe are the factors that allow an optical spatial resolution of more than 10 nanometers. In the Fig. 1.7 and Fig 1.8 shows, an optimal comparison between a conventional Raman spectrum (tip-up) and a TERS spectrum (tip-down). For signal-to-sample separation greater than 30 nm a far field background signal is observed. However, below 30 nm, there is an intensification of the optical signal with spatial correlation of the order of the apex radius of the tip, see Fig. 1.9. The TERS spectra were acquired with AFM technique in feedback tuning fork mode; it shows the characteristic peaks observed in a Malachite green dye sample. In this case, from the increase in Raman intensity between the near and far field

spectrum, a magnification of the signal greater than 10^5, can be estimated, while values greater than 10^8 are attainable [21-29, 56].
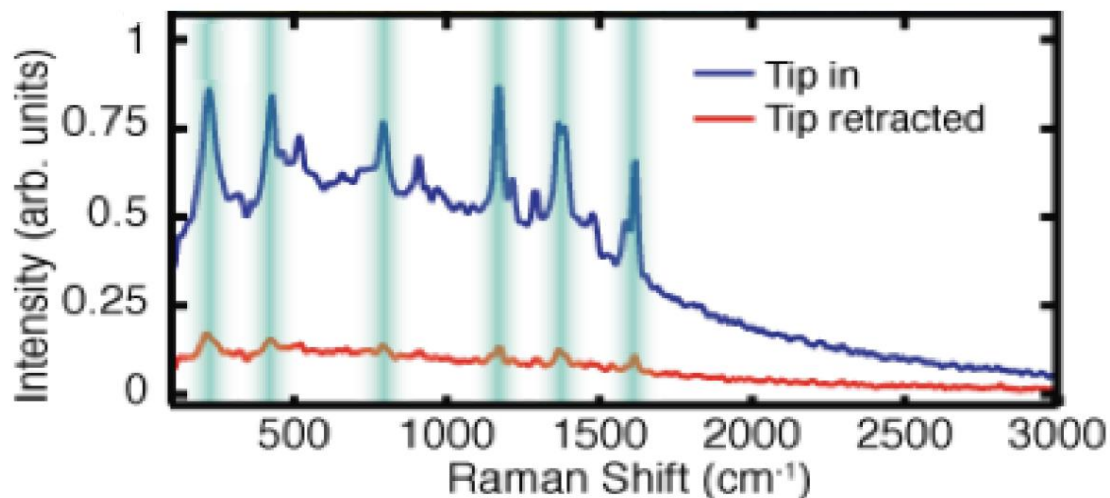
Figure 1.7. Due to the high spatial confinement of the intensified optical field at the apex of the tip, it is observed that the intensified signal would only occur if the sample and the tip have separations less than 30 nm. The spectrum curve was acquired with the tip in shear-force feedback mode, the characteristic peaks are observed for the green Malachite. The near field signal contribution in the TERS becomes apparent when compared to the background signal observed for distant field and / or with the collected tip [21-29, 56].
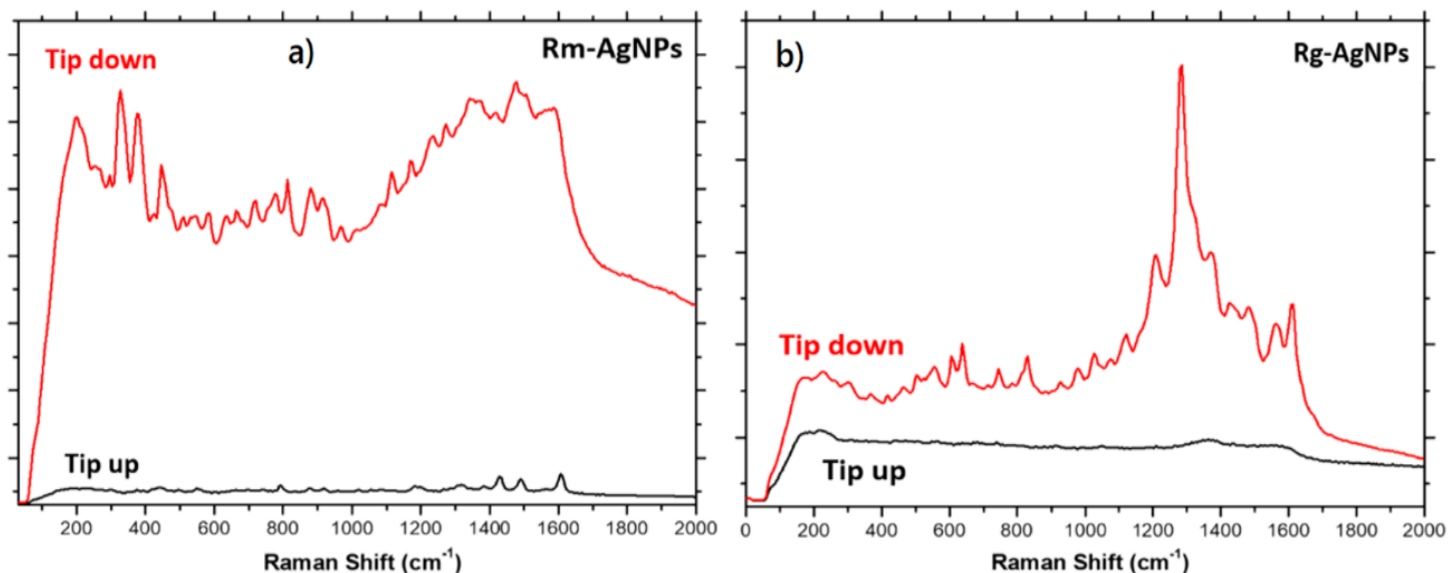
Figure 1.8. Tip-Enhanced Raman Scattering (TERS) of AgNPs produced by the fungi a) Rhodotorula mucilaginosa (Rm-AgNPs) and b) Rhodotorula glutinis (Rg-AgNPs);measures made by the same author; in the chapter 6 discusses the interpretation of these measures.
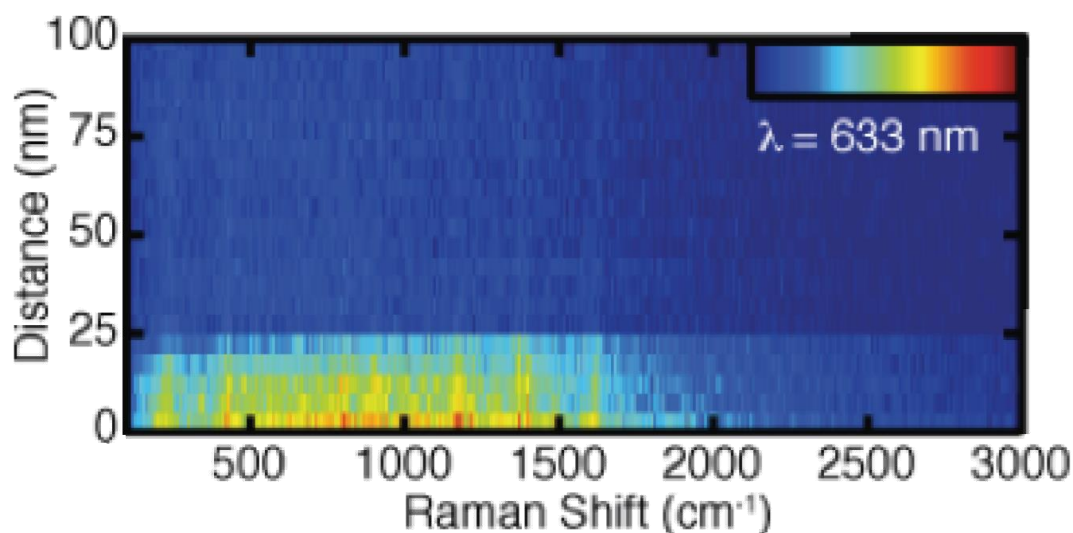
Figure 1.9. Approach curve with spectra acquired for variable tip-sample separation of a monolayer of the dye Malachite Green deposited on an Au substrate. Due to the high spatial confinement of the enhanced optical field at the tip apex, the signal is seen to increase only with tip-sample separations $< \mathbf{25\ nm}$ [21-29, 56].

Finally, the measurements carried out by the SERS technique showed an intensified Raman signal, and the TERS measurements presented a Raman nano metric spatial resolution that make TERS a powerful analytical technique and an important tool for fundamental research in solid state physics in The field of nanoscience. In this work, the basic aspects of improved Raman spectroscopy will be presented as follows: i) a theoretical approach to the fundamental concepts of all these phenomena discussed here oriented towards Raman protein studies, ii) the presentation and discussion of AgNPs biosynthesized by Rhodotorula glutinis and Rhodotorula mucilaginous fungi that show the treatment and interpretation of the results of the measurements made by SEM, AFM and SERS; There is already an article published (see annexed D)), and another in processes to publish (annexed E)). Finally, iii) we proceed to the discussion of the characterizations through the TERS technique, which are not easy to perform for this type of nanomaterials but were successful.

2. THEORETICAL FOUNDATION

2.1. RAMAN SCATTERING.

When an electromagnetic field (light) interacts with a molecule, light can adsorb it, disperse it, or not interact with the molecule. Here, specifically, it is going to refer to the scattering of light, a phenomenon whereby different wavelengths are refracted with different angles when crossing material media; specifically it refers to the scattering of the light that deviates from the direction of propagation of the incident light. If the energy of the photons of an electromagnetic wave closely matches the energy spaces between molecular levels, it can absorb a photon and the molecule crosses to a higher excited energy level (absorption). The interaction of the electric field vector of an electromagnetic wave with the electrons of a compound results in the dispersion of the incident light. Such interactions induce periodic vibrations in the electrons of a compound, producing oscillating electrical moments. Such oscillating electrons are transformed into new sources of radiation emission, that is, scattered light. There are three basic types of dispersion, see Fig. 2.1. **[25-29, 30-37]**.

Stokes $\nu_0 - \Delta\nu$ - Inelastic. Lower frequency (longer wavelength) than the incident light scattering-Stokes Raman.

Rayleigh ν_0 - Elastic. Same frequency (wavelength) as incident light-Rayleigh dispersion.

Anti-stokes $\nu_0 + \Delta\nu$ - Inelastic. Higher frequency (shorter wavelength) than the scattering of the Raman anti-Stokes incident light.

ν_0
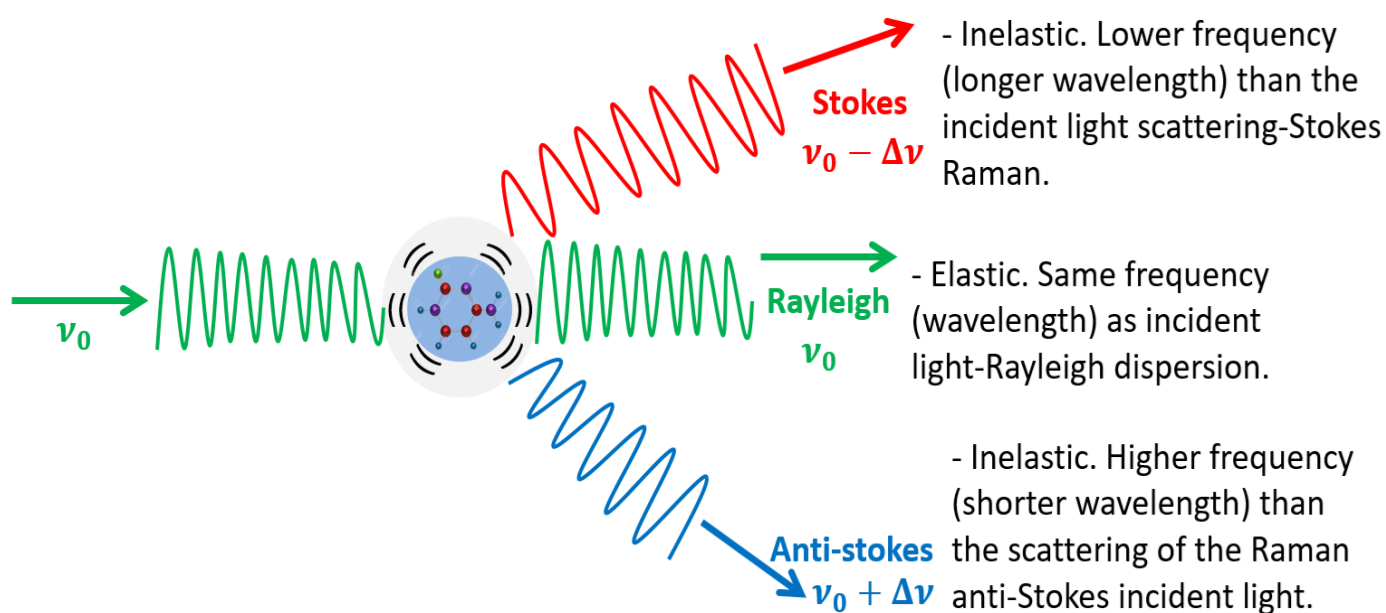
Figure 2.1. Diagrammatic presentation of the three types of light scattering: anti-Stokes Raman scattering, Rayleigh scattering and Stokes Raman scattering.

In an elastic scattering (Rayleigh scattering), the dispersion usually occurs in a different direction and/or polarization; such a process leaves the molecule at the same energy level after the dispersion has occurred (there is no transfer of energy between the molecule and the photon); In other words, Rayleigh scattering does not imply a change in the energy content of the incident light and the scattered light. The objects can be seen as a result of this type of light scattering, see Fig. 2.1. Therefore, no great information about the molecule usually not.

On the other hand, there are two types of inelastic scattering (Raman scattering) that occur in two ways; i) the photon can be scattered with less energy than that of the incident photon (the scattered light has a lower energy than the incident light, therefore, it has a lower frequency, known as scattering stokes) and ii) the photon can be scattered with greater energy than that of the incident photon (the scattered light has a higher energy than the incident light, so it has a higher frequency than the incident light, known as scattering anti-stokes). For the two types of inelastic scattering, the energy difference corresponds to an accompanying transition between two vibrational states in the molecule that implies transitions between the vibration/rotation levels, see Fig. 2.1. For this reason, the analysis of the Raman spectra provides information on molecular properties, such as the shape and type of vibrations. The intensity of the scattered light is influenced by many factors:

1. The size of the illuminated particle or molecule.
2. The location of the observation. The dispersion intensity is a function of the angle with respect to the incident beam.
3. The frequency of the incident light.
4. The intensity of the incident light.

The Raman scattering phenomenon occurs when the incident light in a molecule interacts with the electron cloud of the molecule resulting in a change in the geometry of the electronic cloud, which consequently changes the molecule from its initial vibrational state to a different one, see Fig. 2.2. **[25-29, 30-37]**.
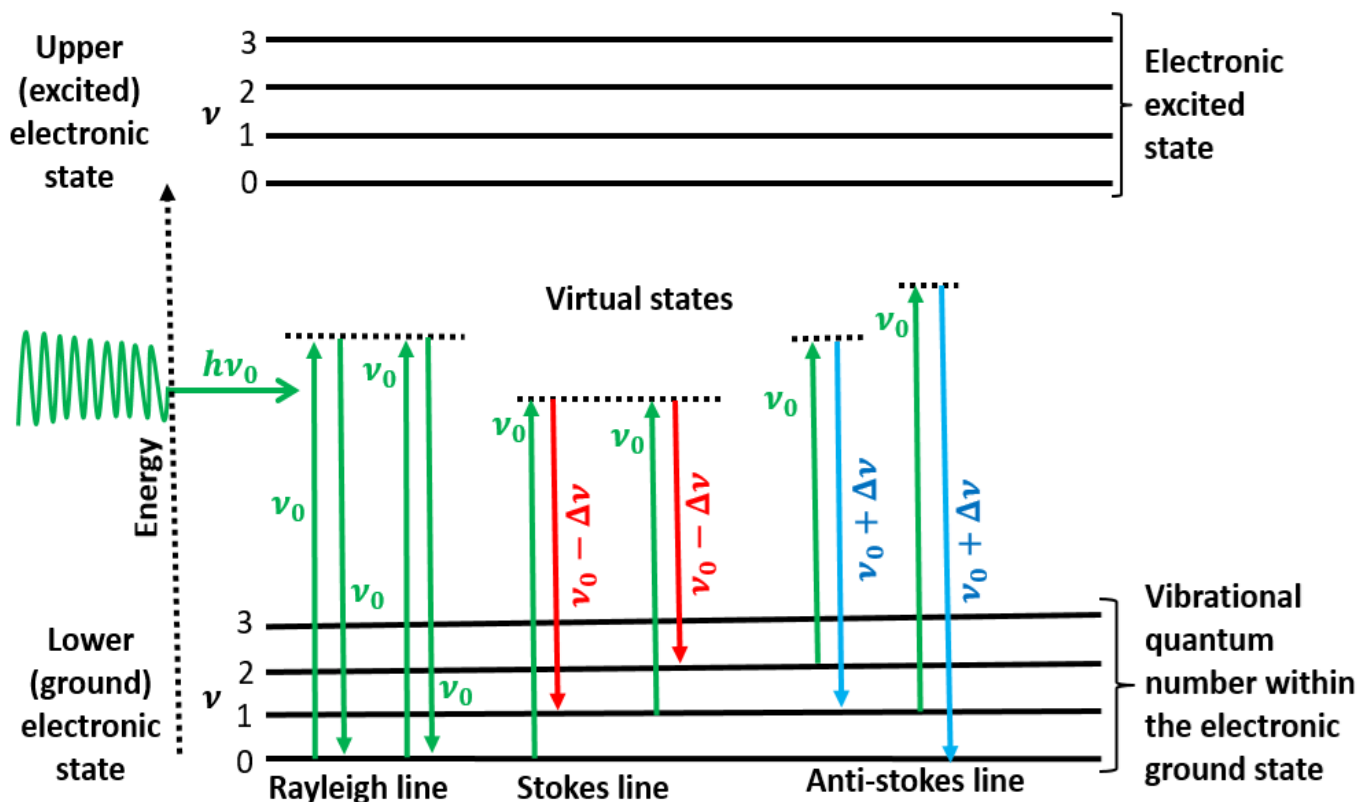
Figure 2.2. Jablonski diagram. The energy diagram of a molecule showing the origin of Raman scattering. Note the different mechanisms of the Stokes and anti-Stokes effects; yet their energy differences (Raman shifts) are the same. The net effect is either an increase or decrease in the vibrational-energy level of a molecule. The molecule is momentarily elevated to a higher energy level (virtual state) but it never reaches an electronic excited state.

In other words, for a molecule to exhibit the Raman effect, the incident light must induce a change in the dipole moment or a change in molecular polarization. The change in polarization can be qualitatively visualized as a geometric change in the shape of the electron cloud. During the process of light scattering, a photon crosses into a "virtual" state and immediately disperses the photon with the same energy (Rayleigh's elastic

scattering) or slightly different (inelastic Raman scattering). This effect mainly involves transitions between the vibrational energy levels of the same electronic state of the molecule (usually the fundamental state), therefore, it belongs to the vibrational spectroscopy.

Consider light scattering as sketched in Fig. 2.3. The scattered light consists of a line at the incident frequency and some weaker lines with higher and lower frequencies as indicated in Fig. 2.4 (a). As an order of magnitude value, the Rayleigh scattering occurs with about $10^{-3}I_0$, Raman scattering with about $10^{-6}I_0$. The physical explanation of the Raman lines (or bands) is straightforward: In Stokes lines, some energy is given to the scattering system (production of phonons); in anti-Stokes scattering, energy is transferred from phonons to the outgoing photon. The three important processes as sketched in Fig. 2.4 (b). **[25-29, 30-37]**.
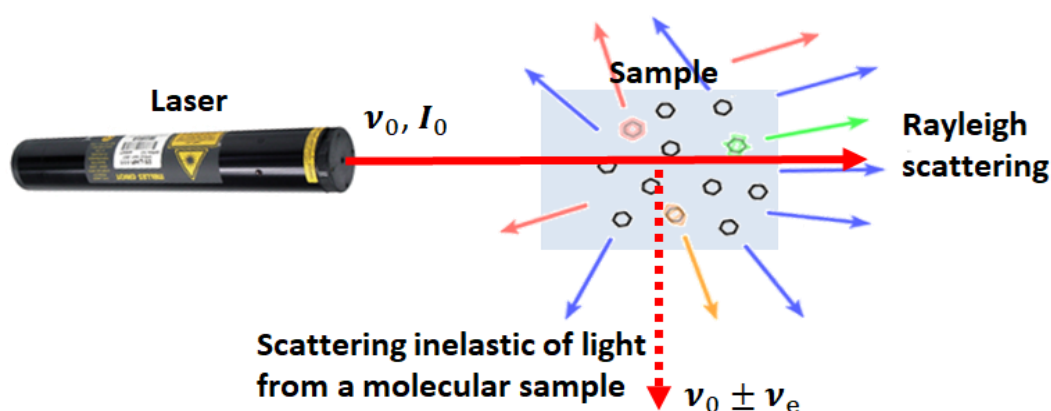
Figure 2.3. Scattering of light from a molecular sample.

The frequency of the Raman scattered light is independent of the wavelength of the incident light. This should not be confused with the fact that the intensity of the Raman scattering is related to the wavelength of the incident light, but in reality, inversely proportional to the wavelength $(1/\lambda^4)$; then, whether a molecule is excited with light (blue 488.0 nm,

green 532 nm or red 632,8 nm), there will be specifically a Raman line $\boldsymbol{\varDelta}$ with exactly the same wavelength difference, see Fig. 2.4. **[25-29, 30-37]**.
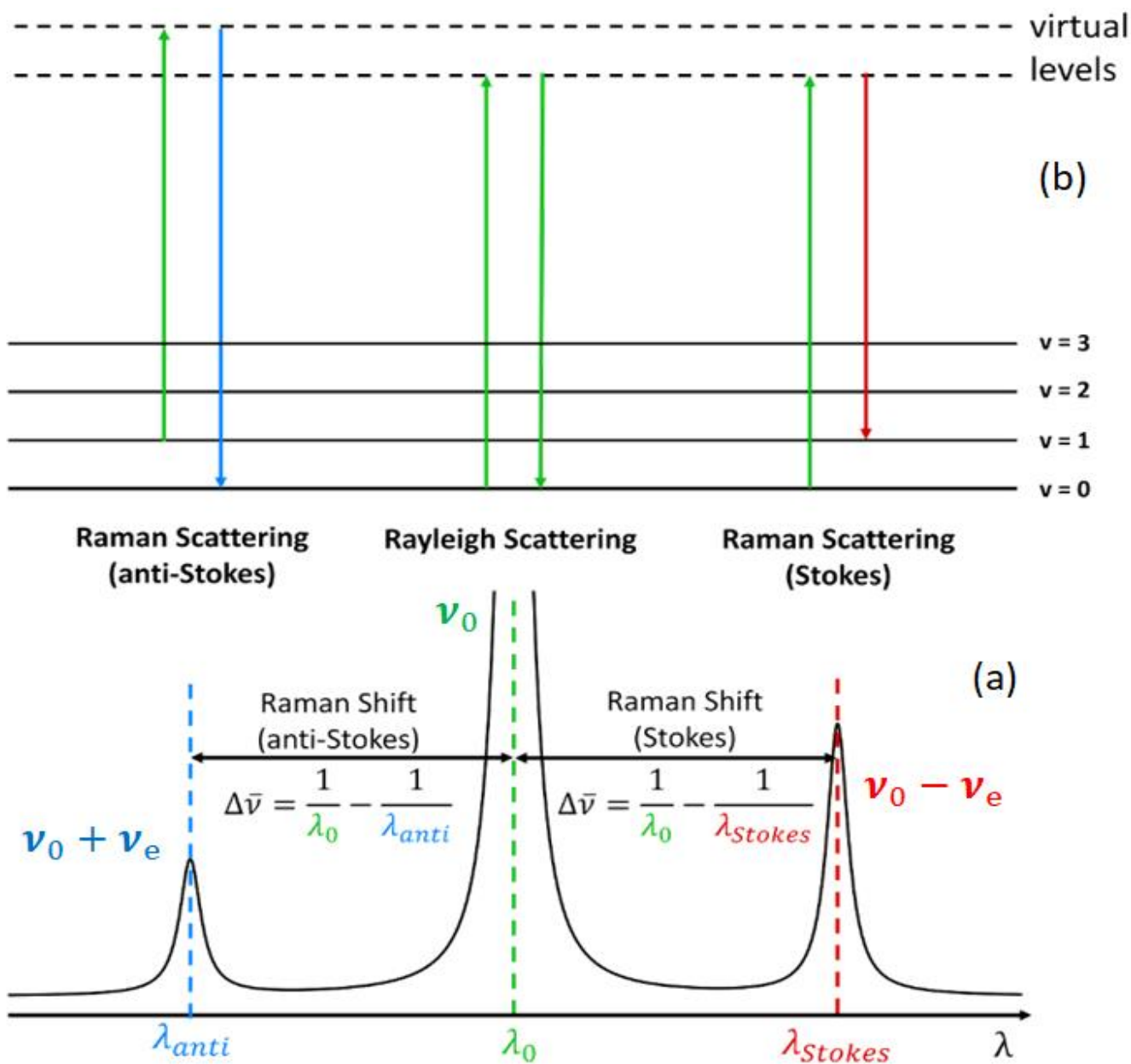
Figure 2.4. (a) Spectrum of Rayleigh and Raman scattering, (b) Change of energy levels from Rayleigh scattering and Raman scattering.

The Stokes and anti-Stokes lines have identical frequency values. However, the Stokes line has a greater intensity than the anti-Stokes line at room temperature. At low temperatures (or an ambient temperature), the vast majority of molecules are at lower vibrational energy levels than at

higher vibrational energy levels. Therefore, a larger fraction of molecules will have Stokes-like transitions than anti-Stokes transitions, and the Stokes line will have greater intensity than the anti-Stokes line. This can also be seen by examining Boltzman's distribution law, which states that the relative population of molecules with more energy increases as the temperature rises [25-29, 32-37].

$$\frac{N_i}{N_0} = e^{-\frac{\Delta E}{k_B T}}$$

Being N_i the number of molecules in the energy state E_i and N_0 is the number of molecules in the energy state E_0; N_i/N_0 is the fraction of molecules in the energy state E_i; k is Boltzman's constant; T is the temperature on the Kelvin scale; and ΔE is the energy difference between the energy states E_i and E_0. Therefore, the intensity of the anti-Stokes line increases (or the intensity of the Stokes line variation) as the temperature rises. The relationship between anti-Stokes and Stokes line are directly related to the fraction of molecules in higher vibrational energy levels.

The Raman Scattering process is intrinsically weak. Since only a very small fraction of light is dispersed inelastically (1 in 10^7 photons is Raman), so Raman lines are usually very weak (only 10^{-6} of the intensity of the Rayleigh line or usually amounts to just $10^{-6} \sim 10^{-12}$ of that of the incident light). Most of the scattered light is the same as the original incident light in terms of photonic energy. This is why a laser is used as a light source: it is an intense and monochromatic light source. Because both, Stokes line and the anti-Stokes line, imply the same difference in vibrational energy (Fig. 2.4.), the difference between the incident light frequency and the scattered frequency in Stokes and the anti-Stokes dispersion is identical. That is, the difference in frequency for the dispersion of Stokes and anti-Stokes is symmetric [37-42].

The intensity of a Stokes line, I_S, is much stronger than the intensity of the anti-Stokes line, I_{AS}, and the ratio of their intensities can be expressed as:

$$\frac{I_S}{I_{AS}} \sim e^{-\frac{\hbar\omega}{k_B T}} \gg 1$$

Where k_B and T stand for the Boltzmann's constant and the absolute temperature, respectively.

2.2. RAMAN DIFFERENTIAL CROSS-SECTION.

Since Raman scaling is a weak phenomenon, it is very important to understand the concept of differential cross section for a given molecule; that is, how many incident photons are absorbed and/or how many are scaled through the Rayleigh or Raman processes. For optical absorption or scattering, the cross section σ_{abs} simply relates the incident power density to the power absorbed by the P_{abs} molecule. The radiation profile (scattering) can be characterized by the angular dependence of the dispersed power. Two angles are required for this to specify a direction $\Omega \equiv (\theta, \phi)$, see Fig. 2.5. The angular dependence of the scattered power can then be formally defined as:

$$\frac{dP_{abs}}{d\Omega}\left[\frac{W}{sr}\right] = \frac{d\sigma_{abs}}{d\Omega}\left[\frac{m^2}{sr}\right]$$

Where the function Ω (solid angle) is called the differential scattered power that by analogy can therefore define a Raman differential scattering cross-section.

$$\frac{dP_{sca}}{d\Omega} = \frac{d\sigma_{sca}}{d\Omega} S_{inc}$$

This defines the efficiency that a particular molecule (with a random orientation with respect to the polarization of the incident field) can scatter Raman light; being P_{sca} is the power of the Raman scattering, that is the

proportional to the number of photons per unit time involved in the process, S_{inc} is the incident power density and $d\Omega$ is the solid angle (sr=steradian).

The Raman cross-section depends on the excitation wavelength and the refractive index of the medium (environment). Raman scattering cross-sections per molecule typically is the range between 10^{-31} and $10^{-29} \frac{cm^2}{sr}$, to the Surface-Enhanced Raman Spectroscopy (SERS) may have a cross section of $10^{-16} \frac{cm^2}{sr}$, this technique will be discussed later [25-29, 32-37].
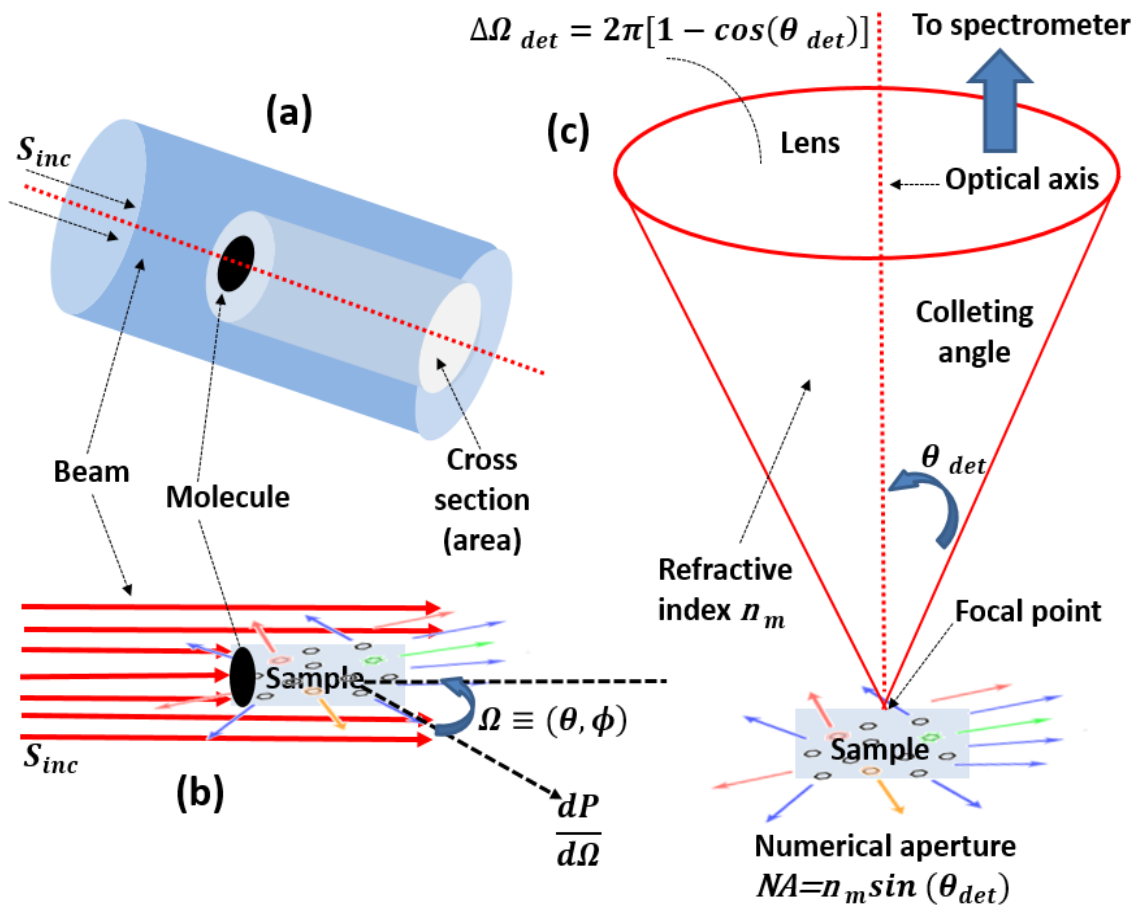
Figure 2.5. (a) Schematic representation of the concept of cross-section, as an area cut out from the incident beam. (b) Similar schematic illustrating the differential scattered power. (c) Schematic representation of the collection optics in a typical Raman scattering experiment. The laser is normally focused to a small spot (typically $1 \sim 10\mu m$ diameter depending on the focusing optics). Note that in many implementations the collecting optics is also used for excitation (in a back-scattering configuration).

2.3. MECHANICS OF RAMAN SCATTERING.

So far, Stokes and anti-Stokes Raman scattering have been explained qualitatively. The scattering of light by a molecule can be expressed easily in terms of classical mechanics. Since the mathematics involved is relatively easy and all three effects (Rayleigh scattering, Stokes, and anti-Stokes Raman scattering) can be explained by one equation, the classical-mechanical treatment of scattering is presented here. If a molecule interacts with light, the electric field of photons will exert oppositely directed forces on the electrons and the nuclei. As a result, the electrons will be displaced relative to the nuclei, and the polarized molecule will have an induced dipole moment caused by the external field. The induced dipole moment $\vec{\mu}_{ind}$ is proportional to the electric field and to a property of the molecule called the polarizability $\overset{\leftrightarrow}{\alpha}$; In a nutshell, focusing a beam with frequency ν_i on a material medium that has a polarizability $\overset{\leftrightarrow}{\alpha}$ will induce a dipole moment $\vec{\mu}_{ind}$:

$$\vec{\mu}_{ind} = \overset{\leftrightarrow}{\alpha}_{mol} \cdot \vec{E}_{loc}$$

Being $\overset{\leftrightarrow}{\alpha}_{mol}$ is a proportionality constant (a tensor) that describes the deformation-related molecular properties of a chemical bond when an electric field $\vec{E}_{loc}$ is incident on it. The electric field is an oscillating function dependent upon the frequency of the light ν_0 [31-37].

$$\vec{E}_{loc} = \vec{E_0} \, cos \, (2\pi\nu_0 t)$$

Substituting in the dipole moment:

$$\vec{\mu}_{ind} = \overset{\leftrightarrow}{\alpha}_{mol} \cdot \vec{E_0} \, cos(2\pi\nu_0 t)$$

The polarizability $\overset{\leftrightarrow}{\alpha}_{mol}$ is dependent upon the position of the nuclei in the molecule. For a molecule containing N atoms, there are $3N$ degrees of freedom available to the nuclei. Of these, $3N - 6$ ($3N - 5$ for a linear molecule) result in vibrations of the molecule. In general, the vibrational motion of all but the simplest molecules is quite complicated. Instantaneous

positions of the nuclei can therefore be expressed relative to their equilibrium positions in terms of the normal coordinates Q_i where $i = 1, 2, \cdots, 3N - 6$. Considering a diatomic molecule with the single normal coordinate Q_1, the dependency of $\overleftrightarrow{\alpha}_{mol}$ on Q_1 is expressed as a series expansion:

$$\overleftrightarrow{\alpha}_{mol} = \alpha_0 + \left(\frac{\partial \alpha}{\partial Q_1}\right)_0 Q_1 + \cdots$$

$$\overleftrightarrow{\alpha}_{mol}(Q) = \alpha(q - q_{eq}) = \alpha_0(q - q_{eq}) + \left(\frac{\partial \alpha(q - q_{eq})}{\partial q}\right)_0 (q - q_{eq}) + \cdots$$

Where α_0 is the equilibrium value of the polarizability. To be active in Raman, the polarization $\overleftrightarrow{\alpha}_{mol}(Q) = \overleftrightarrow{\alpha}(q - q_{eq})$ of a bond must vary as a function of the distance between nuclei. The position of the nuclei is time dependent because the molecule is vibrating with frequency ν_e. Information on the frequency of vibration can be obtained from knowledge of the forces between the vibrating nuclei, and the application of the classical mechanics of small vibrations. This motion can be expressed as:

$$Q_1 = Q_1^0 cos(2\pi\nu_e t)$$

Where Q_1^0 is the maximum vibrational amplitude. It is seen, therefore, that $\overleftrightarrow{\alpha}$ also oscillates at the frequency ν_e; substituting:

$$\vec{\mu}_{ind} = \overleftrightarrow{\alpha}_{mol} \cdot \vec{E}_{loc}$$

$$\vec{\mu}_{ind} = \left[\alpha_0 + \left(\frac{\partial \alpha}{\partial Q_1}\right)_0 Q_1\right] \vec{E_0} \, cos\,(2\pi\nu_0 t)$$

$$\vec{\mu}_{ind} = \left[\alpha_0 + \left(\frac{\partial \alpha}{\partial Q_1}\right)_0 Q_1^0 cos(2\pi\nu_e t)\right] \vec{E_0} \, cos\,(2\pi\nu_0 t)$$

Using $cos\theta cos\varphi = \frac{1}{2}[cos(\theta + \varphi) + cos(\theta - \varphi)]$,

$$\vec{\mu}_{ind} = \underbrace{\alpha_0 E_0 cos\,(2\pi\nu_0 t)} + \frac{1}{2}E_0 Q_1^0 \left(\frac{\partial \alpha}{\partial Q_1}\right)_0 [\underbrace{cos(2\pi t(\nu_0 + \nu_e)} + \underbrace{cos(2\pi t(\nu_0 - \nu_e)}]$$

| **Rayleigh line** | **Anti-stokes line** | **Stokes line** |

This classical derivation for a diatomic molecule predicts three basic lights scattering modes due to the induced dipole moment $\vec{\mu}_{ind}$ oscillating at frequency ν_1:

1- The α_0 term produces scattered light unshifted in frequency (Rayleigh scattering).

2- If $\frac{\partial \alpha}{\partial Q_1} \neq 0$, Raman scattering occurs, and incident light of frequency ν_0 is shifted to scattered light with higher frequency $\nu_0 + \nu_e$, anti-Stokes and lower frequency $\nu_0 - \nu_e$, Stokes.

For a polyatomic molecule containing N atoms, there are $3N - 6$ vibrational modes:

$$\vec{\mu}_{ind} = \alpha_0 E_0 cos\,(2\pi\nu_0 t) + \frac{1}{2}\sum_{i=1}^{3N-6} E_0 Q_1^0 \left(\frac{\partial \alpha}{\partial Q_1}\right)_0 [cos(2\pi t(\nu_0 + \nu_e) + cos(2\pi t(\nu_0 - \nu_e))]$$

The first term refers to Rayleigh scattering (elastic), the second term to anti-Stokes lines, and the third term to Stokes lines. The fundamental difference between Raman and infrared spectroscopy is that $\left(\frac{\partial \alpha}{\partial Q_1}\right)_0$ does not equal zero for Raman scattering [31-37]. This means that a molecule must have a change in its polarizability as it vibrates in order to be Raman active. These expressions is valid for molecules with isotropic polarizability and states that the dipole-moment vector $\vec{\mu}_{ind}$ induced by the electric-field vector $\vec{E}$ is parallel to the electric-field vector. This is not true in general, as the polarizability of most molecules is anisotropic, and the induced-dipole-moment vector points in a different direction than the electric-field vector. A vector is a quantity that has a magnitude as well as a direction. The polarizability should therefore properly be expressed as the symmetric matrix:

$$\vec{\mu}_{ind} = \overleftrightarrow{\alpha}_{mol} \cdot \vec{E}_{loc}$$

The induced dipole moment $\vec{\mu}_{ind}$ and the incident local electric field $\vec{E}_{loc}$ have vector properties, while the molecule's electronically polarized $\overleftrightarrow{\alpha}_{mol}$ is a range two tensor with nine components. The polarizability tensor is often symmetric and only six components are relevant.

$$\begin{bmatrix} \mu_x \\ \mu_y \\ \mu_z \end{bmatrix}_{ind} = \begin{bmatrix} \alpha_{xx} & \alpha_{xy} & \alpha_{xz} \\ \alpha_{yx} & \alpha_{yy} & \alpha_{yz} \\ \alpha_{zx} & \alpha_{zy} & \alpha_{zz} \end{bmatrix}_{mol} \begin{bmatrix} E_x \\ E_y \\ E_z \end{bmatrix}_{loc}$$

Rather than as a constant. Using this matrix expression for $\overleftrightarrow{\alpha}_{mol}$, the components of $\vec{\mu}_{ind}$ become:

$$\mu_x = \alpha_{xx}E_x + \alpha_{xy}E_y + \alpha_{xz}E_z$$

$$\mu_y = \alpha_{yx}E_x + \alpha_{yy}E_y + \alpha_{yz}E_z$$

$$\mu_z = \alpha_{zx}E_x + \alpha_{zy}E_y + \alpha_{zz}E_z$$

Thus, the induced dipole moment should be expressed as:

$$\vec{\mu}_{ind} = \begin{bmatrix} \alpha_{xx} & \alpha_{xy} & \alpha_{xz} \\ \alpha_{yx} & \alpha_{yy} & \alpha_{yz} \\ \alpha_{zx} & \alpha_{zy} & \alpha_{zz} \end{bmatrix}_{mol} \cdot \vec{E}_{loc}$$

The polarizability of the molecule corresponds to a dipole transition moment.

$$< \alpha_{ij} >_{jf} = \int \Psi_i \, \alpha_{ij} \, \Psi_j d\tau$$

For each transition between the vibrational states i and f the tensor components. In Raman effect the components α_{ij} that relate the vectors $\vec{\mu}_{ind}$ and $\vec{E}_{loc}$ are symmetrical $\alpha_{ij} = \alpha_{ji}$.

$$< \alpha_{ij} >_{jf} = \int \Psi_i \left(\alpha_0(Q) + \left(\frac{\partial \alpha(Q)}{\partial q}\right)_0 Q \right) \Psi_j d\tau$$

$$< \alpha_{ij} >_{jf} = \alpha_0(Q) \underbrace{\int \Psi_i \Psi_j d\tau}_{= 0} + \underbrace{\left(\frac{\partial \alpha(Q)}{\partial q}\right)_0}_{\neq 0} \underbrace{\int \Psi_i Q \Psi_j d\tau}_{\text{Selections rules}}$$

Due to the orthogonality of the states $\boldsymbol{\Psi_i}$ and $\boldsymbol{\Psi_j}$; $\int \boldsymbol{\Psi_i \Psi_j} d\tau = \mathbf{0}$; This integral will be nonzero if the integrand is a fully symmetrical function which implies in terms of group theory that the final state of the transition must have a symmetry equal to the coordinate, see Fig. 2.6.
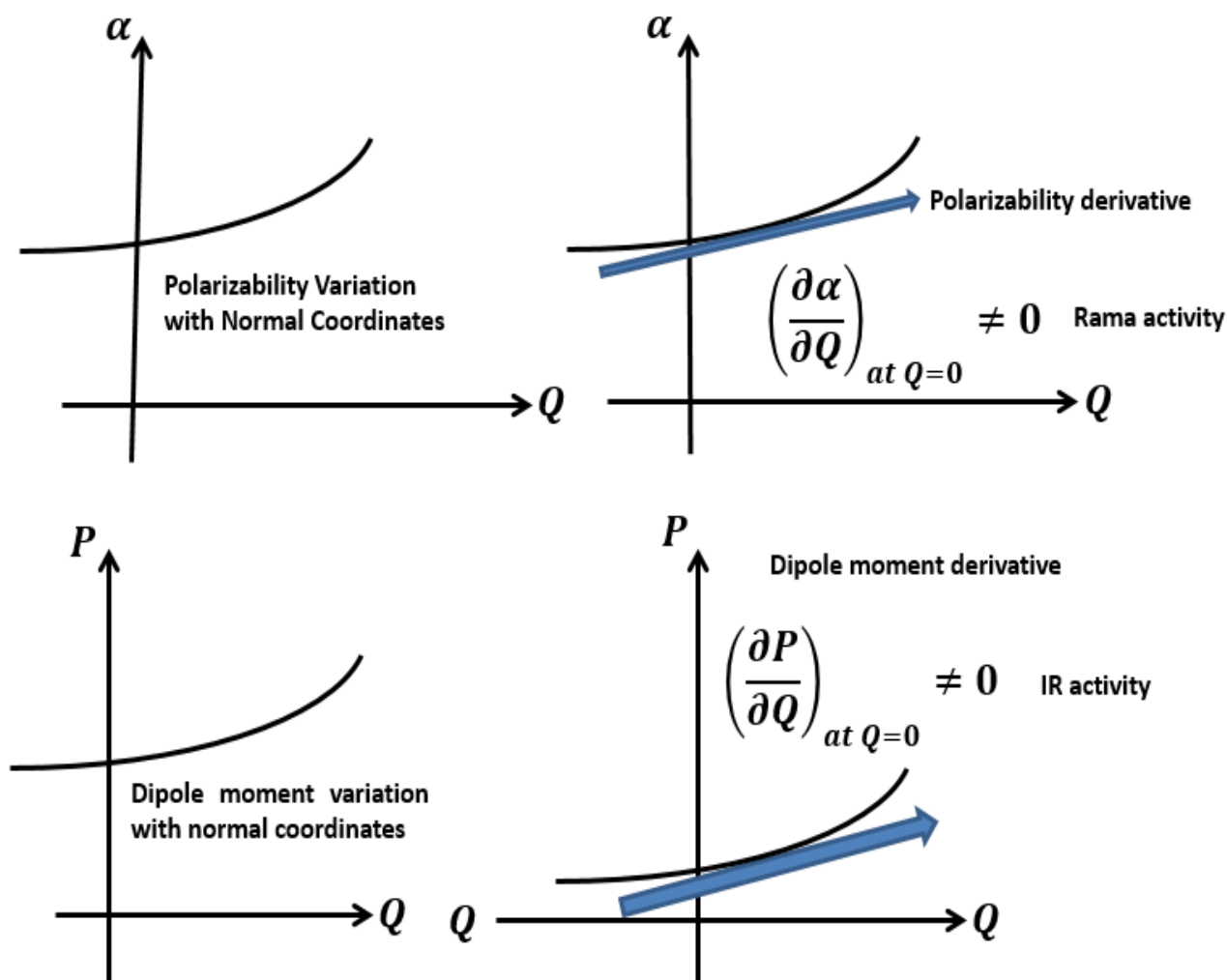
Figure 2.6. When the Raman is active or not.

The molecular polarizability $\overleftrightarrow{\boldsymbol{\alpha}}_{\boldsymbol{mol}}$ is a specific variable function according to the molecule that is a tensor; some of its components may vary during the vibration of the nuclei around their equilibrium position in the electromagnetic field of electrons. In a quantum mechanical treatment of polarizability that when using the simplified theory dependent on second

order time, the Raman transition between states $|i>$ and $|f>$ can be expressed by the tension element:

$$< \alpha_{\rho\sigma} >_{jf} = \sum_{s \neq i,f} \left[\frac{<i|D_\sigma|s><s|D_\rho|f>}{E_i - E_f + h\nu + i\Gamma} + \frac{<i|D_\rho|s><s|D_\sigma|f>}{E_i - E_f - h\nu + i\Gamma} \right]$$

The sum travels all the excited states s of the molecule, the operators D_ρ and D_σ are components of the electric dipole moment operator and Γ is a "damping factor" that may be related to the width of the vibratory levels of the excited state [31-37].

The change of polarization by a given vibratory mode i can be expressed by the polarization derivative (also called a Raman tensor of the normal mode i):

$$R_i(\nu_{inc}) = \left(\frac{\partial \alpha(\nu_{inc})}{\partial Q_i} \right)_{Q_i=0}$$

Each normal mode has its own Raman tensor, that is, if there are N atoms there will be $3N - 5$ Raman tensors for a linear molecule and $3N - 6$ for a nonlinear molecule. The intensity of the Raman dispersion is then proportional to the square of the induced dipole moment, which is the square of the polarization derivative. The selection rules say that if a transition is allowed or prohibited and the allowed transition has a high probability of occurring and will result in a strong band; but the probability of a forbidden transition is so low that the transition will not be observed, in a nutshell, the selection rule for an active Raman vibration means that there will be a change in polarization during vibration.

$$\frac{\partial \alpha}{\partial Q_i} \neq 0$$

The geometry of the molecule is what will predict which bands will be active in Raman. The symmetry elements of a molecule (i.e. center, axes or planes) are associated with the symmetry operations that define all

vibratory movements. Then, the molecules with symmetry elements in their structure define the pattern of their normal vibrational modes. The symmetry of normal vibrational modes influences a Raman tensor and, consequently, the Raman activity of these vibrations. Depending on the degree of polarization change by a particular vibratory mode, it is associated with the intensity of a particular vibrating band in the Raman spectrum. In practice, if a vibration does not greatly change the polarization, then the polarization derivative (and the Raman tensor) will be close to zero and the intensity of the Raman band will be low. The vibratory mode that strongly changed the polarization will be clearly seen in the Raman spectrum as a strong band [31-37].

2.3.1. MOLECULAR VIBRATIONS AND VIBRATIONS STATES.

If N atoms constitute a molecule, there are $3N$ degrees of freedom of movement, three are translational and three are rotational. The remaining $3N(total) - 3(translational) - 3(rotational)$ degrees of freedom are movements where the distances between the atoms change: the length between the chemical bonds and the angles between them. All vibrations of an idealized molecule result from the superposition of $3N - 6$ normal vibrations that do not interact with each other. Many biological molecules are macromolecules, which contain a large number of atoms. This means that they have a tremendously large number of fundamental vibrations. It is impossible to identify all vibrations for a biological molecule. Nevertheless, the understanding of basic vibrational modes in a relatively simple molecule is helpful.

If it have a biomolecule, it is assumed that the energy landscape of it as shown in Fig. 2.7, where the energy of the biomolecule is represented as a function of the conformational coordinate cc. Two types of excitations

can occur. The system can remain within a conformational sub-state (CS) or jump from one CS to another CS. In the first case, the system can be excited within its own vibration levels CS; in the second, there is a conformational excitation. Both are important for the function of biomolecules **[31-37]**.

The total number of vibrations for a nonlinear molecule is $3N - 6$, where N is the number of atoms. Many biological molecules are macromolecules, which contain a large number of atoms. This means that they have a tremendously large amount of fundamental vibrations. It is impossible to identify all the vibrations for a biological molecule. However, understanding basic vibrational modes in a relatively simple biomolecule is useful. In this section, different types of vibrations in diatomic molecules, triatomic molecules, methyl group and cyclic compounds are briefly reviewed. The discussion with the diatomic molecules begins.
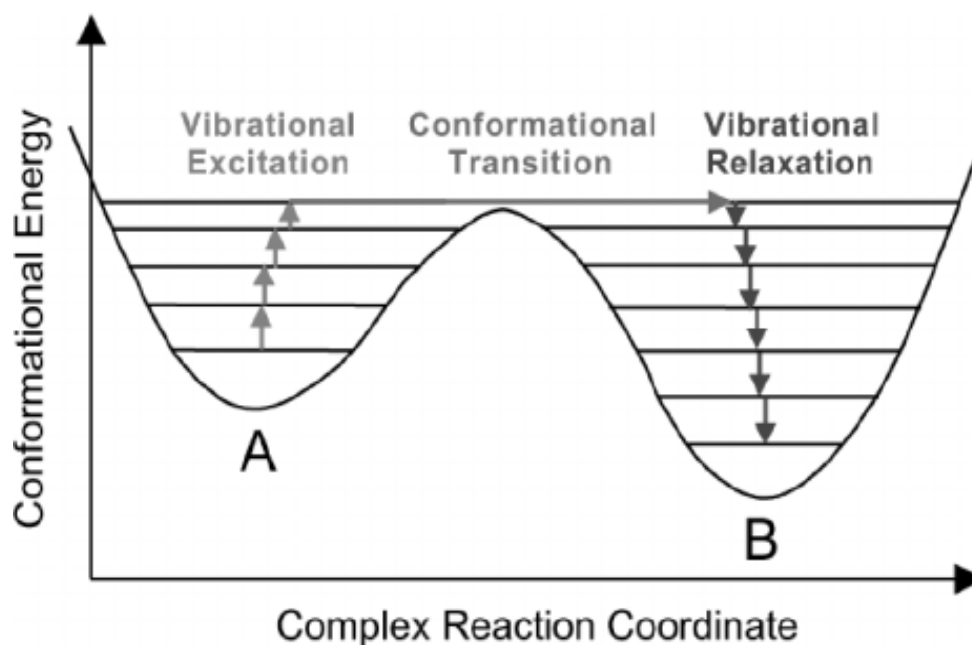
Figure 2.7. Vibrational and conformational excitations.

The vibrations that occur in a molecule are small oscillations of atoms around their equilibrium positions. In a classical mechanical model, the harmonic oscillator can describe the vibrations of the molecules quite accurately. Accordingly, the frequency of a particular vibration $h\nu$ is related to the reduced masses of mixed vibrating atoms and the forces of their interactions described by the force constants f. A vibration or oscillation consists in the transformation, alteration, disturbance or fluctuation of a system over time in which a particle or atom when it loses its equilibrium position due to an external agent returns to it through a restitutive force of type of sinusoidal type. The vibration can be visualized, see Fig. 2.8, in a simpler way like that of two particles connected by a spring. When the spring is stretched and released, the two particles that represent atomic nuclei make a stretching vibration [31-37].
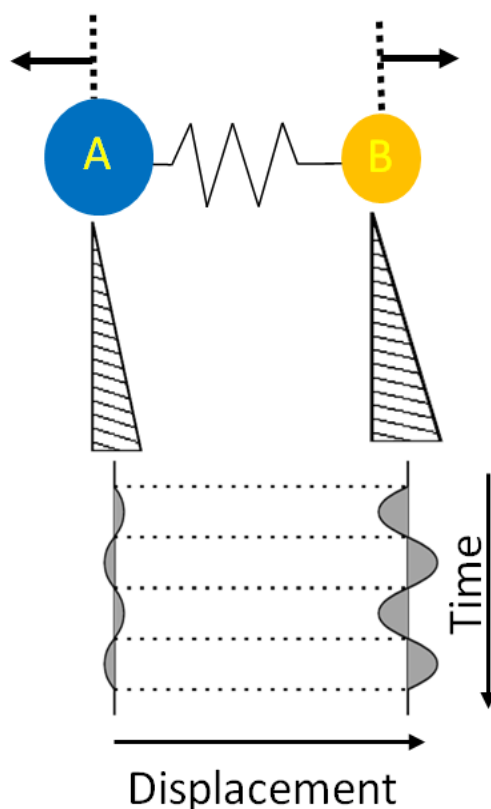
Figure 2.8. Vibration of two atoms can be visualized as the vibration of two connected by a spring.

Taking as a model the elastic vibration described by Hooke's law that depends on the masses of the particles and the constant force of the spring, and taking as a basic system two atoms A and B that are vibrating, the vibration mode is related to the mass reduced $\mu = M_{red}$ of the atoms and the constant force k by:

$$\nu_{vib} = \sqrt{\frac{k}{\mu}}$$

This formula has a very important consequence in the Raman spectra: the lighter the atoms, the higher the vibration frequencies. The constant force is related to the bond force: the stronger the link, the higher the vibration frequency. Note that the vibration frequency is independent of the energy levels between which transitions take place. Vibrational analysis refers to the study of these normal vibrational modes. It is possible to define mass-weighted normal mode coordinates that provide an equivalent description of molecular vibrations. The normal mode coordinate Q_i a given normal mode i ($i = 1, \ldots, 3N - 6$) corresponds to a specific vibratory pattern of equilibrium displacement) in the molecule, for which all atoms oscillate at the same frequency ν_i.

In systems containing more than two atoms, the vibrations can be symmetric or asymmetric with respect to the center of charges of the electronic cloud. If there is no change in the angle between any of the bonds and the plane defined by the remaining atoms, they are classified as "in plane". The opposite case is known as "out of plane" vibrations. Depending on the geometric relationship between the transition moment for a specific vibratory mode and the axis of symmetry for the mode, the vibratory modes can also be classified as parallel or perpendicular **[31-37]**.

There are three basic types of the vibrational normal modes, see Fig. 2.9:

- Bond stretching or Valence stretching vibrations (**ν**); corresponding to the elongation and contraction of a bond between two neighbouring atoms without any change in the bonding angle.

- Bond bending or deformation vibrations (**δ**) often referred to as scissoring, wagging, rocking and twisting. involving movements in the direction perpendicular to that of the chemical bond between two neighboring atoms:

• The scissoring vibration involving in plane movement of atoms changing the angle between bonds.

• The wagging vibration is an in phase, out of plane movement of atoms while other atoms of the molecule are in the plane.

• The rocking vibration, atoms swing back and forth in phase in the symmetry plane of the molecule.

• The twisting vibration involves the twisting of a bond along its main axis.

- Torsion vibration involves the twisting of a bond along its main axis.
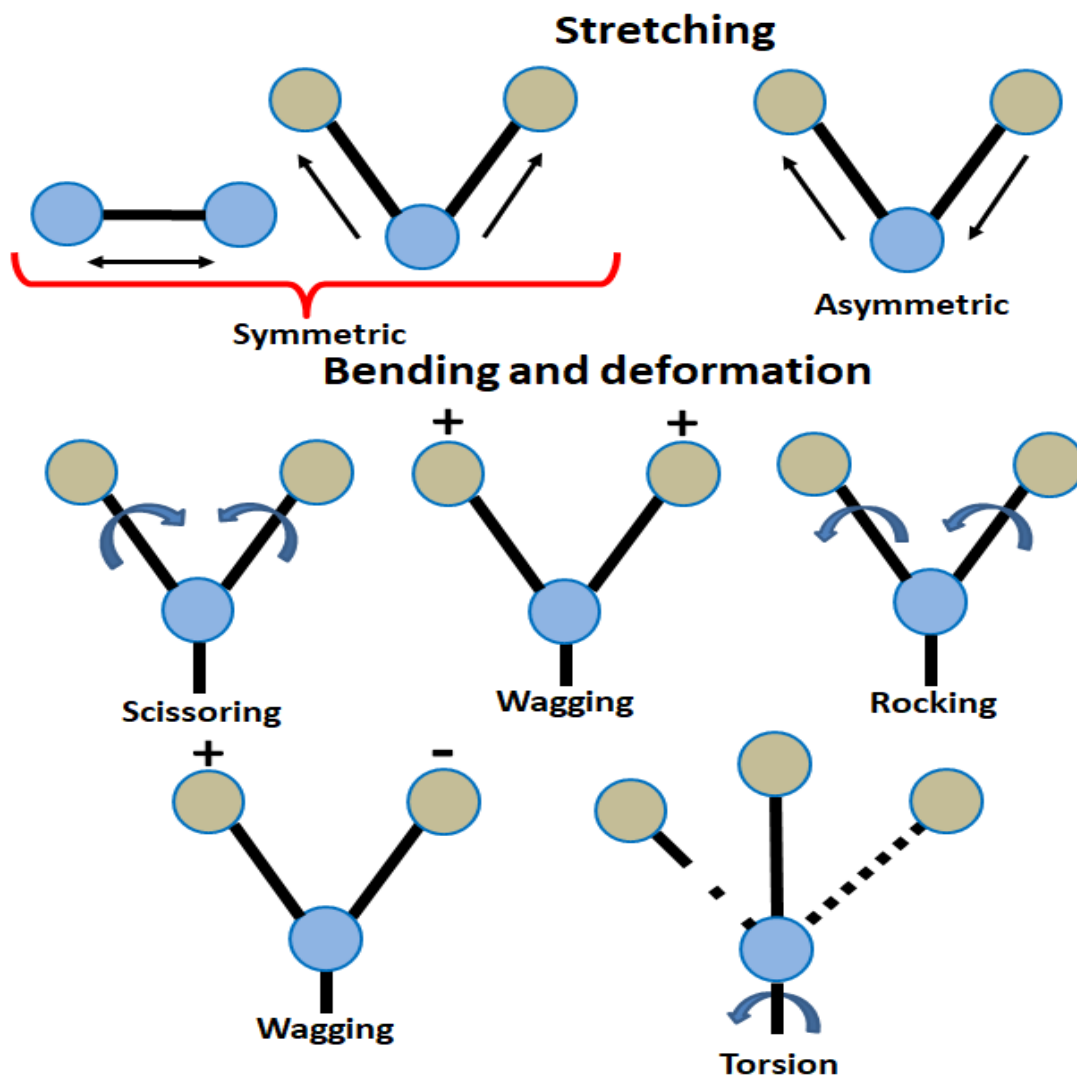
Figure 2.9. Basic types of the normal vibrational modes. Arrows show directions of deflections of atoms, plus and minus signs indicate deflections of atoms above and below the plane **[31-37]**.

For a diatomic molecule consisting of two atoms with masses M_1 and M_2; $\mu = \frac{M_1+M_2}{M_1 M_2}$:

$$\nu_{vib} = \frac{1}{2\pi}\left(\frac{k}{\mu}\right)^{1/2}$$

The Schrödinger equation can be written for their center of mass, M, as:

$$\frac{\hbar}{2M}\nabla(R)^2\psi + [E - V(R)]\psi = 0$$

Where $M = \frac{M_1 M_2}{(M_1 + M_2)}$ is the reduced mass and R the distance between the two nuclei. To find the vibrational energy levels, the form of $V(R)$ must be know. The potential energy $V(R)$ for the harmonic oscillation of two particles is $V = \frac{1}{2}kx^2$ where x refers to the displacement of two particles from their equilibrium positions. A molecule has discrete quantum energy levels instead of continuous energy states as in the case of two particles connected by a spring. In the simplest case, we can take $V(R)$ to be parabolic:

$$V(r) = V_0 + \frac{1}{2}k_v(R - R_e)^2$$

Here k_v is a constant and k_v is the equilibrium distance. A quantum-mechanical treatment of the harmonic-oscillator problem gives a set of states of motion of the atoms with energies given by the formula in these conditions:

$$E_v = v + \frac{1}{2}\hbar\omega_e$$

Where ω_e is the vibrations frequency of the oscillator and $v = 0, 1, 2, 3 \cdots$ is the vibrational quantum number. v Is governed by the selection rule $\Delta v = \pm 1$. The levels will be equally spaced with a separation of 1 quantum of vibrational energy $\hbar\omega_e$. The harmonic-oscillator problem is applicable to polyatomic molecules as well, since the vibrations of a larger molecule can be separated into normal modes of vibration, each of which can be treated independently as simple harmonic motion. A normal mode of vibration is a special combination of movements of the nuclei of the molecule that can be treated independently [31-37].

The total vibrational energy of the molecule is only the sum of the vibrational energy of $E_v = v + \frac{1}{2}\hbar\omega_e$ for each normal mode. The normal coordinate is a set of displacements of N vectors that define the movement of each of the atoms of the molecule to the normal mode. Morse introduced a more realistic potential, see Fig. 2.10:
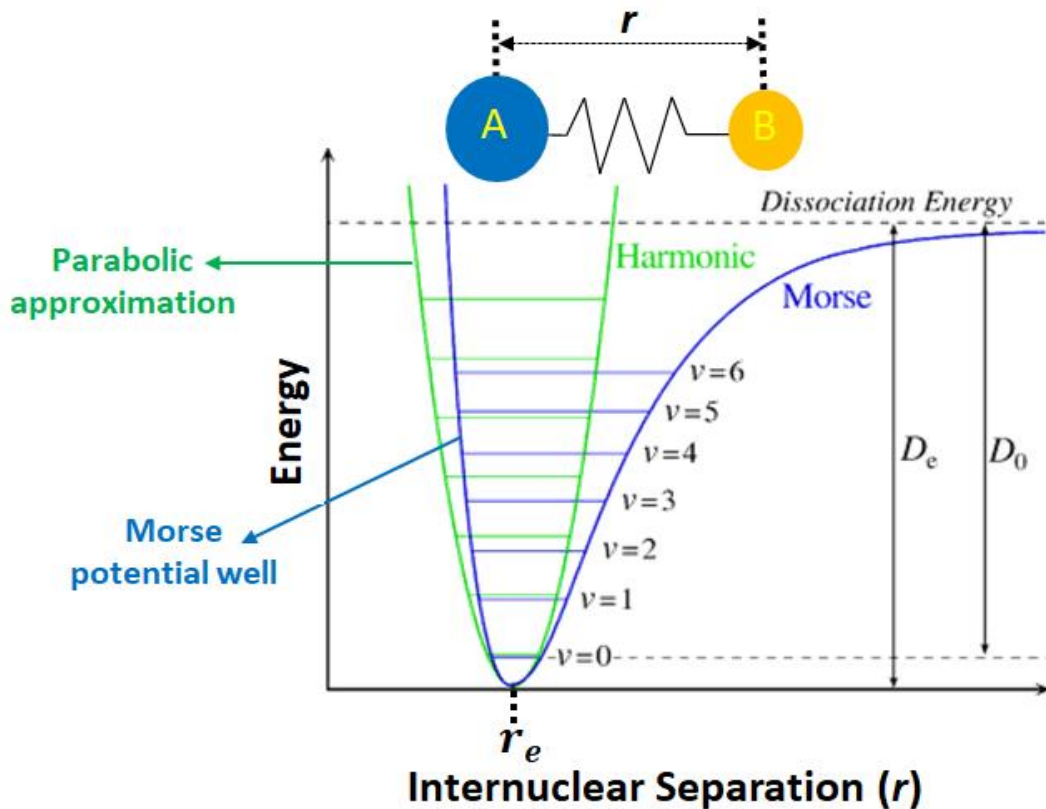
Figure 2.10. Morse potential.

$$V(r) = D_e\left(1 - e^{(-a(R-R_e))}\right)^2$$

Where D_e is the dissociation energy of the diatomic molecule and the coefficient a is connected to the force constant k_v, by $D_e a^2 = \frac{k_v}{2}$. Them:

$$E_{vib} = \hbar\omega_e\left(v + \frac{1}{2}\right) - x_e\hbar\omega_e\left(v + \frac{1}{2}\right)^2$$

With $\omega_e = a\left(\frac{2D_e}{M}\right)^{1/2}$ and $x_e = \left(\frac{\hbar\omega_e}{4D_e}\right)$, being x_e the inter-nuclear distance.

2.3.2. RAMAN SPECTROSCOPY FOR BIOMOLECULAR STUDIES.

While it is difficult to calculate the frequencies of complex vibrations, a large amount of empirical and semi-empirical information is available. The discussion proposed here will be oriented towards biomolecules, towards amino acids and only the most general observations to understand the basic concepts of this work will be mentioned. The analysis of biomolecules (proteins is quite complex). In a diatomic molecule, vibrations along an axis are only possible; in molecules that contain more than two atoms, there are additional normal modes, see Fig 2.11. Raman spectroscopy is one of the techniques currently widely used for biomolecular studies due to the main benefits of Raman spectroscopy for biomolecular applications, which can be summarized as follows **[31-37]**.

- Raman spectroscopy is a highly specific technique that allows the identification of molecules through the specific information of their molecular footprint observed in their Raman spectra. Raman brings the IR information into the visible - visible detectors are very efficient - the optical resolution is much higher than in Infra-Red (IR). Allows you to track event over time.

- Raman spectra can be obtained from molecules in aqueous solutions since the Raman water spectrum is weak in the spectral region where Raman molecule lines are produced ($\mathbf{200- 3300\ cm^{-1}}$).

- The time scale of the Raman escaping effect is almost "instantaneous." It is in a system where rapid chemical exchanges occur; each species contributes with a Raman signal proportional to its concentration.

- Only a small amount (volume) of sample is required to obtain the Raman spectra.

- Raman spectra can be registered in a short time (1 s or even less), at room temperature, and without any preparation.

- The SERS and TERS techniques can be used to obtain the Raman spectra of small quantities of biological samples (nanometer) and in low concentrations.
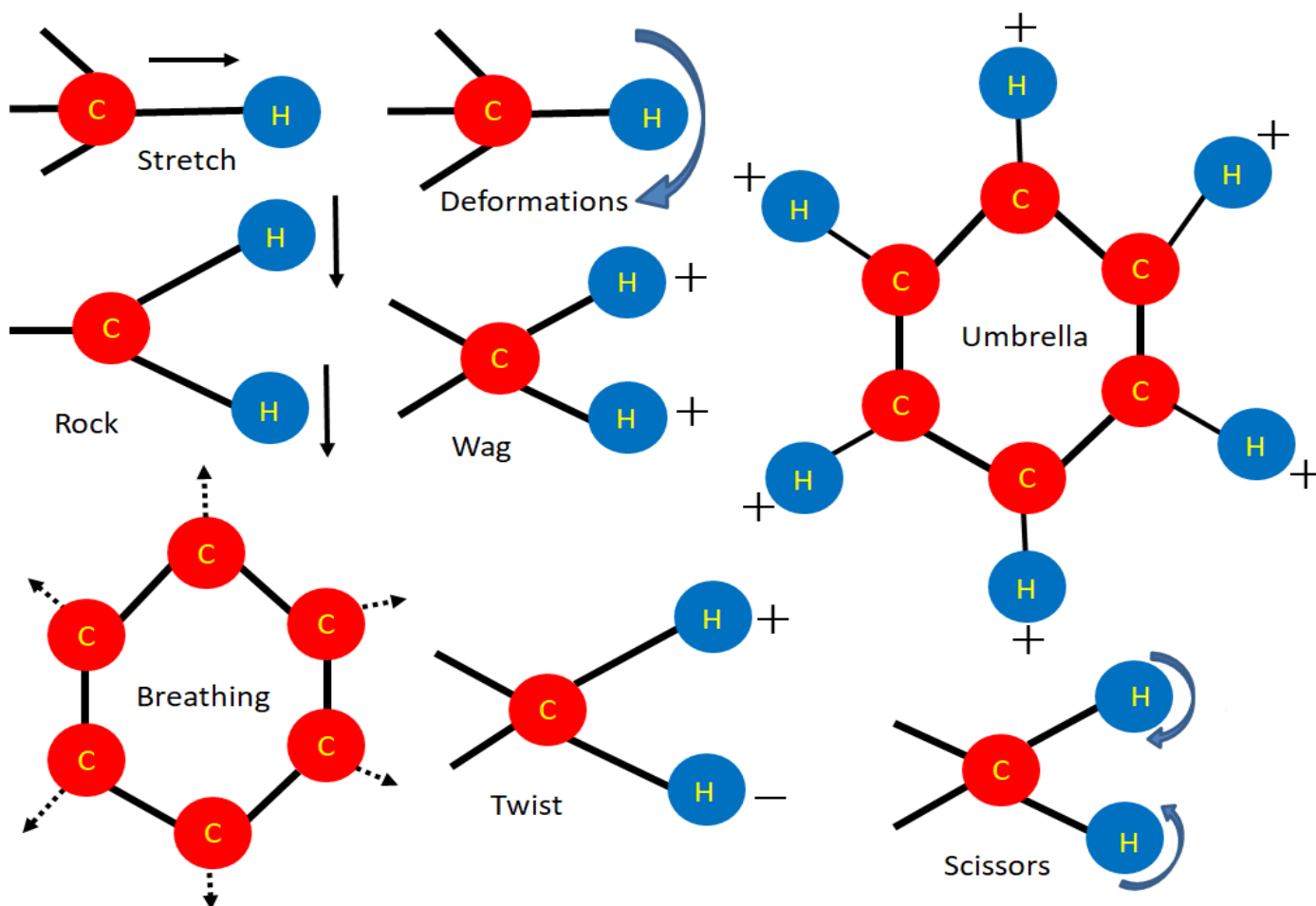
Figure 2. 11. Some vibrational modes: + and − refer to motions perpendicular to the plane **[31-37]**.

Logically there are also certain types of disadvantages that must be taken into account in any Raman measurement; Even so, placing the

advantages and disadvantages on the balance remains one of the best techniques for the study of chemical and structural bonds **[31-37]**.

- The high power of the laser can induce unwanted photochemical effects in the sample (photo bleaching, photodecomposition or burning the sample).

- Raman spectroscopy requires high concentrations of molecules studied (about 0.1-0.01 M).

- Solutions generally require a high level of optical homogeneity.

- In some cases depending on the sample, the Raman spectrum is easily obscured by a competitive process such as fluorescence. This is one of the main disadvantages of Raman stokes, which compared to fluorescence is a very small process. However, in Raman anti-skokes you don't have that problem.

Any molecule produced by a living organism is considered a biomolecule, among which it is possible to mention mainly DNA (DeoxyriboNucleic acid), RNA (RiboNucleic acid), proteins and membrane structures (such as phospholipids), fatty acids and monosaccharides. From a chemical point of view, all biomolecules contain some of the following atoms: carbon, hydrogen, oxygen, nitrogen, phosphorus and sulfur. It is possible to summarize some of the most basic characteristics of the Raman vibrating bands observed in biomolecules (Schrader 1995; Smith and Dent 2005) **[31-37]**:

1- Stretch vibrations associated with chemical bands are more intense than deformation. The vibration of deformation $O - H$ of water at $\sim 1640 \; cm^{-1}$ is weak, while the vibrations of stretching $O - H$ at $3400 - 3600 \; cm^{-1}$ are stronger.

2- Multiple chemical bonds often result in intense modes of stretching. Raman bands due to vibrations $C = C$ (around $1640 cm^{-1}$) are more intense than those due to vibrations $C - C$. On the other hand, vibrations $C = O$ are weak in the Raman spectrum.

3- Stretch vibrations of individual bands containing hydrogen ($C - H$, $S - H$, $N - H$, $O - H$, $P - O - H$, $O - H$) appear in the high frequency region between ($\sim 2500 - 4000 \; cm^{-1}$). The region between ($2000 - 2500 \; cm^{-1}$); is called multiple bands ($N = C = O$, $C \equiv C$, $C \equiv N$) and the region between ($1500 - 2000 cm^{-1}$), double bands ($C = O$, $C = N$, $C = C$, $N = N$).

4- Below $1500 \; cm^{-1}$, many biomolecules have spectral characteristics of vibrations $C - C$ and $C - N$ (both stretching and deformation). This region is generally known as the fingerprint region.

5- Raman bands below $\sim 650 \; cm^{-1}$. generally involve atoms of large atomic mass (such as sulphides or metal-organic groups) and give rise to high intensity Raman stretching vibrations. $S - S$ disulfide bonds in proteins or $Fe - O$ in hemoglobin, both with Raman bands around $500 \; cm^{-1}$.

6- For cyclic compounds, the vibratory mode of "breathing" is usually the most intense. It is a case of $1050\ cm^{-1}$). Raman band of phenylalanine (Phe) amino acid observed in Raman spectra of proteins or nucleobases at $700 - 900\ cm^{-1}$.

Some of the characteristics of the amides can be mentioned. A typical amide is a flat molecule of the form, Fig. 2.12 (c). If R_3 is a hydrogen, two configurations geometrical can be produced, *trans* and *cis* (The *cis-trans* or geometric isomerism is due to the restricted rotation around a carbon-carbon bond), see Fig 2.12 (a) and Fig. 2.12 (b) respectively. Normally, the *trans* configuration is more stable than the *cis*.
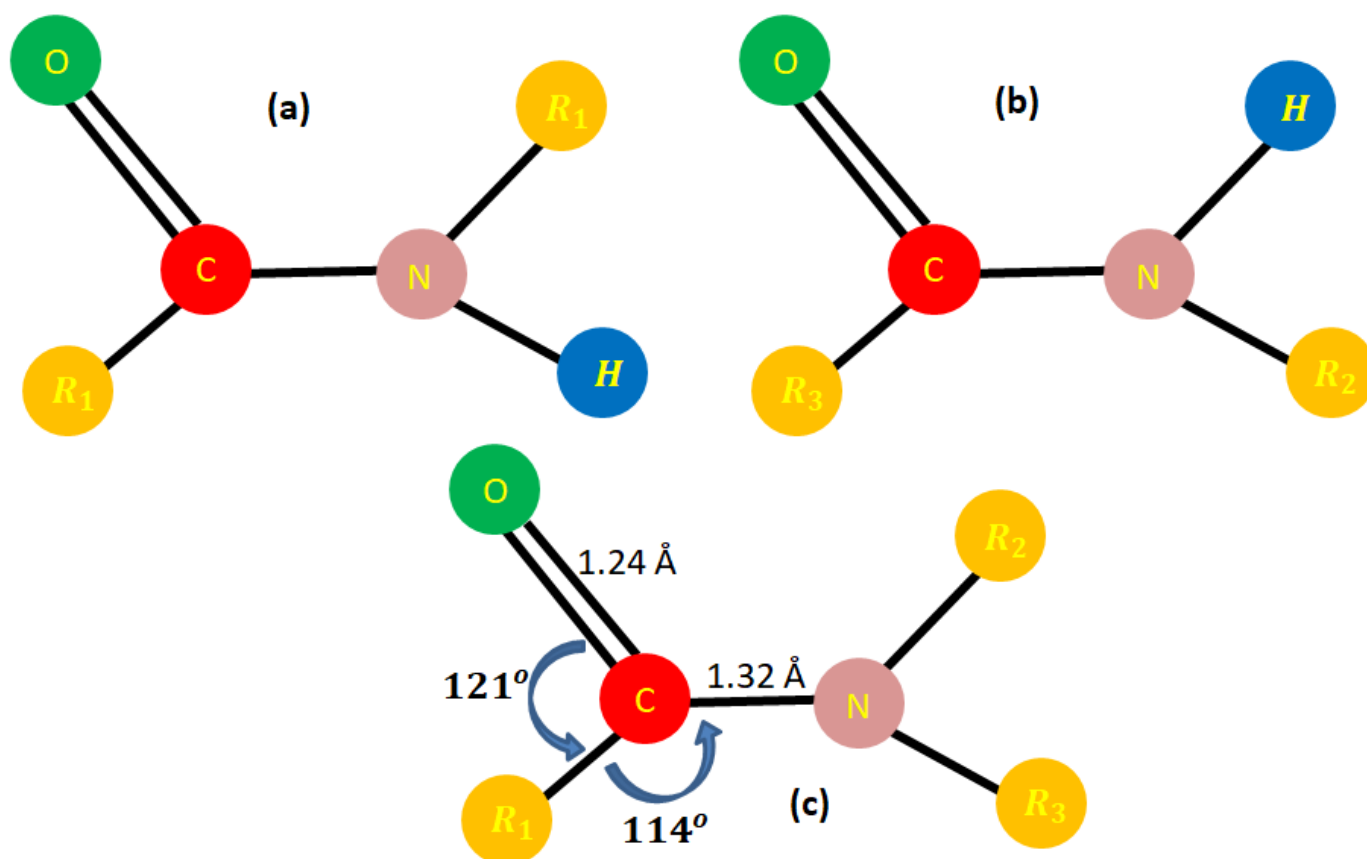
Figure 2.12. Geometric isomerism (a) Trans and (b) Cis amide bonds, and (c) A typical amide [31-37].

The number, position and intensity of the $N - H$ bands of many amides depend on the configuration. The peptide groups in the protein skeleton have five vibrations in the plane ($CONH$ plane) and three outside the plane. A strong band is produced at approximately 3300 cm^{-1} and a somewhat weaker band at 3100 cm^{-1}. These are called amide A and amide B bands. Amide A is caused by the NH stretch vibration; Amide B is the first overtone of the vibration of Amide II. The amide band I occurs at approximately 1650 cm^{-1}; It is mainly caused by the stretching vibration $C = 0$. The amide II bond at 1540 cm^{-1} has a $C - N$ stretch and a NH bending character. The positions of the various bands depend on the conformation of the spine, as indicated in Table 2.1. **[31-37]**.

Table 2.1. Conformation influence on the vibrations position bands.

Band	Assignment	Frequency $\bar{\nu}\,(cm^{-1})$		
Amide A	NH Stretch	Coil	Helix	Sheet
	Half-Width	3250	3290	3260-3290
Amide I	$C = 0$ Stretch	150-200	55-90	55-90
	$C - N$ Stretch	1655	1650	1630
Amide II	NH Bend	1520-1545	1545-1550	1520-1530

2.4. SURFACE-ENHANCED RAMAN SCATTERING, SERS.

According to equation $\vec{\mu}_{ind} = \overleftrightarrow{\alpha}_{mol} \cdot \vec{E}_{loc}$ the magnitude of the induced dipole moment $\vec{\mu}_{ind}$, which characterizes the Raman scaling effect, is given by a product of the molecular polarization molecule $\overleftrightarrow{\alpha}_{mol}$ and the local electric field $\vec{E}_{loc}$ of the frequency ν_{inc}, this shows two possible ways to improve Raman scattering; The interaction of the molecule with a rough metal surface must enhance $\vec{E}_{loc}$ or the $\overleftrightarrow{\alpha}_{mol}$ molecule. Therefore, the mechanism of improvement of SERS is

traditionally separated into two main multiplicative contributions: the 1) electromagnetic and 2) the chemical (or molecular).

2.4.1. SURFACE ENHANCED RAMAN SCATTERING, ELECTROMAGNETIC MECHANISM.

All metals have free electrons, which oscillate on their surface with an external electric field. Some have electrons stuck, electron pairs holes, when interband transfer occurs. In intraband transitions, electrons oscillate freely. The oscillations of these electrons under irradiation of an electromagnetic wave can occur at the plasma frequency. Quantized plasma oscillations are called plasmons. When radiation hits a metal surface, as long as the radiation frequency is close to the excitation of the metal surface plasmons, an intensification of the optical electric field occurs in close proximity to the metal surface. This is a major improvement effect based on the amplification of the electromagnetic field due to resonance of localized oscillations of conduction electrons on the surface metal, so-called Surface Plasmons (SP). This type of resonance is termed dipolar Localized Surface Plasmon Resonance (LSPR) and can be derived from the extinction spectrum (called Surface Plasmon Extinction-SPE), which involves both absorption and elastic dispersion of a particular metal nanostructure. Among the most used metal nanostructures to generate this effect are Au, Ag and Cu **[25, 31-37]**.

If there is resonance between the radiation frequency and the surface plasmon, the electric field near the metal may be significantly larger than the applied field, due to the polarization of the metallic nanoparticle. The existence of plasmons resonances in metallic nanostructures is a necessary condition for observing the SERS effect, and defines the theoretical basis for the explanation of the electromagnetic mechanism involved in this

effect. This mechanism does not depend on the chemical nature of the molecule, as it does not alter its polarizability or the type of molecule-metal interaction.

The resonance frequency $\boldsymbol{\nu_{max}}$ of the plasmons on the surface of the metal nanostructure depends on the dielectric constants of the metal $\boldsymbol{\varepsilon_{metal}(\nu)}$ and the surrounding medium $\boldsymbol{\varepsilon_{med}(\nu)}$. First, the coupling state of the photon with the LSPRs are accompanied by an amplitude remarkably enhanced of the electromagnetic field in the vicinity of the rough nano metal surface, see Fig. 2.13 a). The embedded-adsorbed molecule on the metal nano surface is subjected to an $\vec{\boldsymbol{E}}_{loc}$ intensely strong. Second, the molecular dipole radiates Raman photons scattering but not in free space but in close proximity of nano metal. Stokes photons are shifted in frequency $\boldsymbol{\nu_{sc} = \nu_{inc} - \nu_{vib}}$ for a particular vibratory mode, Fig. 2.13 b) that in itself can excite an LSPR of the metal nanostructure in Fig. 2.13. The enhancement of the local field and the enhancement of Raman scattering have the same physical origin: the electromagnetic field are coupled with the LSPRs of the nano metallic substrate. Although the coupling may not be identical, the resonances should be at least qualitatively similar for both enhancements **[25, 31-37]**.

The overall intensity of the SERS effect depends on both the "incoming" $\boldsymbol{\nu_{inc}}$ and "outgoing" $\boldsymbol{\nu_{sc} = \nu_{inc} - \nu_{vib}}$ fields:

$$\boldsymbol{I_{SERS} = I_{inc}(\nu_{inc}) \cdot I(\nu_{sc}) = \left|\vec{\boldsymbol{E}}_{inc}(\nu_{inc})\right|^2 \left|\vec{\boldsymbol{E}}(\nu_{sc})\right|^2}$$

Therefore, the best SERS enhancement requires that both the incident radiation, in ν_{inc}, and the Raman shifted radiation, in $\nu_{sc} = \nu_{inc} - \nu_{vib}$, be in resonance (coupled) with the LSPR peak of the metal nanostructure. In general, the AgNPs spherical with typical dimensions between 20 to 100 nm are necessary to meet LSPR resonance conditions with visible light.
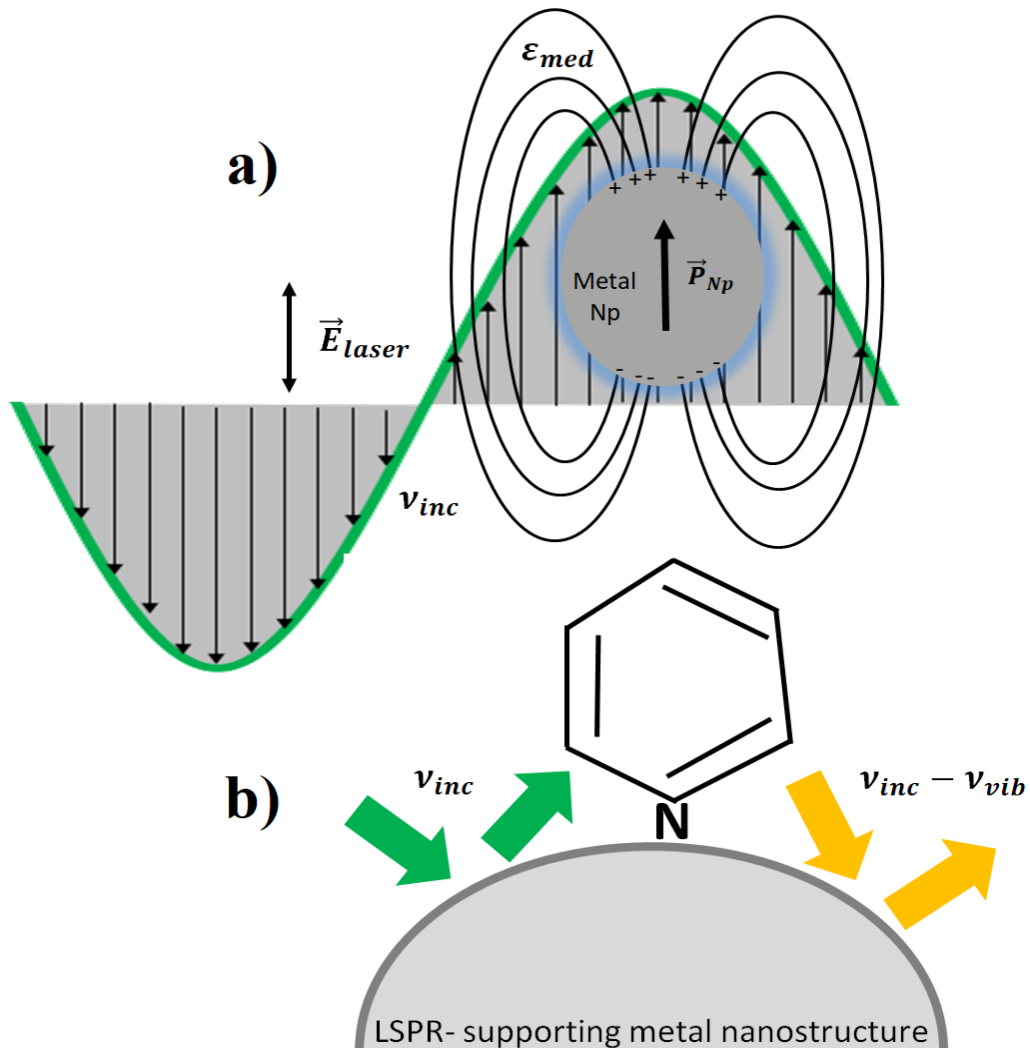
Figura 2.13. The enhancement of the local electromagnetic field, SERS effect. a) A metal nanoparticle acts as a nanoanthena by excitation of a resonance of localized dipolar surface plasmons (LSPR). b) Both the "incoming" ν_{inc} and the "outgoing" $\nu_{sc} = \nu_{inc} - \nu_{vib}$ fields are enhanced by inelastic scaling of light in the metal nanostructure that supports the LSPR [32].

The LSPRs depend largely on the size and shape of the metal nanostructures, Schatz et al. 2006; and also strongly as soon as the nanostructures are spaced apart from each other, due to the existence of coupling generated mainly from the LSPRs interactions of the individual nanostructures with the other nearby and neighboring nanostructures, Le Ru and Etchegoin 2009. Certain localized resonances generated in the nanosized gaps between NPs (hot spots) are the source of extremely high enhancement ($\sim 10^{11}$), Stockman et al. 1992. In simple cases, the I_{SERS} can be reduced to the factor $\left|\vec{E}_{inc}(\nu_{inc})\right|^4$, Le Ru and Etchegoin 2009. The moderate increase in E_{loc}/E_{inc} leads to major Raman scattering enhanced called the SERS Enhancement Factor (EF). The electromagnetic field enhancement also depends on the metal properties and the distance that the molecule has from the surface of the nanostructure. The electromagnetic field EF, $EF_{em}(\nu_{sc})$ can be explicitly described for a small metallic sphere (its radius r is less than one twentieth of the wavelength of the incident light) as:

$$EF_{em}(\nu_{sc}) \cong \left|\frac{\varepsilon(\nu_{inc}) - \varepsilon_0}{\varepsilon(\nu_{inc}) + 2\varepsilon_0}\right|^2 \left|\frac{\varepsilon(\nu_{sc}) - \varepsilon_0}{\varepsilon(\nu_{sc}) + 2\varepsilon_0}\right|^2 \left(\frac{r}{r+d}\right)^{12}$$

Being $\varepsilon(\nu)$ the complex dielectric function that depends on the frequency of the metal, ε_0 is the dielectric constant of the bulk medium and d is the distance of the molecule from the surface. The free-electron-like (Noble) metals (Ag, Au, Cu) are the proper materials for surface-enhancing substrates when are exited with common visible light to near-IR. Ag and Au are the most commonly used metals for SERS applications; Ag can be used in a wide range of excitation from 400 to 1200 nm and Au from 600 to 1200 nm. It should be noted, the dispersed molecule does not necessarily need to be in direct contact with the metal nanosurface. I_{SERS} is

proportional to $\sim(1/d)^{12}$ and, therefore, decreases rapidly with increasing distance d from the surface. The Raman enhancer effect has been detectable for $d \leq 5\text{--}10$ nm away from the nanometal surface (Aroca 2006) [25, 31-37]. The interaction between the incident light (laser) and the metal nanostructures (in this case represented by metal nanoparticles) and the embedded-adsorbed molecule (target molecule) and its relation with SERS are illustrated in Fig 2.14. The coupling of the electric field of the incident laser, $\vec{E}_{laser}$, with the electric field of the metal nanoparticles, $\vec{E}_{Np}$, constitutes the local electric field, $\vec{E}_{loc}$, around the nanoparticles.
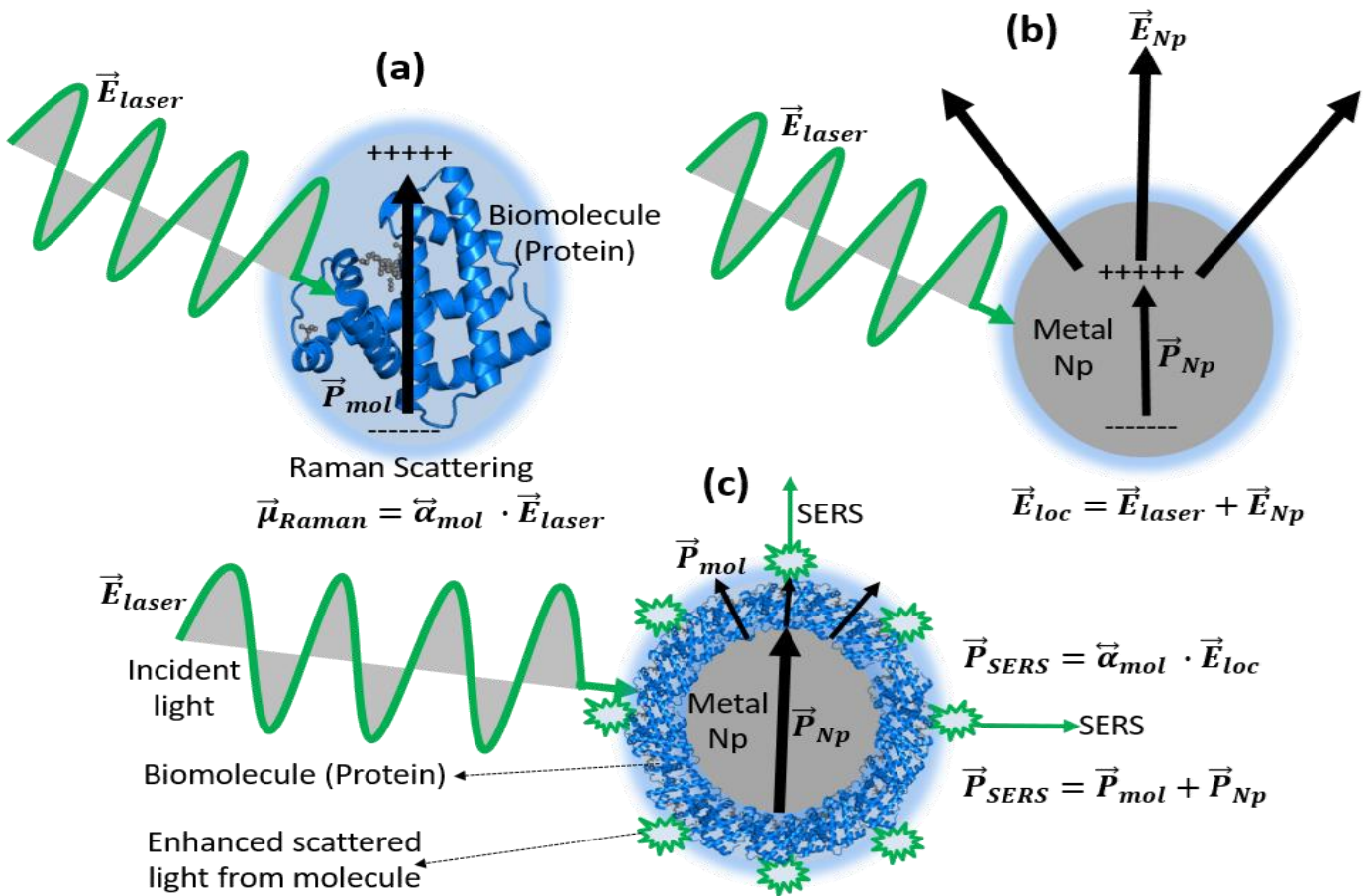
Figure 2.14. (a) Dipole moment of the molecule (protein), $\vec{P}_{mol}$, induced by the LASER, (b) $\vec{E}_{loc}$ around metal nanoparticles formed by the electric field of the incident laser, $\vec{E}_{laser}$, and nanoparticles, $\vec{E}_{Np}$, and (c) SERS effect. The molecule adsorbed on the metal surface is polarized by $\vec{E}_{loc}$ inducing the molecular dipole, $\vec{P}_{mol}$, whose irradiation can also polarize the metal, inducing a dipole in the metal nanoparticles $\vec{P}_{Np}$ [32].

The two components of the $\vec{E}_{loc}$ directly influence the magnitude of the induced dipole moment of the molecule, $\vec{P}_{mol}$ which are embedded-adsorbed on the surface of the metal nanoparticle, see Fig. 2.14 (c). That is, when the target molecule is adsorbed on the metal surface, the $\vec{E}_{loc}$ polarizes it by inducing an intense dipole moment $\vec{P}_{mol}$, see Fig. 2.14. The electric field of the incident laser, $\vec{E}_{laser}$ induced a molecular dipole moment on the molecule, $\vec{P}_{mol}$, and de metal nanoparticle (Metal Np), $\vec{P}_{Np}$, that oscillates at the same frequency as the induced molecular dipole $\vec{P}_{mol}$; generating an coupling that generates an intensification of the $\vec{E}_{loc}$ which manifests itself in a significant enhancement of Raman scattering **[25, 31-38]**.

2.4.2. SURFACE ENHANCED RAMAN SCATTERING, CHEMICAL (MOLECULAR) MECHANISM.

The chemical (or molecular) or charge transfer mechanism involves the resonance between the incident radiation and an electronic state generated by the chemical adsorption of the molecule on the metal surface (intermediate state of charge transfer), this is reflected in an increase in the polarization tensor $\overleftrightarrow{\alpha}_{mol}$ of the molecule and, consequently, in the cross section of Raman scaling. This allows concluding that the chemical mechanism depends on the molecular chemical nature, different from the electromagnetic mechanism. This mechanism has a number of requirements, such as the existence of special "active sites", the formation of a chemical bond of metal adsorbate, sometimes called the first layer effect (Otto 2005). The most common model to explain this mechanism is the transfer of charge between the molecule and the metal surface (Brolo et al. 1997; Le Ru and Etchegoin 2009) **[25, 31-38]**.

In fact, the molecule is expected to be chemisorbed in the metal, which is, bound to the enthalpy of adsorption comparable to the chemical bond energy allowing the formation of a complex charge-transfer between the molecule and the metal surface. The general model of the charge transfer process involves the transfer of an electron from the Fermi level of the metal to the Lowest Unoccupied Molecular Orbital (LUMO) of the molecule as illustrated in Fig. 2.15.
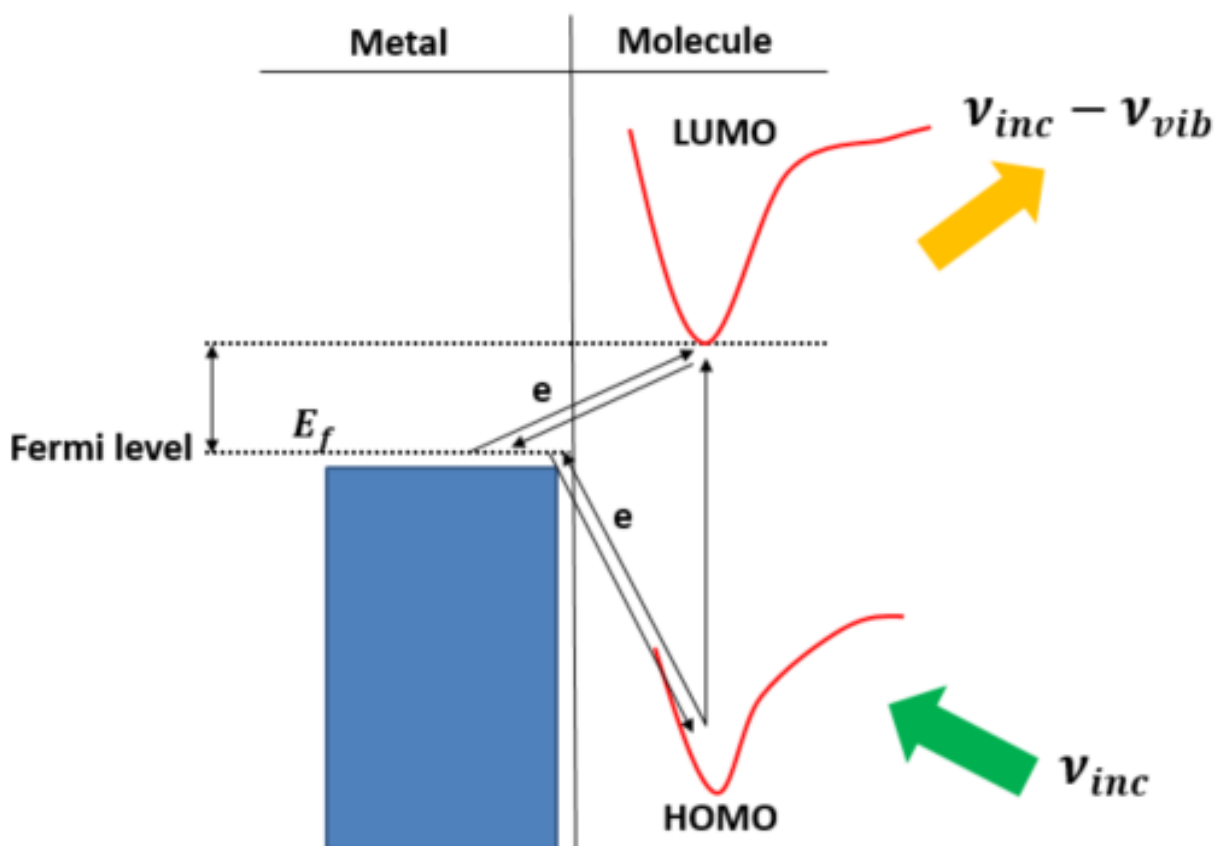
Figure 2.15. SERS Charge-transfer mechanism between molecule-metal nanoparticle. LUMO the lowest molecular orbital unoccupied, HOMO the highest molecular orbital occupied. Potential well (Morse potential) curves in the fundamental and excited state of the molecule as well as a metal conduction band are illustrated **[32].**

The proposed model is the chemical adsorption from the electron interaction between molecular adsorbate orbitals and metal conduction electrons, a chemical-absorption that occurs as a function of magnetic radiation and the provocation of two types of charge transfer; the first,

electron transfer from busy orbitals, Higthest Occupied Molecular Orbital (HOMO), of the absorbed molecule to metal states above the Fermi level and the second, transfer of metal electrons below the Fermi level to unoccupied adsorbate orbitals, LUMO (Lowest Unoccupied Molecular Orbital) [32].

The model proposes that by receiving the incident photon, the metal electron is excited by creating an electron-hole pair. This electron is transferred to the adsorbed molecule, changing its configuration. This electron then returns to its original level in the metal, causing the adsorbed molecule to become vibrationally excited. When the molecule returns to its ground state, the scattering photon originates. The inclusion of the electronic states of the metal enables the occurrence of electronic energy transitions than the intrinsic absorbed molecule.

Other techniques similar to the SERS technique have been developed through instrumental variations and/or in the phenomenological part. One of these emerging techniques is the Tip-Enhanced Raman Spectroscopy (TERS), which basically uses localized surface plasmons resonance to intensify the optical electric field but with the difference that this occurs located only at the apex of the tip probe. The tip usually comes from a Scanning Tunnel Microscope (STM), or an Atomic Force Microscope (AFM) that allows exquisite control over the position of the hot spot and its characteristics (defined primarily by the distance between the tip and the substrate) Therefore, this is a variant of achieving the conditions for the SERS effect, since allow (in principle) the combination of spectroscopy SERS with microscopy (AFM or STM), possibly at the level of a single molecule. TERS is a technique that is relatively new and growing but you will surely see a great activity in the coming years [25, 31-37].

2.5. PLASMONIC PROPERTIES OF AgNPs.

SERS can be used as a tool for the study of plasmonic substrates and, reciprocally, some plasmonic substrates can turn out to be very good SERS substrates. Indeed, plasmons are at the core of SERS electromagnetic effects and/or enhancements. A plasmon is therefore a quantum quasi-particle representing the elementary excitations, or modes, of the charge density oscillations in a plasma, and the polariton is a quasiparticles resulting from strong coupling of electromagnetic waves with an electric or magnetic dipole-carrying excitation. The concept of plasmons was firstly explained by Mie's theory in 1908, where he solved Maxwell's equations for homogeneous spherical particles with a flat monochromatic wave, thus describing the extinction spectrum (absorption+scattering) of metallic particles. When a spherical metallic nanoparticle, much smaller than the wavelength of the incident radiation, is irradiated by a flat monochromatic wave, the oscillating electric field leads to a coherent oscillation of electrons in the conduction band. This collective oscillation of the electronic cloud of the metal excited by the incident radiation is called localized surface plasmon resonance (LSPR), commonly known as plasmons **[20-29]**.

Many dierent expressions appear in this context, among them: plasmon, plasmon resonance, radiative plasmon resonance, surface plasmon, surface plasmon polariton (SPP), localized surface plasmon polariton/Resonant (LSPP/R), propagating surface plasmon polariton/Resonant (PSPP/R), and in many cases arbitrary combinations of the aforementioned. It is easy sometimes to lose sight of the main concepts and understand what is really meant from a specific standpoint, especially considering that they are not always used consistently or even correctly across the literature. With this in mind, we will attempt in the following to

give a brief overview at an introductory level of the various concepts related to plasmons **[29-34]**. Plasmons have the property to radiate, that is, they can scattering the incident light to the neighborhood. The amount of scattered light is a property of the wavelength of the incident light ($\boldsymbol{\omega}$) and the nature of the material, given by the metal's dielectric function ($\boldsymbol{\varepsilon_{metal}}$):

$$\varepsilon_{metal} = \varepsilon'(\omega) + i\varepsilon''(\omega)$$

Being $\boldsymbol{\varepsilon'(\omega)}$ and $\boldsymbol{i\varepsilon''(\omega)}$ the real and imaginary components, respectively, of the dielectric function.

When will a measurement be made on the AgNPs spherical. The incident electric field, $\boldsymbol{\vec{E}_{Laser} = E_0\hat{z}}$, will induce a local electric field, $\boldsymbol{\vec{E}_{Local}}$, which in turn will depend on the shape and size of the nanoparticle, the dielectric function of the metal and the medium around the nanoparticles, both of which are dependent on the wavelength from light. see Fig 2.16.

$$\vec{P} = 4\pi\varepsilon_0\varepsilon_m a^3 \frac{\varepsilon - \varepsilon_m}{\varepsilon + 2\varepsilon_m} \mathbf{E_0}\,\hat{z}$$

$$\vec{E}_{Laser} = E_0\hat{z}$$

a

ε_{metal}

AgNPs

ε_{medio}
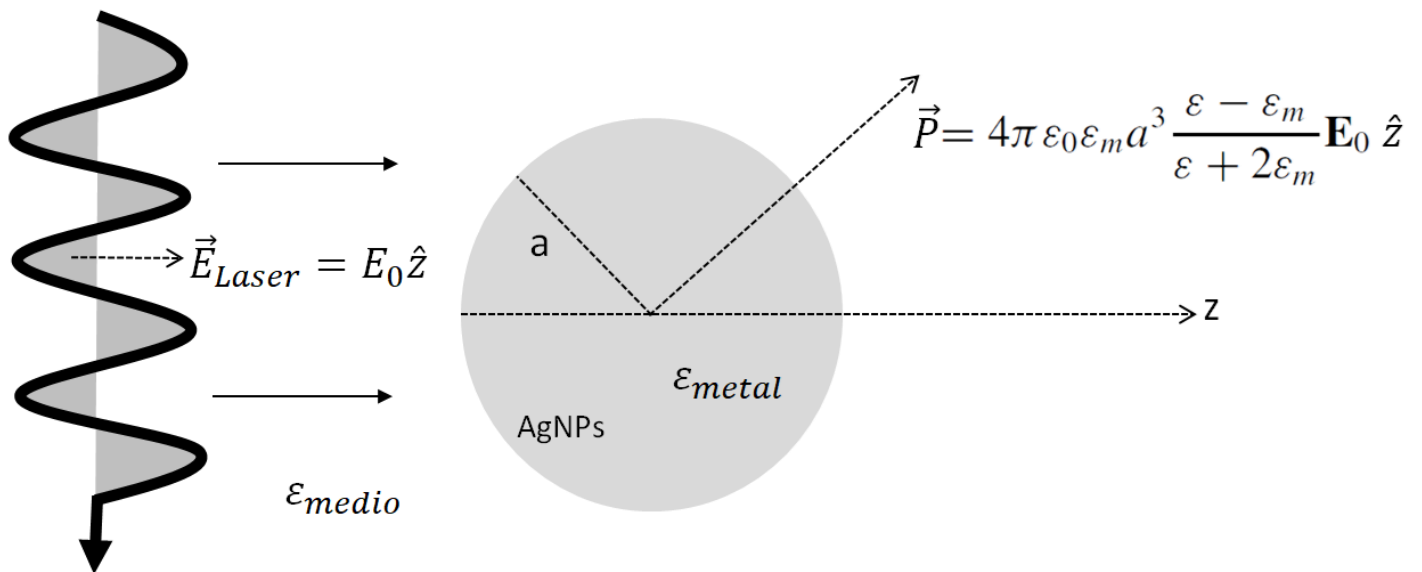
Figure 2.16. Sketch of a homogeneous sphere placed into an electrostatic field **[29-34]**.

The interaction of a particle of size d with the electromagnetic field can be analyzed using the simple quasi-static approximation provided that $d \ll \lambda$, i.e. the particle is much smaller than the wavelength of light in the surrounding medium. In this case, the phase of the harmonically oscillating electromagnetic field is practically constant over the particle volume, so that one can calculate the spatial field distribution by assuming the simplified problem of a particle in an electrostatic field. Solving for a electrostatic approach **[29-34]**.

$$\Phi_{in} = -\frac{3\varepsilon_{medio}}{\varepsilon_{metal} + 2\varepsilon_{medio}} E_0 \, r \, cos\theta$$

$$\Phi_{out} = -E_0 \, r \, cos\theta + \frac{3\varepsilon_{medio}}{\varepsilon_{metal} + 2\varepsilon_{medio}} E_0 \, a^3 \, \frac{cos\theta}{r^3}$$

Obtaining the values for the dipole moments, external, polarizability and the local electric field:

$$\Phi_{out} = -E_0 \, r \, cos\theta + \frac{\vec{P} \cdot \vec{r}}{4\pi\varepsilon_0\varepsilon_{medio} \, r^3}$$

$$\vec{P} = 4\pi\varepsilon_0\varepsilon_{medio} \, a^3 \, \frac{\varepsilon_{metal} - \varepsilon_{medio}}{\varepsilon_{metal} + 2\varepsilon_{medio}} E_0\hat{z} = \varepsilon_0\varepsilon_{medio} \, \alpha E_0\hat{z}$$

Where:

$$\alpha = 4\pi \, a^3 \, \frac{-\varepsilon_{medio}}{\varepsilon_{metal} + 2\varepsilon_{medio}}$$

Where ε_{metal} is the dielectric function of the metal and ε_{medio} is the dielectric function of the medium around the spherical AgNPs. In this way, we can deduce that the electric field is maximum (that is, there is the best

spreading of the nanoparticles) when the following resonance condition is established:

$$Re[\varepsilon_{metal}(\omega)] \approx -2\varepsilon_{medio} \quad \text{and} \quad Im[\varepsilon_{metal}(\omega)] < 1.$$

This relationship is called the Fröhlich condition and the associated mode (in an oscillating field) the *dipole surface plasmon* of the spherical metal nanoparticle. With a $\vec{E}_{Local} = -\vec{\nabla}\Phi_{out}$:

$$\vec{E}_{Local} = E_0 + \frac{3\varepsilon_{medio}}{\varepsilon_{metal} + 2\varepsilon_{medio}} E_0 \, a^3 \, \frac{cos\theta}{r^3}$$

AgNPs spherical are thus ideal platforms for optical sensing of changes in refractive index. Up to this point, we have been on the firm ground of electrostatics, which we will now leave when turning our attention to the electromagnetic fields radiated by a small particle excited at its plasmon resonance. For a small sphere with $a \ll \lambda$, its representation as an ideal dipole is valid in the quasi-static regime, i.e. allowing for time-varying fields but neglecting spatial retardation effects over the particle volume. Under plane-wave illumination with $\vec{E}(\vec{r}, t) = E_0 e^{-i\omega t}\hat{z}$, the fields induce an oscillating dipole moment $\vec{P} = \varepsilon_0\varepsilon_{medio} \, \alpha E_0 e^{-i\omega t}\hat{z}$ (in the SERS case will be illumination with a gaussian laser and TERS will be gaussian doughnut mode laser polarization). The radiation of this dipole leads to scattering of the plane wave by the sphere, which can be represented as radiation by a point dipole **[29-34]**.

AgNPs and other noble metals and their respective aggregates meet this resonance condition and, therefore, may contain surface plasmons located in regions smaller than the wavelength of the incident radiation.

This allows a high concentration of electromagnetic energy, generating an intense electromagnetic field in the visible region, called hot spots. Fig. 2.17 shows a comparison of the optical properties (real and imaginary parts of the dielectric functions) of various metals, making it possible to observe the resonance conditions for different metals.
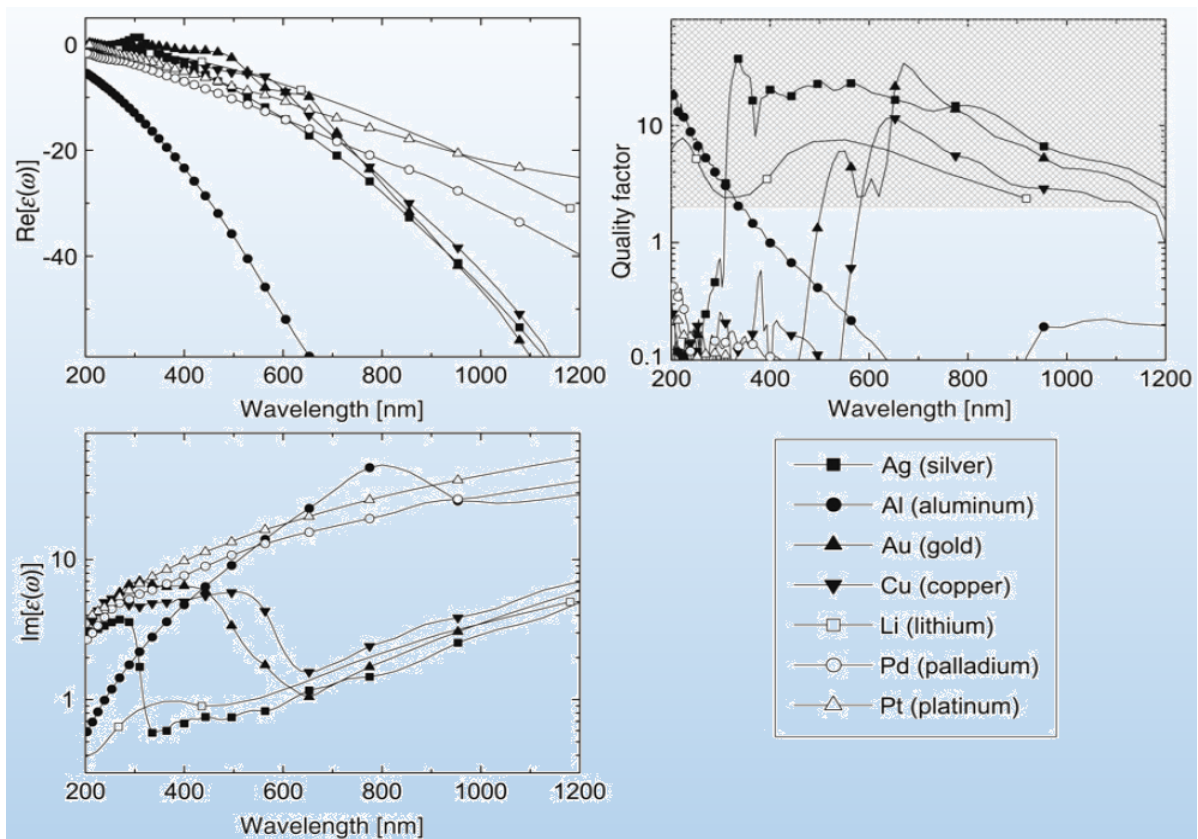
Figure 2.17. Optical properties of a variety of metals in the visible region. The real (left side) and imaginary (right side) components of the metal's dielectric function (ε_{metal}) are plotted by the wavelength. Adapted from Le Ru et al **[29]**.

A comparison of the optical properties (real and imaginary parts of the dielectric function) of various metals is showing in Fig. 2.17. There are two important types of plasmons: localized surface plasmon polaritons (LSPP) and propagating surface plasmons polaritons (PSPP). In the former, the plasmons remain static, stationary in a specific region, where there is a resonance nanogap, in the latter, and the plasmons can spread over the entire surface and in some cases, and the two types can exist at the same

time. In them, the $\mathrm{Re}(\boldsymbol{\varepsilon}(\boldsymbol{\omega}))$ is also linked to the existence of plasmons and plasmon resonances [29-34].

The monotonous decay of $\mathrm{Re}(\boldsymbol{\varepsilon}(\boldsymbol{\omega}))$ from small values in UV to negative values in visible, and very negative values in infrared, is common to all metals and is in fact predicted by the Drude model (for typical plasma frequencies in UV) This is one of the most important characteristics of metals when it comes to optical properties, and is a consequence of the optical response of free (conduction) electrons, as simply explained by the Drude model. The negativity of the $\mathrm{Re}(\boldsymbol{\varepsilon}(\boldsymbol{\omega}))$ at visible wavelengths is also the origin of many of the known optical properties of metals, including plasmon-related effects. [29].

The optical properties of metallic nanoparticles, more specifically the position of the absorption plasmon, are dependent on the metal's dielectric function. In the model of Mie's original work, he considers a spherical nanoparticle as an exact solution, but in reality the nanoparticles may differ in shape, size and aggregation, causing variations in absorption and spreading. Thus, the shape and size are characteristics that also determine the optical properties, in Fig. 2.18. Therefore, the manufacture of metallic nanoparticles of different shapes and sizes makes it possible to adjust the position of the absorption plasmon and, consequently, the scattering, according to the desired purpose. In the case of the SERS and/or TERS effects it means synchronizing the position of the absorption plasmon with the angular frequency of the laser used in the measurements [20, 23, 28].
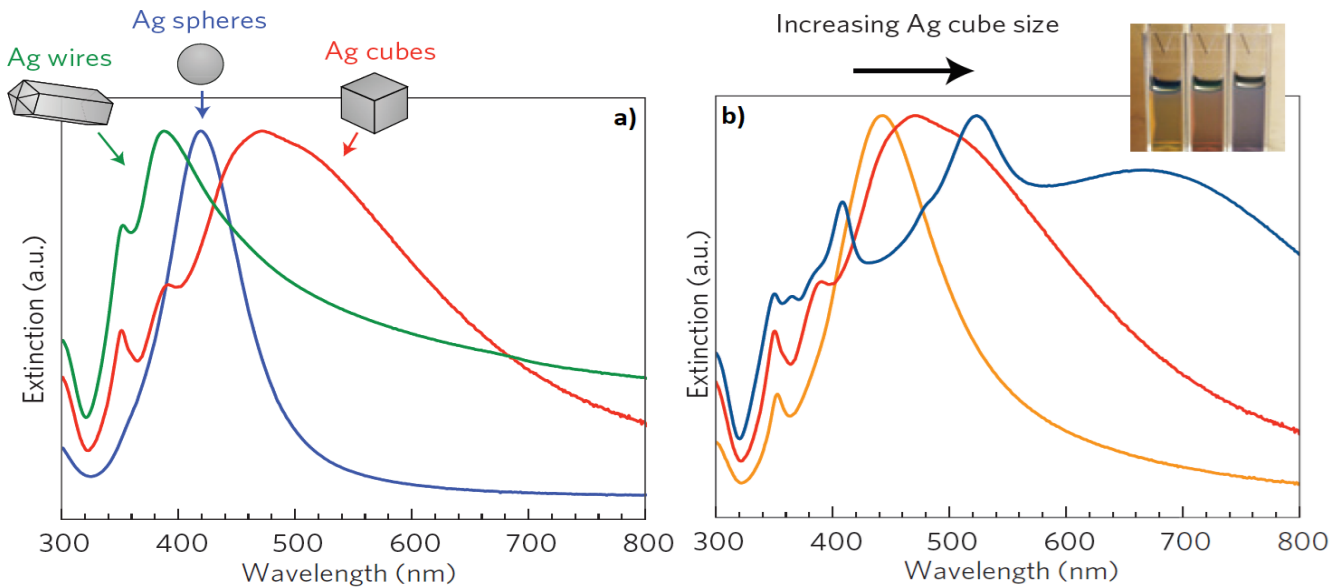
Firuge 2.18. a) Extinction spectra for AgNPs in cube, wire and sphere formats. The wire-shaped nanoparticles are **90 ± 12 nm** *in diameter, the cubic ones have an edge length of* **79 ± 12 nm** *and the spherical ones are* **38 ± 12 nm** *in diameter. b) Extinction spectra for Ag nano cubes as a function of size* **56 ± 8 nm**, **79 ± 13 nm** *and* **129 ± 7 nm** *(edge length) corresponding to the orange, red and blue spectra, respectively. The detail shows a photograph of the three nanocube samples in ethanol suspension. Adapted from Linic et al.* **[23].**

2.5.1. HOT SPOT.

Hot spots are highly localized regions of intense local field enhancement believed to be caused by local surface plasmons resonances (LSPR). Formed within the interstitial crevices present in metallic nanostructures, such hot spots have been claimed to provide extraordinary enhancements of up to 10^{15} orders of magnitude in the SERS technique in areas of subwavelength localization.

Different types of generic hot spots that have been proposed in the literature. These include (a) those formed between two closely spaced metal nanoparticles (AgNPs) by the coupled plasmons (see Fig. 2.19 a)), (b) hot spots formed at sharp nanoscale geometrical features through the "lightening rod" effect (see Fig 2.19 b)) formed by Au-tip, and (c) highly

enhancing chemically active binding sites (see Fig 2.19 c)). The ambiguity in the exact enhancement mechanism at work within the observed hot spots and the number of active molecules, the magnitude of hot spot enhancement, and the lack of a robust method to define the single molecular signature have led to much debate within the literature. Another form to obtain hot spot is placing closely a metal noble tip on other metal surface (see Fig. 2.19 d)) call Gap Plasmon (GP) **[29-34]**.

Tip-enhanced Raman spectroscopy (TERS) offers the best possible idealized hot spot control of the characteristics a single hot spot. This is controlling the characteristics and spatial positioning of a SERS active hot spot with respect to molecules of interest is a challenge fundamental to the development of SERS both for understanding and for application. TERS involves the combination of an extremely sharp metalized tip with the spatial control of a scanning probe microscope (SPM) such as an AFM. When under illumination, the electromagnetic field is enhanced at the apex of the tip due to the LSPR and results in enhanced Raman scattering from molecules in close proximity **[25-27, 39]**.

Over the last few years, many theoretical studies have been carried out that investigate the hot spots formed by the interaction of light with metallic (spherical) nanostructures. Most of these studies have investigated the interstitial spatial location of the improved field using a two-sphere model, shown schematically in Fig. 2.20 a). This has the advantage of being relatively simple and, therefore, easy to solve, while providing a good physical view of the phenomenon. These early models showed that the EM enhanced for these AgNPs depends largely on the particle size, shape, separation that exists between them, as well as the dielectric properties of the environment and the metal itself and the arrangement with

respect to the direction of polarization of the incident light. Several studies suggested that such unions can lead to strong highly localized improvements that can possibly reach a factor of $\sim 10^{11}$. A model of the enhanced factor precisely in the hot spot formed between two ~ 25 nm AgNPs spherical separated by ~ 2 nm as a function of the incident wavelength is shown in Fig. 2.20 b).
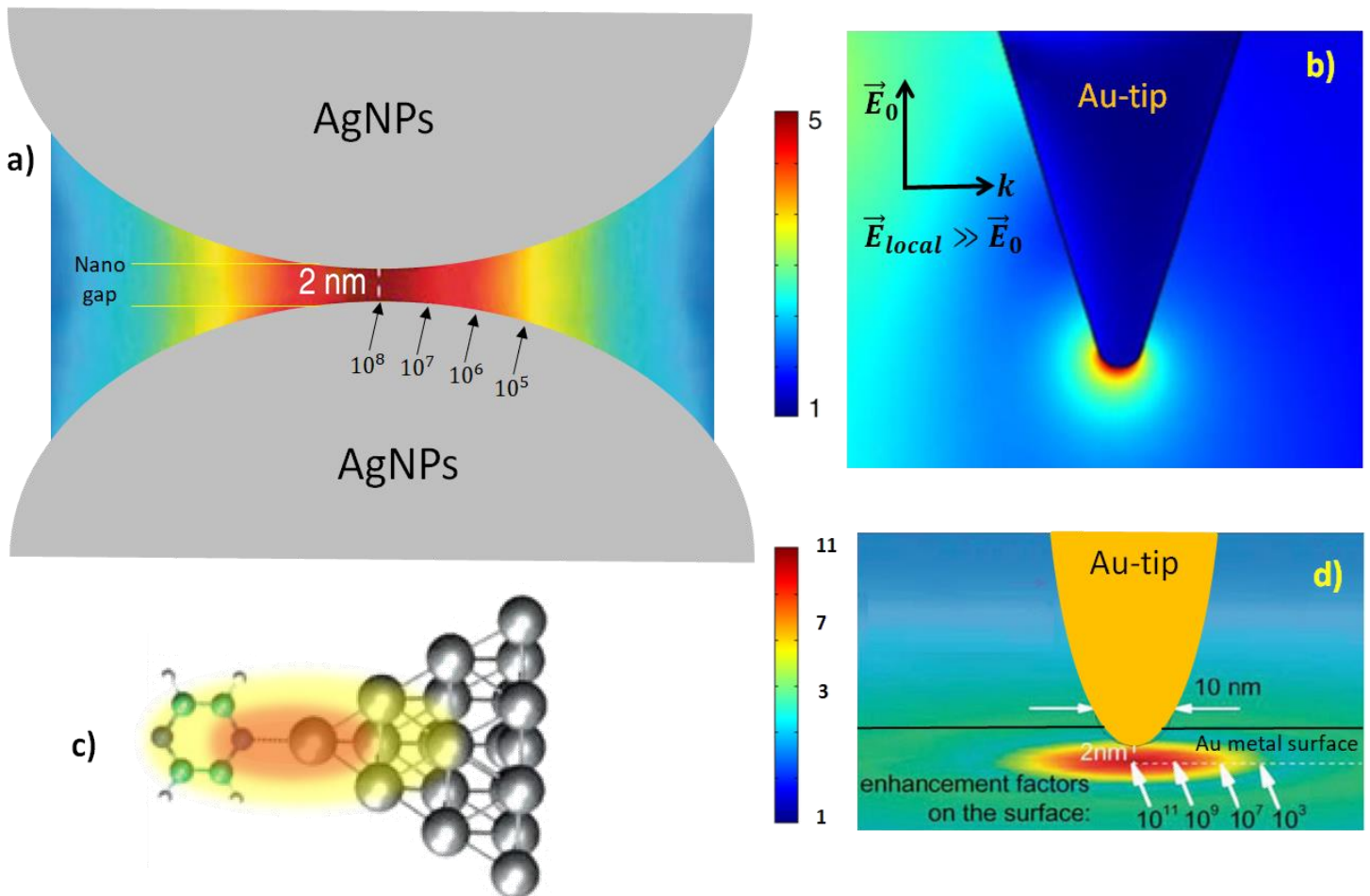
Figure 2.19. Examples of different types of generic hot spot: a) The hot spot formed between two AgNPs spherical closely placed resulting from a coupled plasmon resonance. b) The hot spot formed at a sharp geometrical feature Au-tip for electric field on Doughnut mode Laser polarization. c) Surface complex formed when a molecule adsorbs strongly onto a metal surface, chemical hot spot. d) TERS enhancement factor distribution for an Au-tip over an Au-surface separated by $\sim 2\ nm$ in formed a Gap Plasmons enhanced. Figure adapted from References [19, 25-27, 39].
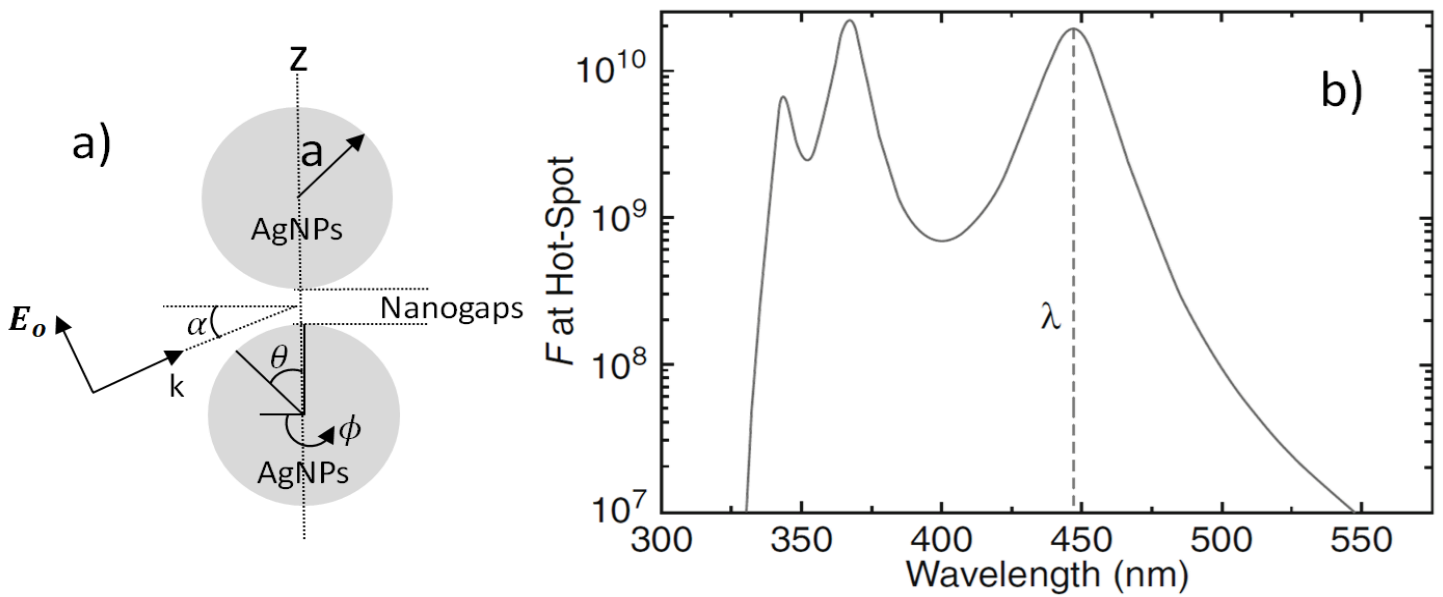
*Figure 2.20. a) Simplified geometry scheme formed by two spheres of radius a separated by a nano gap for electromagnetic calculation. b) The enhanced factor in the hot spot formed between two ~**25 nm** for AgNPs aspheric separated by ~**2** nm. Dipolar plasmon resonance occurs at $\lambda = $ **448** nm with other peaks due to higher order interactions. Figure adapted from* [28, 29].

Typically, it is very difficult to achieve the precise molecular control required to position a molecule inside the hot spot experimentally and, therefore, a more general approach to calculations is the simplified model of two hot spot spheres. The results of previous models show that the maximum enhanced depends critically on the separation between the particles, the radius of the particle, the dielectric material of the particle and the orientation of the dimer with respect to the polarization of the incident light [28, 29, 39].

3. TIP-ENHANCED RAMAN SPECTROSCOPY, TERS

The discussion starts talking about Scanning Near-Field Optical Microscopy (SNOM), technique developed as a combination of an SPM and an optical microscope, in which the spatial resolution is determined by the resolution of the SPM, while the detected signals come from the many optical interactions between the probe tip and the sample at very close distances. As a result, the SNOM achieves a higher spatial resolution than classical light microscopy using a conventional objective lens, which is strictly limited by the diffraction light limit. The mechanism for creating SNOM images is different from traditional optical microscopy. First, the light intensity is detected as a result of the strong electromagnetic interaction between the probe tip and the sample structure in the near field regime evanescent photons. In this regard, SNOM probes can be divided into probes with aperture (see Fig. 3.1. a)) and without aperture (see Fig. 3.1. b)).

When using solid metal tips without openings in order to magnify the intensity of Raman scattering, the technique is commonly referred to the acronym TERS, whose discussion is centered on this work. The advantages of the solid metal tips are referred to the localized excitations of the polarized electric charges at the tip surfaces to be enlightened with a polarized laser. When a metallic probe having a nanometric tip diameter is illuminated with an optical field, conductive free electrons collectively oscillate at the surface of the metal. The quantum of the induced oscillation is referred as Surface Plasmon Polariton (SPP) **[25, 39]**. The key point of TERS is to create a strong and localized light source using a sharp metal tip. Classical electromagnetic theory predicts that the incident field will be enhanced greatly at the end of the tip at resonance because of the excitation of localized surface plasma polaritons (LSPP) (Zayats, 1999) **[26]**. The

LSPP are linked to the lightning rod effect; it suggests that when an isolated sharp metal tip is illuminated, the p component of the field will be greatly enhanced at resonance (Novotny et al., 1997). The concentrated electrons (and the positive charge) at the tip apex can generate a strong external electric field. Photon energy is confined in the local vicinity of the tip apex due to lightning rod effects induced by the sharp curvatures (Novotny and Hecht 2006) generating a strong and spatially localized field amplitude enhancement. Therefore, the metallic tip works as a photon reservoir. The local electric field is used as a nanolight source to excite photon-matter interactions which are very important in the amplification of Raman signals at the nanoscale, where the signal level becomes even smaller as the sample volume is reduced. The solid metal tips of TERS operate as a simple disperser and nano-metric pickups, such as a "nanowane" or a "nanoligth" of SPP in the evanescent optical field **[39]**.

For TERS based on the lightning rod effect, epi-illumination (transmission mode) is popular, because a large numerical aperture (NA) microscope objective can be used to afford a tight focus. This is crucial for decreasing the background noise induced by far-field illumination. Nevertheless, there are two disadvantages of this type of transmission–illumination setup. First, a transparent sample is necessary. Second, this setup is not efficient for creating a p-polarized component from a linearly polarized illumination beam. To overcome this problem, different solutions have been adopted, annular illumination (Hayazawa et al., 2000) or modifying the wave front using a wave plate (Novotny et al., 1998; Saito et al., 2005). It should be mentioned that no matter which method is chosen to create a p component for the illumination, a high NA objective is required, see Fig 3.1 c) **[25, 26].** Another method uses the gap mode of the electromagnetic field (Aravind and Metiu, 1983). In theory, the p

component of the electromagnetic field at a tip–substrate junction can be enhanced more than 100 times under the resonant condition of the gap mode. With this method, a 10^6 times enhancement of Raman signal intensity was achieved recently (Pettinger et al., 2004). For gap mode TERS, side illumination scheme is normally employed, because an opaque metal substrate is showed on the Fig 3.1. d), this also leads to an inherent disadvantage, that a long-working distance objective must be used. Consequently, the NA of the objective is low and the area of far-field illumination is large. Considering that the enhanced electromagnetic field at the tip sample junction is localized in an area of tens of nanometers, the background induced from the far-field illumination is relatively larger than in the epi-illumination method discussed above. Similar to the lightning rod effect, the existence of a p-polarized component of the illumination is crucial to excite the gap mode and only this component can be greatly enhanced (Aravind and Metiu, 1983) **[25, 26, 39]**.

This effect enhancement the Raman signal that can be successfully used most often in the region of visible wavelength, related to the frequencies of the surface plasmas generated in noble metals such as gold and silver, which are generally the most commonly used metals for efficient intensification**,** TERS It is a different technique where the objective is to increase the spatial resolution or the local collection of Raman signals with size tip resolution **[24, 25, 26, 27]**. The tip enhanced was initially developed as an elastic optical scattering microscopy in which the topographic contrast obtained by a SPM becomes an optical contrast in the near field (evanescent photon region). A photodetector detects the photons scattered elastically without a spectrometer (non-spectroscopic information) sweeping a sample from point to point and obtaining an image, but no additional information is obtained from the material.

Consequently, this type of near field microscopy was and is mainly dedicated to the detailed optical analysis of samples where the quality goes beyond the diffraction limit, however, the qualities of these images are linked to the characteristics attributed to movement, distance control and size of the probe tip, who also is even influenced by the type of topography and hardness of the sample.
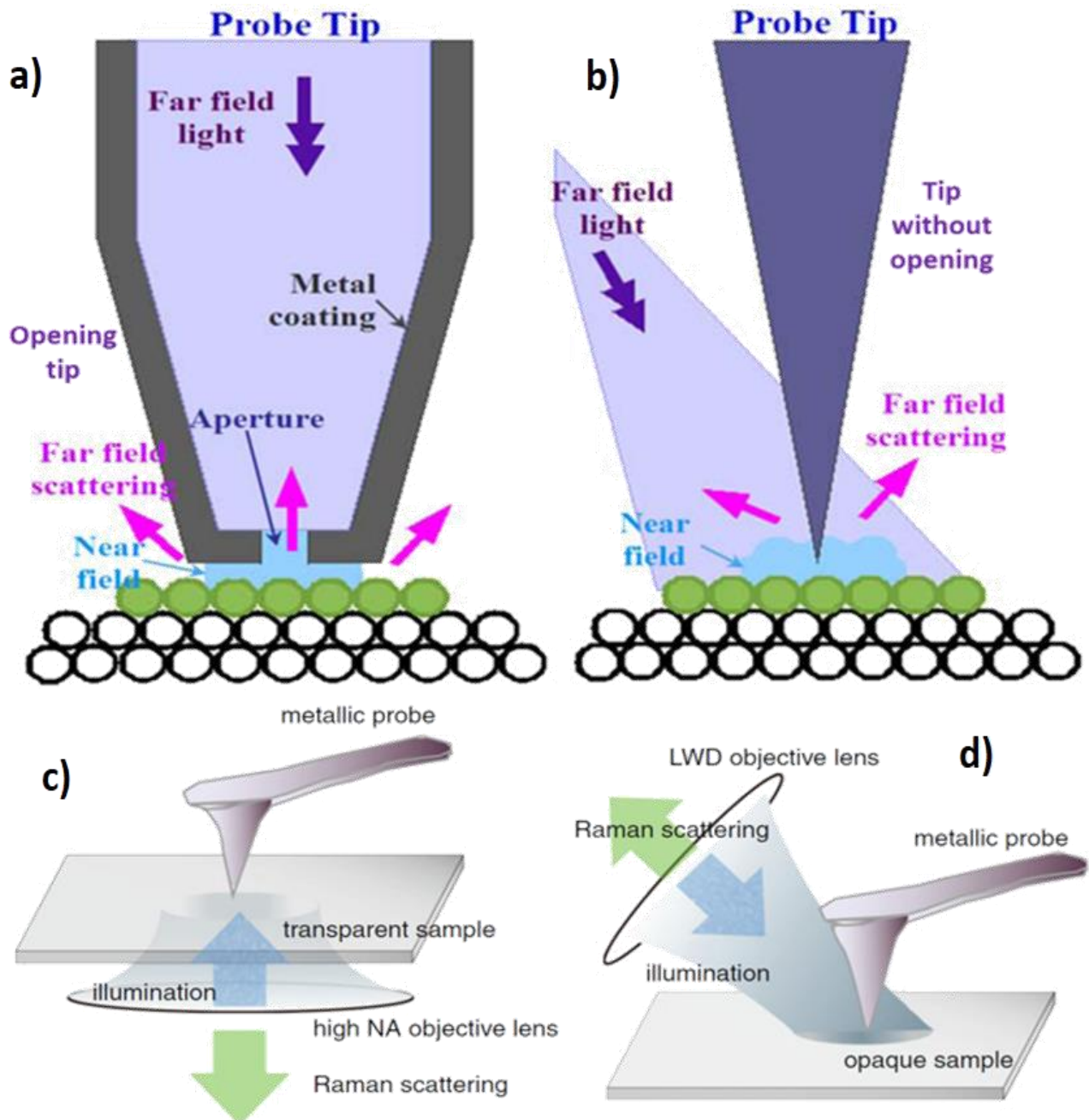
Figure 3.1. SNOM scheme for a) transmission with aperture tip and b) reflection mode without aperture. c) TERS based on the ''lightning rod'' effect and d) gap mode TERS, side illumination [25, 26, 39].

Today, through these techniques, the highest spatial resolution achieved so far is $\sim 0,5\ nm$. Probably due to the lack of additional information that it could provide and which is not observable from optical and topographical contrast alone, and the technical labor standards they require. Then, in order to obtain additional information on the optical interactions, Raman scattering with polarized Laser were added at the probe tip looking for nanometric structures can increase the scattering cross-section intensity from a "weak" conventional Raman to a Raman Enhanced by a factor of $\sim 10^3$ to $\sim 10^{11}$ times at the nanoscale, due to the SPP that are generated at the tip apex **[23, 24, 25, 39]**. Note that the enhancement of the tip is not only in the incident light, but also in the scattered light. In the case of Raman scattering, the magnification factor can be $|E_i|^2|E_s|^2 \sim |E|^4$ assuming that Raman shift (cm^{-1}) between the incident field E_i and the scattered field E_s, is insignificant light. It should be mentioned that the idea of TERS was initially conceived of the SERS effect that only happens in the surfaces of metallic nanostructures when they are illuminated with a laser, with which it shares an analogous phenomenology **[39-42]**.

In 1985, Wessel J. reported on the conceptual basis of surface-intensified optical microscopy in which metallic nanoparticles irradiated with Laser with piezo-electric positioning elements show an intensification in the dispersion index of scattered photons. The photons scattered with different frequencies (Raman scattering) are detected by means of a spectrometer **[24]**. Motivated by the reported by Wessel J. and the development of elastic scattering in non-apertured tips at SNOM, was reported the preliminary experimental results at the conference on intensified tipped Raman spectroscopy in 1999 **[25]**. Immediately afterwards, three groups independently reported intensified tipped Raman

spectroscopy in 2000. In these three pioneer cases, the system consisted of an inverted optical microscope with the transmission and reflection options working in conjunction with an AFM head as illustrated in Fig. 3.1 a) and b). One of the most successful applications of TERS is for the characterization of nanomaterials and even for the detection of individual molecules. Among nanomaterials, carbon nanotubes have been extensively studied with the use of TERS, where physical properties such as chirality, diameter and defects have been successfully investigated. The carbon nanotubes were visualized densely packaged at a spatial resolution of 20 nm, this is shown in Fig. 3. 2, where the resolution power of the TERS is clearly shown in comparison to the confocal Raman [25, 26]. In order to better understand how the TERS makes it possible to obtain this type of image and contrast and what is the relation between the near field and the spatial resolution, the Angular Spectrum Representation will be discussed later.
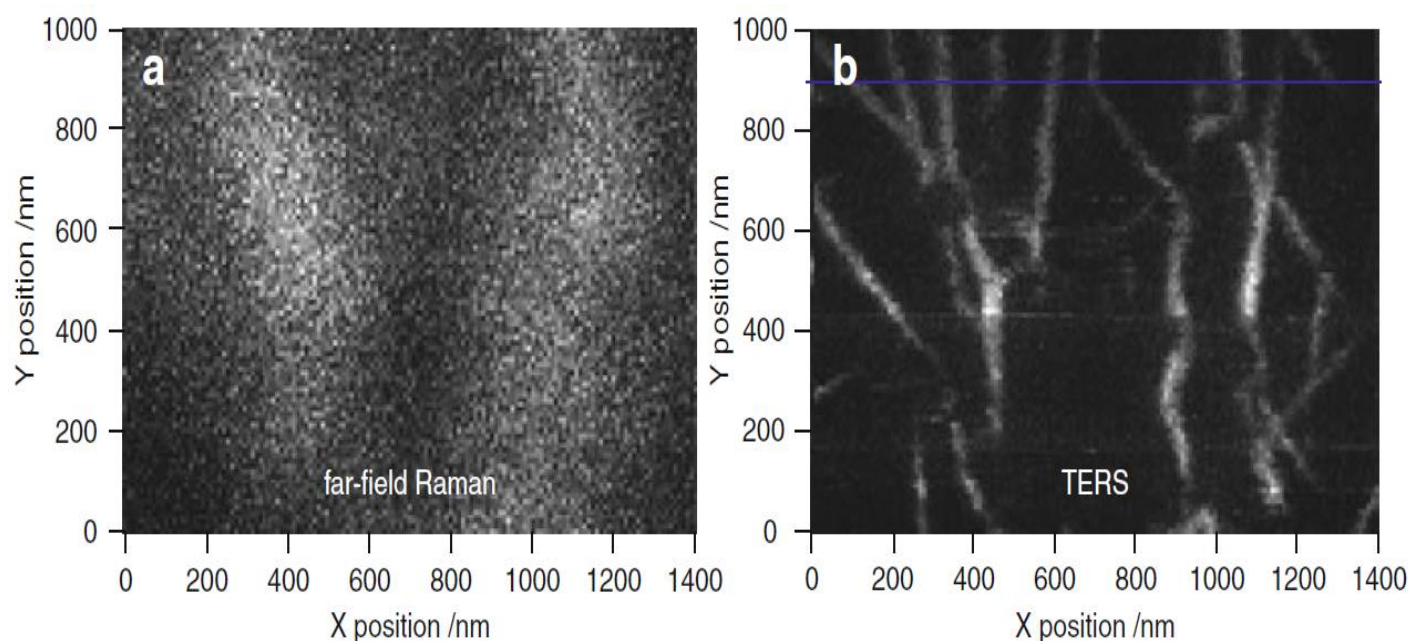
Figure 3.2. a) Confocal Raman and b) TERS image of a single wall carbon nanotube. The contrast in the images reflects the local intensity of the Raman G band in $1595\ cm^{-1}$. The excitation wavelength is $532\ nm$. The tip is a silver-coated cantilever tip [32, 39].

3.1. ANGULAR SPECTRUM REPRESENTATION.

In this section, the Angular Representation of the spectrum will be used to describe the propagations of the optical fields. It is a very useful mathematical tool to understand the basic theoretical mechanisms that give the TERS system the ability to generate optical images with a spatial resolution greater than the diffraction limit of light. To better understand the cause by which this mechanism leads to higher resolutions, it is necessary first to analyze how an electromagnetic wave propagates when it is emitted by a point source. More specifically, the evolution, along an arbitrary z axis, and from the field issued by a particular point source.

It is considered a light-emitting source whose frequency is ω, located in $\vec{r}_0 = 0$, the objective is to describe the evolution of the electric field in a position $\vec{r} = (x, y, z)$ from the source. The way the electric field of an emitted electromagnetic wave at a point evolves along an arbitrary direction z is shown in Fig. 3.3. The way the electric field of the electromagnetic wave emitted at the point $z = 0$ evolves into the position $z > 0$ can be described considering the angular spectrum representation of the electric field, also called spectral components. In the z direction, the two-dimensional Fourier transform of the electric field is $\vec{E} = \vec{E}_{inc} + \vec{E}_{sct}$, where E_{inc} and E_{sct} are the incident and scattered electric fields respectively in $z = cte$; this is described as:

$$\widehat{\vec{E}}(k_x, k_y; z) = \frac{1}{4\pi^2} \iint\limits_{-\infty}^{+\infty} \vec{E}(x, y, z) e^{-i[k_x x + k_y y]} \, dx \, dy$$

Where k_x, k_y, and k_z are the projections of the wave vector on the Cartesian axes x, y and z being $k = (k_x^2 + k_y^2 + k_z^2)^{1/2} = \frac{\omega}{c} n = \frac{2\pi}{\lambda} n$ the

light wave vector modulus, n the refractive index of the medium and $\lambda(\omega)$ the wavelength of (frequency) scattered light. For simplicity the terms of time were omitted. The Fourier transform in the reciprocal space in the plane $z = cte$ will be:

$$\vec{E}(x,y,z) = \int\limits_{-\infty}^{+\infty}\!\!\!\int \hat{\vec{E}}(k_x, k_y; z)e^{i[k_x x + k_y y]}\, dk_x\, dk_y$$
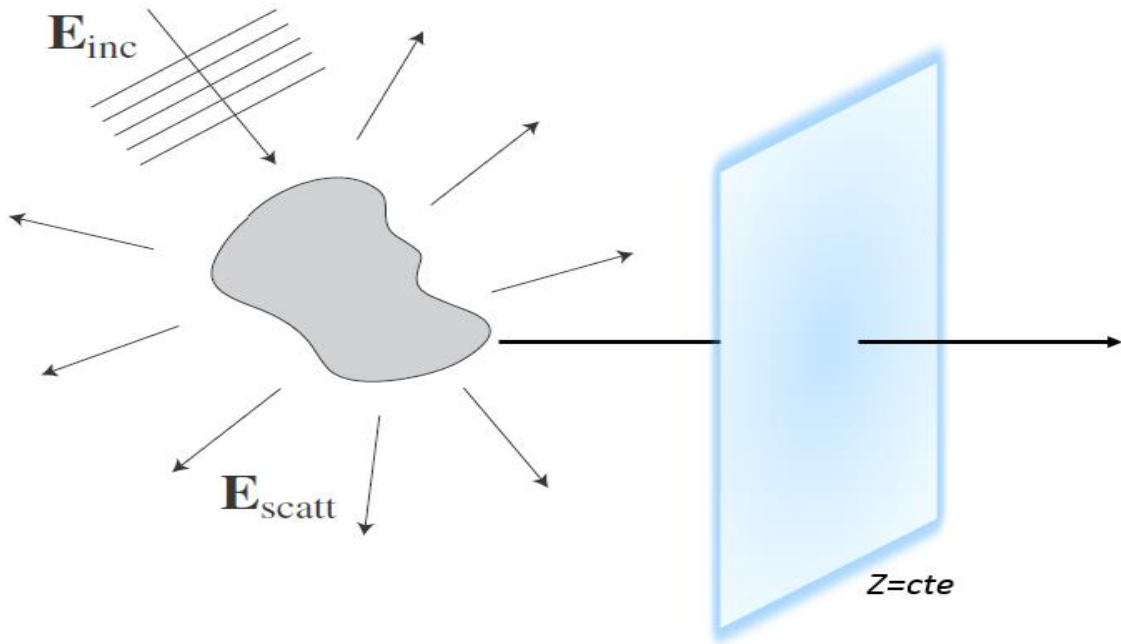
Figure 3.3. Angular representation of the spectrum, the fields are calculated in planes $z = cte$ perpendicular to the arbitrarily chosen $z-axis$, adapted from L. NOVOTNY; 2012 [39].

We can separate the spatial and temporal components of $\vec{E}(\vec{r},t) = \vec{E}(x,y,z,t)$ by writing the same as: $\vec{E}(\vec{r},t) = \vec{E}(\vec{r})e^{-i\omega t}$, where the angular frequency **is** $\omega = 2\pi c/\lambda$. The information that can be obtained regarding the Fourier components when applying the optical electric field with angular frequency ω, $\vec{E}(x,y,z) = Re\{\vec{E}(x,y,z)e^{-i\omega t}\}$, has to satisfy the sum of the integral made on the special frequency spectrum k_x and k_y (does not act on the coordinates x, y, z) and solving the Helmholtz wave paraxial equation, if it has:

$$\nabla^2 \vec{E}(\vec{r},t) - \frac{1}{c^2}\frac{\partial^2}{\partial t^2}\vec{E}(\vec{r},t) = 0$$

$$(\nabla^2 + k^2)\vec{E}(x,y,z) = 0$$

$$(\nabla^2 + k^2)\int\limits_{-\infty}^{+\infty}\widehat{\widehat{E}}(k_x, k_y; z)e^{i[k_x x + k_y y]}\, dk_x\, dk_y = 0$$

$$\int\limits_{-\infty}^{+\infty}\left[\left(\frac{\partial^2}{\partial x^2} + \frac{\partial^2}{\partial y^2} + \frac{\partial^2}{\partial z^2}\right) + k^2\right]\widehat{\widehat{E}}(k_x, k_y; z)e^{i[k_x x + k_y y]}\, dk_x\, dk_y = 0$$

$$\int\limits_{-\infty}^{+\infty}\left[\left(-k_x^2 - k_y^2 + \frac{\partial^2}{\partial z^2}\right) + k^2\right]\widehat{\widehat{E}}(k_x, k_y; z)e^{i[k_x x + k_y y]}\, dk_x\, dk_y = 0$$

The previous integral will be satisfied for:

$$\left[\frac{\partial^2}{\partial z^2} + k^2\right]\widehat{\widehat{E}}(k_x, k_y; z) = 0$$

Where $k_z = \sqrt{k^2 - k_x^2 - k_y^2}$ getting solutions:

$$\widehat{\widehat{E}}(k_x, k_y; z) = \widehat{\widehat{E}}(k_x, k_y; 0)e^{\pm i k_z z}$$

Which leads to:

$$\vec{E}(x,y,z) = \int\limits_{-\infty}^{+\infty}\widehat{\widehat{E}}(k_x, k_y; 0)e^{i[k_x x + k_y y \pm k_z z]}\, dk_x\, dk_y \rightarrow equação\ (*)$$

All of the above means that the field in the $z = cte$ plane can be found if its Fourier components at $z = 0$ are known, the term $e^{\pm i k_z z}$ controls the propagation of the wave. Note that the positive sign on the exponent means a wave propagating in the direction $z > 0$, while the negative signifies a wave propagating in the direction $z < 0$, the behavior

of the two being completely analogous. For this reason, $e^{\pm i k_z z}$, is called the propagator in the reciprocal space, where the modulus is: $k_z = (k^2 - k_x^2 - k_y^2)^{1/2}$. Sequentially, one has to ensure that each of the Fourier components, $\widehat{\vec{E}}$, of the field, $\vec{E}$, is such that they satisfy the Maxwell equations. Considering the space without free loads, $\rho = 0$, if it has to satisfy the Gaussian law, $\nabla \cdot \widehat{\vec{E}}(x, y; z) = 0$; then according to equation (*):

$$\nabla \cdot \vec{E}(x, y; z) = 0$$

$$\nabla \cdot \vec{E}(x, y; z) = \int\!\!\!\int_{-\infty}^{+\infty} \left[\frac{\partial}{\partial x}\hat{x} + \frac{\partial}{\partial y}\hat{y} + \frac{\partial}{\partial z}\hat{z}\right] \cdot \widehat{\vec{E}}(k_x, k_y; 0)e^{i[k_x x + k_y y + k_z z]}dk_x dk_y = 0$$

$$\nabla \cdot \vec{E}(x, y; z) = \int\!\!\!\int_{-\infty}^{+\infty} \left[i\,k_x\,\hat{x} + i\,k_y\hat{y} + i\,k_z\,\hat{y}\right] \cdot \widehat{\vec{E}}(k_x, k_y; 0)e^{i[k_x x + k_y y + k_z z]}dk_x dk_y = 0$$

$$\nabla \cdot \vec{E}(x, y; z) = i \int\!\!\!\int_{-\infty}^{+\infty} \vec{k} \cdot \widehat{\vec{E}}(k_x, k_y; 0)e^{i[k_x x + k_y y + k_z z]}\,dk_x dk_y = 0$$

For this equation to be sure, if it has to do:

$$\widehat{\vec{E}}(k_x, k_y; 0) \cdot \vec{k} = 0$$

Consequently, at this point in the discussion the following should be taken into account: by the way, it was defined:

$$k = \sqrt{k_x^2 + k_y^2 + k_z^2} = \frac{\omega}{c}n = \frac{2\pi}{\lambda}n \,,$$

Where $k_z = \sqrt{k^2 - k_x^2 - k_y^2} = \sqrt{\left(\frac{2\pi}{\lambda}n\right)^2 - k_\parallel^2}$, being $k_\parallel^2 = k_y^2 + k_z^2$.

This means that the wave propagation vector $\vec{k}$ must always be perpendicular to the Fourier components of the electric field, which is an intrinsic characteristic of electromagnetic waves. So what follows is to analyze how the propagation behavior of the components $\widehat{\vec{E}}(k_x, k_y; 0)$ to values k_z, where k_z can have real or imaginary values, that is:

a) For values: $\quad k^2 \geq k_x^2 + k_y^2 \Longrightarrow k_z \in Re$

$$\widehat{\vec{E}} \propto e^{i[k_x\, x + k_y\, y]} e^{i[k_z\, z]}$$

This is a flat wave, far field.

That is to say, when $k_{\parallel} \leq \frac{2\pi}{\lambda} n$, k_z will be real and the wave propagates by carrying the distant field information corresponding to the conventional light.

b) For values: $\quad k^2 < k_x^2 + k_y^2 \Longrightarrow k_z \in Im$

$$\widehat{\vec{E}} \propto e^{i[k_x\, x + k_y\, y]} e^{-i[k_z\, z]}$$

This is an evanescent wave, near field.

That is to say, when $k_{\parallel} > \frac{2\pi}{\lambda} n$, k_z will have imaginary values and the electric field will decay exponentially in the direction of propagation (evanescent wave), in this case the z direction, this being the near field component **[33, 34, 35]**.

The interpretation h ere can be that an electromagnetic wave propagating by any means (satisfying the conditions discussed above), at a

given point in space, can always be understood as a superposition of several spectral components. All these components will also be waves that satisfy Maxwell's equations at that point. Some will be propagating waves while others will exhibit an exponential decay with increasing distance between the source and the point of observation. If one takes into account that each of the spectral components carries part of the information of a signal emitted by the source (for example, a molecule or a nanostructure) it can be understood that, as it distances itself from the source, information is lost in the form of evanescent components. If you want to get as much detail as possible of an object that emits/scatters light, we should not only collect its emitted / scattered light in all directions but also collect them as close to the source as possible so that all the information that is contained in the evanescent components of the spectrum. We will see in the next section how this can be done in practice **[30, 43, 44, 45]**.

The reader may find further details of this mathematical development relative to the spectral angular representation of optical fields as well as the analysis of the loss of information and any other related referents and / or other field distributions in the book by L. Novotny & B. Hetcht are developed **[30]**.

3.1.1. INFORMATIONS AND FIELD PROPAGATION.

From a strict point of view, in theory, there may be innumerable spectral components in any field, being those propagated as plane waves restricted to the values, $k^2 \geq k_x^2 + k_y^2$, and those that propagate like evanescent waves, $k^2 < k_x^2 + k_y^2$, If all these values are taken and bounded by a circle that has a radius $k = \frac{\omega}{c} n$, the evanescent waves have a value of

$\sqrt{k_x^2 + k_y^2} > \frac{\omega}{c}n$, and the flat waves a value of $\sqrt{k_x^2 + k_y^2} \leq \frac{\omega}{c}n$, this is illustrated in Fig. 3.4 and Fig. 3.5. [30, 39].
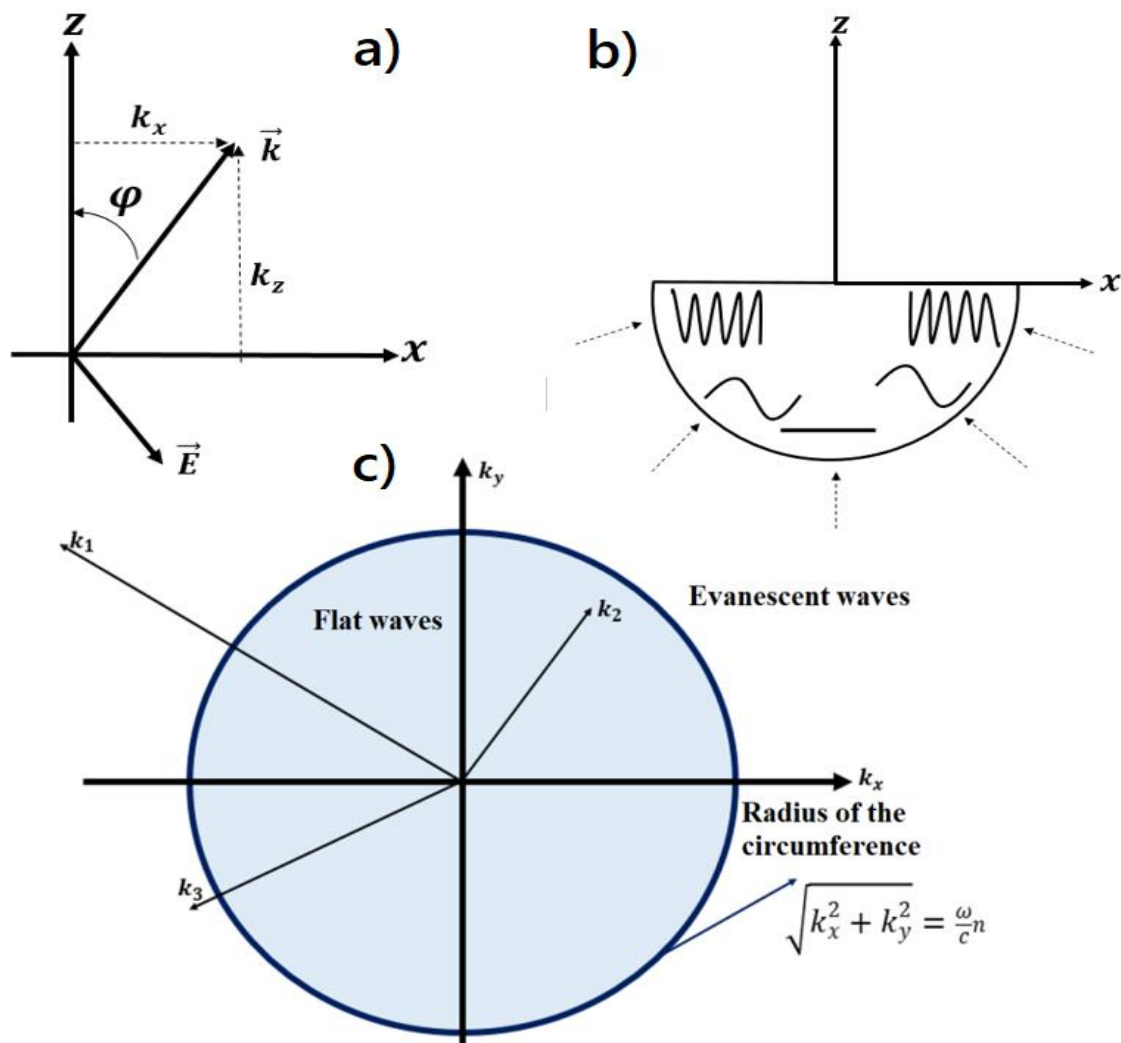
*Figure 3.4. a) Representation of a plane wave propagating at an angle **ϕ** to the z axis. (b) Illustration of the transverse spatial frequencies of plane waves incident from different angles. The transverse wavenumber $\sqrt{k_x^2 + k_y^2}$ depends on the angle of incidence and is limited to the interval $[\mathbf{0} \dots \mathbf{k}]$. c) Representation of the possible values of $\sqrt{k_x^2 + k_y^2}$ and their influence on the behavior of a spectral component. Any vector k that is within the circle, with radius $\mathbf{k} = \frac{\omega}{c}n$, for example $\mathbf{k_2}$, will be associated with a plane wave type spectral component in the distant field. For vectors $\mathbf{k}$ outside the circle, such as $\mathbf{k_1}$ and $\mathbf{k_3}$, we will always have evanescent waves of the near field, the ones farther from the edge of the circle will have an exponential decay faster than those close to the circle; that is, the component related to $\mathbf{k_3}$ has a smoother decay than that of $\mathbf{k_1}$. Adapted from L. NOVOTNY; 2012 [39].*

However, they are not all considered for a description of a physical system; plus the sum of $k_x^2 + k_y^2$ exceeds k^2, the faster the decay with distance. However, given an infinite distance from the emitter plane, all evanescent components will have declined asymptotically to zero, either "fast" or "slowly." Thus, the information that can be obtained from an object at great distances will be filtered by a low-pass filter of spatial frequencies: $k = \sqrt{k_x^2 + k_y^2} \leq \frac{\omega}{c}n$. Whenever the term $\sqrt{k_x^2 + k_y^2}$ is greater than $k = \frac{\omega}{c}n$ and the spectral component will be "filtered" as it evanesces on the way to the detector, and the information it carries will be lost. Since we have components that decay extremely fast, there is always loss of information, no matter the distance between detector and object, this loss being greater as distance increases and we leave the near-field regime [30, 38, 43, 44, 45]. Fig. 3.5. Illustrates the situations; on the left the electric field $\vec{E}$ emanating from a narrow subwavelength source is shown together with its angular spectrum calculated by the inverse of equation (*).
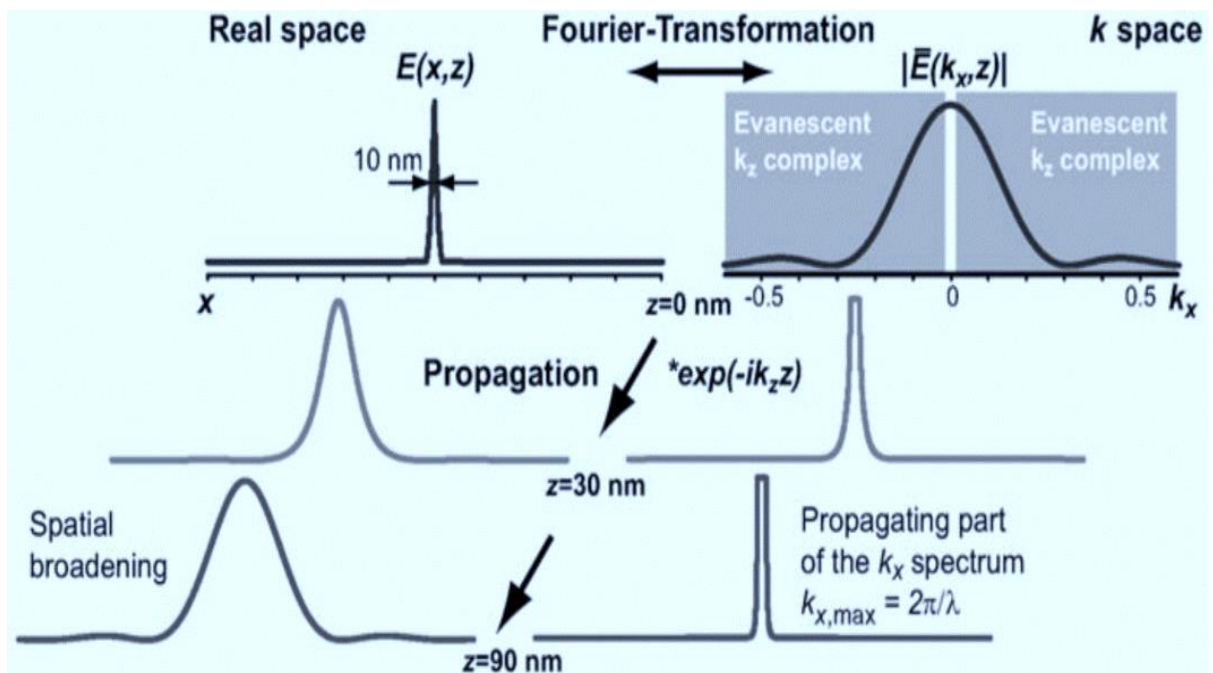
Figure 3.5. Schematic representation illustrating the propagation of waves and the loss of spatial information with the Fourier-Transformation link k-space with real-space. Adapted from Achim Hartschuh 2008 [38].

On the Fig. 3.5. Top row: Initial field distribution $\vec{E}(x, z = 0)$ at a 10 nm wide source in the x-z plane (left) and corresponding angular spectrum $\widehat{\vec{E}}(k_x, 0)$ (right). The spectrum contains both evanescent and propagating waves near the source. The two lower rows illustrate the development of the fields at a distance of z=30 nm and z=90 nm. Only waves with $k_x \leq (2\pi/\lambda) \approx 0.0126\ nm^{-1}$ propagate when light with a wavelength of $\lambda = 500\ nm$ is used in a vacuum. Evanescent waves decay exponentially following $e^{(-k_z z)}$. The decay of high spatial frequencies leads to spatial broadening and loss of spatial information, see Fig. 3.6. **[38]**.
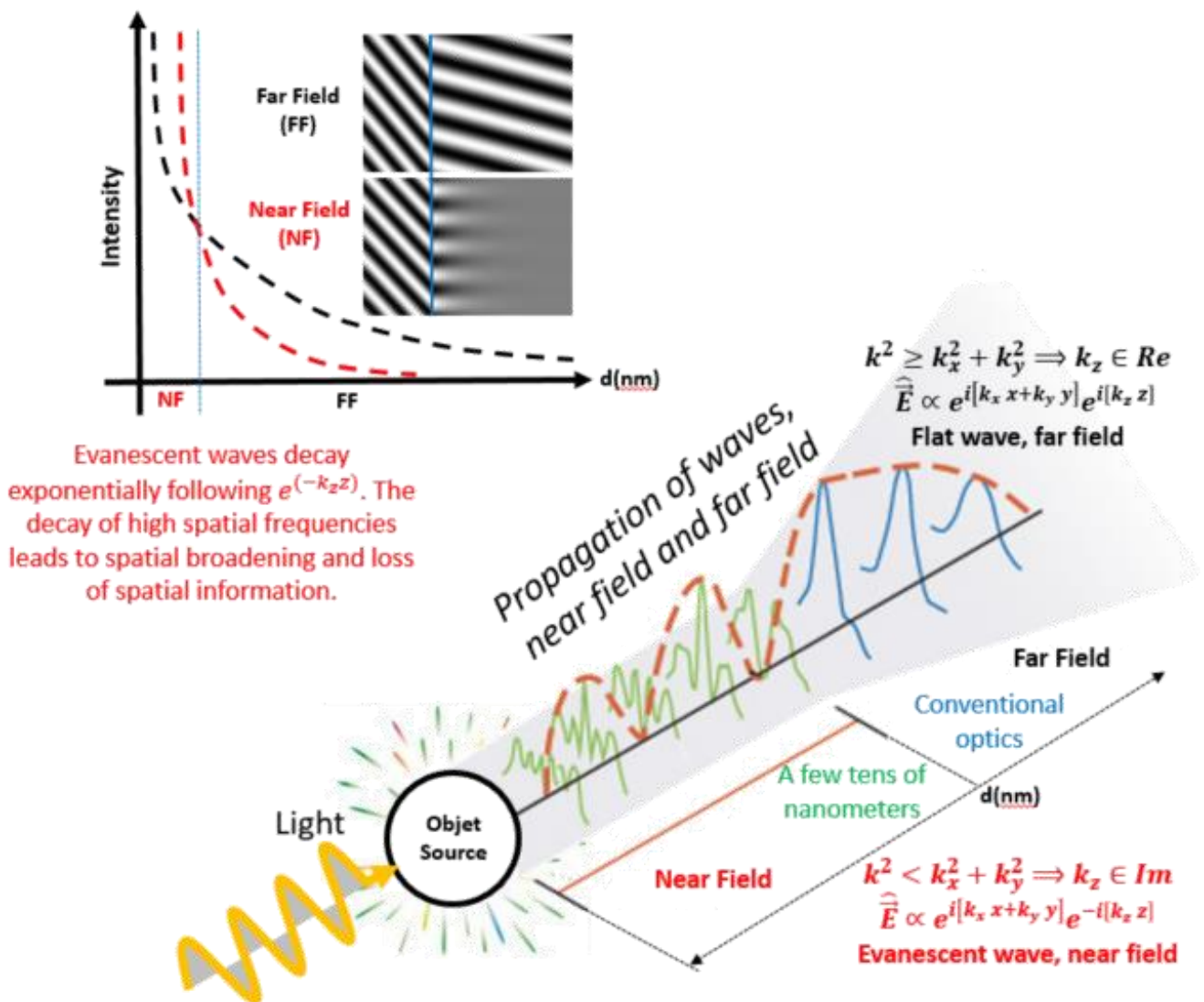
Figure 3.6. Schematic representation illustrating the propagation of waves, near field and far field **[30, 38, 43, 44, 45]**.

3.1.2. RESOLUTION LIMIT.

The diffraction limit is directly related to the maximum possible spatial resolution to be obtained in an optical experiment, that is to say, the minimum distance that can exist between two points in the object plane so that its images are discernible, distinguishable from each other. This limit is established by criteria, where the best known are Abbé and Rayleigh. Each criterion uses a different physical system for the calculations, such as electric dipoles aligned in a given direction or as diffraction slits respectively. The Abbé criterion considers the overlap between two functions (point spread function) of two electric dipoles with axes perpendicular to the optical axis (see Fig. 3.7) **[46]**, while Rayleigh uses a diffraction grating spectrometer (see Fig. 3.8) **[47]**.
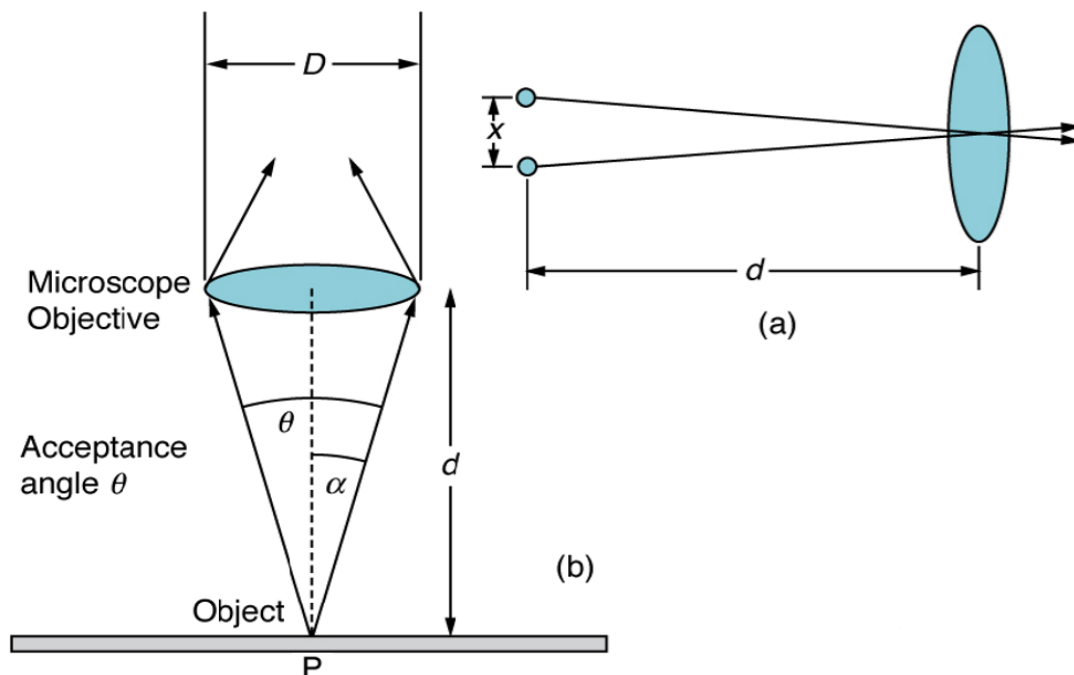
*Figure 3.7. The Abbé criterion; (a) have two point objects separated by a distance **x**, where **d** is the distance between the specimen and the objective lens, and have used the small angle approximation (i.e., we have assumed that **x** is much smaller than **d**), so that $\tan\theta \approx \sin\theta \approx \theta$. (b) shows a lens and an object at point P. (b) Shows a lens and an object at point P. The NA here is a measure of the ability of the lens to gather light and resolve fine detail. The angle subtended by the lens at its focus is defined to be $\theta = 2\alpha$, $\sin\alpha = \frac{D}{2d}$ and $NA = n\sin\alpha$; where **n** is the index of refraction of the medium between the objective lens and the object at point **P**.*

$$x = d\,\theta \approx 1,22\frac{d\,\lambda}{D}$$

$$2\,d\,\alpha \approx 1,22\frac{\lambda}{D} = \frac{x}{d}$$

$$x = 1,22\frac{\lambda\,d}{D} = 1.22\frac{\lambda}{2\,sin\,\alpha} = 0,61\frac{\lambda}{NA}$$

$$\Delta x \approx \frac{0,61\,\lambda}{NA}$$

Where λ and NA are the wavelength of light used in the experiment and the numerical aperture of such a lens, respectively. These criteria to be subject to such assumptions have different expressions for the diffraction limit while being related at the same time. For the maximum spatial resolution of a conventional optical microscopy system, where an objective lens for focusing/detection is used under the Rayleigh criterion say:
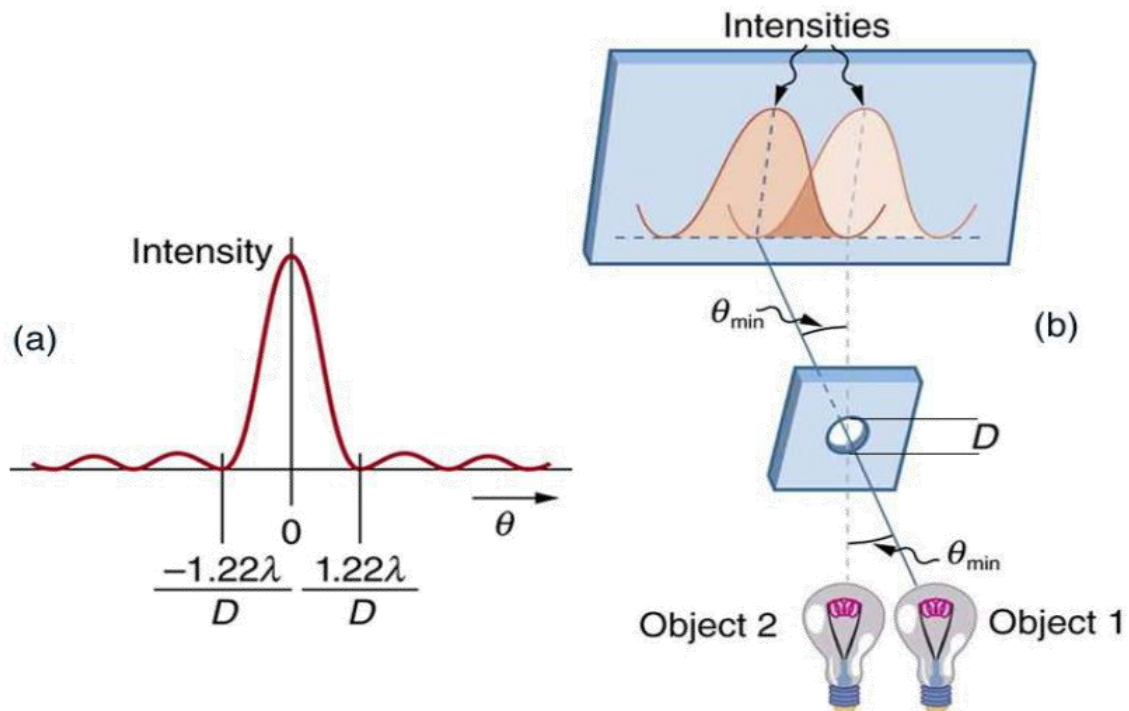
Figure 3.8. Rayleigh criterion; (a) Graph of intensity of the diffraction pattern for a circular aperture. Note that, similar to a single slit, the central maximum is wider and brighter than those to the sides. (b) Two point objects produce overlapping diffraction patterns. Shown here is the Rayleigh criterion for being just resolvable. The central maximum of one pattern lies on the first minimum of the other.

$$\theta \approx 1,22\frac{\lambda}{D}$$

Where θ is the angular resolution (in radians), λ is the wavelength of light, and D is the diameter of the aperture of the lens. The $1,22$ factor is derived from the calculation of the position of the first circular ring around the central disc diffraction pattern of Airy. The resolution mentioned above is also known as angular resolution and can become as a spatial resolution, Δx, multiplying the angle θ (in radians) with the distance to the object. For a conventional lens, this distance is close to the focal length, $f = d$, of the lens.

All the criteria mentioned above, in practice in conventional optical systems reach spatial resolutions of the order of approximately $(\lambda/2) \approx 250$ nm for visible light, this is the maximum information I can obtain. To understand any definition for the diffraction limit, we must phenomenologically understand what is happening; all information emitted by a source that emits electromagnetic waves is divided into two types of waves, evanescent waves and distant field waves, between these two types of waves all information travels; what most of the time is that most of the information is lost very quickly in the far field, on the way to the detector (more precisely, the information carried by the evanescent Fourier components that only survive a few tens of nanometers from the source source). Bearing in mind that everything discussed above on the propagation of electromagnetic wave information, for a sufficiently large distance, all information will be lost, especially in the near field; This also means that the range where $k_\parallel$ is large, the spatial frequency high, this is related to the range where $r_\parallel = \frac{1}{k_\parallel}$ which is small. This means that information related to small details or separations in the sample is contained in the near field and will not be detected far from the source [30].

To understand how these values impact spatial resolution, consider that the emitted wave at the origin is the sum of flat waves described by electric fields with Gaussian distribution of spatial frequencies. Far from the source, all information regarding the near field will be lost and the Gaussian distribution should have band width $\Delta k_\parallel = \frac{2\pi}{\lambda} n$. Since the Fourier transform of a Gaussian distribution is another Gaussian distribution with band width $\Delta r_\parallel = \frac{1}{\Delta k_\parallel}$, we see that the best resolution in a distant field regime is $\Delta r_\parallel = \frac{\lambda}{2\pi n}$, where $\Delta r_\parallel = \sqrt{\Delta x^2 + \Delta y^2}$. This limit of resolution calculated by the Gaussian distribution is quite optimistic. The components that evolve during propagation of the beam are "filtered" and only the constrained ones remain within the interval $(k_x^2 + k_y^2)^{1/2} \leq \frac{\omega}{c} n = \frac{2\pi}{\lambda} n$, as shown in Fig. 3.4; we now analyze the best resolution that can be obtained in an experiment in the case where a beam propagates until it loses all its evanescent components (conventional microscopy). We have this situation, the k, for the components of the angular spectrum of this beam, with width: $\Delta k_\parallel = \frac{2\pi}{\lambda} n$. If the distribution of these k is of the Gaussian type in the Fourier space, this implies that, in real space, this beam will also be represented by a Gaussian distribution, whose width will be given by: $\Delta r_\parallel = \frac{1}{\Delta k_\parallel}$. This width of the real field is associated with the possibility of resolving the image of an object, that is, the limit of spatial resolution (given by the diffraction limit) associated with the experiment is obtained by the width at half height of the distribution of the electric field that reaches the sample at that point. If two objects are separated by a distance less than this value, $\Delta r_\parallel$, it will not be possible to differentiate their positions optically. Thus, the diffraction limit will be given by $\Delta r_\parallel = \frac{\lambda}{2\pi n}$. The above case relies on the fact that it is supposedly possible to prove the entire spectrum of special frequencies that reach an objective lens, which is

not true, since its $NA = n\,sen\,\theta$ is a limiting factor, where θ is defined as half the collection angle (would be perfect if the collection angle were π where we would have $n\,sen\frac{\pi}{2} = n$). In the present case, taking into account the capacity of the objective, one has:

$$\Delta r_\parallel = \frac{\lambda}{2\pi NA}$$

However, despite being a good approximation, it provides a higher resolution than that given by the Abbé boundary, which is approximately 3, 8 times smaller and closer to the values obtained experimentally. But it is evident that with this reasoning the diffraction limit exists due to the loss of evanescent components that cannot reach the detector. Note that according to equation $\Delta r_\parallel = \frac{1}{\Delta k_\parallel}$ if have an arbitrarily large width $\Delta k_\parallel$, it would be able to optically define the position of any object with exactness. In practice, it has been mentioned before, during propagation, some components will always be lost, their k being no longer accessible in the far-field scheme. To overcome this obstacle is the near-field spectroscopy, which consists of using the apex of a metal tip with a hole and without a hole, which serves as an optical antenna, very close to the object of study, in order to overcome the diffraction limit, collecting these evanescent components before they are lost. Placing such an antenna (serving as a light source and receiver) within a few nanometers of its object may complicate obtaining the desired signal, as it becomes part of the system it is testing, and data analysis must take into account the presence of the it. For example, in near field Raman spectroscopy measurements, one must analyze in the detected signal which portions of the light intensity are given by the fluorescence of the tip and which composes the Raman signal of the sample. Another complication is that, because the metal tip cannot be moved into the object (in most cases), the measurements will always be restricted to the surface of the studied material. In conclusion, for each type of near-field source

used (metal tip, fiber optic aperture, etc.), the effects of the interaction will be different, and care in the analysis of the results should be adequate **[30, 48, 49]**.

As a consequence of the representation of a point object in a distant field by the point scattering function, point objects cannot now be located indefinitely, that is, if two source points are considerably close, in a distant field, their point scattering functions they can overlap, being indistinguishable from a single point scattering function, associated with a single point object. Consider the situation in the Fig. 3.9, an ideal electromagnetic point source is located at the focus of a high-**NA** aplanatic objective lens with focal length f. This lens collimates the rays emanating from the point source and a second lens with focal length $f^{'}$ focuses the fields on the image plane at $z = 0$.
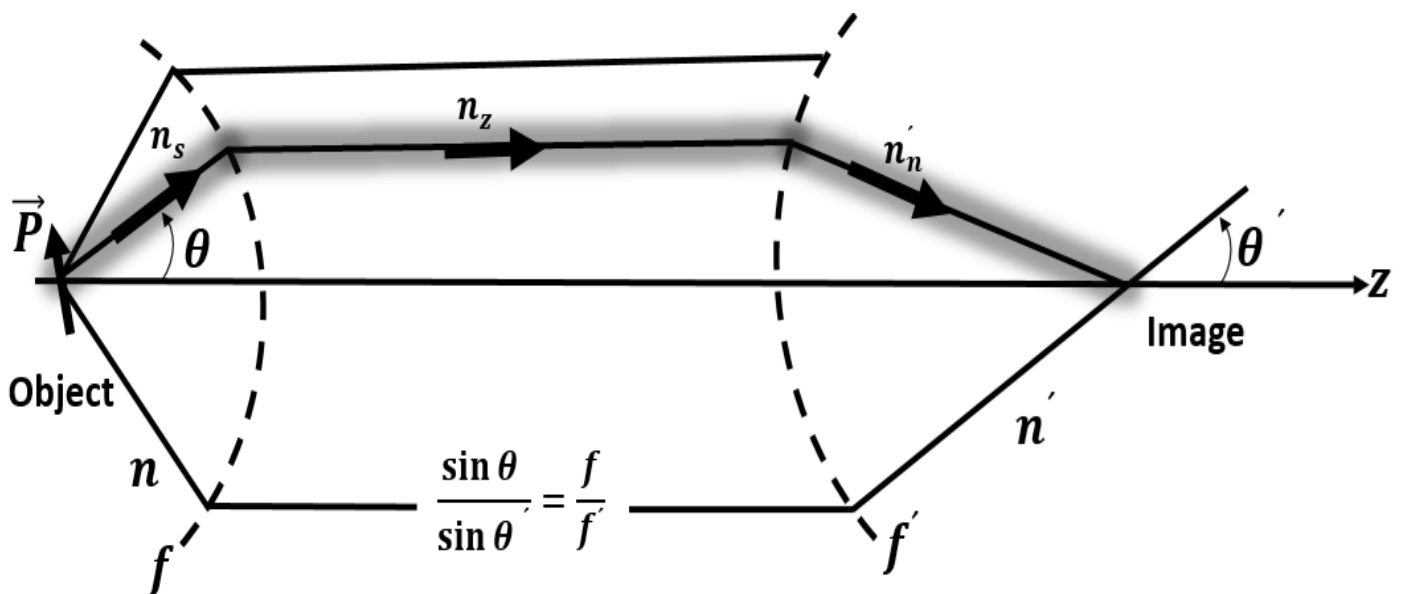
Figure 3.9. Configuration used for the calculation of the point- spread function. The source is an arbitrarily oriented electric dipole with moment **p**. *The dipole radiation is collected with a high-NA aplanatic objective lens and focused by a second lens on the image plane at* **z** = **0**. *Adapted from L. NOVOTNY* **[30]**.

Bearing in mind that the previously described point objects are electrical dipoles, as presented in (NOVOTNY; HECHT, 2012), and that these are aligned with the x-axis and their point scattering function can be identified as the square module of the electric field, $\left|\vec{E}(x, y, z = 0)\right|^2$, within of the paraxial approximation, the point spreading function associated with the dipole is given by:

$$\lim_{\theta_{max} \leq \pi/2} \left|\vec{E}(x, y, z = 0)\right|^2 = \frac{\pi^2 P_x^2 NA^4}{\varepsilon_0^2 nn'\lambda^6 M^2}\left[2\frac{J_1(2\pi\tilde{\rho})}{(2\pi\tilde{\rho})}\right]^2, \tilde{\rho} = \frac{NA\rho}{M\lambda}$$

Where $NA = n\,sin\,\theta_{max}$, is the numerical aperture of the lens used for detection and $M = nf'/n'f$, magnification of the optical system; and $J_1(2\pi\tilde{\rho})$ is the Airy Function, characteristic of the point spreading function for an electric dipole in the paraxial approach. The Airy function associated with the square of the electric field has an ellipsoidal shape as a characteristic; however, for the total energy associated with the radiation that propagates from the emitting dipole, it is necessary to consider the square of the magnetic field, which is associated with the electric field by a $\pi/2$ rotation. Considering the joint contribution of the electric and magnetic fields, the dot scattering function associated with the electric dipole in a distant field has a circular aspect. The Airy function is characterized by the presence of a central maximum and alternating maximum and minimum. The distance between the center of the central maximum and the first minimum, Δx, is known as the radius of the Airy disk and is a characteristic of the point spreading function.

$$\Delta x = 0,6098\frac{M\lambda}{NA}$$

Once the theory of the point scattering function and the Airy disks have been established as a consequence of the limited amount of information detectable by a distant observer, due to the attenuation of the evanescent waves and the numerical opening of the detector, it is possible

to introduce the criteria of Abbe and Rayleigh to address spatial resolution. This according to Abbe, two object points are distinguishable in the distant field if their scattering functions in the image plane are such that the minimum of one of them coincides with the maximum of the other,

$$Min[\Delta r_\parallel] = 0,6098 \frac{M\lambda}{NA}$$

According to Rayleigh, two object points are distinguishable in the distant field if their wave functions are such that at least the maximum of Airy's second disk of the scattering function of one of the points coincides with the first minimum of the scattering function of the other point **[30]**.

3.2. NEAR FIELD OPTICAL MICROSCOPY WITH SOLID TIPS.

Field enhancement near nanoscale metal structures plays a central role for optical phenomena such as surface-enhanced Raman spectroscopy (SERS), second harmonic generation (SHG), near-field microscopy and Tip-enhanced Raman spectroscopy. According to Fourier optics, a small aperture or small object with a finite size can be considered as an overlap of sets of gratings, which have large distributions of network constants from much smaller to larger than the wavelength of light. These concepts are illustrated in Fig. 3.10. The small aperture (Fig. 3.10 b)) and the small object (Fig. 3.10 a)) with the same size ($= 2a$, which is much smaller than the length of wave of light) become the same sinusoidal function, through the Fourier transform. Among these networks, the network with a network constant greater than the wavelength can diffract the light at a suitable angle to satisfy the diffraction condition. Therefore, the diffracted light propagates in a specific direction. On the other hand, the network with a network constant less than the light wavelength does not satisfy the light propagation condition. Consequently, the diffracted light becomes an evanescent field that cannot propagate from the network structure and

remains localized to the object. With this concept of evanescent field components, the light field is confined and located very close to the aperture or object, which results in the generation of a nanowire (nano light) source, which has the size corresponding to the diameter ($= 2a$) of the aperture or object. This is because the evanescent light components have a wave number k, which is much larger than the light propagation component, see Fig. 3.10 c). The concept of light-confining, as shown in Fig. 3.1 a) and b) and Fig. 3.10 a) and b), were initially obtained in the near-field microscopy, SNOM, mentioned earlier, where typical configurations of aperture probes are usually made of sharp metal-coated sharp optical fiber in order to block light leakage from the cone except in the aperture. Non-aperture probes, however, are usually cantilever silicon tips Atomic Force Microscopes (AFM) or very pure chemically sharp metal strands **[30, 39, 50-52]**.

Theoretically, the same spatial resolution can be expected in the same way with the near field microscopy technique with apertures and without aperture. Higher spatial resolution requires a smaller aperture in the optical fiber as a sample, Fig. 3.10 b), or with a smaller sharp tip diameter, Fig. 3.10 a). However, according to Fig. 3.10 c), the wave number a becomes larger when a becomes smaller. In addition, a smaller opening diameter or a smaller tip diameter would mean more components that are evanescent. However, for practical experimental reasons, it is more difficult to detect signals in the nano dimensions because they are very weak signals; in addition, the smaller aperture makes the near field signal too weak. This is crucial in particular for Raman applications because the Raman scattering cross-section is extremely small, which results in the use of large aperture (low resolution) or unreal long acquisition time **[39, 50-52]**.
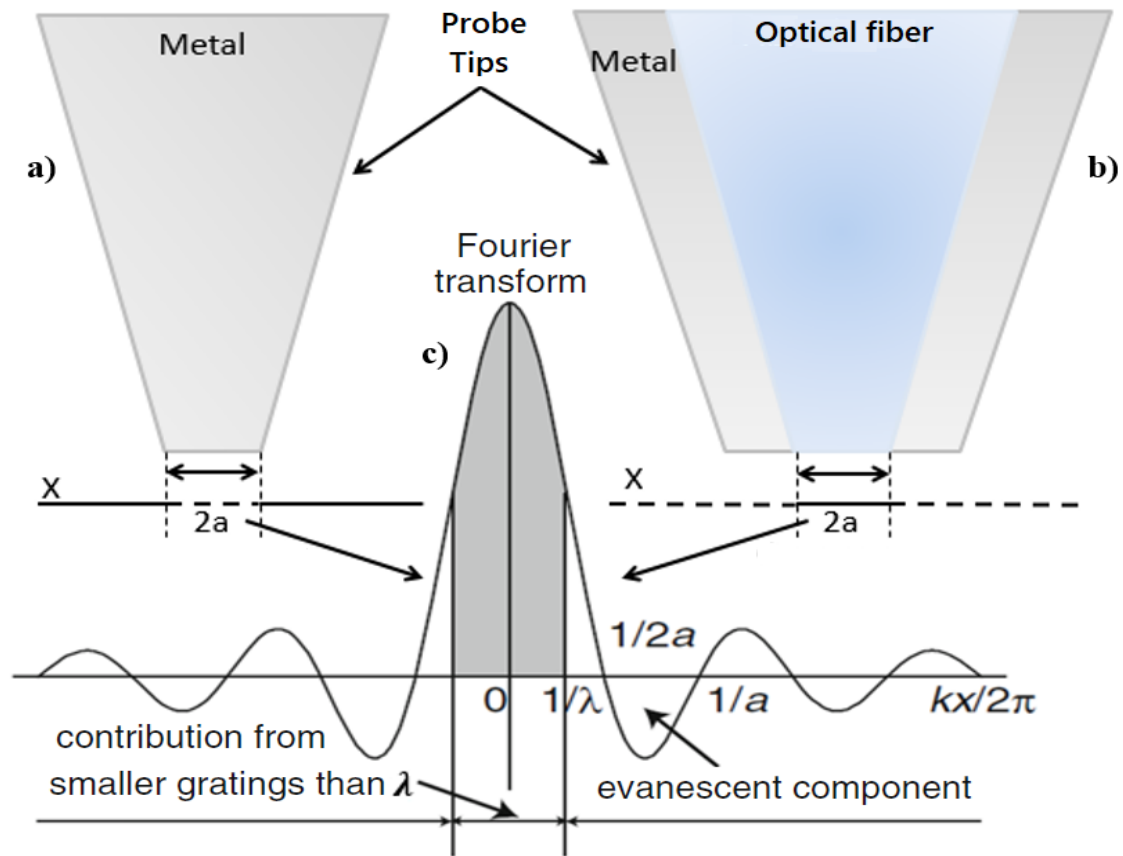
Figure 3.10. Concepts of scanning probe a) without aperture, b) aperture and c) Fourier transform of a scanning tip **[39, 50-52]**.

On the other hand, an increase of the signal can be expected in the case of solid probes without aperture, especially when the tip probes are made of noble metals. This signal enhanced is specifically expected when the tip diameter becomes smaller (nm), corresponding to higher spatial resolution and intensification of the optical electric field by the action of the metal tip when LSPP and the lightning rod effect are generated upon being illuminated by an excitation laser beam polarized. The conductive free electrons that oscillate collectively on the metal surface, these induced oscillations of polarized and quantized charges on the surface make the concentrated electrons (and the positive charge) on the tip apex generating a very strong external electric field. Any photon energy will be confined in the local vicinity of the tip apex, see Fig. 3.11. Therefore, the metal tip

function is to be as a reservoir of photons, a nanowire amplifier, and a well-localized **[26, 30, 39, 50-52]**.
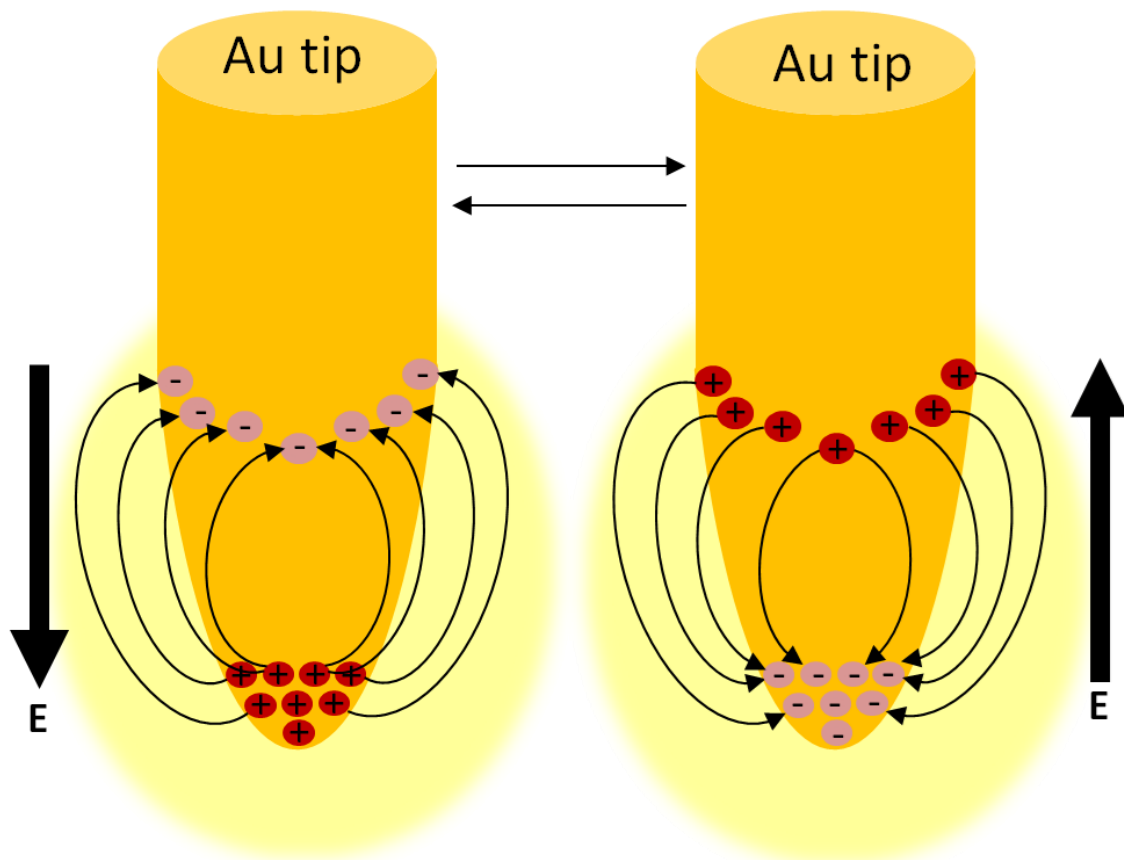
Figure 3.11. Oscillation of electrons in a metallic tip structure **[26, 30, 39]**.

The enhancement originates from a combination of the electrostatic lightning rod effect, which is due to the geometric uniqueness, sharply of the pointed structures, and the Localized Surface Plasmons (LSP) resonance that depends substantially on the excitation wavelength. The incident light drives, conducts the free electrons in the metal along the polarization direction. While the charge density is zero inside the metal at any instant of time, the charges accumulate on the surface of the metal. When the incident polarization is perpendicular to the tip axis, diametrically opposite points on the tip surface have opposite charges. As a consequence, the foremost end of the tip remains uncharged and no field enhancement is achieved. In contrast, when the incident polarization is

parallel to the tip axis, the induced surface charge density is almost rotationally symmetric and has the highest amplitude at the end of the tip [26, 30, 39, 50-52].

The local electric field is used as a nanolight source to excite photon–matter interaction, including fluorescence (Hayazawa et al., 1999; Hamman et al., 2000), second harmonic generation (Zayats and Sandoghdar, 2000) and Raman scattering (Inouye et al., 1999; Hayazawa et al., 2000; Stockle et al., 2000) under the tip. In particular, the enhancement of Raman scattering by metallic nanostructures has been widely investigated as SERS since 1970s (Chang and Furtak, 1981; Moskovits, 1985). The most notable effects in the interaction of light with metallic nanostructures (Au-tip) is the improvement of strong and spatially located field amplitude, due to the effects of the lightning rod induced by acute curvatures (Novotny and Hecht 2006). The resonance frequencies associated with such oscillations and, therefore, the optical properties can be adjusted over a wide spectral range according to the material and shape of the nanostructure. In particular, gold and silver can sustain plasma oscillations at optical frequencies.

Likewise, in the case of tips, the electric field has been calculated using a variety of numerical methods that depend on the electromagnetic mechanism. So far, several analytical methods have been used to calculate the electromagnetic field, the finite-time domain method (FDTD), the contour element method (MEC), the finite element method (FEM) and the multiple multipolar method (MMP). All these methods, at least qualitatively, result in the same conclusion to intensify the field at the tip apex. In Fig. 3.12a, the local electric field distribution shown near a silver probe tip calculated by deriving the numerical solution from the Maxwell

equations. It can be seen that the optical field is highly confined in a small volume near the end of the tip. In addition to space confinement, the optical field is strongly amplified up to 15 times and up to 225 times that corresponds to the electric field strength. Methods or calculation models, however, can vary factor improvement; however, the intensified field size is comparable with the probe tip in any case. In Fig. 3.12b the same tip is shown, but with an S polarization excitation light. The field enhancement is very small, even only 3 times, compared to the polarized excitation light P, in Fig. 3.12b. The role of the SPP is clearly evident in the case of a dielectric tip, Fig. 3.12c, or a semiconductor tip, Fig. 3.12d. The maximum field, in these cases, 1.7 and 2.6 times, respectively. All of the above has been shown to have a metal probe tip strongly amplified and well located the optical field through the PPS resonance effect at the apex. This allowed optically to observe a wide variety of materials with nano metric spatial resolution and thus was and is very promising for enhanced Raman intensified tip spectroscopy **[26, 30, 39, 50-52]**.

The metal tip is the most important component of the TERS system. The tip radius, material, structure and resonance of the SPP must be properly controlled to perform highly successful and high resolution TERS measurements in a reproducible manner. The resolution of the TERS images is basically determined by the sharpness of the tip apex. The tip diameter is typically required to be in the range of several tens of nanometers or less. Therefore, it is also important to control the spectral response of the metal tip to match the frequency of the polarized excitation light. The control and place of plasma resonance at the tip is the nanometer rod size and this remains a very challenging problem today in the development and improvement of TERS. As materials for making the tips, noble metals such as silver and gold are the most commonly used. These

metals are good plasmonic materials in the visible to the near infrared, due to which they have little imaginary part of the dielectric function and of a negative value of the real part in this spectral band **[28]**. In addition, gold and silver are no longer "metals" but "dielectrics" in ultraviolet (UV), where photon energy exceeds plasma frequencies. In this spectral range, aluminum is also used as a plasmonically active material **[30, 39]**.
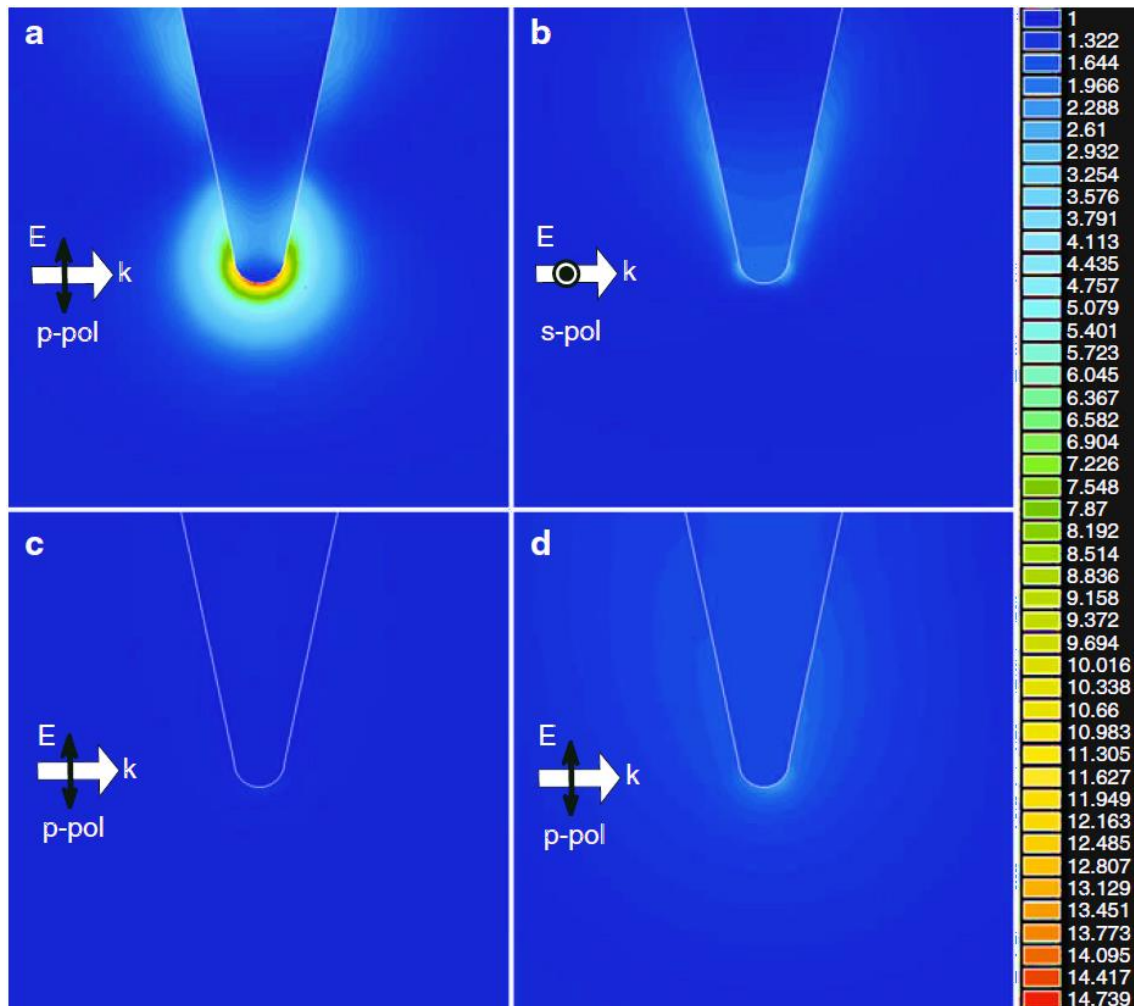
*Figure 3.12: Distribution of the electric field at the apex of the tip of a silver tip ($30\,nm$) excited by (a) polarization p and (b) light with polarization s, ($\lambda = 532\,nm$). (c) And (d) are the field distribution of SiO_2 and silicon tip with polarized light p. Form Kumar et al. **[39]**.*

Heretofore, typically two types of metal tips have been described. One is an arm or swing that is coated in metal, the cantilever, and the other is a chemical etching forging. The cantilever is conveniently made from a

commercially available silicon support arm or balance (Si) of an AFM or the commercially available silicon nitrite (Si_3N_4), and then depositing a thin metal film over the tip surface, see Fig. 3.13a. Where the metal has a purity of above 99.999%, which is thermally evaporated under vacuum and deposited on the surface of the probe slowly at a rate of less than 1Å/s to avoid damaging the apex of the tip. The deposition thickness is easily obtained and is typically several tens of nanometers and a small diameter of a few tens of nanometers at the apex of the tip. The second type of metal probe is an acid-etched noble metal wire, Fig. 3.13b, which is used in both systems, on which TERS and STMs are based as well as in AFM systems operated by a cutting force feedback mechanism, in which the wire is attached to one of the feet of a tuning fork. The chemical tiling of the silver wires can be done with perchloric acid, ethanol and deionized water solution and the gold wires are etched with hydrochloric acid and/or mixed with a solution of ethanol **[25, 26, 30, 39]**.

Intensification values in the intensification of the Raman signal reported experimentally using solid metal tips are typically between 10^3 to 10^4 orders of magnitude, as was mentioned above, but may increase further; However, the enhancement factor also depends on the amount and type of molecules. Nevertheless, what further enhances the quality and size of the optical field generated with a good intensification is the size and surface of the tip apex. In fact, this suggests that if a good control in the manufacture of the tips is achieved, specifically in size ($\approx 20\,nm$) and surface (as smooth and smooth as possible) gives qualities of enhancement to be achieved that could be attainable up to $\sim 10^{11}$ order of magnitude, similar intensification to be able to detect even a single molecule **[30-39]**.
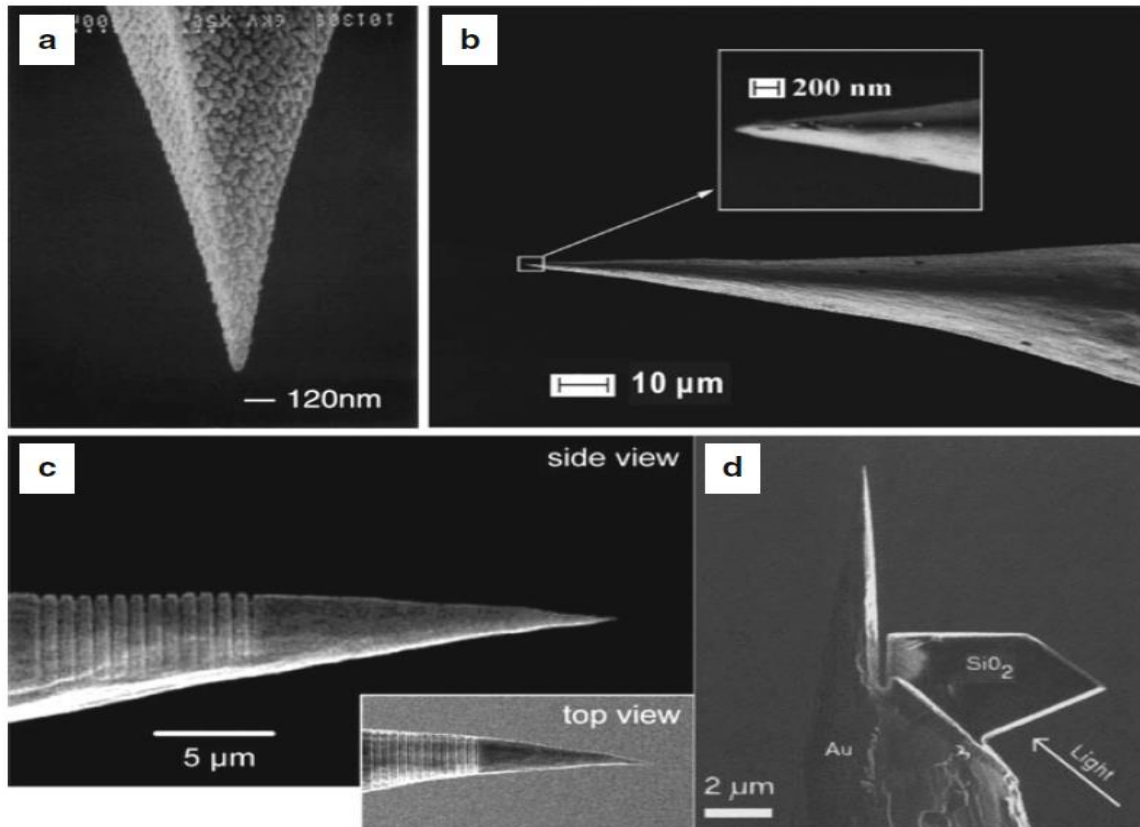
Figure 3.13. SEM images of various types of metal probe tips. a) an Ag-coated Si Cantilever; b) Ag type made by chemical wire forging; c) metal probe with a grid made on an axis; d) metal probe with an Otto coupler. Form Kumar et al. **[39]**.

In any case, the enhancement in the intensification in a metal tip is related to the LSPP, therefore, the investigation of the spectra and the improvements in that specific part in how to generate plasmons are of great importance. It should be borne in mind that the spectral measurement of light scattered by a metal tip is to find out which band of the electromagnetic spectrum works best. Typically, the measured spectra show a single resonance peak with the peak width of about 100 nm, and the position of the peak in the visible NIR appears approximately between 500 and 800 nm when a gold or silver tip is used. A gold tip shows the resonance peak at the wavelength relatively longer than the wavelength relative to silver due to the difference in dielectric function **[25, 26, 30, 39]**.

The main factor of maximum performance in TERS is expected to be when the plasmons on tip apex and the excitation laser are spectrally combined. In practice, the operating wavelength is defined for the available laser installation used for the TERS experiment. One technique for controlling the SPP resonant wavelength on the tip is to modify the refractive index of the probe tip base material, for example at the metal-coated Si tips; It is known that the resonance wavelength of the nano-tip plasmons is affected by the environment; increasing the refractive index of the medium surrounding the tip apex shifts the resonant wavelength to the longer side, and vice versa. By replacing the refractive index of Si ($\boldsymbol{n} = \boldsymbol{4,4}$) with lower levels, such as $\boldsymbol{n} = \boldsymbol{1.5}$ (SiO_2) and $\boldsymbol{n} = \boldsymbol{1.4}$ (AlF_2) which provides a resonance of blue-displaced plasmons. A probe of this type is used in combination with the blue to green laser and an improvement is observed. The substitution of the refractive index is done by covering the surface of the Si probe with a low index material of, or thermally oxidizing the surface of the Si probe. The advantages of the latter method is that the tip does not become opaque after the index is modified and the effective index can be continuously adjusted by the thickness of the oxidized layer, which provides flexibility to optimize the resonant wavelength of the plasmons **[25, 26, 30, 39]**.

Another important aspect when considering the probe tip is the coupling efficiency between the plasmonic peak and the light and far field peak because the probe tip plasmons are initially triggered by light from the far field, therefore the detector also have to be at far field. Increasing the coupling efficiency of detection in both lighting and in-detection is a direct strategy to achieve a higher signal-to-noise ratio in the TERS. So far, only a few methods have been reported for an efficient coupling of laser light with the tip. The probe shown in the Fig. 3.13c has a grid in the tip body. The

incoming distant field light becomes efficient for SPP that propagate toward the apex of the tip through the grid. Without the grid, the coupling between the surface plasmons and the distant field light is limited, due to the incompatibility of the wave vector. Without the grating, the coupling between the surface plasmon and the far-field light becomes limited because of the wave vector mismatch. The grating is fabricated by focused ion beam (FIB). The probe shown in Fig. 3.13d also aims to fill the gap in wave vector mismatch, but uses an evanescent field generated on a micro-prism fabricated near the probe surface (Otto configuration). These techniques are especially effective for the probes made by wire etching **[25, 26, 30, 39]**

3.3. LOCAL ELECTRIC FIELD ENHANCED DUE TO A METAL TIP.

The interaction of an optical electric field with a metallic tip can be modeled considering that the tip behaves like an electric dipole, a reasonable assumption, since an electric field acting on a metal causes a separation of the electric charges of these, giving rise to an induced dipole. Let $\vec{\mu}_{Dp-tip}(\omega)$ the effective dipole be induced at the tip apex and considering that it has radial symmetry and the z axis coincides with the tip axis, due to the polarizabilities in the $\alpha_\parallel$ parallel, and $\alpha_\perp$ perpendicular directions, to the z direction, $\vec{\mu}_{D-tip}$ can be determined as response to the application of an external electric field, $\vec{E}_{ext}$:

$$\vec{\mu}_{Dp-tip}(\omega) = \overset{\leftrightarrow}{\alpha}_{Au-tip} \cdot \vec{E}_{ext}$$

$$\begin{bmatrix} \mu_x \\ \mu_y \\ \mu_z \end{bmatrix}_{Dp-tip} = \begin{bmatrix} \alpha_{xx} & \alpha_{xy} & \alpha_{xz} \\ \alpha_{yx} & \alpha_{yy} & \alpha_{yz} \\ \alpha_{zx} & \alpha_{zy} & \alpha_{zz} \end{bmatrix}_{Au-tip} \begin{bmatrix} E_x \\ E_y \\ E_z \end{bmatrix}_{ext}$$

Due to the symmetry of the problem:

$$\vec{\mu}_{Dp-tip}(\omega) = \begin{bmatrix} \alpha_\perp & 0 & 0 \\ 0 & \alpha_\perp & 0 \\ 0 & 0 & \alpha_\parallel \end{bmatrix}_{Au-tip} \vec{E}_0(\omega)$$

Where $\vec{E}_0(\omega)$ is the exciting electric field in the absence of the tip, the z-axis coincides with the tip-axis, and the polarizability $\alpha_\perp = 2\pi\varepsilon_0 R^3 \frac{\varepsilon(\omega)-1}{\varepsilon(\omega)+2}$ and $\alpha_\parallel = \pi\varepsilon_0 R^3 f_{Ench}(\omega)$, being $f_{Ench}(\omega)$ the enhanced amplification factor and R is radius. The effective dipole, the electric field in the vicinity of the tip can be determined in general form as:

$$\vec{E}(\vec{r}, \omega) = \vec{E}_0(\vec{r}, \omega) + \frac{\omega^2}{\varepsilon_0 c^2} \overleftrightarrow{G}(\vec{r}, \vec{r}_0, \omega)\vec{\mu}(\omega)$$

Being $\overleftrightarrow{G}, \vec{\mu}$ the Green functions, Based on the previous expression, Novotny simulated the intensification field in the vicinity of the apex of a metallic tip as a function of the direction of the applied external electric field, see Fig 3.14. [30, 53, 54].
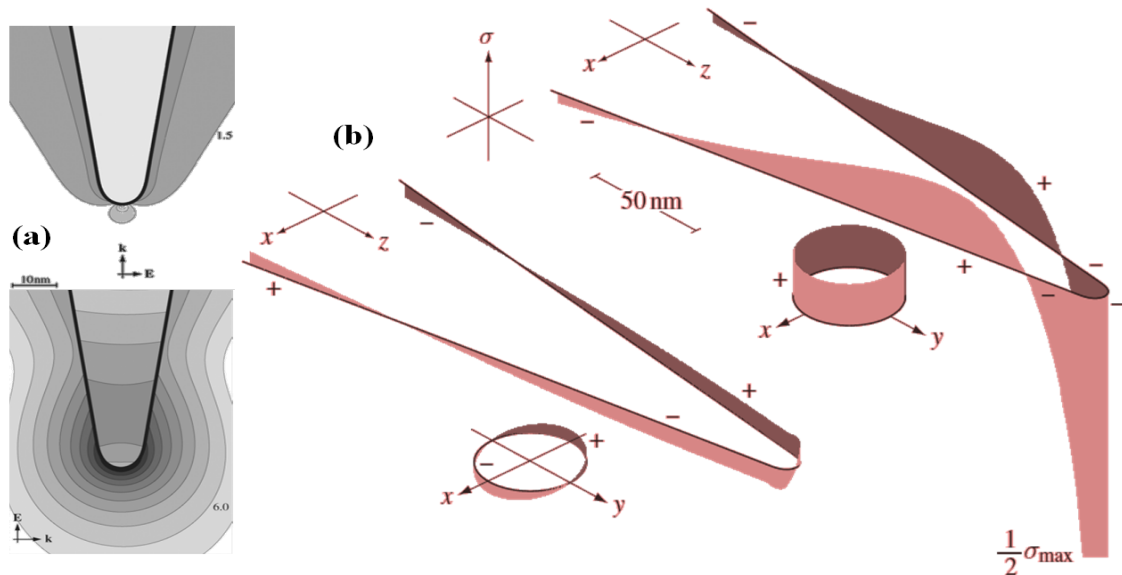
Figure 3.14. (a) Electric field strength for fields parallel and perpendicular to the tip axis, (b) Effect of an incident-polarized field on the densities of charges induced in a metal tip. It is a simulation for the electric field response depending on the direction of the applied field. Fields whose direction is aligned with the tip axis show greater amplification. Adapted from L. NOVOTNY; 2012 [30].

3.3.1. RAMAN SIGNAL ENHANCED.

The intensity of the Raman signal is very low, when compared to the excitation intensity, it represents only $\mathbf{10^{-10}}$ of this [ZHANG, MINGQIAN et al., 2012], a problem that takes on greater dimensions when it comes to the individual characterization of nanometric structures. However, through TERS, these problems can be overcome, since the alignment of the metal tip with the convenient polarization laser beam promotes the local intensification of the electric field, which leads to an intensification of the Raman signal intensity.

To date, the enhancement mechanism of TERS is not completely understood. Several interpretations have been proposed. One of the enhancement mechanisms is the so-called electromagnetic (EM) mechanism. In this mechanism, it is considered that the incident EM field is locally amplified and confined by the tip. The related effects are usually distinguished as the surface plasmon resonance, substrate (mirror charge) effect, and lightning rod effect. Classical electromagnetic theory predicts that surface plasmon enhancement can be generated at the metallic tip apex when the wavelengths of the excitation laser and surface plasmons coincide. This gives rise to an enhanced electric field that occurs on the sample substrate in SERS. The most common experimental application of this mechanism is the use of AFM tips coated with a noble metal film, generally Ag or Au for example.

The magnitude of the field-enhancement factor is crucial for imaging applications. The direct illumination of the sample surface gives rise to a far-field background signal. If we consider an optical interaction that is based on an nth-order nonlinear process and assume that only the sample surface is active, then the far-field background will be proportional to:

$S_{ff} \sim A I_0^n$, where A is the illuminated surface area and I_0 is the laser intensity. The signal that we wish to detect and investigate (the near-field signal) is excited by the enhanced field at the tip. If we designate the enhancement factor for the electric field intensity ($|\vec{E}^2|$) by f_i then the near-field signal of interest is proportional to: $S_{nf} \sim a(f_i I_0)^n$, being a is a reduced area given by the tip size. A simple estimate of the enhanced of the Raman signal I_{Raman} from the alignment of the metal tip with the laser beam can be made taking into account the ratio between the transmission (exited state) rates $k_{ex}(\lambda_{ex})$ (index ex) and radiation $k_{rad}(\lambda_{rad})$ (index rad) rates, in both situations, with a tip (tip index) and without tip (index 0):

$$I_{Raman} = \left(\frac{\dfrac{\text{how much it excited the tip} - on}{\text{how much it exited the tip} - off}}{\dfrac{\text{how much it radiates the tip} - off}{\text{how much it radiates the tip} - on}} \right) = \frac{\dfrac{k_{ex-tip}}{k_{ex-0}}}{\dfrac{k_{rad-0}}{k_{rad-tip}}}$$

$$I_{Raman} = \frac{\dfrac{k_{ex-tip}}{k_{ex-0}}}{\dfrac{k_{rad-0}}{k_{rad-tip}}} = \frac{k_{ex-tip}}{k_{ex-0}} \cdot \frac{k_{rad-tip}}{k_{rad-0}}$$

The excitation ratio are proportional to the square of the local electric field, $|\vec{E_L}|^2$, and to the squares of the incident and dispersed electric fields. This defines the amplification factor, $\vec{E_I} = |\vec{E_t} - \vec{E_v}|^2$; as the enhanced factor, f_{enc}, is defined as the ratio between the field with the tip posed and the field with the tip pointed away, with the ω_I and $\omega_l - \omega_v$, being the incident and scattered frequencies respectively; to consider $\omega_l - \omega_v \ll \omega_I$, them, the amplification factor can be approximated as:

$$I_{Raman} = \frac{k_{ex-tip}}{k_{ex-0}} \cdot \frac{k_{rad-tip}}{k_{rad-0}} = \left[\frac{\vec{E}_{tip}(\omega_I)}{\vec{E}_0(\omega_I)} \right]^2 \left[\frac{\vec{E}_{tip}(\omega_I - \omega_v)}{\vec{E}_0(\omega_I - \omega_v)} \right]^2$$

$$I_{Raman} \approx \left[\frac{\vec{E}_{tip}(\omega_I)}{\vec{E}_0(\omega_I)} \right]^4$$

$$I_{Raman} = f_{enh}^4$$

If the signal is required to be stronger than the background it was necessary that at least the condition is met: $S_{nf}/S_{ff} > 1$. This means that the interaction produced by the Raman signal intensification must always be much greater in the nf so that the previous relationship is always greater than 1. From the above it can be considered:

$$\frac{a(f_i I_0)^n}{A I_0^n} > 1 \rightarrow f_i \geq \sqrt[n]{\frac{A}{a}}$$

For a first-order process ($n = 1$), for a second order linear process onwards, at least the minimum intensification factor must be 20. This is analogous to what was discussed in section 2.5.1 for the SERS case. The Raman enhanced example that are in the Fig. 1.4. The above estimate represents an overestimation of the TERS amplification power (KUMAR; RAE; ROY, 2014), since the practical result depends on a series of instrumental factors, with the type of lighting employed, the type and the individual characteristics the tip used and the control mechanism for the tip-sample distance (DOMKE; PETTINGER, 2010).

In the SERS, the enhancement is dependent on material properties and geometrical parameters of sample substrates when the tip and the illumination wavelength are fixed, which are called the substrate effect in the TERS. This effect can be well explained by considering the role of the image dipole. When the metal is close to a perfect mirror (i.e., a perfect conductor), the image tip becomes similar to the real tip and the field enhancement remains high. Moreover, according to this enhancement map, IR light can always be used to obtain reasonable enhancement, since all metals become good conductors in this wavelength region. Regarding the lightning rod effect, when a sharp metal tip is illuminated by light of a

different polarized direction to the tip shank, an increase in the local surface charge density occurs at its apex. The EM field at the tip apex is both enhanced and confined. Both the polarization of the incident field and the presence of geometrical singularities at the tip can increase the local charge density. Kneipp et al. investigated the electromagnetic enhancement effects of metal colloids on the Raman scattering of SWNTs (carbon nanotubes) and reported the enhancement in the order of 10^{12}. Fig. 3.15 shows the lightning rod effect [30, 53-55].
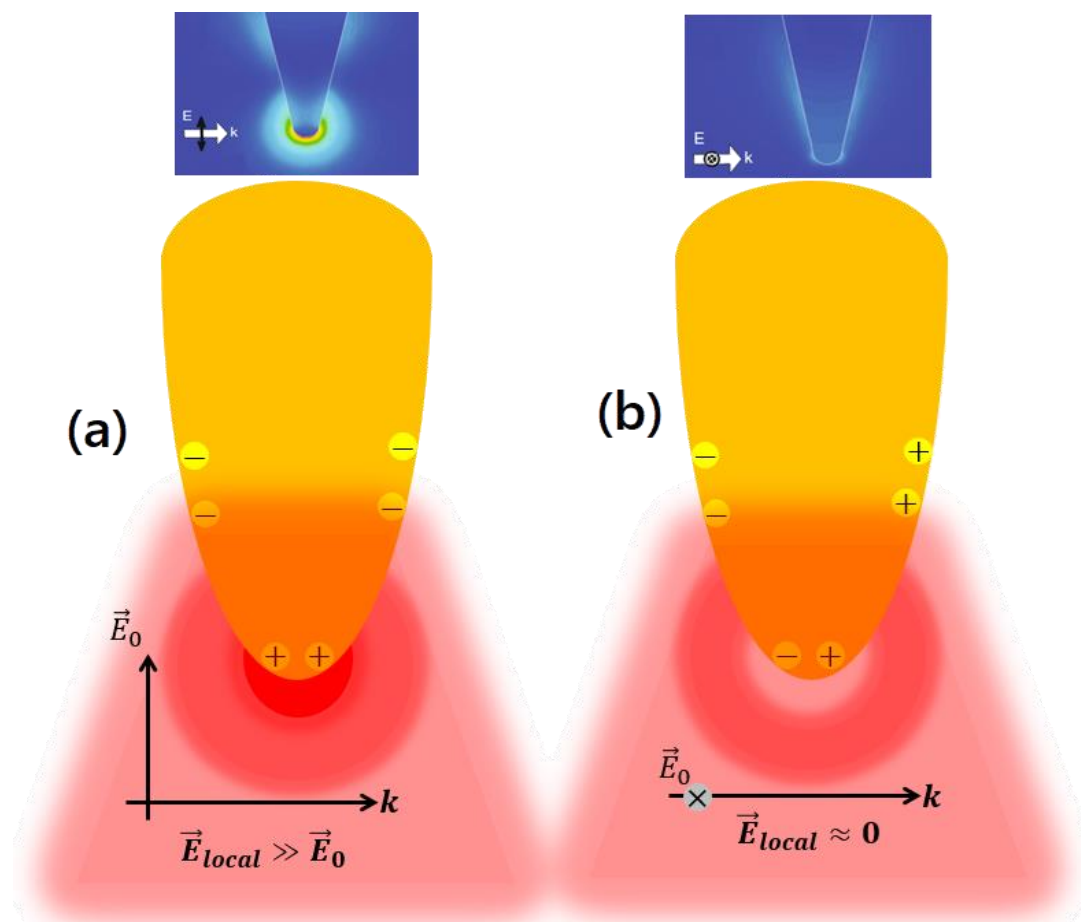
Figure 3.15. (a) Field distribution for an incident electric field vector parallel to the tip shaft showing localization of the electric field at the tip apex. (b) Field distribution for an incident electric field oriented non-parallel to the tip shaft. The field is no longer confined to the tip apex. [30, 39].

4. PROTEINS

To highlight the structural complexity of the proteins in this section, we present a brief description of their structure; we will talk about general basic concepts of the building block of proteins and the importance of these in the organization of conformation of living beings.

Living beings are highly organized and structured, following a hierarchy that ranges from nanometers to several meters. The atom is the fundamental unit of matter consists of a dense nucleus surrounded by a cloud of electrons. Atoms form molecules that are chemical structures that consist of at least two atoms joined by one or more chemical bonds. Many biologically important molecules are macromolecules, which are large molecules that are generally formed by polymerization (a polymer is a large molecule that is formed by combining smaller units called monomers). An example of a macromolecule is deoxyribonucleic acid (DNA), which contains the instructions for the structure and functioning of all living organisms.

Fig. 4.1 illustrates a sequence explaining how atoms are organized and form structures, from simple groups of atoms, through simpler organisms to well-structured organisms and indicating an approximate size and the number of atoms that make it up; the sequence shows in a series of clearly distinguishable systems, as expected, complexity increases as the number of atoms increases. At present, it is impossible to predict the behavior of an organism from the individual properties of atoms. It can only reach an understanding by breaking the sequence into pieces and studying them one by one; for example, how the properties of biomolecules depend on the properties of their building blocks **[16, 35]**.
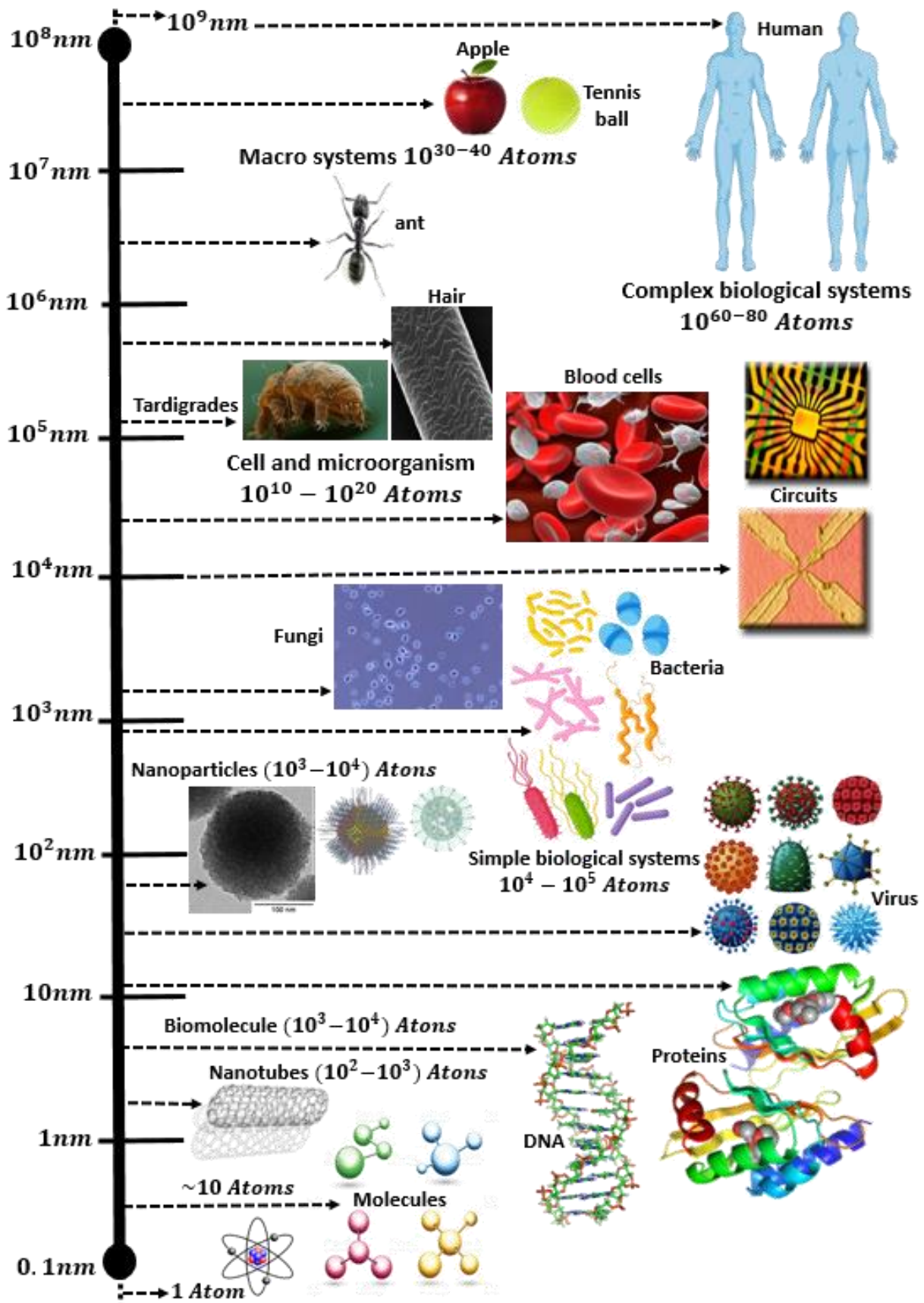
Figure 4.1. A comparison: from atoms to organisms. The number of atoms is, of course, only approximate, but it gives an idea of the size of the system.

More details on the hierarchy of living systems are given in Fig. 4.2. The phenomena that occur at different levels change markedly as the atom is passed to the more complex systems; as they increase, the size and dimensions, the number of atoms increases, the proportion of the number of atoms of the surface with respect to the number of atoms of the volume modifies the behavior of the system. Each new level allows the exploration of processes that cannot be studied at lower levels. Some typical processes are listed in Fig. 4.3 [16, 35].
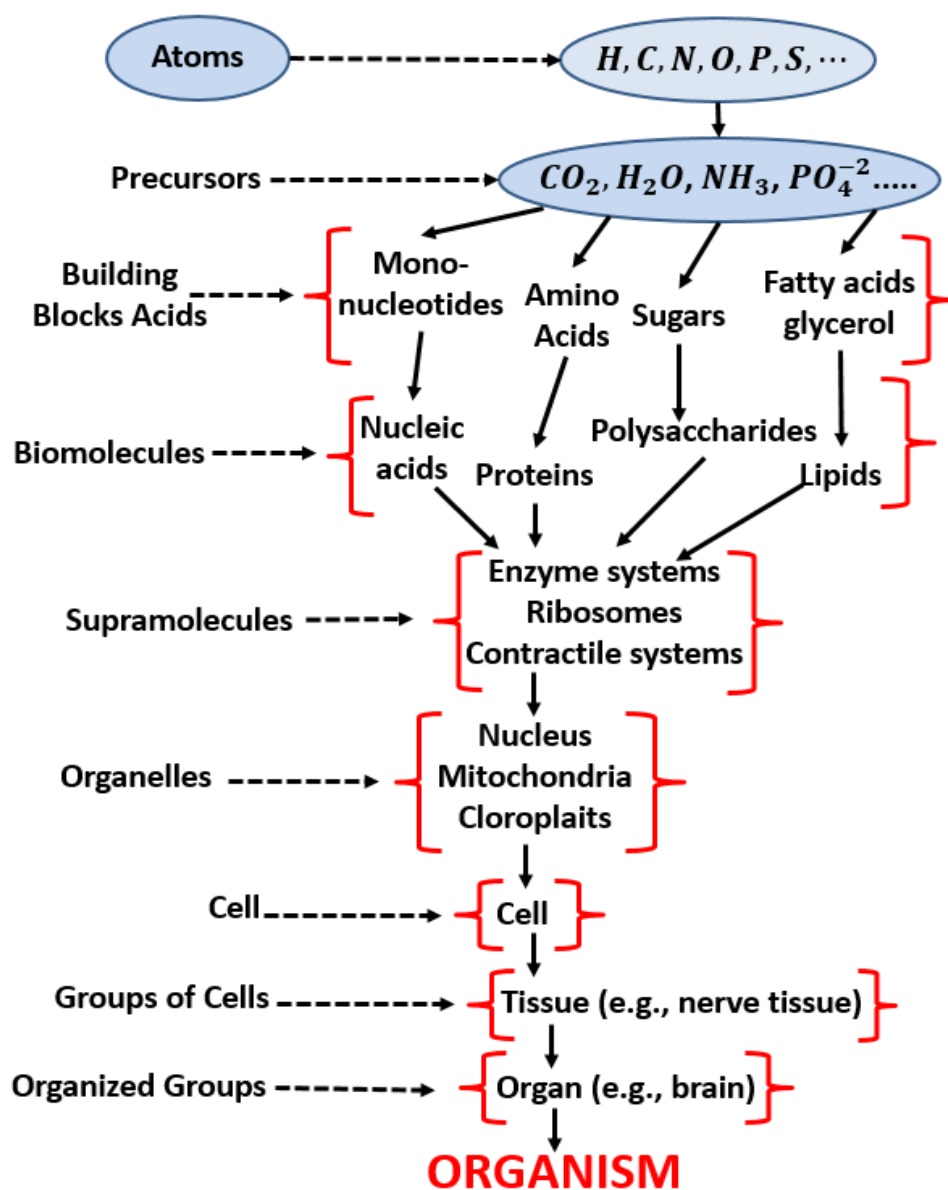
Figure 4.2. The Hierarchy of Living Systems in building blocks.

It is likely that further investigation of biomolecules and biomolecular complexes will lead to the discovery and understanding of other phenomena that cannot be seen in simpler systems.
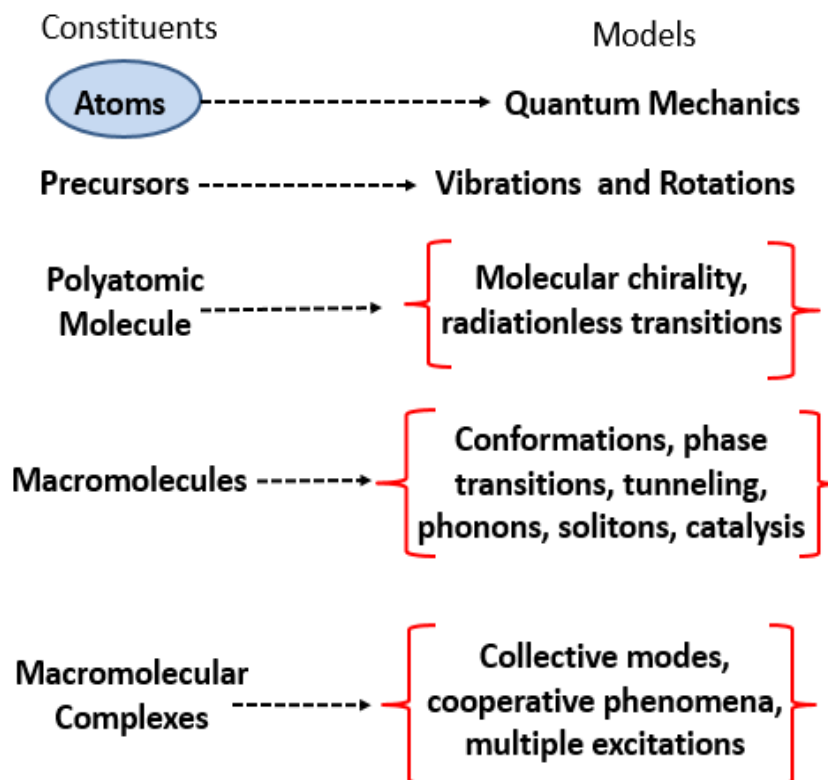
Figure 4.3. Molecular Organization and Characteristic Phenomena.

In 1960, British biochemist John Kendrew used X-ray diffraction to photograph myoglobin with a resolution of 2 Å (Angstrom), and became the first person to determine the three-dimensional structure of a protein. A short time later, Max Perutz, Kendrew's colleague at the University of Cambridge determined the structure of a similar, but more complex, hemoglobin protein. For these feats, the two scientists received the 1962 Nobel Prize in Chemistry. Since then, the structures of tens of thousands of different proteins have been determined in high resolution and details. Today, research with proteins continues; understanding better the architectural, functional and energetic principles of proteins, and the way of interaction between them will allow us to understand and understand many

chemical and biological processes that will open the doors to clarity how biological nanomachines work (viruses and bacteria). There is not even a single process in which proteins do not participate, because in addition to being actively involved in the set of chemical reactions, many cells are made up of proteins **[16, 35]**.

Thus, the functions of proteins are:

- assume the role of enzymes, directly influencing the acceleration of a chemical reaction;

- move muscles (performed by myosin and actin);

- Hormonal composition;

- Antibody composition;

- Blood clotting;

- Oxygen transport (done by hemoglobin).

A protein is a linear chain of biological polymers constructed from 20 amino acid compounds; see Table 4.1, which bind differently to yield different proteins. A long network of amino acids is called a polypeptide, and every protein is made up of one or more such chains. In other words, the proteins are composed of Carbon, Hydrogen, Oxygen and Nitrogen molecules. The chain contains from the order of 100 to 200 amino acids. Of particular interest are globular proteins, which act, for example, as enzymes (catalysis). In the appropriate solvent, these systems have complex shapes that include multiple folds, loops and curves, as shown in Fig. 4.4 (a).

Can classify proteins in relation to their origin, separating them into 3 groups: animal protein; vegetable and synthetic protein. Animal origin as its name suggests, is the protein found in animal flesh, which provides virtually all essential amino acids. It is worth mentioning that, because it is almost complete, this type of protein enables the optimal functioning of the

human organism. Vegetal origin Found in vegetables, this protein has less nutritional value as it has fewer essential amino acids in its composition and the synthetic protein is obtained through laboratory manipulations, ie, has several nutritional variations. It is widely used by people who want to make a food replacement, seeking sources of protein other than those of animal and vegetable origin **[16, 35]**.

There are two general classes of protein molecules: (i) globular proteins and (ii) fibrous proteins. Globular proteins are generally compact, soluble and spherical. Fibrous proteins are typically elongated and insoluble. These may have one or more of four types of protein structure. These types of structure are called primary, secondary, tertiary and quaternary structure.

4.1. PRIMARY STRUCTURE.

The primary structure is the amino acid sequence of the protein that describes the unique order in which they bind to form a protein. Proteins are constructed from a set of 20 amino acids that form the polypeptide chain and the order in which they are found, see table 4.1. The protein sequence is written listing the amino acids from the N terminal end to the C terminal end. In this, the sequence of articulated planes that constitute the peptide bonds cannot rotate, and the carbon, nitrogen and oxygen atoms that participate in them are located in the same plane. See Fig. 4.4 (a). In general, amino acids have the following structural properties; a carbon (the alpha carbon) attached to the four groups below:

- A hydrogen atom (H)

- A carboxyl group ($COOH$)

- An amino group (NH_2)

- A "variable" group or "R" group.
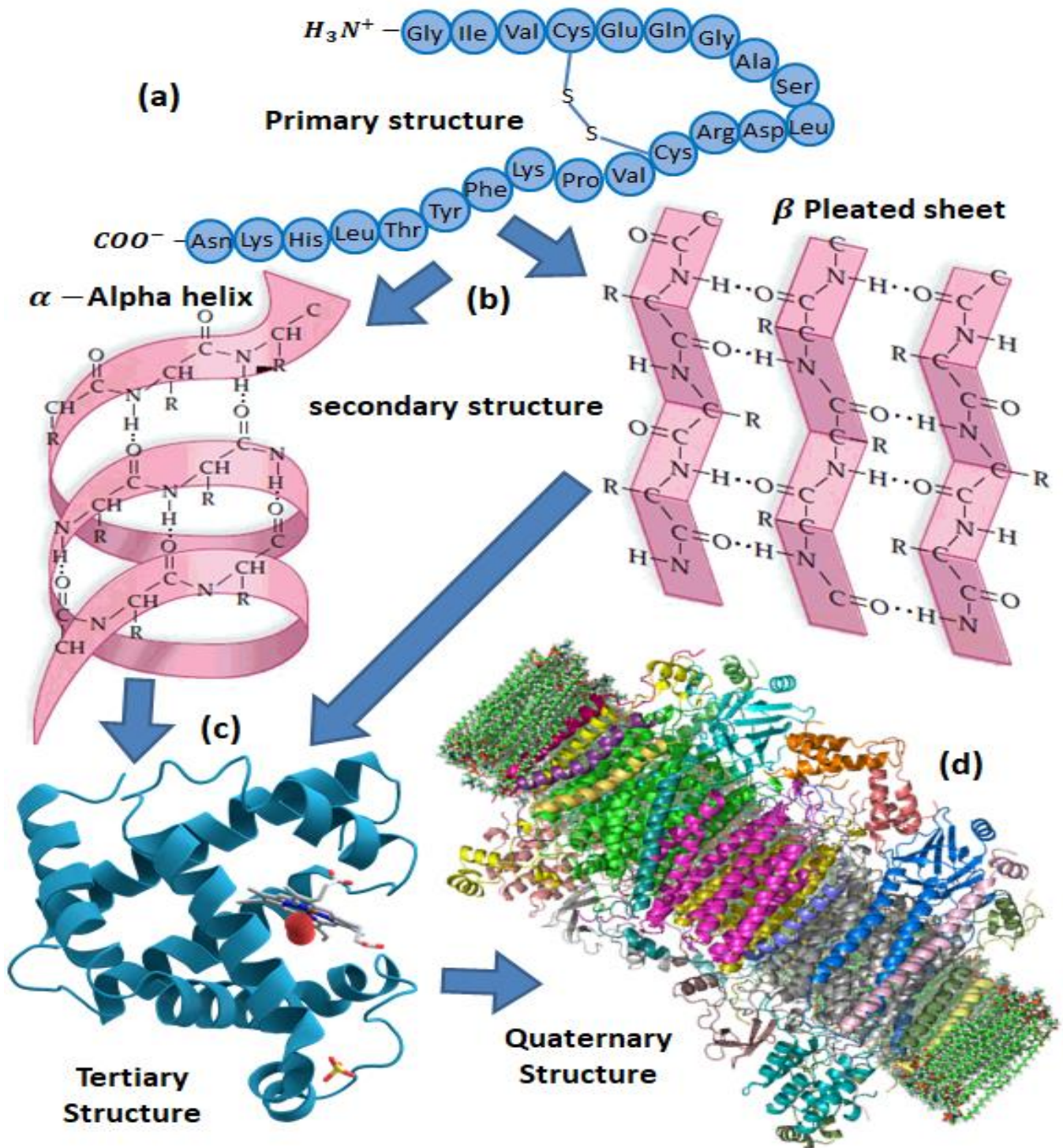
*Figure 4.4. The four levels of protein structure. (a) The first level is the amino acid sequence of the chains, (b) the second level includes the helical segments (spring-like, **α−Alpha helix**) and the sheet-shaped segments (**β−Pleated sheet**) of the proteins, as well as connection ties. Other proteins may include other secondary elements, in which the chain is more extended (i.e. less compact) than in the helices. (c) The third level includes the complete three-dimensional organization of each of the chains. (d) Finally, the fourth level includes the arrangement of the different chains that are generally 4mm in size or more.*

All amino acids have the alpha carbon ($\boldsymbol{C_\alpha}$), see Fig. 4.4 (b) attached to a hydrogen atom, a carboxyl group and an amino group. The "R" group varies between amino acids and determines the differences between these protein monomers. The amino acid sequence of a protein is determined by the information found in the cellular genetic code. The order of the amino acids in a polypeptide chain is unique and specific for a particular protein. Alteration of a single amino acid causes a genetic mutation, which usually results in a protein that does not work. The amino acid sequence determines the primary structure. This level of the structure is maintained by peptide bonds. By convention, it is written from the end of the amino terminal group to the final carboxyl group **[16]**. Peptide bonds form the skeleton of the protein, from which the amino acid side chains emerge. Proteins differ in the sequence and number of amino acids. Although a peptide can adopt different conformations, each protein has a unique three-dimensional structure under physiological conditions, which turns out to be the most stable of all possible, that is, the one with the greatest number of weak interactions between its atoms. The amino acid sequence that forms a protein determines its three-dimensional structure and its function. The so-called polymorphic proteins admit variations in their primary structure, retaining their function. Variations in some areas of the proteins have little or no impact on their function, but there are critical areas, in which any variation affects the structure, and therefore the function of the protein **[35]**.

4.2. SECONDARY STRUCTURE.

Refers to the folding of a polypeptide chain that gives the protein its 3D shape. The term "secondary structure" refers to the structure that spatially adopts a part of the polypeptide. It occurs when the hydrogens in the sequence interact through hydrogen bonds. Two types of structures are particularly stable and frequent in proteins: the $\boldsymbol{\alpha}-$helix and the

β −lamina. These are the two forms of secondary structures observed in proteins. α −Helix structure resembles a spiral spring and is maintained by hydrogen bonds in the polypeptide chain. α −Helix spirals folding of the polypeptide chain on itself. It is stable through hydrogen bridges that exist between the groups $N - H$ and $C = O$ with the R groups facing outwards. To form this structure, the carboxyl group of each amino acid (n) is linked by a hydrogen bridge to the amino group of another amino acid ($n + 4$). It is a stable structure because it results in a maximum number of interactions, if these links are broken, the secondary structure is lost. β −Lamina structure appears to be folded or pleated and is held together by hydrogen bonding between folded chain polypeptide units adjacent to each other. β −Folded sheet, the folding does not originate a helical structure but a folded sheet, the chain is stretched and the structure is spatially zigzag forming sheets (folded sheets β). The arrangement can be parallel or antiparallel. It can occur between nearby or distant regions of the polypeptide. The R groups protrude from the sheet in both directions, alternately. The β conformation is stabilized by hydrogen bonds, as in the previous case, but in this case, they are transversal. See Fig. 4.4 b). In the β sheets the spins are formed by the union by a hydrogen bridge of the amino acid n and the $n + 3$ [16, 35].

4.3. TERTIARY STRUCTURE.

It is the folded and complete structure of the 3D chain of a protein's polypeptide chain; see Fig. 4.4 c). Several types of bonds and forces influence a tertiary structure protein; it occurs when certain attractions are present between α −Helix and β −Folded sheet. This is specific to each protein and determines its function because the physical and chemical characteristics of the molecule depend on the tertiary structure. The regions of the protein with a defined secondary structure are called dominos so the

tertiary structure defines the interactions between the different domains that form it. Tertiary folding is not immediate, first groups of structures called domains are grouped together and then articulated to form the final tertiary structure. This folding is facilitated by junctions called disulfide bridges, $S-S$ that are established between the sulfur atoms of the amino acid cysteine **[16, 35]**.

It informs us about the disposition of the secondary structure of a polypeptide when folded over itself causing a globular conformation. Said globular conformation in proteins facilitates their solubility in water and this allows them to perform transport, enzymatic, hormonal functions, etc. (globular proteins). Proteins that fail to form these tertiary structures keep their secondary structure elongated (filamentous or fibrillar proteins). They are insoluble in water and in saline solutions, so they have skeletal functions (Ex: connective tissue, bone collagen) The function of the protein therefore depends on the tertiary structure, so any changes that are produced in the disposition of this structure can cause the loss of its biological activity, a process that we know under the name of denaturation. The tertiary structure constitutes a set of folds that originate from the union between certain areas of the polypeptide chain. These junctions are made by means of links between the side chains of the amino acids, and can be of the following types:

· Disulfide bridges: they are strong covalent bonds between the *SH* groups of the cysteine amino acids.

· Electrostatic forces: these are ionic type links between the groups of opposite electric charges. They occur between radical groups of acidic amino acids and basic amino acids.

· Hydrogen bonds.

· Van der Waals forces: they are weak unions that occur before apolar amino acids.

Hydrophobic interactions contribute greatly to folding and shaping a protein. The "R" group of the amino acid is hydrophobic or hydrophilic. Amino acids with hydrophilic "R" groups will seek contact with their aqueous environment, while amino acids with hydrophobic "R" groups will seek to avoid water and position themselves at the center of the protein. The hydrogen bonding in the polypeptide chain and between amino acid groups "R" helps stabilize the protein structure, keeping the protein in the form established by hydrophobic interactions. Due to protein, folding, ionic bonding can occur between the positively and negatively charged "R" groups that approach each other. Folding may also result in covalent bonding between the "R" amino acid groups. This type of bond forms what is called a disulfide bridge. Interactions called van der Waals forces also help stabilize the protein structure. These interactions belong to the attractive and repulsive forces that occur between molecules that become polarized. The loss of the tertiary structure of a protein implies the loss of its function. There is talk of denaturation when the change in the structure of the protein is so great that it cannot maintain its function. Most proteins can be denatured by heat, extreme pH, solvents, or detergents. Denaturation does not imply the rupture of covalent bonds, but the weak interactions that maintain the three-dimensional structure **[16, 35]**.

4. 4. QUATERNARY STRUCTURE.

Refers to the structure of a protein macromolecule formed by interactions between multiple polypeptide chains. It is only present in proteins that consist of more than one chain of amino acids. The quaternary structure refers to the junctions between the different polypeptide chains

that form the protein, giving rise to a three-dimensional structure. Each polypeptide chain is referred to as a subunit, see Fig. 4.4 d). Quaternary-structured proteins may consist of more than one type of protein subunit. They can also be composed of different subunits. Hemoglobin is an example of a quaternary structure protein. Hemoglobin, found in the blood, is an iron-containing protein that binds oxygen molecules. It contains four subunits: two alpha subunits and two beta subunits. It informs of the union of several polypeptide chains with tertiary structure to form a protein complex. Each of these polypeptide chains is called a protomer or protein subunit. Depending on the number of subunits that are associated, proteins that have a quaternary structure are called:

· Dimers: ex. hexokinase enzyme

· Tetramers: ex. hemoglobin

· Pentamers: ex. RNA polymerase enzyme

· Polymers: ex. Actin, myosin and poliovirus capsid (it has 60
 protein subunits).

The type of union that predominates in this type of structure are weak links **[16, 35]**.

4.5. AMINO ACIDS, THE BUILDING BLOCKS.

The primary building blocks of proteins are amino acids; the proteins are described as amino acids (organic molecule) with an amino group (NH_2) and a carboxyl group ($COOH$). The general structure of an α−amino acid is established by the presence of a central carbon (C_α, in light blue in the Fig. 4.5) surrounded attached to a carboxyl group (α−carboxyl, enclosed in green dotted lines in the Fig. 4.5), an amino group (α−amino, in blue dotted lines in the Fig. 4.5), and a hydrogen and a "R" (residue) that represents the "side chain" (in orange dotted lines in the

Fig. 4.5); specific for each amino acid. Both carboxyl and amino are functional groups susceptible to ionization depending on pH changes. This is, C_α, its hydrogen atom with the $\alpha-$carboxyl group, and the $\alpha-$amino groups; this part is called the "backbone", and is identical in all amino acid. The third part includes the side-chain, which is different in each amino acid; in other words, the side-chain group is what differentiates between amino acids. Due to the uniqueness of the side-chain residue, amino acids are often referred to as residues when incorporated within the protein chain. See Fig. 4.5 **[16, 35]**.
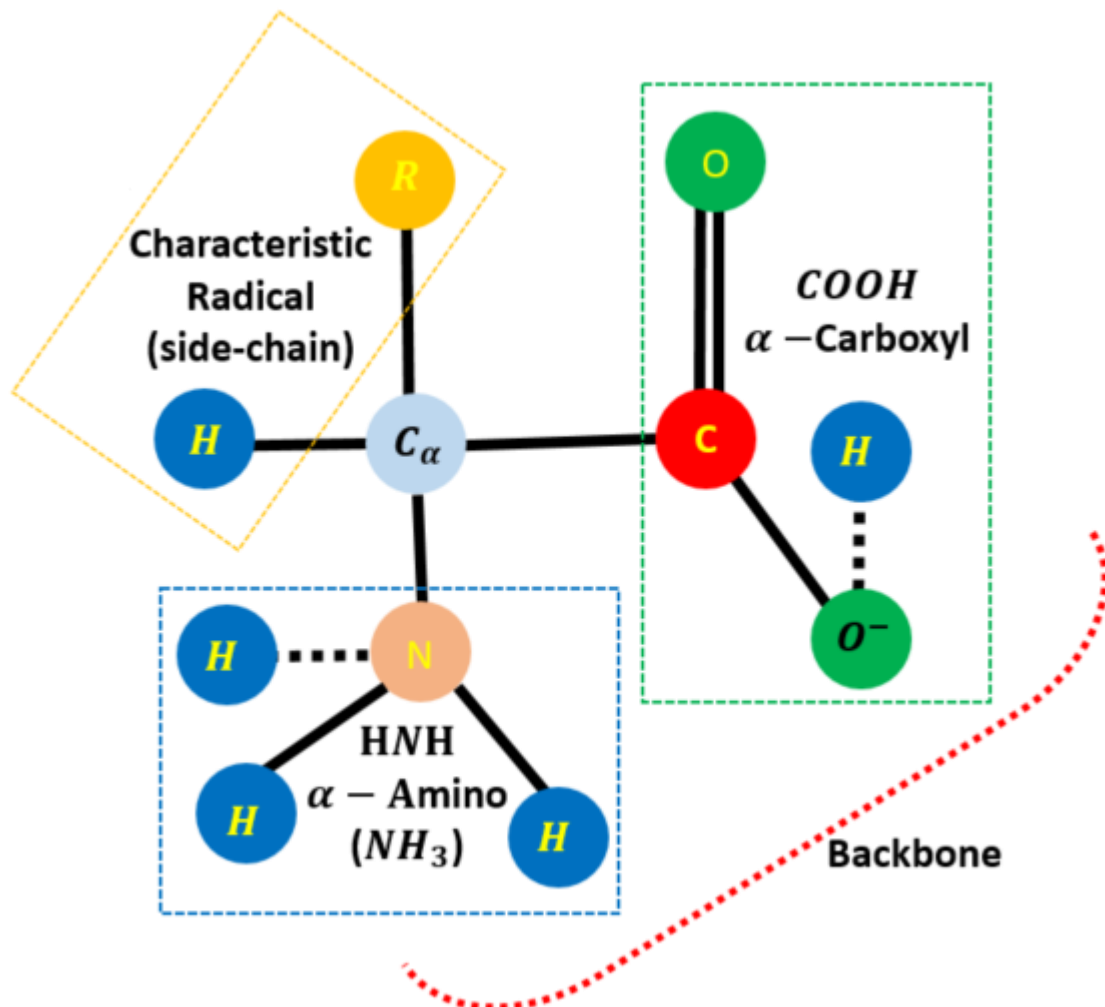
Figure 4.5. General structure of an amino acid. All amino acids are built around a central carbon atom, C_α. The dotted line means that atoms may be missing, when the amino acid is ionized.

Of the four ligands positions (valences; H, R, NH_2 and $COOH$), two connect the amino acid with the other building blocks in the chain, the third carries a hydrogen atom; the fourth position joins the side chain or residue R that determines the specific properties of the amino acid. The main chain or backbone of the polypeptide chain is established by the formation of peptide bonds between amino acids. The backbone consists of the amide N, the $\alpha-$carbon and the carbonyl C linked together. That is, the individual building blocks in a protein are linked by peptide bonds. A peptide bond is a chemical bond that occurs between two molecules, when the carboxyl group of one molecule reacts with the amine group of another molecule, releasing a molecule of water (H_2O). That is, a synthesis reaction by dehydration that occurs between molecules of amino acids, this link has a covalent character and is so strong that it practically never breaks due to thermal effects. Peptide bonds formation summary:

$$COOH \cdots HNH \rightarrow -NH - CO - +H_2O$$
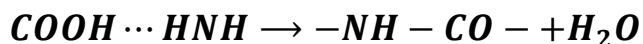
The resulting polypeptide chain is shown in Fig. 4.6; they are amino acids that consist of a main chain of polypeptides with a side chain (R) per amino acid residue. The spine is nonspecific; all the specificity is in the side chain. In addition to the components shown, proteins contain two terminal groups: The amino terminal NH_3^+ denoted by N and the carboxyl terminal NHC_2^- denoted by C [16, 35].

All amino acids can exist in two different forms, related to each other by a mirror reflection, Fig. 4.7. D and L stand for dextro (right) and levulo (left). The two forms rotate the polarization of light in different directions. In nature, only the L-amino acids are biologically active.

The amino acids are divided in four groups:

I. Amino acids with non-polar residues (hydrophobic). These amino acids are less soluble in water than polar amino acids.

II. Amino acids with polar residues without charge. The polar R groups of these amino acids can be linked by hydrogen with water and, therefore, are more soluble in water than those of group I.

III. Amino acids with negatively charged R groups (acids). Members of this class have a negative pH charge.

IV. Amino acids with positively charged (basic) R groups. Some have a net positive charge and others (the most reactive) may have a positive or negative charge. Basic amino acids have a positive charge at pH 7. Histidine is a borderline case; at pH 7 only about 10% has a positive charge; at pH 6, the percentage is about 50.
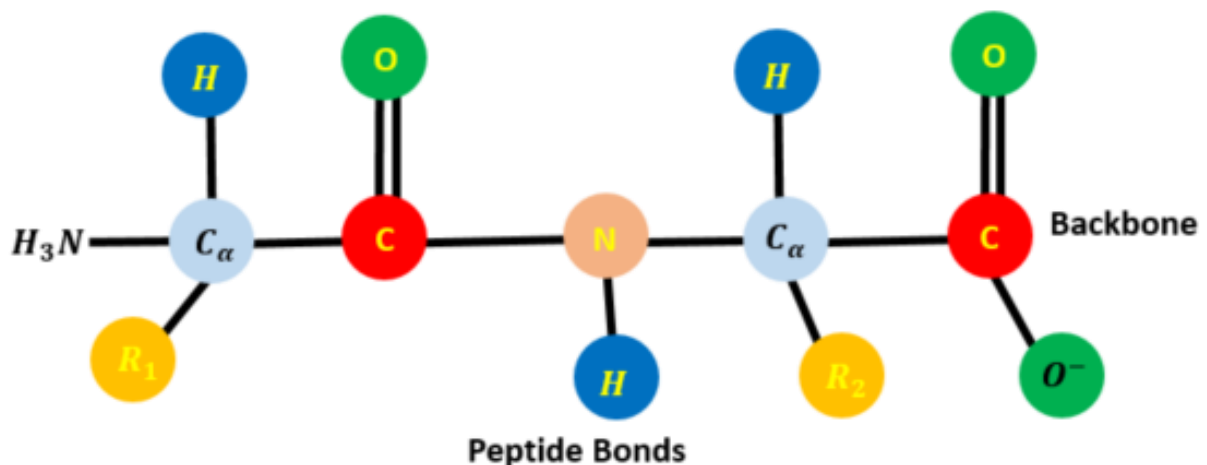
Figure 4.6. A polypeptide chain formed from individual amino acids through peptide bonds. The twenty common amino acids are given in Table 4.1.
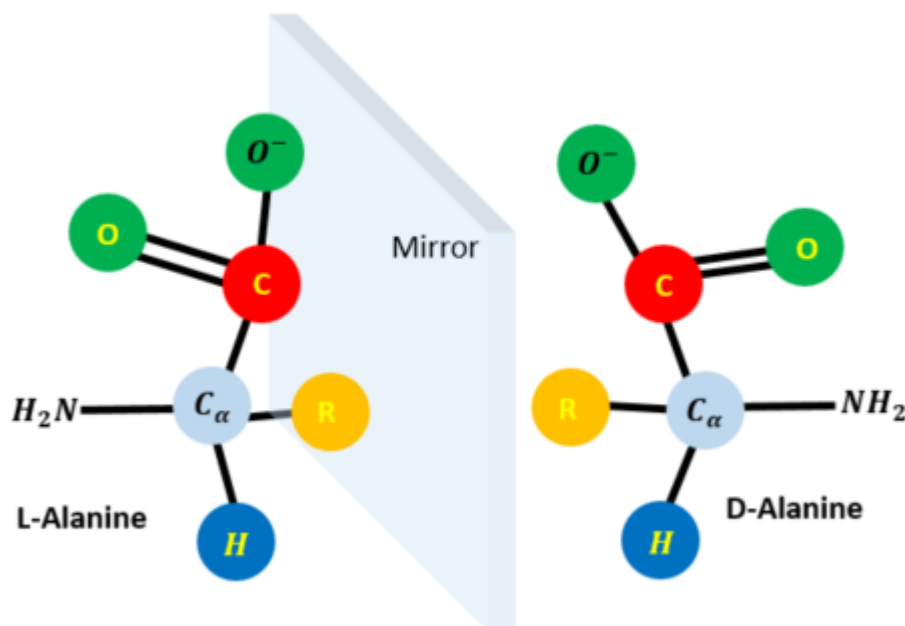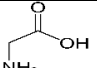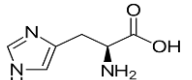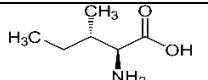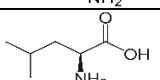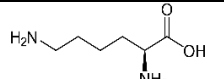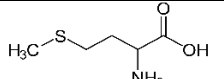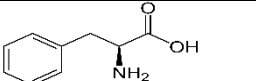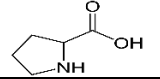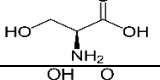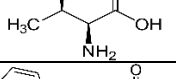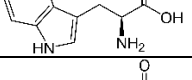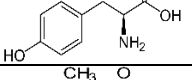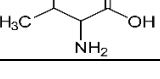
Figure 4.7. The L and D configurations of the amino acid alanine.

Table 4.1. Properties of protein building blocks, the length (L) is for the side chain only. The molecular weight is for the entire amino acid. Subtract 17.9 (molecular weight of water) to obtain the net molecular weight of the residue. The polarity indicates whether the amino acid is nonpolar or polar with a net positive, negative, or neutral charge at pH=6. In amino acid nomenclature, the numbering of the main chain carbons is started from the carboxyl carbon **[16, 35]**.

Amino Acid (Symbol)	Radical Side chain	Molecular Weight (amu)	Polarity	Chemical structure	L (nm)	Molecular formula
Alanine ALA	CH_3	89.094	nonpolar		0.28	$C_3H_7NCO_2$
Arginine ARG	$NH_2C(NH)_2(CH_2)_3$	174.203	basic polar		0.88	$C_6H_{14}N_4O_2H_{15}$
Asparagine ASN	$NH_2CH(CH_2)_3$	132.119	polar		0.51	$C_4H_8N_2O_3$
Aspartic acid ASP	$COOH(CH_2)$	133.104	acidic polar		0.50	$C_4H_7NO_4$
Cysteine CYS	$SH(CH_2)$	121.154	nonpolar		0.43	$C_3H_7NO_2S$
Glutamine GLN	$NH_2CO(CH_2)_2$	146.146	polar		0.64	$C_5H_{10}N_2O_3$
Glutamic acid GLU	$COOH(CH_2)_2$	147.131	acidic polar		0.63	$C_5H_9NO_4$

Glycine GLY	H	75.067	nonpolar		0.15	$C_2H_5NO_2$
Histidine HIS	$(C_3N_2H_4)CH_2$	155.156	basic polar		0.65	$C_6H_9N_3O_2$
Isoleucine ILE	$(CH_3)_2CH_2CH$	131.175	nonpolar		0.53	$C_6H_{13}NO_2$
Leucine LEU	$(CH_3)_2CH(CH_2)$	131.175	nonpolar		0.53	$C_6H_{13}NO_2$
Lysine LYS	$NH_2(CH_3)_4$	146.189	basic polar		0.77	$C_6H_{14}N_2O_2$
Methionine MET	$CH_3S(CH_2)_2$	149.208	nonpolar		0.69	$C_5H_{11}NO_2S$
Phenylalanine PHE	$(C_6H_5)CH_2$	165.192	nonpolar		0.69	$C_9H_{11}NO_2$
Proline PRO	$3CH_2$	115.132	nonpolar		0.68	$C_5H_9NO_2$
Serine SER	$OH(CH_2)$	105.093	polar		0.38	$C_3H_7NO_3$
Threonine THR	$CH_3(CH)CH$	119.119	polar		0.40	$C_4H_9NO_3$
Tryptophan TRP	$(C_6H_4)HNC_2CH_2$	204.228	nonpolar		0.81	$C_{11}H_{12}N_2O_2$
Tyrosine TYR	$(OHC_6H_4)CH_2$	181.191	polar		0.77	$C_9H_{11}NO_3$
Valine VAL	$(CH_3)_2CH$	117.148	nonpolar		0.40	$C_5H_{11}NO_2$

4.6. RAMAN SPECTRUM OF PROTEINS.

Raman spectra of most biomolecules have a widely similar shape that covers a range of approximately 400 to 3500 cm^{-1} Raman shift from the excitation laser. However, a detailed spectral analysis based on the normal mode analysis of all spectral characteristics can reveal important structural and functional characteristics of biomolecules. In general, the spectral region between 400 and 1800 cm^{-1} is known as the "fingerprint region" being the most important Raman vibrational bands of proteins. It contains most of the Raman bands used to identify various structural characteristics of proteins and appears to be different from one protein to

another. However, this spectral region is complex and sometimes cannot be used directly in the identification of biomolecules due to the large number of related components and variables.

The information obtained from a Raman spectrum is varied:

• The position of the band provides information on the molecular species present in the sample.

• The mid-bandwidth provides information about the structure of the sample.

• The intensity of the band may be related to the concentration of the species.

• Band change is a function of several external factors: temperature, pH, hydrogen bonds and chemical reactions.

Protein amide bands can have up to nine normal modes of vibration. These are called A, B and I-VII in order of decreasing frequency; they have their origin in the vibrations of the different atomic groups of the polypeptide chain (group $C = O$, group $N - H$, group $C - N$). The most important amide bands are the amide bands I, II and III. In fact, these Raman vibrating bands are strongly related to the structure and conformation of proteins [28, 31, 33, 57].

• Amide I, a band located in the spectral range of 1610-1700 cm^{-1}, originated primarily (80%) in the vibrations of the carbonyl groups ($C = O$) of the polypeptide chain [28, 35, 36]. The individual vibrations are

coupled by an electrostatic dipole interaction, which leads to the formation of a wide Raman band called the amide band I. The coupling between the individual vibrations $C = O$ depends on the relative positions in the space of the $C = O$ bonds. , which, in turn, depend on the secondary structure of the protein. Therefore, the different types of secondary structures (α −helix, β −sheet) are characterized by amide bands of slightly different position and shape. The exact position of the band is determined by the conformation of the skeleton and the hydrogen bond pattern.

• Amide II is in the band region of 1510 to 1580 cm^{-1} and is more complex than amide I. The origin of the amide II band is 40% to 60% NH flexion in the plane and 18% to 40% stretch $C − N$. Inspection of the amide band II generally provides little help in distinguishing between the turn and sheet conformation.

• Amide III has its origin mainly in $C − N$ flexion (40%) and $H − N$ stretch (30%). The structure of an amide band III that has a spectral range from 1200 to 1350 cm^{-1} and can be correlated with the amide band I, providing complementary structural information about the structure of the protein and making it possible to obtain additional details about the amide I band.

• Stretching of $S − S$ sulfides bonds. Experimental studies in model systems show that the frequency of disulfide bridge vibration associated with the S-S elongation is in the spectral range 500–545 cm^{-1} for proteins whose structure contains $S − S$ bridges, the Raman $S − S$ bands also they are in the 500-550 cm^{-1} range. The factors that affect the frequency of vibration are the relative conformation of the $C_\alpha − C_\beta S − S' − C'_\beta − C'_\alpha$

atoms around the $C_\beta - S$ and $C_\beta - S'$ bonds, the mode coupling and links of hydrogen.

• Aromatic amino acids. Some of the vibrating bands such as tyrosine (Tyr) or tryptophan (Trp) are the most sensitive to Raman; in fact, detailed information on the microenvironment of these aromatic side chains can be obtained, for example, through variations in intensity of the vibratory modes or changes in the intensity ratio of Fermi resonance doublets, from 835 to 853 cm^{-1}. These bands are very sensitive to the environment, more precisely to the extent of the H binding of the phenolic hydroxyl, see the table 4.2.

Table 4.2. Important Raman modes of aromatic amino acids within the protein structure [28].

Aromatic Residues	Means Frequency cm^{-1}
Phe	620, (1000-1030), (1170-1200), 1605
Tyr	640, 830, 850, (1170-1200), 1590, (1610-1616)
Trp	750, 1011, (1340-1360), (1582- 1584), (1618-1621)
His	(310-3160)

If aromatic amino acids are near a binding site, or if they are exposed to a different environment due to conformational changes in the protein when bound, it is anticipated that this will be reflected in the Raman spectrum [28, 31, 33, 57].

5. SAMPLE PREPARATION AND TECHNICAL DATA

Rhodotorula glutinis (Rg) and Rhodotorula mucilaginosa (Rm) synthesis process mediated by fungi were made according to the procedure and reported in Cunha et al. and. Noronha et al. Further details on the biogenic synthesis are elsewhere **[10-14]**. The fungus was obtained from soil in the soil of the Pici campus of the Federal University of Ceará. After being synthesized, Rg- and Rm-AgNPs are placed in deionized water in well-covered glass containers; they are stored in a dry and dark place to avoid oxidation, so has access easy and quick according be necessary to AgNPs for further studies and/or applications (nanoparticles can be stored in this solution for many months). A synthesis process summary of Rg- and Rm-AgNPs is shown in the Fig. 5.1 and a preparations summary (deposition on glass/silicon sheets) for characterizations is illustrated in Fig. 5.2.
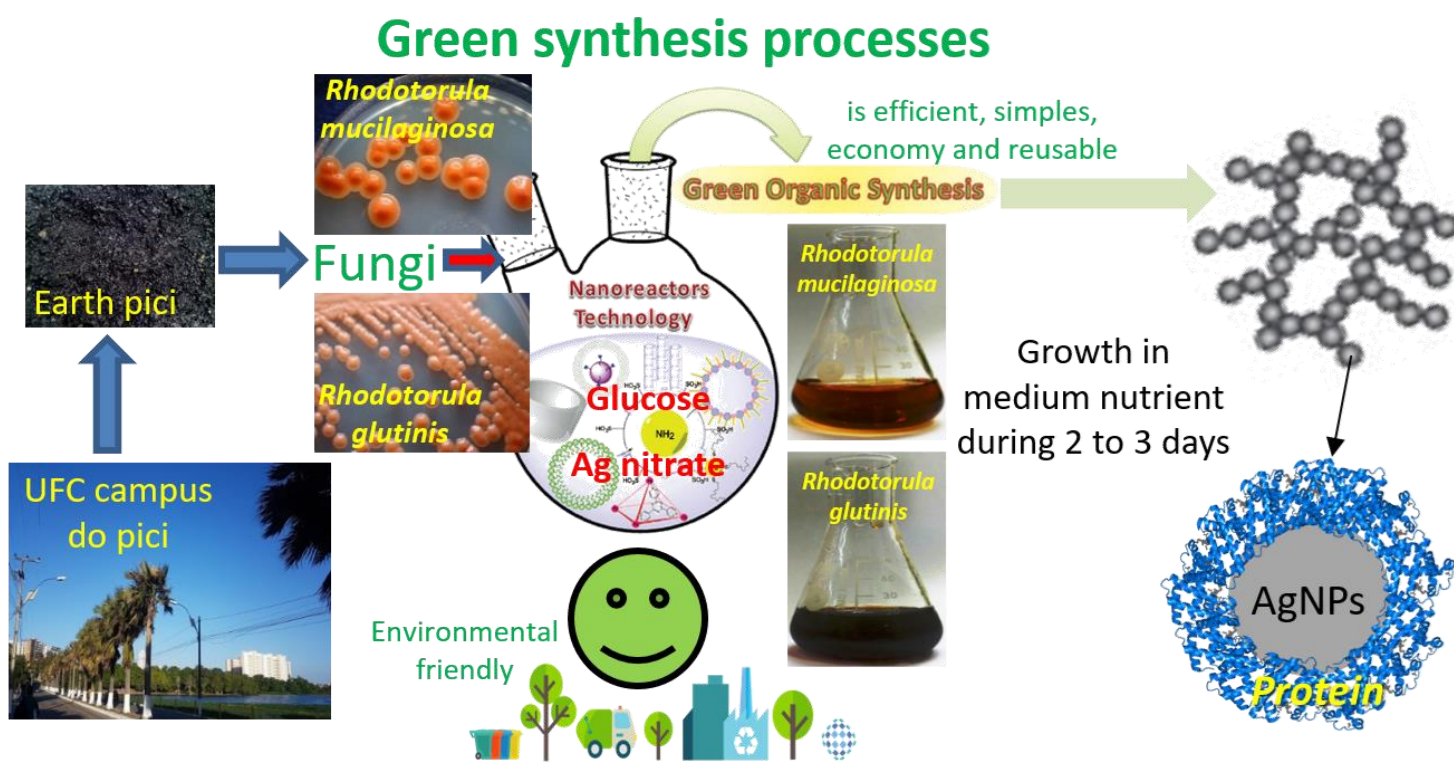
Figure 5.1. Synthesis process summary of Rg- and Rm-AgNPs **[10-14]**.
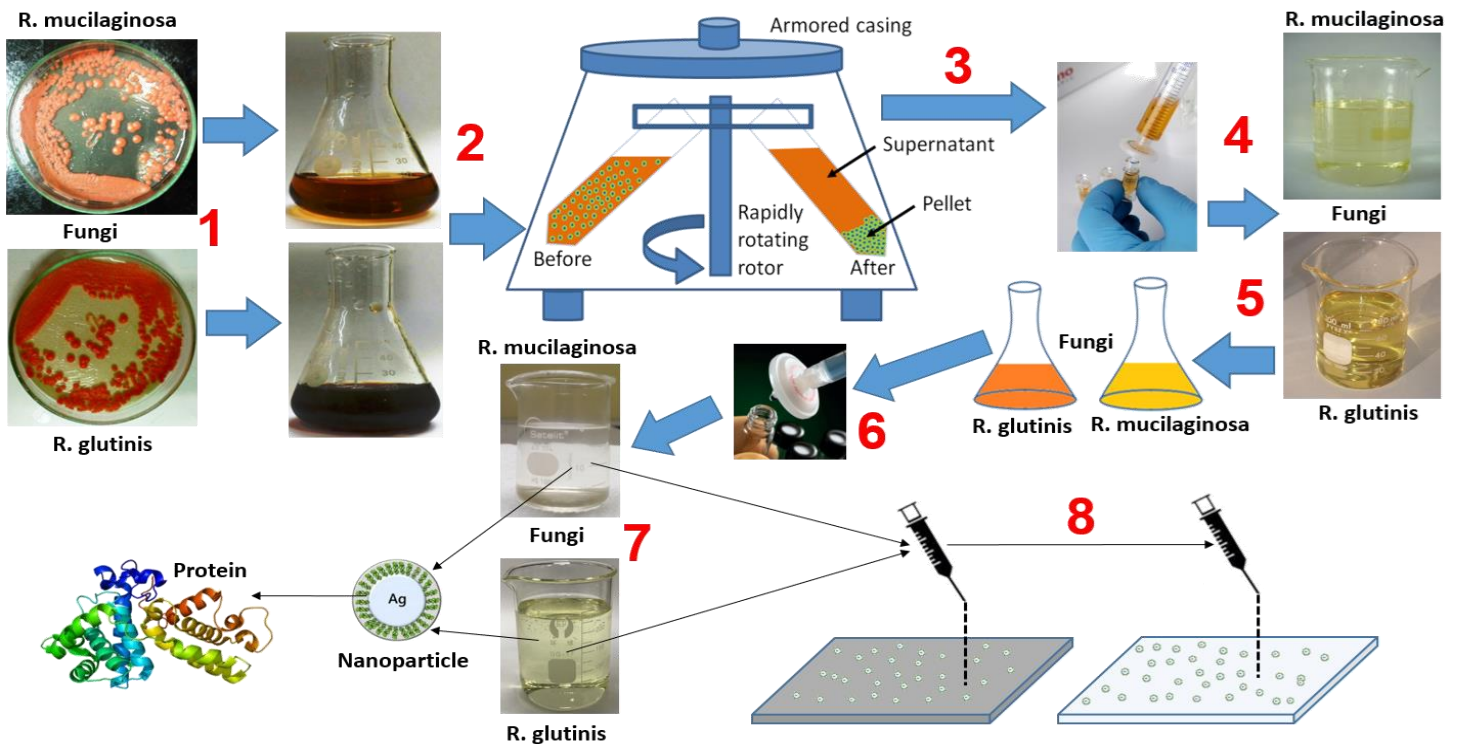
Figure 5.2. Summary of the synthesis process and deposition of the samples for the AFM, SEM and Raman characterization [10-14].

1- Fungus growths.

2- After to growth in medium nutrient during 2 to 3 days, next they take a part of the liquid where the nanoparticles are stored for centrifugation.

3- The nanoparticles are centrifuged (3 times during 20 minutes) and washed (with deionized water) to separate the nanoparticles from the enzyme and sucrose broth.

4- Proceed to do the first filtration with a 0.45 um membrane.

5- For Raman (SERS) and AFM measurements 10 ml of the suspension of the stored nanoparticles were taken, and these were sonicated for 20 minutes after addition of 10 ml of deionized water (i.e. diluted AgNPs suspension). For Raman (TERS) measurements, 10 mL of AgNPs in

suspension are taken and sonicated for 40 min in addition of 40 ml of deionized water (to make TERS measurements the samples must be much more diluted than for the SERS and AFM measurements).

6- Is filtered once more, The Rm-AgNPs liquid is transparent to the almost transparent Rg-AgNPs.

7- 10 ml more is added and sonic for 5 minutes.

8- With a micropipette place 2 to 3 one drops in the middle of a 0.2 mm glass sheet (For TERS measurements) and Silicon sheet (for SEM measurements) to next coverslip and left to dry for 48 hours at room temperature, on a well-leveled table (The drying was carried out on a metal plate placed on an optical table grounded, to minimize the effects of charges and/or vibrations that may interfere with the deposition process and increase particle agglomerates) so that when drying the drop the nanoparticles remain in the center of the sheet (a glass lid is placed 1 cm above the sample, on the sides it is left open for air to circulate, this is to prevent that some material foreign falls on the material) for approximately 24 to 36 hours at room temperature; the drying time will depend on the humidity of the environment, if a dehumidifier is available, the time can be reduced to 12-16 hours.

An objective lens of 100x/NA=0.90 was used in the optical microscope that was conjugated to a Raman spectrometer (WITec alpha300) to SERS measurements; SERS spectra were acquired in a time-series with an acquisition time of 1 s using a green laser, $\lambda = \mathbf{532}$ nm wavelength, Gaussian field profile with ~15 mW maximum output power adjustable. For TERS measurement a HeNe Red laser with emission on

$\lambda = 632.8$ nm wavelength, linearly polarized, Gaussian field profile and with ~22 mW output power constant using a 60x/NA=1.39 Nikon oil immersion objective lens, and an ANDOR and MCL-RHK-REV9 as system control. For AFM characterizations, an Asylum Research MFP-3D-BIO atomic force microscope was used in the tapping mode with silicon 10 nm apex tip. For SEM characterization, one drop of the diluted AgNPs suspension was deposited on a silicon substrate (Si). The SEM characterization was carried out using the Quanta 450 FEG microscope (FEI). The photoluminescence (PL) emission spectra were measured on individual particles in a confocal microscope, using a CW diode laser at 473 nm for excitation together with a laser line filter and a 490 nm longpass filter in the detection path. Dark field scans were recorded using broadband (300 nm to 2.5 um), incoherent illumination at a shallow angle, and an NA=0.7 microscope objective to collect the elastically scattered light only. A pinhole in the detection allowed to select the light, scattered off an individual particle, and to record its spectrum. Additionally, we illuminated the particles by a HeNe laser at 633 nm (~5 mW) to test the influence of laser heating and the plasmon resonance. The scattered light either was sent to an APD single-photon counter or to a spectrometer and a 550 nm short pass filter was included in the optical path to remove the laser light. It should be said that all depositions of AgNps (on silicon and on glass) were made following the same protocol and drying.

6. MEASUREMENTS RESULTS AND DISCUSSION

6.1. SEM CHARATERZATION.

The characterizations began by making images of scanning electron Microscopy (SEM), trying to obtain morphology and size information. SEM technique is a versatile tool that has already been successfully employed to characterize fungal AgNPs **[58-61]**. Fig 6.1 present SEM images on a silicon substrate of the bio-synthesized nanoparticles. The images show AgNPs with different sizes and spherical shapes, although irregular spheres are also present. For both Rg- and Rm-AgNP, it is possible to observe isolated nanoparticles and agglomerates. However, nanoparticles synthesized by the fungus *R. Glutinis* (Fig. 6. 1a) tend to form aggregates, while those synthesized by *R. Mucilaginosa* (Fig. 6. 1b) appear well-isolated. It is probable that each protein created by each fungus has its own intrinsic way of creating and organizing AgNps. The AgPNs biosynthesized by R. Mucilaginosa seem generally better isolated and organized than those biosynthesized by R. Glutinis that appear agglomerated, stacked with each other. The histograms shown in Fig. 1c and 1d were constructed with 115 AgNPs that allowed calculating the average size of 58 nm for Rg-AgNPs and 30 nm for Rm-AgNPs. Noronha *et al.* **[14]** obtained higher values for Rg-AgNPs (108 nm) and Rm-AgNPs (119 nm) using dynamic light scattering (DLS) to analyze the same samples considered here. This difference can be attributed to the fact that the protein layer covering the silver core could be invisible in SEM and/or to aggregates in the solution used for the DLS experiment.

6.2. AFM CHARATERIZATIONS.

An additional characterization was performed by employing Atomic Force Microscopy (AFM) in the intermittent contact mode (tapping-mode); see Fig 6.2; in order to obtain information on the biogenic layer (proteins)

that covers the nanoparticles. The AFM tapping operation mode is particularly interesting for this work since it is sensitive to different compositions through the phase image. Besides the cantilever amplitude, the movement of the probe can be characterized by its phase relative to a drive oscillator. The phase signal changes when the probe finds regions of different composition, thus phase imaging is a powerful tool that is sensitive to the rigidity/smoothness of the surface, i. e. dissipative force between the tip and the sample surface. This allows the mapping of surfaces to identify constituents with different hardnesses and/or to find different materials involved.
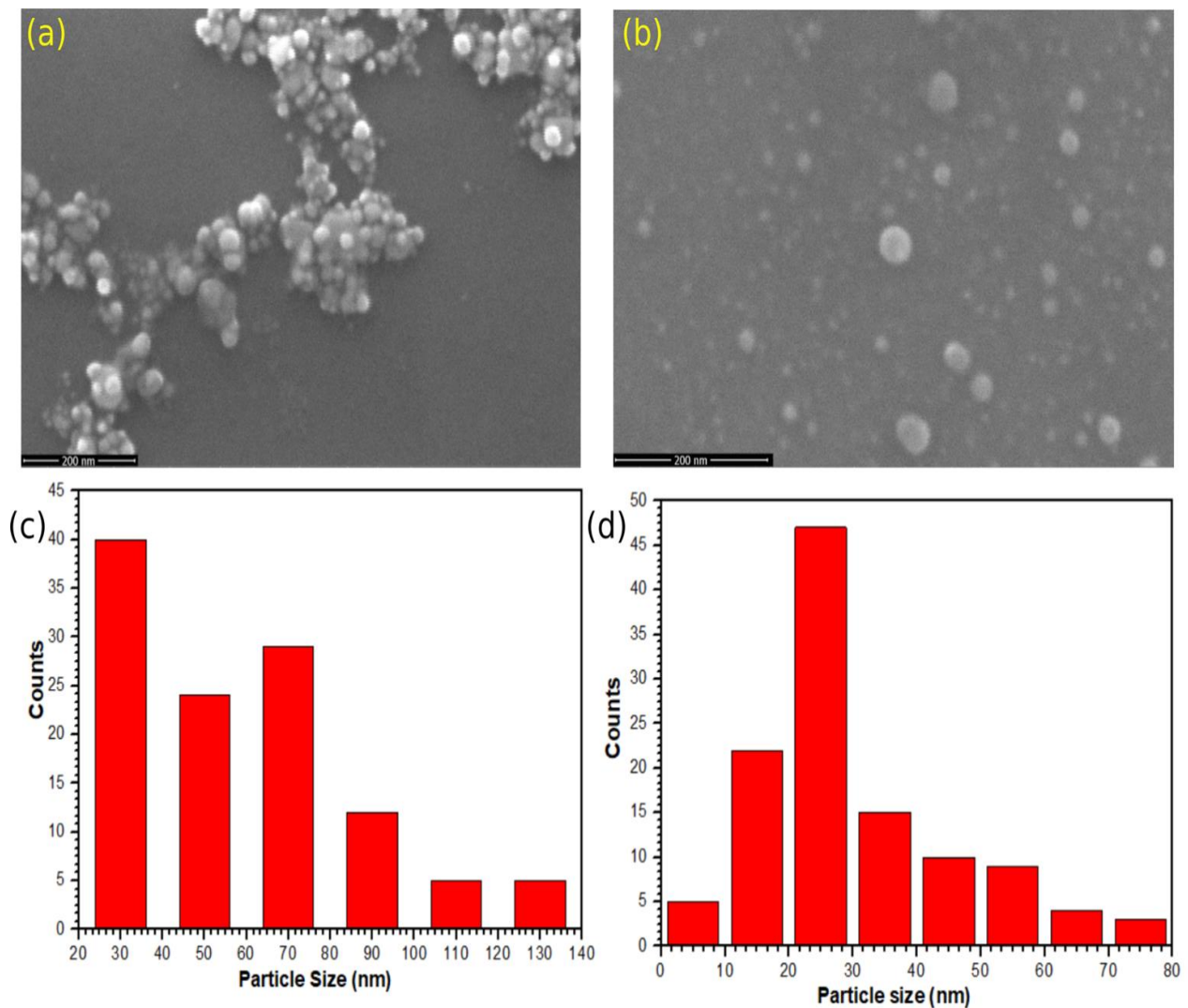
Figure 6. 1. (a) R. glutinis AgNPs SEM image and (c) size histogram; (b) R. mucilaginosa AgNPs SEM image and (d) size histogram.

This type of operation in AFM allows to obtain high-resolution topographic images of sample surfaces that can be easily damaged (soft surfaces), or that do not adhere freely (easily) to the substrate where they are deposited, or that are difficult to obtain images by other AFM techniques. The tapping mode overcomes the problems associated with friction, adhesion, electrostatic forces and other difficulties that affect conventional AFM scanning methods by alternately placing the tip in contact with the surface to provide high resolution and then lift the tip of the surface to avoid dragging it across the surface. The piezo movement causes the cantilever to oscillate with a large amplitude (typically greater than 20 nm) when the tip is not in contact with the surface, see Fig 6.2. Then, the oscillating tip moves toward the surface until it begins to lightly touch the surface. During scanning, the tip oscillates vertically and makes intermittent contact with the surface (the tip is constantly rising and disengaging), usually at a frequency of 50,000 to 500,000 cycles per second.

As the tip oscillates and begins to have intermittent contact with the surface, the oscillation of the overhang (arm where the tip goes) is reduced due to the loss of energy caused by the tip when the tip comes into contact with the surface, this reduction in the amplitude of oscillation is used to identify and measure the surface and internal characteristics of the sample; if you have a sample composed of different materials (with different densities of composition) the tip when tapping the surface of the sample changes the response (change the angle with which the tip hits) this is detected in the equipment. During operation the amplitude of cantilever oscillation is kept constant by a feedback loop. The selection of the optimum oscillation frequency is assisted by software and the force on the sample is automatically set and maintained at the lowest possible level.

When the tip passes over a bump on the surface, the overhang has less room to swing and the amplitude of the oscillation decreases. On the contrary, when the tip passes over a depression, the cantilever has more space to oscillate and the amplitude increases (approaching the maximum amplitude of free air). The tip oscillation amplitude is measured by the detector and the input to the controller electronics. The digital feedback circuit adjusts the separation of the tip of the sample to maintain constant amplitude and force in the sample. When the tip makes contact with the surface, the high frequency (50k-500k Hz) makes the surfaces rigid (viscoelastic), and the adhesion forces of the tip sample are greatly reduced.
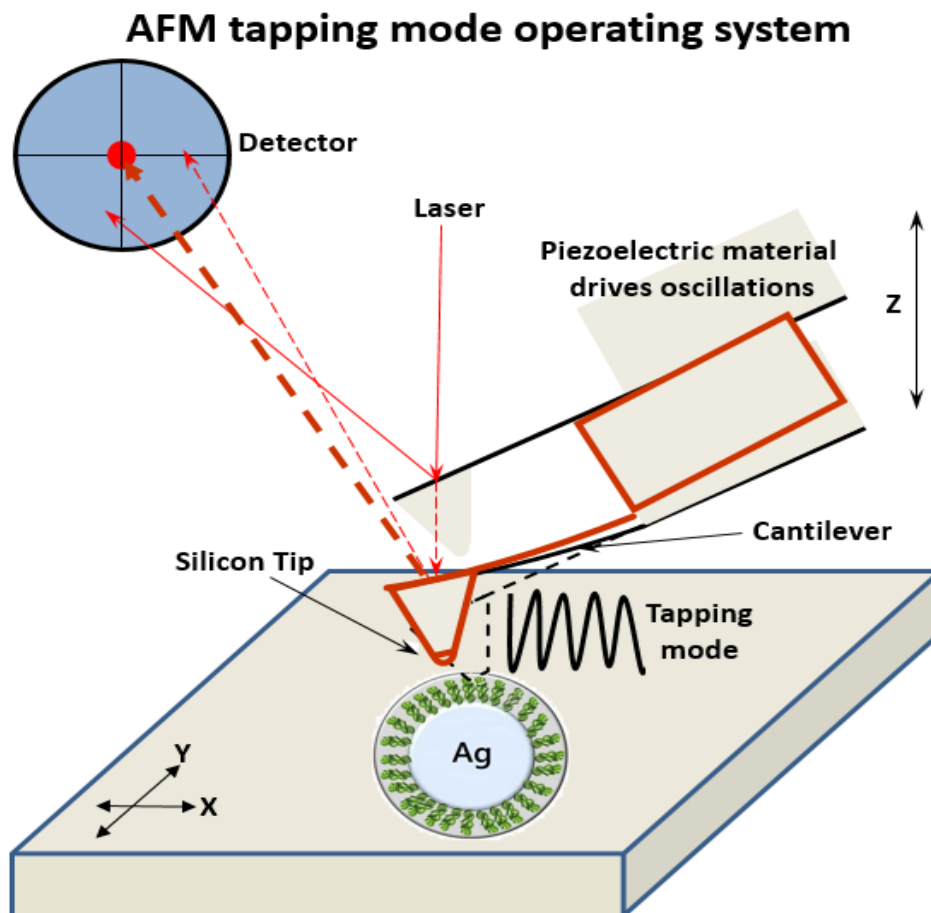
Figure 6. 2. Atomic Force Microscopy (AFM) in the intermittent contact mode (tapping-mode) operating system.

Fig. 6.3a) and 6.3b) show the AFM topography for Rm- and Rg-AgNPs, respectively. Just like in the SEM images above, AFM confirms that the nanoparticles synthesized by the fungus R. Glutinis tend to agglomerate (Fig. 6.3 (b)). Fig. 6.3 (e) and (f) show a histogram of the particle sizes for Rm- and Rg-AgNPs, respectively, made with 80 particles taken from the topography images. Due to the agglomeration of the Rg-AgNPs, their histogram has larger values for the nanoparticle sizes than that for Rm-AgNPs. The mean size calculated from AFM topography are ~56 nm and ~85 nm to Rm- and Rg-AgNPs respectively. This allows the mapping of surfaces to identify constituents with different hardnesses and/or to find different materials involved. Fig. 6.3c) and 6.3d) show AFM phase images for Rm- and Rg-AgNPs correspondingly. Importantly, the contrast of these images demonstrates the existence of a solid nucleus (i.e. Ag) for each nanoparticle with a wrapping layer (i.e. protein) involving it.

The donut-shaped aspect in the phase images is not present in the corresponding spots of the topography images shown in Fig. 6.3a) and 6.3b). These images show a profile made considering a horizontal line crossing the nanoparticles indicated by the arrows with a FWHM (Full Width at Half Maximum) of ~21 nm attributed to the protein capping layer width. It should be noted that this value is experimental minimum limit for the NP considered since the measured profile is a convolution of the tip diameter with the layer width. Using this method, it is possible to estimate the width of the protein layer biosynthesized by fungi to be approximately 24 nm for Rm-AgNPs and 21 nm for Rg-AgNP, while the diameters of the solid core of the particle are estimated around 37 nm and 71 for Rm- and Rg-AgNPs respectively. The Rg nanoparticles tend to agglomerate; this can induce errors in the estimation of the real sizes of Rg-AgNPs, even though the values obtained here have good agreement with the literature [13].
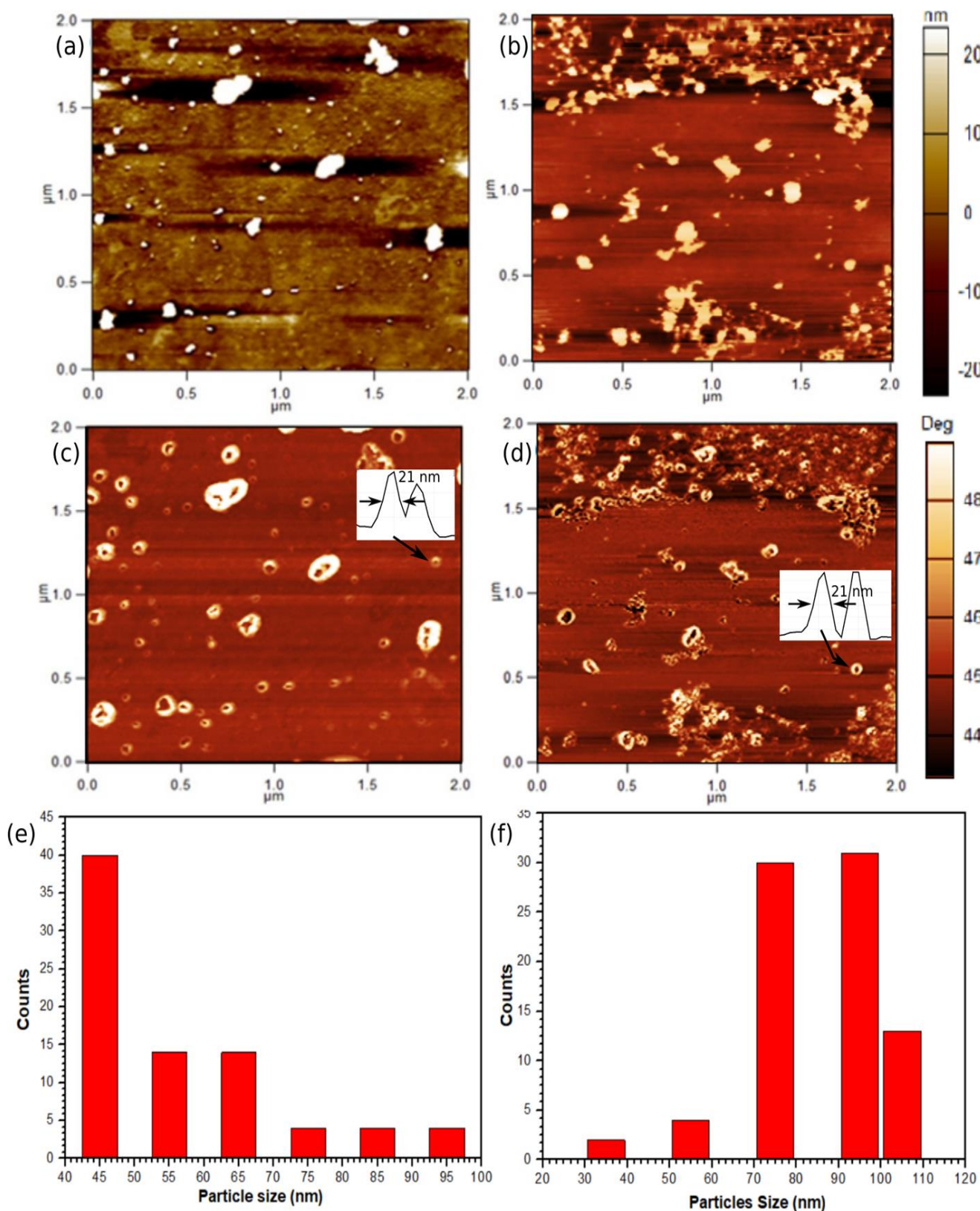
Figure 6.3. Atomic Force Microscopy measurement images of the nanoparticles, the left column images refers to R. Mucilaginosa sample while the right column refers to R. Glutinis. (a,d) AFM topography images; (b,e) AFM phase images; (c,f) size histograms of the topography images.

From the FWHM statistical calculations see Fig 6.4, made using the AFM data; bring quantitative information about morphological parameters of AgNPs; total size (AFM topography, particle diameter), core size (AFM Phase, protein solid core diameter) and protein layer (AFM Phase, protein layer thickness). The calculations made to the AgNPs size nucleus in this part were almost the same size calculated for the AgNPs from SEM images; this tells us that the images made by SEM do not capture the organic layer (protein layer); in SEM, only can see the solid silver nucleus. Table 6.1 summarizes the analysis of the AFM and SEM measurements, including the DLS values for comparison [13]. The AFM tapping mode used to generate images give a morphological and quantitative information that are much more convenient and easy to use than using a SEM or a TEM technique. It is likely that characterizing by TEM will be able to observe some type of protein layer or some biological material however, the TEM technique requires much more advanced and careful sample preparation than for an AFM, in addition to the fact that the operating and maintenance costs of a TEM are much higher than those of an AFM.
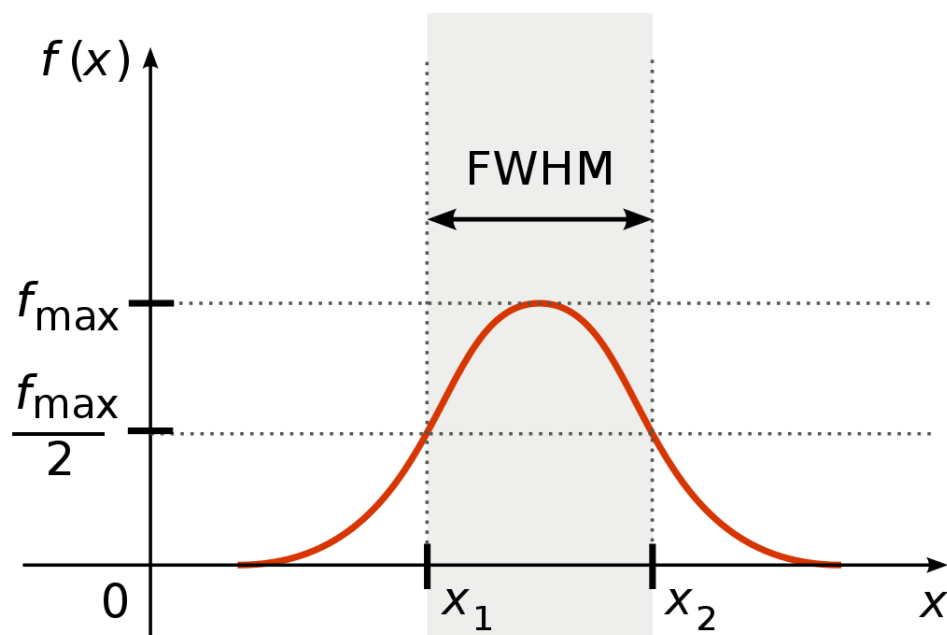
Figure 6.4. *Full Width at Half Maximum (FWHM) curve.*

Table 6. 1. AgNPs sizes according to the AFM analysis.

AgNPs	Rm-AgNPs	Rg-AgNPs
AFM topography, particle diameter (nm) average; SD	**56; s≈6**	**85; s≈7**
AFM Phase, protein layer thickness (nm) average; SD	**24; s≈2**	**21; s≈2**
AFM Phase, protein solid core diameter (nm) average; SD	**35; s≈2**	**69; s≈7**
SEM image, particle diameter (nm) average; SD	**30; s≈3**	**58; s≈9**
DLS Noronha *et al.* [13]	**108 nm**	
TEM and DLS, Navin Jain *et al*. [61]	**54 nm and 40-60 nm**	
TEM and DLS, Varahalarao Vadlapudi *et al.* [62]	**15 nm and 65-75 nm**	

6. 3. PHOTOLUMINESCENCE CHARATERIZATION.

Photoluminescence (PL) spectroscopy is an effective technique to study the optical properties of silver nanoparticles in order to evaluate potential applications of materials, such as in photonics. PL emission spectra are shown in Fig. 6.5 for excitation with a blue laser ($\lambda = \mathbf{473}$ nm, 2.62 eV). The spectra shown in Fig. 6.5 a) and Fig 6.5 b) were acquired for different nanoparticles, but all the spectra for the same Rg or Rm fungus specie are similar, with a very broad peak at 570 nm. Similar spectra have been reported in the literature for AgNPs stabilized in soluble starch **[64]** as well as for AgNPs biologically synthesized by fungus **[65]**. Variations in the emission wavelength could come from size deviations **[66, 67]**, but this was not observed in the spectra shown in Fig. 6.5 a) and b), indicating homogeneity in the sizes of the NPs analyzed.

6. 4. SERS CHARATERIZATIONS.

One of the central parts of this works is try to obtain Raman measurements of the AgNPs coated with proteins using SERS technique

that allow to extract information of the interaction and general structure of these bioelements without establishing the precise three-dimensional location of individual structural elements (the proteins in studies are in amorphous state). SERS is an extension of Raman spectroscopy that explores the enhanced local fields at metallic nanostructures, thus allowing for the detection of very small amounts of sample **[68]**. With SERS, several vibratory modes can be used for the analysis of peptide structures. In the study of protein conformation, two aspects are mainly due. One is the peptide-skeleton structure or secondary structure. The other is the arrangement of the many side chains in a protein, or tertiary structure. Of course, sometimes there is no clear dividing line between secondary and tertiary structures.
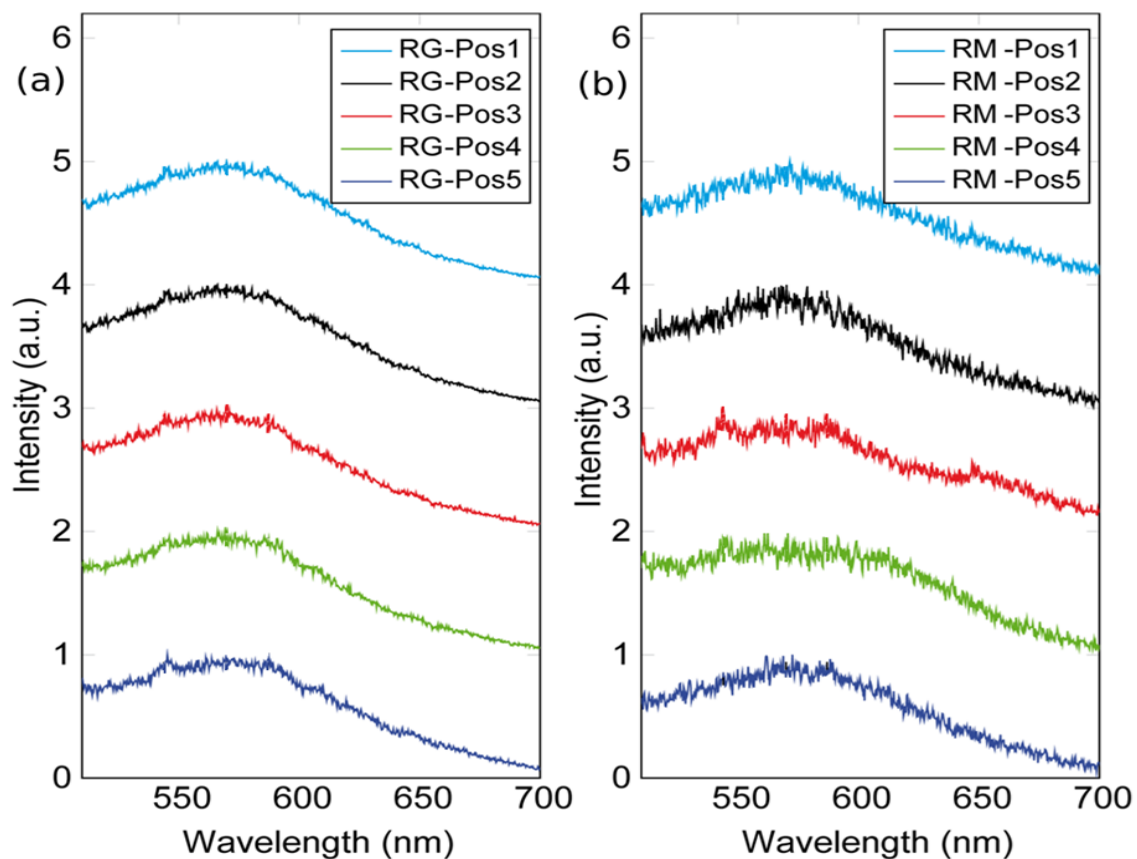
Figure 6.5. Photoluminescence measurements for (a) R. glutinis (RG) and (b) R. mucilaginosa (RM).

There are several typical peptide-skeleton arrangements, such as α−helix, β−sheet, β−turn, γ−turn, ω−turn and the random coil. Raman spectroscopy provides information on the peptide backbone, geometry of disulfide bonds, and the environment of some side chains such as those of tyrosine, tryptophan, and methionine. Raman spectroscopy can detect the presence of disulfide bonds, methionine residues, and sulfhydryl groups (SH); such detection involves tedious procedures when done by conventional chemical methods.

The most characteristic bands are associated with the peptide bond $CONH$ group is nearly planar because of resonance stabilization. The bonds ψ and ϕ on both sides of a peptide bond are fixed for a particular conformation and ultimately affect the vibrational modes of a peptide bond, see Fig. 6.6. The spectra have well-defined peaks and improved sensitivity due to SERS effect referred to as amide I to VII, with the vibrational assignments according to Table 6.2. Most of the peaks shown in Fig. 6.7 (c) and Fig. 6.7 (d) are in the region from (1200-1700) cm^{-1} and could be assigned to $C - O$ stretching, $N - H$ bending and $C - N$ stretching [69].

Thus, considering that amide II has very weak Raman signal, the peaks could be related mostly to amide I and III. It is not possible to classify the proteins according to their secondary structures, i.e., α−helix, β−sheet, or mixed structures (α/β, $\alpha + \beta$), based on the obtained Raman spectra due to the large amount of peaks distributed in a wide range of frequencies. These peaks might be related to α−helix or β−sheet structures. However, narrow and relatively intense Raman bands are found between 500 and 900 cm^{-1} both in M3 and G3 spectra, and it can be associated with protein mixed structures [69, 70].
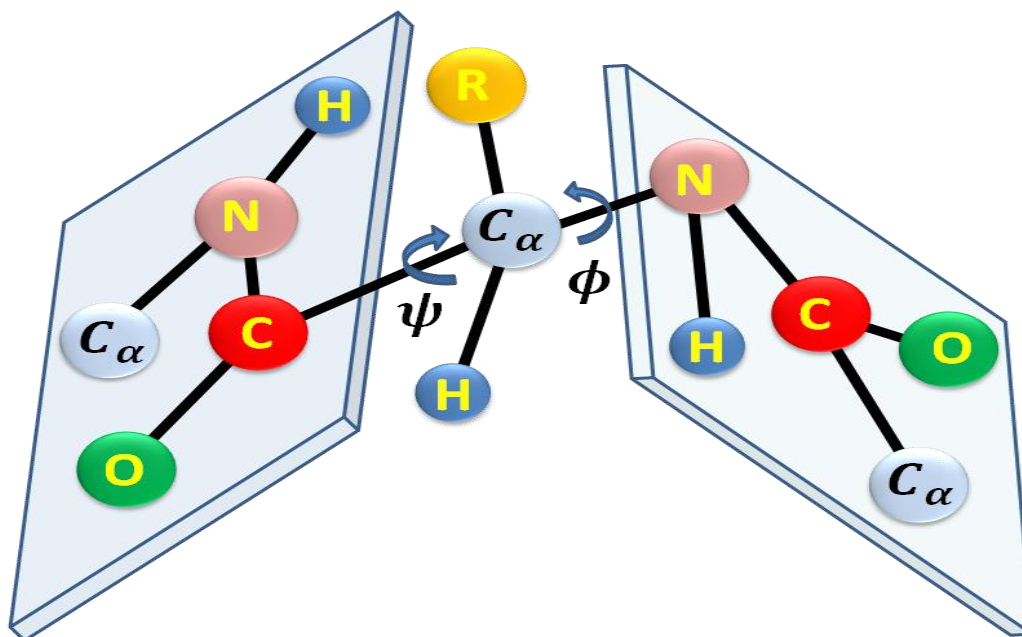
Figure 6.6. The rotation of a peptide backbone is restricted to the $C_{(\alpha)} - C$ and $N - C_{(\alpha)}$ bonds. Spatial orientation of the peptide backbone (conformation) is determined by the angles of rotation of ψ and ϕ, which are known as Ramachandran angles. The peptide bond, $CONH$, has no free rotation along the $C - N$ axis because $CONH$ lies in the same plane because of resonance, as shown here.

Table 6.2. Raman Shift of AgNPs produced by R. glutinis and R. mucilaginosa.

R. glutinis	R. mucilaginosa	Assignment*
(1600-1690) cm^{-1}		Amide I, $C = O$ stretching/hydrogen bonding coupled with $COOH$
(1480-1580) cm^{-1}		Amide II, $N\text{–}H$ groups bending vibrations, $C\text{–}N$ stretch
(1230-1300) cm^{-1}		Amide III, $C\text{–}N$ stretch, 30% $N\text{–}H$ bend, $C - C$ stretching, $C - H$ flexion
(625-770) cm^{-1}		Amide IV, OCN bending
(640-800) cm^{-1}		Amide V, out-of-plane NH bending
(540-600) cm^{-1}		Amide VI, out-of-plane $C = O$ bending
220 cm^{-1}		Stretching $Ag - O$, Silver oxide
200 cm^{-1}		Amide VII, Skeletal mode
*Refs. [74-79].		

The Raman spectra vary with time for acquisitions at the same sample spot, even for small acquisition times. This fact was investigated in time series measurements in a single spot, in which 100 measurements were made using 0.1 s for each acquisition, with an elapsed time between acquisitions of 1 s due to experimental limitations of the equipment. The acquired spectra are shown in Fig. 6.7 (a) and Fig. 6.7 (b) for Rm- and Rg-AgNPs respectively, with selected spectra shown in Fig. 6.7 (c) and Fig. 6.7(d) for the indicated orange lines. The peaks around 500, 900-1000 and 1600 cm^{-1} might be assigned to a shift of the NH_2 twisting, wagging, rocking and scissoring modes, respectively, indicating an amine-silver interaction [70]. Moreover, for both Rm- and Rg-AgNPs, the Raman spectra vanish (or become too weak) after approximately 40 s and 55 s, respectively.

On visual inspection, of the three Raman spectra showed in Fig. 6.7 (c) and Fig. 6.7 (d) show the trend of the intensity change and the position of the peaks for the three spectra, which seems to indicate that the emissions Raman's are strongly correlated in time; drastic jumps of intensity and position that occur simultaneously. The stabilization of biogenic AgNPs results from the capping protein structures, usually oligopeptides lying on the surface of the nanoparticle, thus conferring stability and preventing the oxidation of Ag^0 to Ag^+. Various substances can break this energy balance leading to the collapse of the nanoparticle. The substances that cause this effect are those that alter the conformation structure of the oligopeptides or alter their load content, destabilizing the protein and consequently the silver nanoparticle. Among these, we can mention oxidizing or reducing agents, lasers and heat [71, 72].
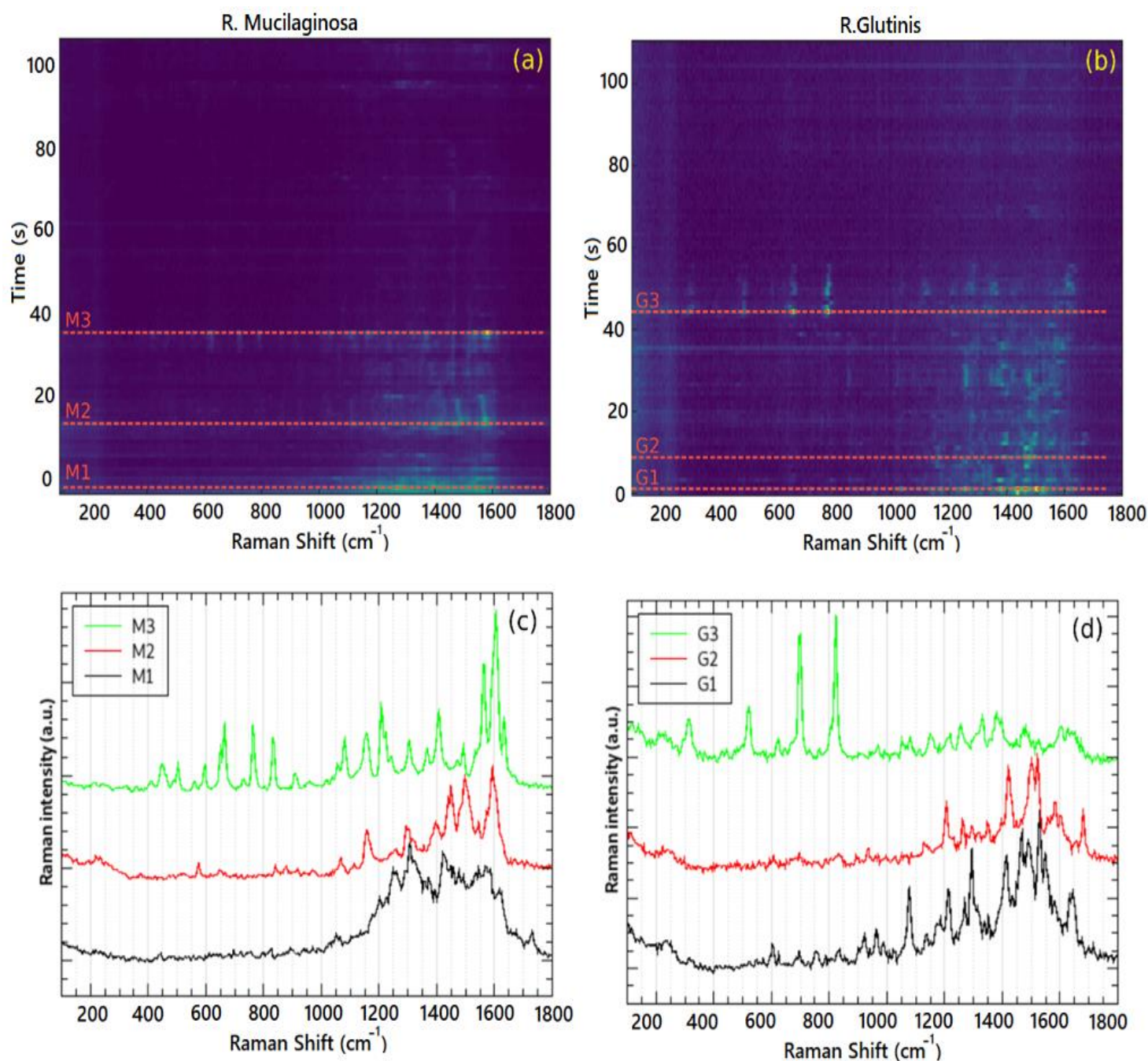
Figure 6.7. (a) Time series Raman spectra in a single point of Rm-AgNPs and (b) Rg-AgNPs with an acquisition time of 0.1 s per spectrum. (c) Selected Raman spectra of the sample Rm-AgNPs indicated in the lines M1, M2 and M3 of image (b). (c) Selected Raman spectra of the sample Rg-AgNPs indicated in the lines G1, G2 and G3 of image (b).

These may be some of the facts that can explain the instability of the Raman spectra described above, however a relevant one to explain the temporal fluctuations may be due to the transfer of electrons that regulate the molecule-metal interaction under the excitation of light. This is

particularly relevant for proteins due to the complex landscape and energy range that they possess together with the interlacing of vibrational modes **[73]**. This behavior deserves some interest to unravel the role played by charge transfers in SERS and can even serve to understand the photophysical processes at the interfaces that occur in optoelectronic devices.

Another possible explanation for the instabilities observed in the Raman spectra might be related to modifications of the silver core, eg. small changes in its shape, heating or even melting due to the laser energy transfer. This hypothesis was verified employing a dark-field setup equipped with an additional HeNe laser, as described in the "Experimental Details" section. Dark-field microscopy is a very useful tool to study metal particles either in biological or in materials science fields **[80, 81]**.

6. 5. DARK-FIELD SCATTERING CHARACTERIZATIONS.

The Fig. 6.8 (c) shows a dark-field APD image of Rm-AgNPs by raster scanning a sample region; the bright points indicate the location of Rm nanoparticles. Fig. 6.8 (a) shows the scattered light for the chosen spots indicated in Fig. 6.8 (c) with 1 s of acquisition time for every spectrum. The image shown in Fig. 6.8 (a) is homogeneous, indicating the stability of the nanoparticle under these measurement conditions. Keeping the same experimental conditions, the HeNe laser was turned on and focused on the same sample spot. The acquired spectra thus obtained are summarized in Fig. 6.8 (b). This figure is similar to Fig. 6.8 (a) up to about 75 seconds, which can be considered the starting time for a decrease in the scattering intensity. Fig. 6.8 (d) shows three sample spectra after a delayed time of 19 s, 99 s and 166 s of sample exposure to the HeNe laser.
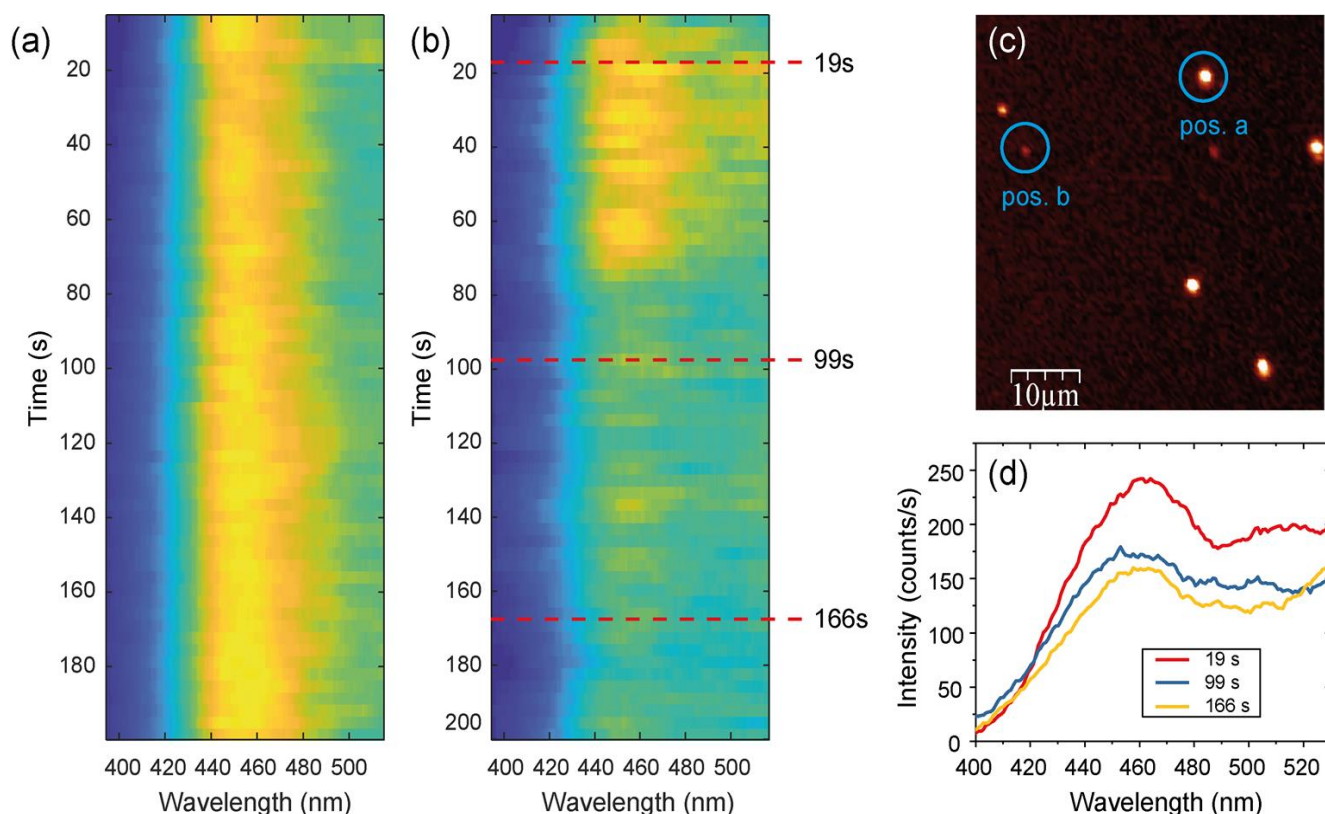
Figure 6.8. Dark-field scattering images for the R. mucilaginosa sample using white light illumination (a) without additional red laser excitation and (b) with additional red laser turned on. The images were acquired in the spots indicated in image (c). (c) Dark-field image of the Rm-AgNPs made by raster scanning the sample with white light illumination. (d) Spectra on the orange lines indicated in image (b).

It is clear that the peaks weaken their intensities, although they do not alter their positions and/or widths. This is good evidence that, besides the protein conformations, the metallic cores are also affected by the laser. It is important to comment that Rg-AgNP exhibit a similar behavior. Throughout both sample materials, the degree as to which the scattering spectra were influenced by laser heating was very diverse. A possible cause for this behavior is the diversity in the microscopic shape of the individual particles (c.f. Fig. 6.1). In Fig. 6.9, we can see the measurements of Raman in dark field in time series, the results were almost the same as those shown in Fig. 6.7, a Raman fluctuating in the time.
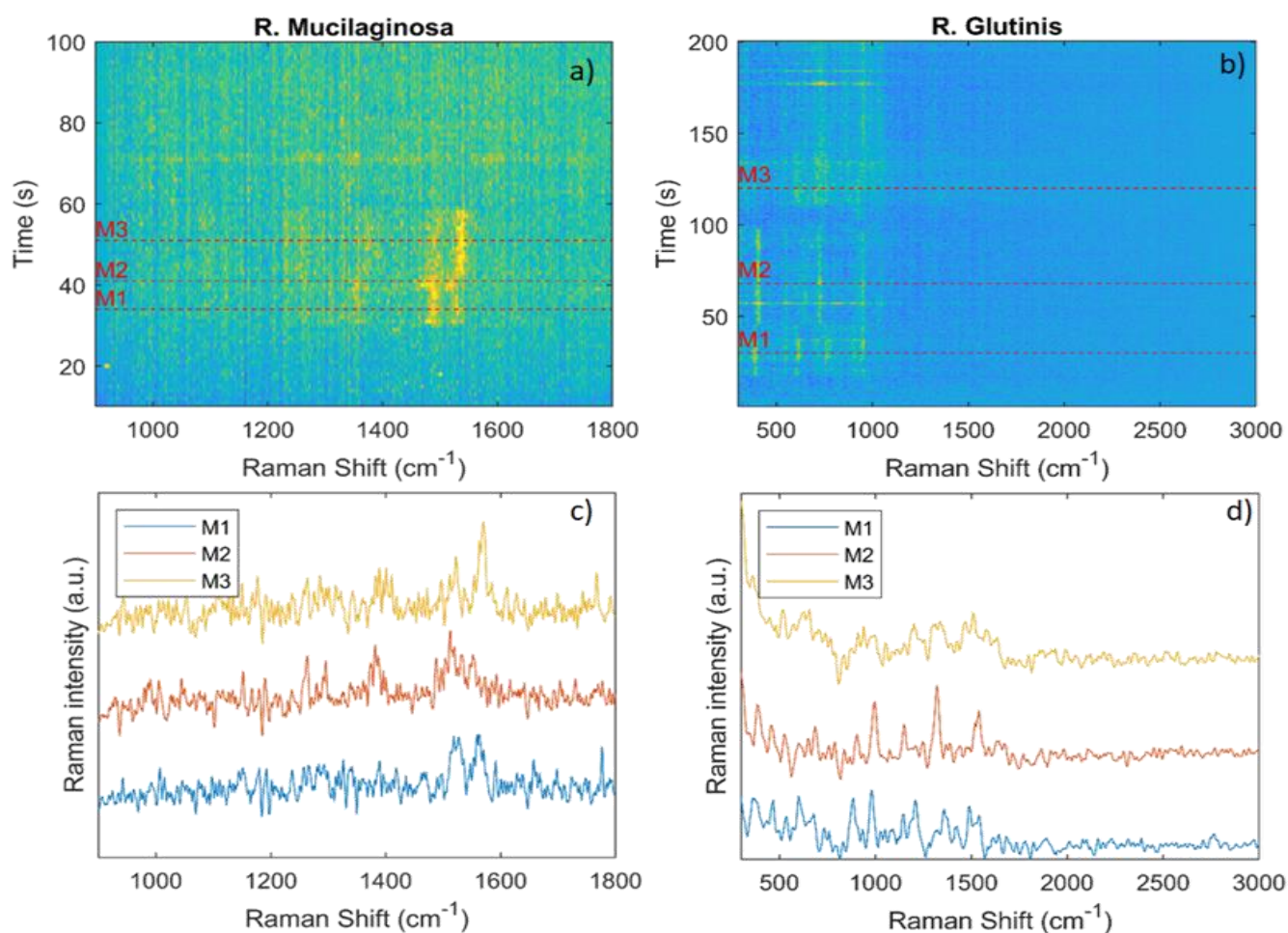
Figure 6.9. a) Time series Raman spectra in a single point of Rm-AgNP and b) Rg-AgNP of Dark-field scattering; c) and d) three Raman spectra selected point of Rm-AgNP and (b) Rg-AgNP.

6. 6. TERS CHARATERIZATIONS.

With the objective to obtain significant Raman information from individual Rg- and Rm-AgNPs and to acquire more detailed information on the interaction of the Ag nucleus and protein coverage in order to establish a basis for future studies on biogenic proteins or the like. The application of Raman spectroscopy to study protein circles at the Bulk level has been known since the last decade. Raman spectra provide information about proteins and their competitors, as well as interactions between protein subunits, amine acid and/or nucleic acids. Cesar Rodrigues Fernandes, PhD thesis 2015 **[83]** and Christiano Balbino da Silva, PhD thesis 2019 **[84]** are two exemples.

Obtaining a single Raman spectrum from amorphous proteins that coating-enveloping AgNPs through conventional micro-Raman configurations is a challenge, because the Raman effect is intrinsically weak and that the study system size is in the nano metric scale below the diffraction limit. A rapidly advancing variant of Raman spectroscopy is the tip-enhanced Raman scattering (TERS) that offers an alternative solution to obtain Raman signals from samples at the nano level, which, like the SERS technique, exploits the phenomenon of metals that with appropriately nano sized features are able to localize regions of charge density at their surface when illuminated by appropriate electromagnetic radiation. These are the so-called localized surface plasmons resonant (LSPR), who can interact constructively with the electric field component of the incident light, which results in an enhancement of many orders of magnitude to the light intensity, so with the SERS and TERS techniques is possible significantly amplify the enhancement of the scattered Raman photons. While SERS uses the LSPR generated on nano patterned particles surfaces to enhance microscopic or bulk-phase measurements; TERS uses the combination of LSPR and the lightning rod effect to generate an enhanced electromagnetic field at the apex of a sharp metallic tip probe positioned in the focal spot of an excitation doughnut mode laser polarized with which can do a scan on a nano metric sample and select the area where want to obtain an enhancement Raman signal. The sample tip scans provides an AFM spatial resolution while collecting vibrational structural information from an enhancement Raman measurement. TERS to overcome the diffraction and sensitivity limitations of conventional Raman spectroscopy **[26-29]**.

Consequently, the TERS technique is a great option for the study of this type of materials by providing vibrational spectroscopic information with a spatial resolution below diffraction limit (the resolution Raman limit

TERS will depend on the tip size, in this case were used tips of approximately 15-20 nm) even to characterize Rg- and Rm-AgNPs protein-coated at the molecular level. In order to perform the TERS measurements, a much more diluted sample was prepared than the one made for the SERS measurements, this with the purpose of finding isolated nanoparticles more frequently and reducing the agglomerates of the AgNPs (the AgNPs tend to agglomerate). Having samples of AgNPs as dispersed as possible, isolated or at least with small agglomerates is necessary to obtain good measurements using this technique; Au-tip can be damaged if the deposited AgNPs are very tumultuous or with too many agglomerates. Despite the apparent simplicity of the TERS principle, its experimental implementation remains highly challenging, which is reflected by the fact that only a handful of academic groups have actually reported successful and consistent TERS measurements, despite commercial systems being available **[31-40]**.

AgNPs are characterized by being plasmonic and having strong interaction with photons through localized surface plasmon resonance excitation (LSPR). LSPRs can be described as the photon-induced resonant collective oscillation to the valence electrons, which stabilizes when the frequency of the photons coincides with the natural frequency of the surface electrons oscillating against the restoring force of the positive nuclei. The wavelength of the resonant photon is different for different metals. Rm- and Rg-AgNPs exhibit highest absorption peak resonant behavior when interacting with ultraviolet visible (UV-vis) located approximately at $\sim\lambda = \mathbf{412}$ and $\sim\lambda = \mathbf{416}$ nm for Rm- and Rg-AgNPs respectively; in Fig. 6.10 can see the absorption curves respective. The resonant wavelength and LSPRs intensity not depend only on the nature of the metal, but also on the size and shape of the metal nanostructures.
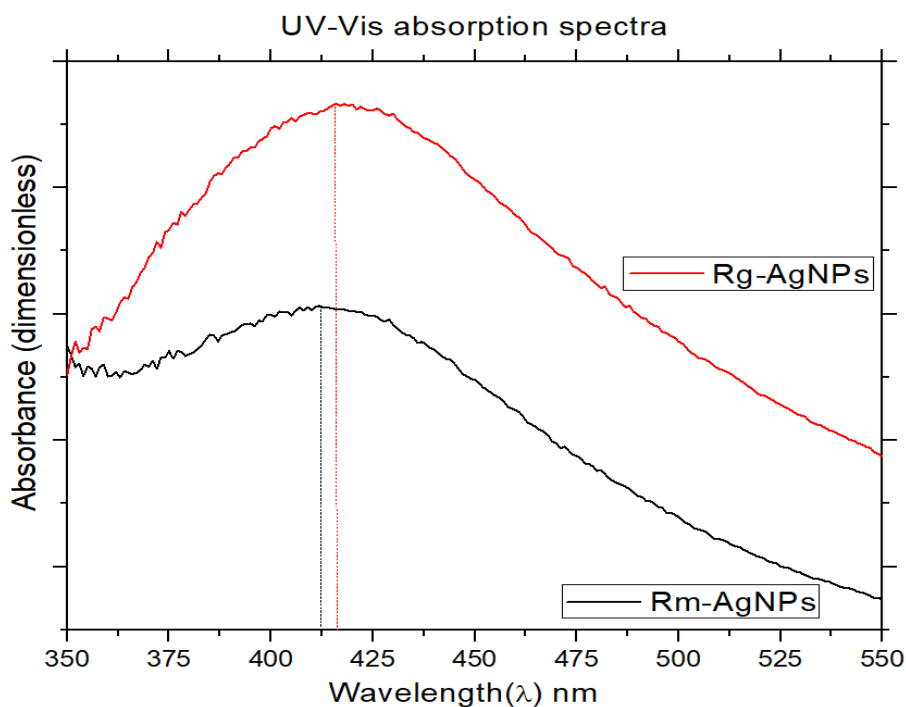
Figure 6.10. UV–Vis spectra of Rg- (red line) and Rm-AgNPs (black line).

After performing several scans in the sample with the APD (see annex) looking to find optical response for the 1600 cm^{-1} filter, from the regions that gave a signal in this filter, those with some type of Raman far-field (Rff) signal were selected; in one of these regions the Au-tip was landed. Fig. 6.11 illustrates the process to obtain an Rff signal (tip-out, far field regimen) and a Raman near field (Rnf) signal, when the tip is landed-placed on the sample and interacts with the evanescent waves (tip-on, regimen near field).

The Au-Tip is the most critical component in TERS, because it serves as a near-field optical nano antenna. The size, shape, structure and tip composition strongly affect the LSPR generation, in this sense the tip quality in to generate LSPR determine to great success of the TERS characterizations. It should be noted that it is important to develop manufacturing procedures that can produce tips with high measurements factors and reproducible geometries. In the present work, the Au-tips were

manufactured by the chemical etching methods (David Gingery et al., Michael G. Boyle et al., Tae Won Huh et al., Bo Yang et al.) as AFM Au-tip scanning, obtaining Au-tips of around 15 to 20 nm of apex size.

$$I_{Raman} \approx \left[\frac{\vec{E}_{tip-in}(\nu_I)}{\vec{E}_{tip-out}(\nu_I)}\right]^4$$

$$I_{Raman} = f_{enh}^4$$
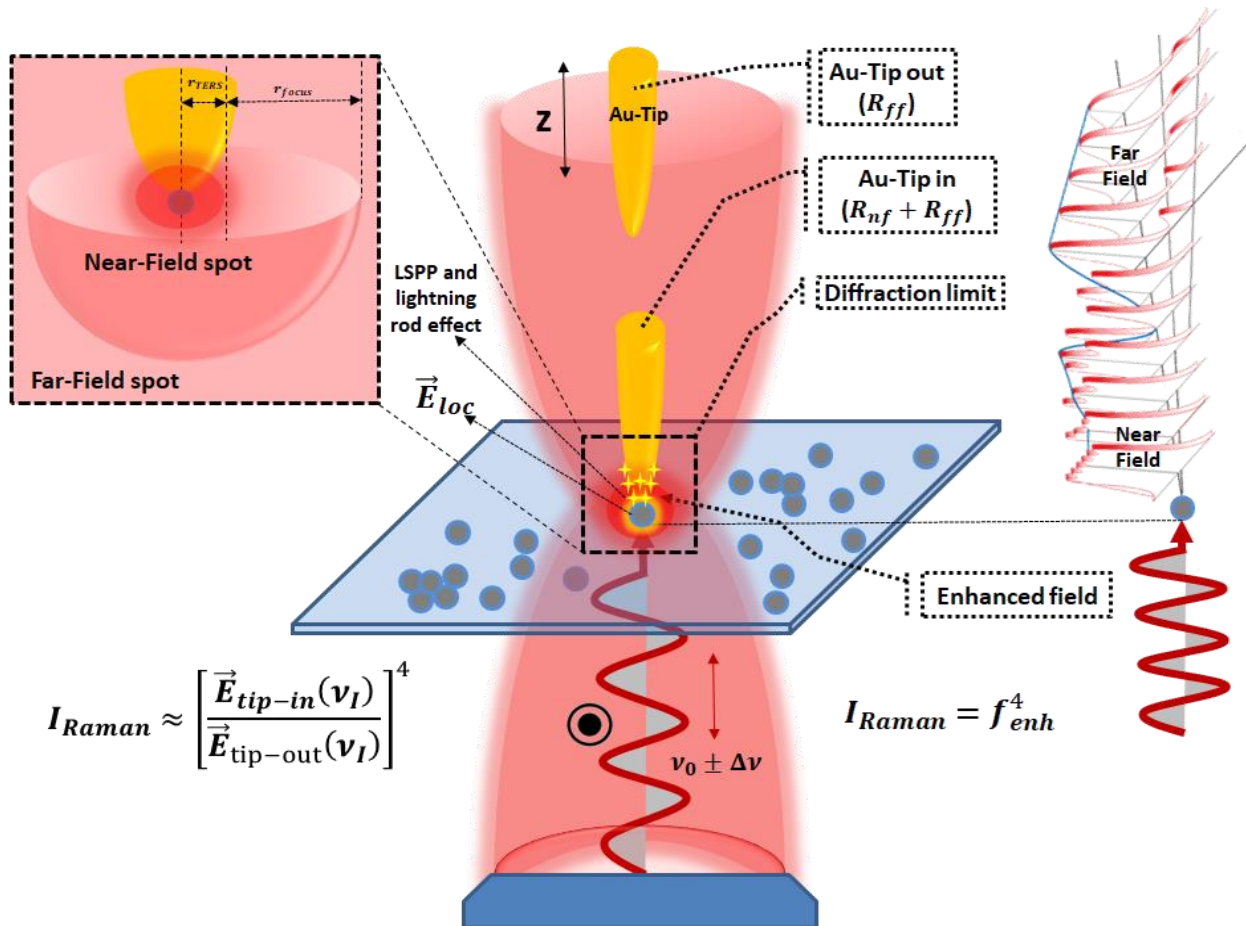
Figure 6.11. TERS technique schematic representation in transmission lighting mode on the $z -$axis on the Au-tip in a transparent sample. When the Au-tip is away, the Raman measurement obtained is in Rff regime, when the Au-tip is landed on the sample the Raman measurement obtained is in Rnf regime [25, 26].

TERS Au-tip probes must be correctly aligned with the excitation laser of the confocal Raman spectroscopy system for efficient excitation of the LSPR, see Fig. 6.12. The TERS hyperspectrum (Fig 6.12 c)) was acquired along the surface sample scanning in the xy direction (MCL control) in complete synchronization and alignment with the Au-tip AFM tuning-fork system of piezoelectric control (z-direction); the position of the Au-tip AFM always remained in the focus and in the hip laser center. The

tip-focus alignment is very important in the measurement realization because it guarantees the z-polarized electric field on the tip shaft (a good synchrony and coincidence in the hyperspectrum and AFM images). This involves a number of steps, including positioning TERS probes at the center of the focal spot of the excitation laser while maintaining SPM feedback and locating the 'hotspot' at the TERS probe apex using the APD (see annexed A)). Successful hyperspectrum imaging requires a delicate balance between different experimental and acquisition parameters, including laser power, spectrum integration time and maintenance of the SPM feedback between the TERS Au-tip probe and the sample surface.
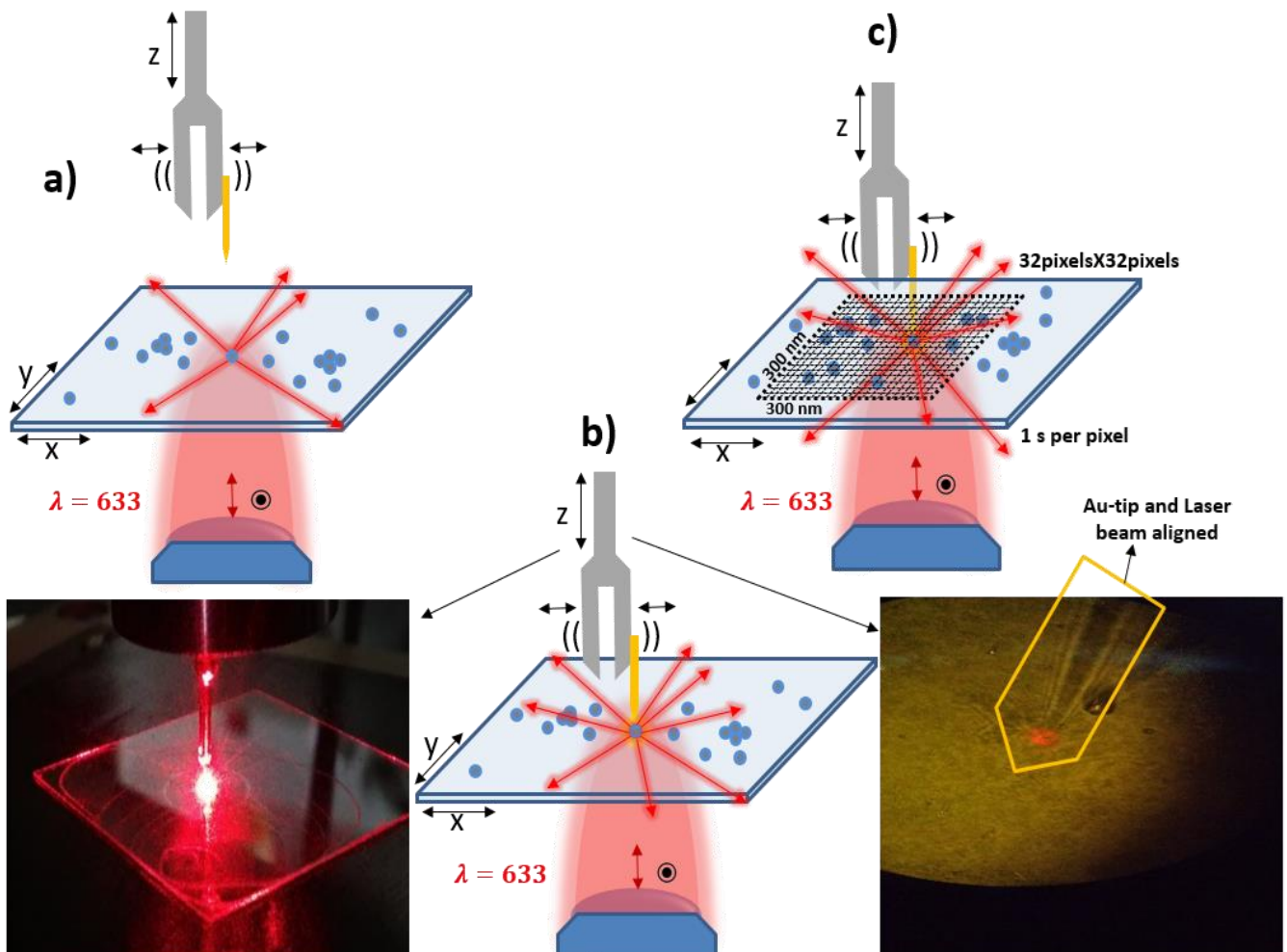
Figure 6.12. AFM TERS Tuning-fork system. a) Raman spectra obtained on one single point with the Au-tip away (tip-out). b) Raman spectra obtained on one single point with aligned laser beam and Au-tip landed (tip-on). c) Hyperspectrum (vibrational scanning image maps).

In Fig. 6.13 and 6.14 can see the Raman spectra obtained on one single point (possibly some little agglomerate that were on the laser focus hip and gave an Rff signal) but done in two different way. Firstly, with the tip away from the sample (Tip-out, black line on Fig. 6.13 and 6.14 for Rg- and Rm-AgNPs respectively, in the way illustrated in Fig. 6.12 a)) and second with the landed tip on the sample (Tip-on, red line on see Fig. 6.13 and 6.14 for Rg- and Rm-AgNPs sample respectively, in the way illustrated in Fig. 6.12 b)). In the second, an enhancement Raman spectra signal is obtained by the TERS technique in the Rnf regime can be clearly perceived. Done this, proceeded to make a hyperspectrum (vibrational mapping image, see Fig. 6.12 c)) in a nanometric scale to obtain an Rnf signal from the protein-coated for the Rg- and Rm-AgNPs on 1600 cm^{-1} peak, and so with the scan can find AgNPs isolated on the periphery where the tip firstly landed.

A flat-field Nikon oil immersion objective lens was used, with the aberration and corrected infinity with 60x magnification, and NA=1.4. Using a step size well below the diffraction limit, a scan is performed in an area of $\boldsymbol{300X300\ nm^2}$ with 32x32 pixels with measurement time of 1 s per pixel, as illustrate Fig. 6.12 c). In the Fig. 6.15 a) and 6.16 a) can see the hyperspectrum image on 1600 cm^{-1} peak for Rg- and Rm-AgNPs respectively. A red laser ($\boldsymbol{\lambda = 633}$ nm wavelength) with a power spot on sample between 200 and 500 uW was used, and a 20 nm Au-tip apex size.

On Fig. 6.15 b) and 6.16 b) can see the 32x32 pixels points AFM image for Rg- and Rm-AgNps samples respectively and on Fig. 6.15 c) and Fig. 6.16 c) can see also SEM images with 500 nm scale ruler for Rg- and Rm-AgNPs; these show how scattered and isolated AgNPs are found together with a few agglomerates. From 3-D AFM image, see Fig. 6.15 d)

and 6.16 d), can be calculated the maximum height of small agglomerates in 64 and 67 nm for Rg- and Rm-AgNPs respectively. In general can say that from the images in Fig. 6.15 and Fig. 6.16 could be noted the good coincidence, match between the spectroscopic image (Fig. 6.15 a) and Fig. 6.16 a)) and the AFM image (Fig. 6.15 b) and Fig. 6.16 b)). It is important pointing that spherical AgNPs with $\sim(30-50)$ nm size does not generate plasmons (or very little) ta $\lambda = 633$ nm wavelength (see Fig. 6.10), so the plasmons that are generating in this system type of Raman-enhanced signal are due to the scanning Au-tip interacting with spherical AgNPs in the Rnf regime. A specific type of plasmons were generated, called gap plasmons.

When a TERS Au-tip is brought into close proximity to a metallic surface, an image dipole is induced in the surface that acts in the manner of a second tip. When a protein of size lower that subwavelength is sandwiched between the Au-tip apex and an AgNPs surface elements, this Gap Plasmons (GP) mechanics generates a great enchantment Raman signal. This is illustrated in the scheme showed in the Fig 6.17. The GP allow one to reach strong field confinement, low losses, and high effective index of refraction. In this context, the GP modes localized in the sandwich between the Au-tip apex and AgNPs surface determine the optical response of the nano antenna allowing obtaining a proteins Raman signal beyond the limit of diffraction. The excitations of the localized GP modes represented in the Fig 6.17 is the most important TERS mechanism. The GP resonance frequency is a function that depends of tip-substrate separation, the TERS size tip, and the used substrate metal.
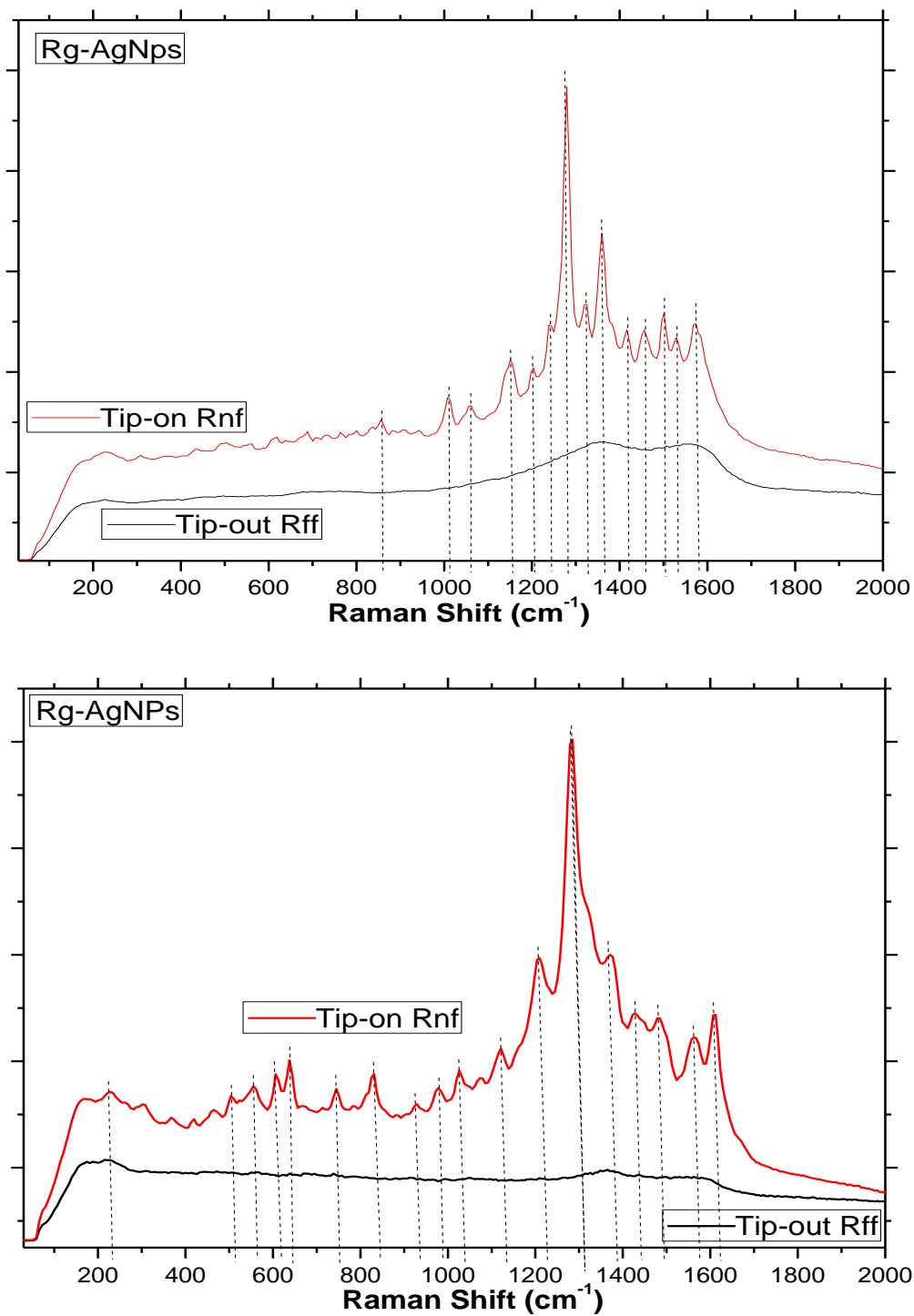
Figure 6.13. Rg-AgNPs sample Rff signal (black line) Tip-out, Rnf signal (red line) Tip-on.
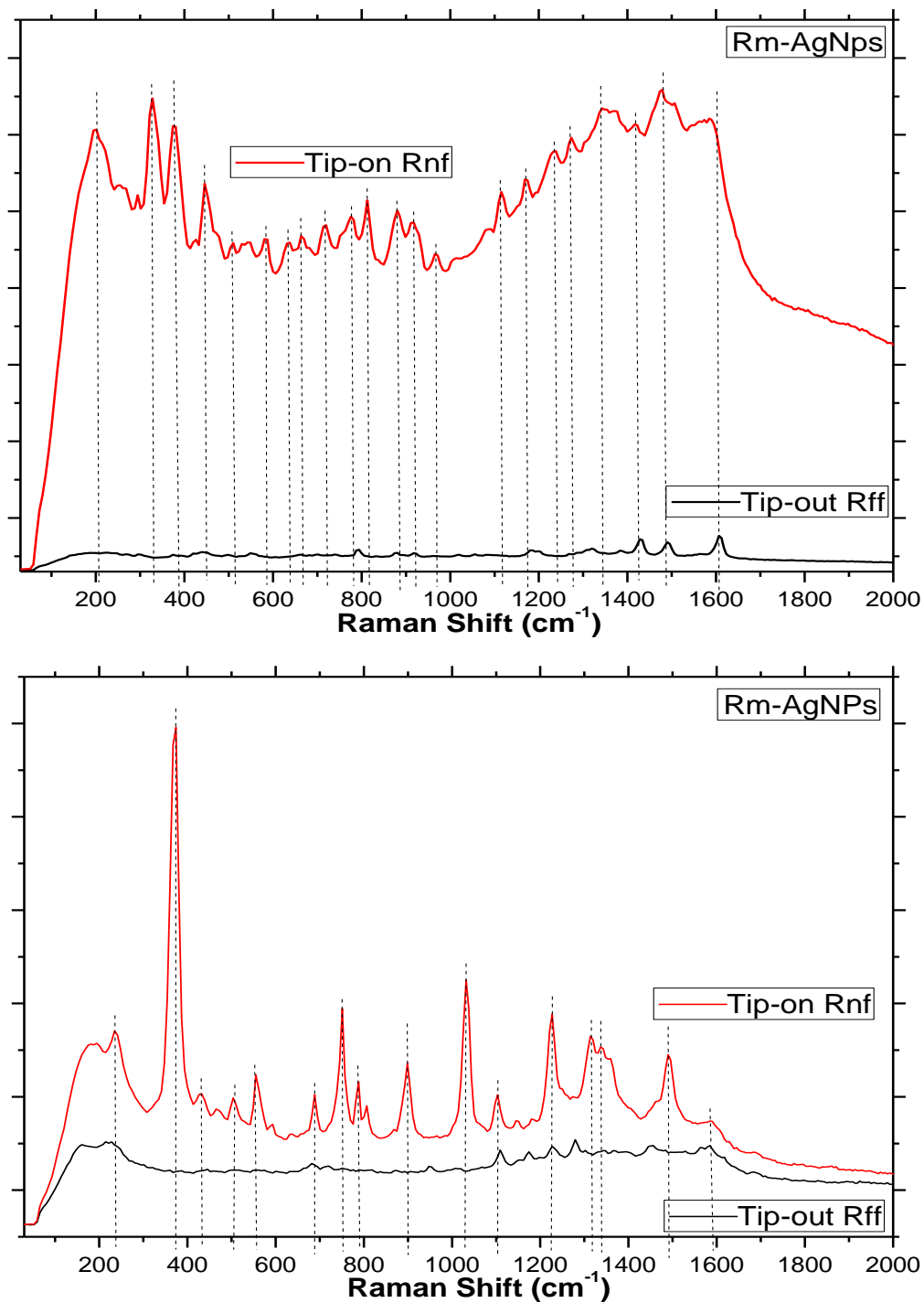
Figure 6.14. Rm-AgNPs sample Rff signal (black line) Tip-out, Rnf signal (red line) Tip-on.
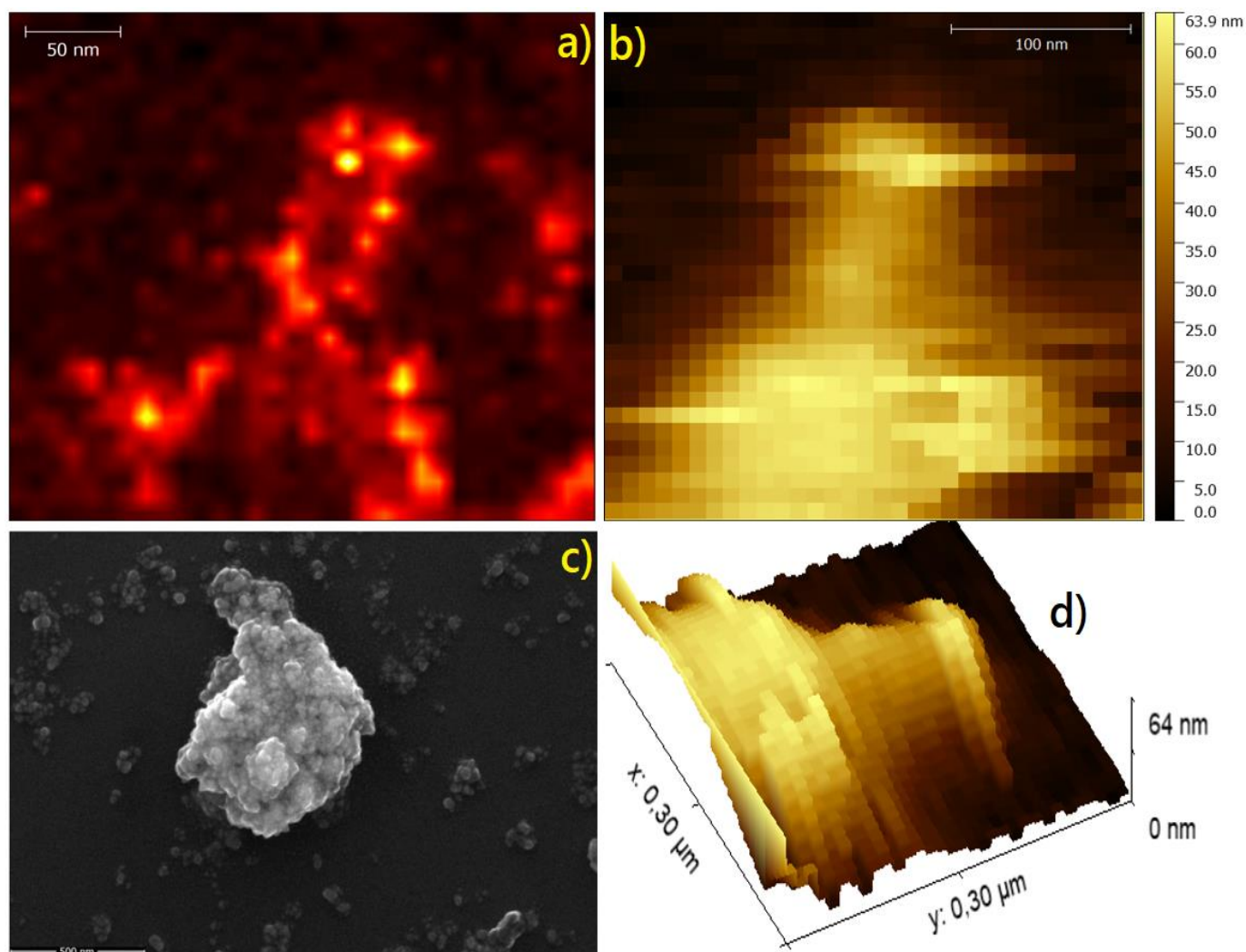
Figure 6.15. Rg-AgNPs sample. a) **$1600\ cm^{-1}$** *TERS image, b) the AFM image associated; c) SEM imagethe and c) 3D-AFM image.*

Taking into account the system type under study, the Raman spectra obtained from the proteins were very stable in time and in the peaks positions, and more defined than those obtained by the SERS technique (time fluctuating signal). Subsequently, spectroscopic information was assigned regarding the topographic characteristics with their respective Raman signals. Since the spatial differentiation between different domains of composition is difficult to achieve only by topographic characteristics, the combination of morphology and spectral data allows a much more detailed characterization of the Rg- and Rm-AgNps, see Fig. 6.18 and 6.19 respectively. In these images, two points (A and B) were chosen where

isolated particle spectra could be obtained (a spectrum with the Au-tip before passing on the AgNPs, others when the Au-tip is on the AgNPS and another after the Au-tip passed on AgNPs).
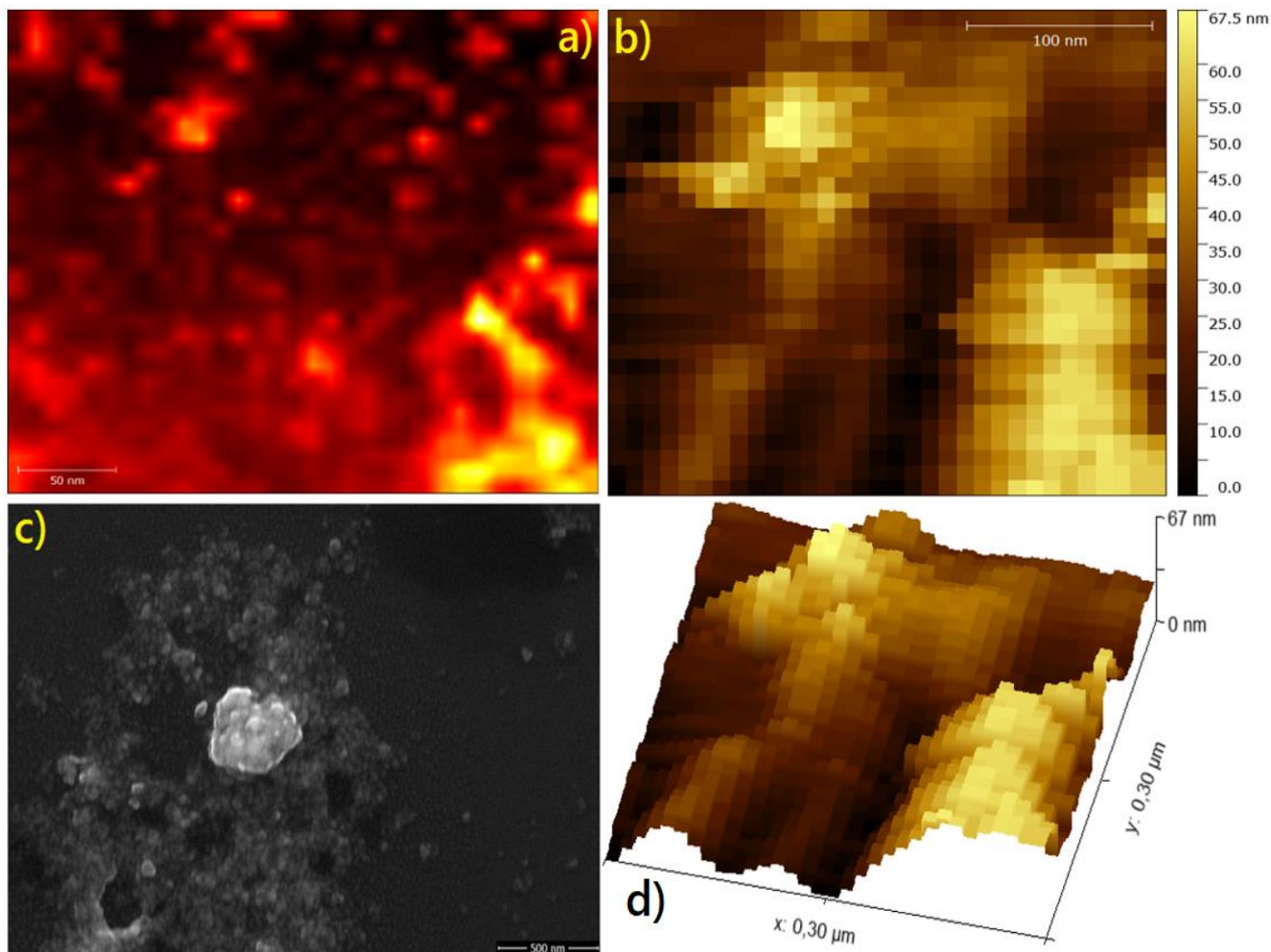
Figure 6.16. Rm-AgNPs sample. a) **$1600 \ cm^{-1}$** *TERS image, b) the AFM image associated; c) SEM imagethe and c) 3D-AFM image.*

A typical Raman spectrum of a protein is mainly composed of three main vibratory mode contributions, which originate from the skeleton of the polypeptide (amide bands) and from the side chains of aromatic and non-aromatic amino acid residues. The amide bands I, II and III arise from vibration in the plane of the peptide bond. The different vibration modes are responsible for each of these bands **[28, 31-36, 69]**; see Fig. 6.20.
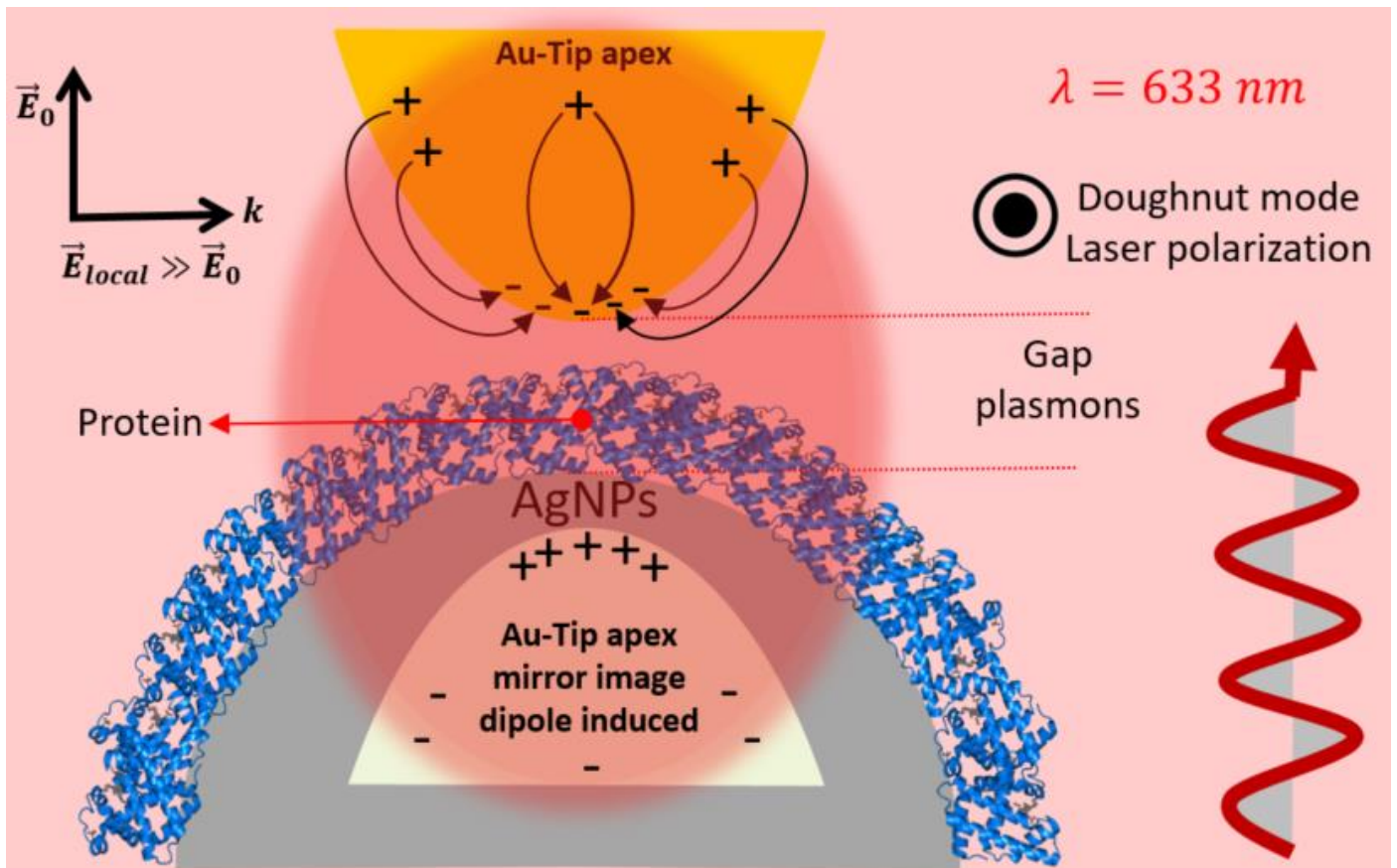
Figure 6.17. Schematic illustrating the process that generates the gap plasmons when the Au-tip interacts with Rm- and Rg-AgNPs.

By observing the results of the TERS measurements, the following general characteristic characteristics associated with the Raman intensities associated with the vibrations of the protein subgroups can be made. Stretch vibrations involving peptide bonds $C = O$ and $C - N$ are expected to produce high Raman intensities possibly due to the large polarization changes associated with their stretching vibrations. It can also be expected that there will be vibrations in the plane of the rings of the aromatic side chains of the amino acids Trp, Tyr, Phe and Raman bands of high intensity can be produced. Stretching the vibrations of the $C - C$, $C - N$ and $CO - O$ bonds can produce intense Raman bands, especially if they involve concerted symmetrical shifts of the side chain skeletons. It may also happen that the deformations of the ring outside the main plane of the

bonds and the bending movements of the exocyclic substituents are usually weak in the Raman spectra of proteins **[28, 31-36, 69]**.

The Raman bands associated with the flexion and stretching modes of the individual hydrogenic substituents $C-H$, $N-H$ and $O-H$ are generally weak, but their collective spectral intensities, which result from the large number of such clusters in a protein, It can be high. Vibrations involving the displacement of heavy atoms such as sulfur in the CS stretch modes of Met and Cys, and the SS stretch of cystine, SH stretch of cysteine and stretch in metalloproteins are expected to be relatively intense **[28, 31-36, 69]**.

In general, we can take a small part of one peptide bond and describe this as linking two amino acids, and the two adjacent $C-C$ and $N-C$ bonds. The peptide bond itself is basically fixed geometrically, as the $C-N$ bond has partial double bond character and, therefore, the peptide group, i.e., $OC-NH$, is essentially planar. It usually exhibits a *trans* geometry, i.e., the oxygen and hydrogen are in *trans* positions in the peptide bond **[28, 31-36, 69]**.

In Fig. 6.21, a section of a backbone structure is shown. Because the peptide bond geometry is fixed, variations in the geometry can only be achieved by variations in the dihedral angles ϕ and ψ. Taking into account the steric hindrance as a constraint, basic structures can be derived: the right-handed α−helix, the β−sheet structure, and the unordered or random coil structure. These are the secondary structural elements, which can be addressed by vibrational spectroscopy **[28, 31-36, 69]**.

From the all Raman spectrum obtained, we can identify the most significant peaks that are listed in the Tables 6.3 and Table 6.4 for the Rg- and Rm-AgNps respectively. In black are the found peaks in common by the SERS and TERS techniques, in blue have a new Amida III´ region that was found more frequently by the TERS technique than in SERS technique and in red a peak that was only found by the technique TERS, The shift to high frequencies of the $S - S$ stretching band is induced by a trans $C_\alpha - S$ conformational and possible $S - S$ TGT Cys-amino acid **[28, 31-36, 69]**.

It should be noted that the system used to perfomance TERS measutement was of the type so-called 'non-gap mode', designed to use an Au-tip probe in contact with a dielectric substrate. However, due to the type of sample analyzed here, at the time of taking the measurements there is an interaction sandwich Autip-protein-AgNPs that by contrast is the case when an Au-tip probe is in contact with a metallic substrate, so called 'gap mode', see Fig. 6.17.

To conclude the discussion about the TERS measures, it is important to point out that in order to satisfactorily carry out this type of measurement we need to have very transparent samples (or at least as transparent as possible) because the system used is an inverted microscope . This is one more reason to be careful in the preparation of the sample.
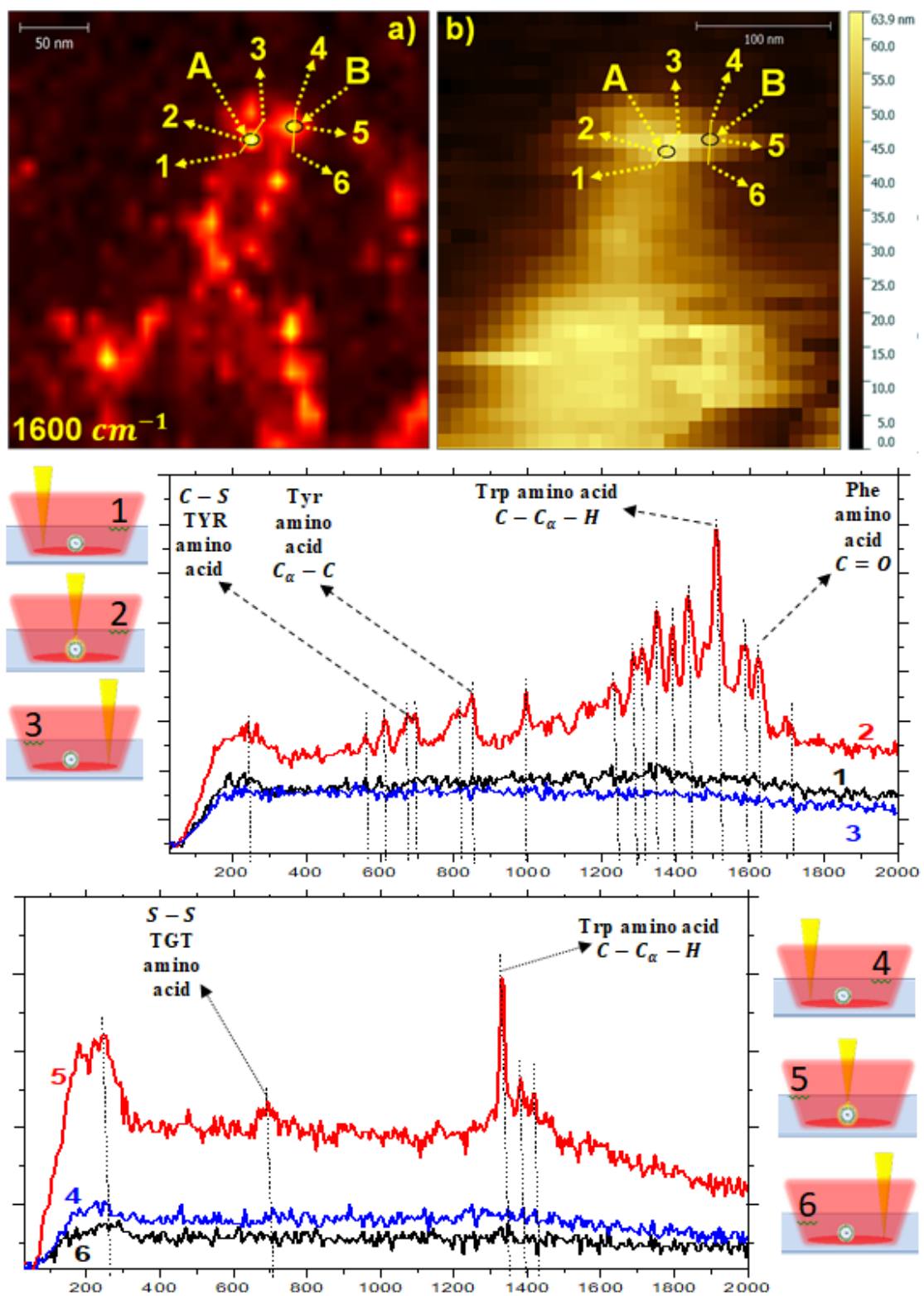
Figure 6.18. Rg-AgNPs Raman spectrum obtained at two points; A point (1, 2, 3) and B point (4, 5, 6).
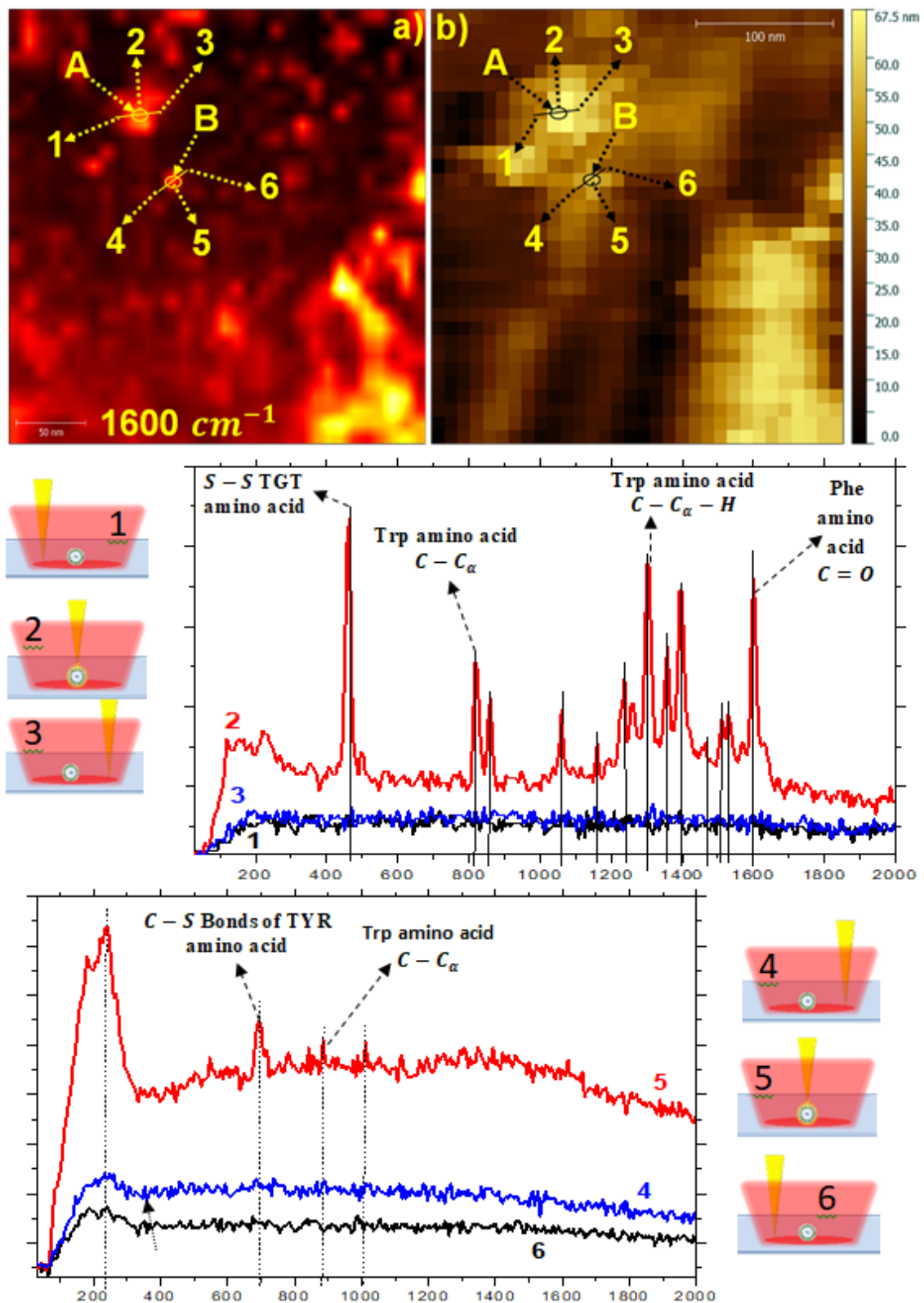
Figure 6.19. Rm-AgNPs Raman spectrum obtained at two points; A point (1, 2, 3) and B point (4, 5, 6).
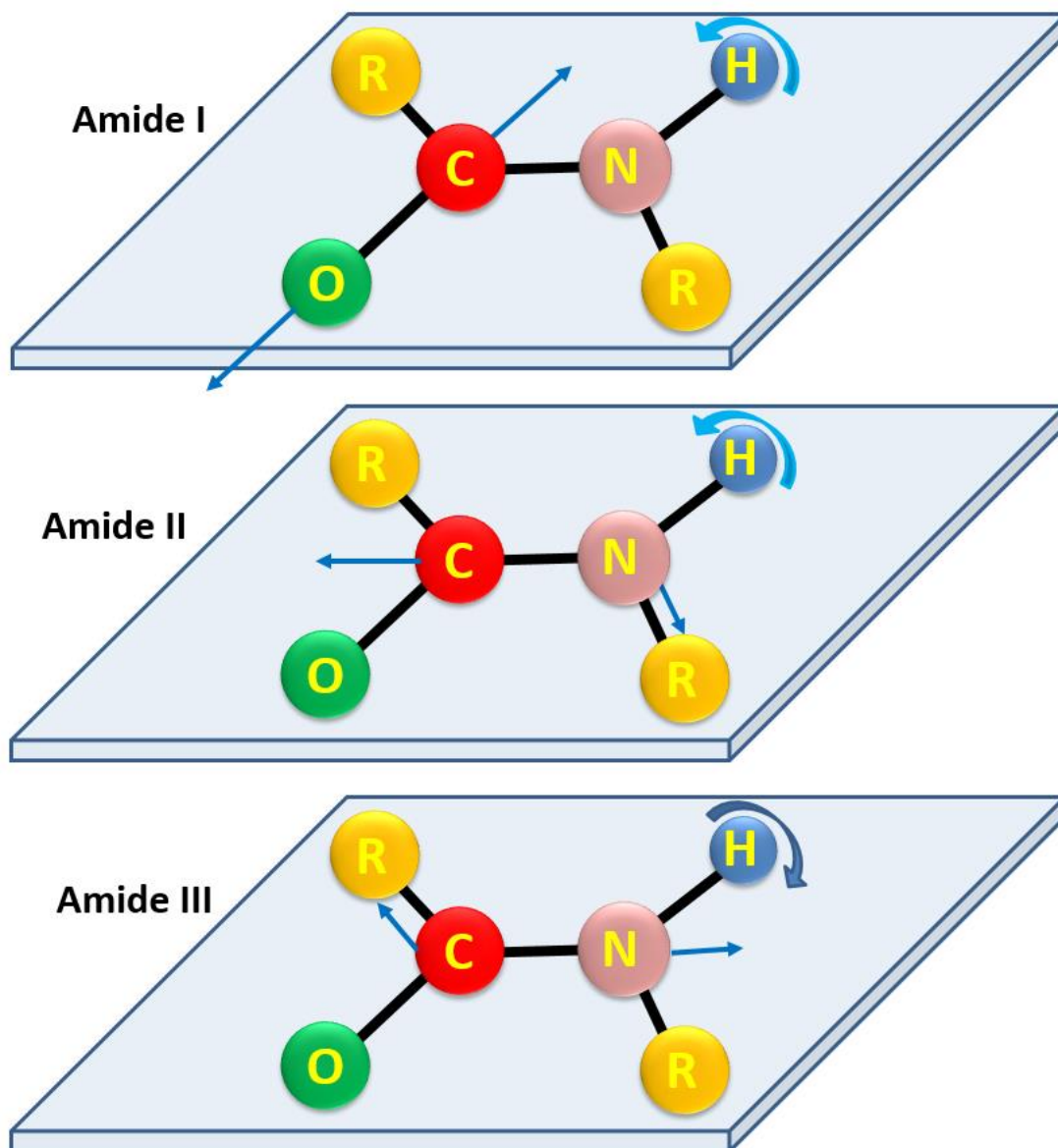
Figure 6.20. The in-plane vibrational modes of the peptide bond. Among the three modes shown in the figure, the amide I and III bands in the Raman spectra are indices of the peptide-backbone conformation of a protein. The amide II mode is either Raman inactive or very weak **[36]**.
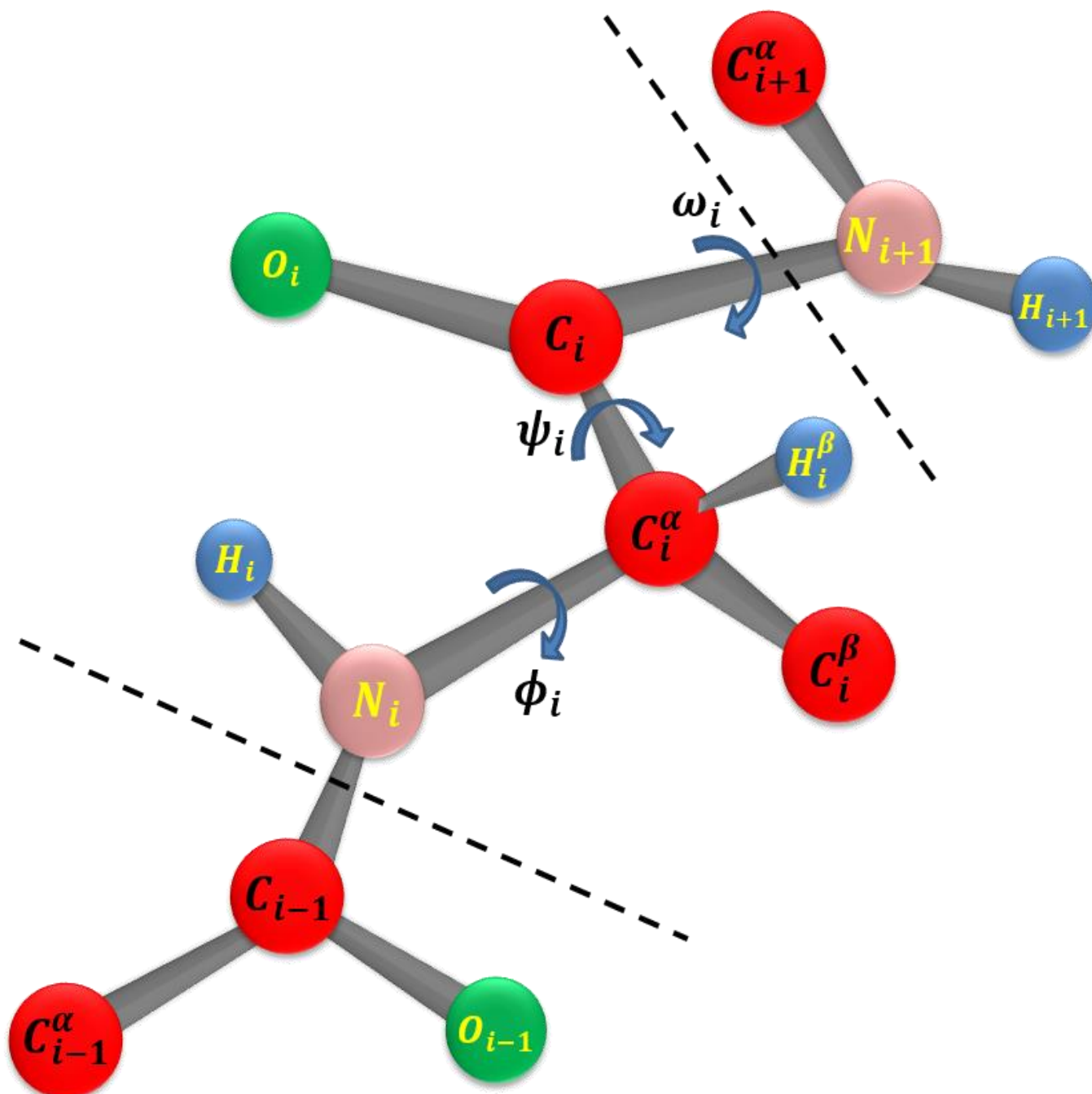
Figure 6.21. Short stretch of a peptide chain indicating the peptide bonds and the dihedral angles ϕ *and* ψ*.* ω *Is the angle of the peptide bond, which is* 180° *or* 0° *for the trans- and cis-peptide geometries* **[28, 33, 36]***.*

Table 6.3. Tentative assignment of protein contributed TERS spectra of Rg-AgNPs.

R. glutinis	Assignment*	Protein or component (*)
α −helix Amide I β −sheet	~1700 cm^{-1} **Originates from the peptide ESTER bond**	**ESTER is a chemical compound derived from an acid (organic or inorganic) in which at least one −OH (hydroxyl) group is replaced by an −O−alkyl (alkoxy) group.**
	~1650 cm^{-1} $C = O$ **Stretches the vibration, generally appears at a frequency close to the neighborhood of this frequency peak.**	**Tyr, Trp, Phe amino acid.**
	~1615 cm^{-1} $C = O$ **Stretching vibrations mode of** $COOH$.	**PROLINE is a protein-genic amino acid generated in protein biosynthesis.**
Amide II	~1589 cm^{-1} ~1504 cm^{-1}	**Try, Trp (band frequency), Chy and Ala amino acid. has been correlated to the dihedral angle between the indole ring and the peptide bond plane; Sensitive to W orientation and cation −π interaction**
Amide II	~1436 cm^{-1} CH_2 **Stretching**	**Phe amino acid.**
Amide II	~1392 cm^{-1} CO_2 **Stretching**	**Ala amino acid.**
Amide III′ α −helix	~1344 cm^{-1} ~1307 cm^{-1} $C − C_\alpha − H$ **Stretching and** $N − H$ **bend**	**Tryptophan doublet, Trp amino acid.**
Amide III β −sheet	~1280 cm^{-1} ~1220 cm^{-1} $N − H$ **and** $N − H$ **bend**	**Phe, Ala, Glu amino acid.**
Amide III′ Skeleton α −helix	~1002 cm^{-1} ~992 cm^{-1} $N − C_\alpha − H$	**Phe, The phenylalanine bands are overwhelmed by the Trp and Tyr bands as their Raman cross sections are almost 10 times stronger than those of Phe.**
β −sheet	~884 cm^{-1} ~842 cm^{-1} $C − N$ **deflection**	**Tyrosine doublet, Trp.**
Amide IV	~780 cm^{-1} $C_\alpha − C$ **stretching**	**Carbonyl in-plane bending motion, Cation−π Interaction.**
Amide IV	~672 cm^{-1} ~612 cm^{-1} OCN **bending**	**Phenylalanine**
Amide VII	~220 cm^{-1}	**Stretching** $Ag − O$, **Silver oxide**
Amide VII	~200 cm^{-1}	**Skeletal mode** α −helix **and** β −sheet
*Refs. [28, 31-36, 69, 74-79, 85-94].		

Table 6.4. Tentative assignment of protein contributed TERS spectra of Rm-AgNPs.

R. mucilaginosa	Assignment*	Protein or component (*)
α −helix Amide I β −sheet	~1630 cm^{-1} ~1600 cm^{-1} $C = O$ Stretches the vibration, Stretching vibrations mode of $COOH$	Tyr, Trp, Phe amino acid. PROLINE is a protein-genic amino acid generated in protein biosynthesis.
Amide II	~1568 cm^{-1} ~1532 cm^{-1} ~1508 cm^{-1}	Try, Trp, Chy and Ala amino acid. has been correlated to the dihedral angle between the indole ring and the peptide bond plane; Sensitive to W orientation and cation − π interaction
Amide II	~1466 cm^{-1} CH_2 Stretching	Phe amino acid.
Amide II	~1394 cm^{-1} ~1356 cm^{-1} ~1300 cm^{-1} CO_2 Stretching	Ala amino acid.
Amide III′ α −helix	~1344 cm^{-1} ~1307 cm^{-1} $C − C_\alpha − H$ Stretching and $N−H$ bend	Tryptophan doublet, Trp amino acid.
Amide III β −sheet	~1258 cm^{-1} ~123 cm^{-1} ~1158 cm^{-1} $N−H$ and $N−H$ bend	Phe, Ala, Glu amino acid.
Amide III′ Skeleton α −helix	~1060 cm^{-1} ~1008 cm^{-1} $N − C_\alpha − H$	Phe, The phenylalanine bands are overwhelmed by the Trp and Tyr bands as their Raman cross sections are almost 10 times stronger than those of Phe.
β −sheet	~884 cm^{-1} ~862 cm^{-1} ~840 cm^{-1} ~817 cm^{-1} $C−N$ deflection	Tyrosine doublet, Trp.
Amide IV	~777 cm^{-1} $C_\alpha − C$ stretching	Carbonyl in-plane bending motion, Cation−π Interaction.
Amide IV	~691 cm^{-1} OCN bending	Phenylalanine
Amide VI	~543 cm^{-1}, ~500 cm^{-1} $S − S$ stretching and ~466 cm^{-1} out-of-plane $C = O$ bending	The shift to high frequencies of the $S−S$ stretching band is induced by a *trans* $C_\alpha − S$ conformational and possible $S − S$ TGT Cys-amino acid.
Amide VII	~220 cm^{-1}	Stretching $Ag − O$, Silver oxide
Amide VII	~200 cm^{-1}	Skeletal mode α −helix and β −sheet
*Refs. [28, 31-36, 69, 74-79, 85-94].		

7. CONCLUSIONS

In this contribution, silver nanoparticles encapsulated by a protein-capping layer were studied by SEM, AFM and optical spectroscopy techniques. These nanoparticles were produced by two fungi: R. glutinis and R. mucilaginosa. AFM phase-image allowed the estimation of the protein-capping layer width to 21 nm (R. glutinis) and 24 nm (R. mucilaginosa). The enhanced Raman spectra obtained are very unstable in the SERS measurements, indicating that the structural conformation of the protein involving the silver core is affected by the laser and/or by the enhanced fields from the silver core. The results presented here allowed the identification of α−helix, β−sheet and protein mixed structures. The protein-silver interaction seems to happen through the amine group. Raman spectroscopic signatures of this group could be identified for most particles. Dark-field measurements showed that not only the protein structure is affected by the laser, but also the silver metallic core, contributing to the instabilities found in the Raman spectra, temporal fluctuations. Our results are important for defining the proper applications of biogenic nanoparticles and their limitations. On the other hand, the TERS measurements were stable.

The Tip-Enhanced Raman Scattering has been successfully applied to AgNPs study synthesized by fungi, in AgNPs isolated and in small agglomerate. The enhanced Raman spectra obtained were stable, more than the SERS enhanced, indicating that the structural conformations of the protein involving the silver core just is affected by plasmons generated between Au-tip and Ag-nucleus, gap plasmons. The results presented here allowed the identification of α−helix, β−sheet and protein mixed structures. The protein Au-tip interaction seems to happen through the amine group. The enhanced Raman spectroscopy, SERS and TERS, are a

powerful tool for structural characterization of proteins and detect the main constituent amino acids. Together with the techniques of AFM and SEM, enhanced Raman spectroscopy is a powerful spectroscopic approach to the structural characterization of biological material on the nanoscale. These findings can help to make viable the applications of SERS and TERS techniques in the diseases detection, substances and new medications associated with protein folding.

It was demonstrated that the TERS technique can be used to correctly detect and characterize biological material of only a few protein quantity, quantity molecules, nanometers; Although informations TERS vibrational data obtained from protein samples can be very complex (which generally are), carefully considered data processing steps can reveal useful information. The studies carried out here on the Rm- and Rg-AgNPs and in general, for any biological type material, a very good preparation is needed to facilitate good characterization and data collection, and this is one of the limitations in the TERS technique. These problems apply especially to measurements recorded under native conditions. As TERS is a surface sensitive technique, materials such as cells or tissues, or that tend to agglomerate a lot, must be pretreated so that the internal compartments are accessible without interference from the embedding media or deposition.

The results obtained here show once again that TERS is a technique with a sub-nanometric spatial resolution, with more and more promising applications; However, there are still unresolved questions about how to improve AFM images made in hyperspectros, how to perform hyperspectros in larger areas and with prolonged measurement times without losing alignment, to use other metal tip types. However, the ability to probe-scanning and to do images individual molecules and address how

the spatial context of the molecule affects chemical behavior seems to be within the scope of the feasible. The field is expected to see an increase in publications that use nanoscale spectroscopic images in the coming years.

TERS has demonstrated its applicability to the characterization of proteins and potential use to other types of biological systems. With the measurements obtained here, it proved to be especially useful for providing important information on nanobiological samples. Its applicability in biology or, what is more interesting, in the biomedical field.

The study of molecules (especially proteins or amino acids in amorphous or crystalline state) is not an easy task. His Raman spectra are complex and often difficult to interpret. Some of the difficulties can also be overcome by improving Raman spectrometers and measurements, by thorough preparation of the sample before measurement. Although the theoretical description of the light scattered by a molecule located in the gap between a substrate and a tip is not fully achieved, TERS allowed the nanometric scale description of the Rg- and Rm-AgNPs coated with proteins satisfactorily.

TERS show structural information can be derived from specific Raman vibrating bands, the Rg- and Rm-AgNPs, both, tend to give Raman response in the amide I, amide II and amide III bands, but only Rm-AgNP presents in the amine band VI, sulfide, which was absent in Rg-AgNPs; this band is associated with the stretching of the S-S sulfur bridge, stretching band is induced by a trans C_α-S conformational. The other Raman peaks are shared almost together Rg- and Rm-AgNPs.

8. REFERENCES

[1] Hulkoti, N. I.; Taranath, T. C. Biosynthesis of nanoparticles using microbes-A review. Colloids Surf., B 2014, 121, 474-483.

[2] Gour, A.; Jain, N. K. Advances in green synthesis of nanoparticles. Artif. Cells, Nanomed., Biotechnol. 2019, 47, 844-851.

[3] Erdogan, O.; Abbak, M.; Demirbolat, G. M.; BirtekocakI, F.; AkselI, M.; Salih, P.; CevikI, O. Green synthesis of silver nanoparticles via Cynara scolymus leaf extracts: The characterization, anticancer potential with photodynamic therapy in MCF7 cells. PLoS One 2019, 14, No. e0216496.

[4] Ahluwalia, V.; Kumar, J.; Sisodia, R.; Shakil, N. A.; Walia, S. S. Green synthesis of silver nanoparticles by Trichoderma harzianum and their bio-efficacy evaluation against Staphylococcus aureus and Klebsiella pneumonia. Ind. Crops Prod. 2014, 55, 202-206.

[5] Cutzu, R.; Coi, A.; Rosso, F.; Bardi, L.; Ciani, M.; Budroni, M.; Zara, G.; Zara, S.; Mannazzu, I. From crude glycerol to carotenoids by using a Rhodotorula glutinis mutant. World J. Microbiol. Biotechnol. 2013, 29, 1009-1017.

[6] Hernandez-Almanza, A.; Montañez, J. C.; Aguilar-Gonzalez, M. A.; Martínez-Avila, C.; Rodriguez-Herrera, R.; Aguilar, C. N. Rhodotorula glutinis as source of pigments and metabolites for food industry. Food Biosci. 2014, 5, 64-72.

[7] Da Silva, J.; Da Silva, F. L. H.; Santos, S. F. M.; Ribeiro, J. E. S.; De Medeiros, L. L.; Ferreira, A. L. O. Biomass and lipid production by the yeast Rhodotorula mucilaginosa using cassava wastewater as the subtrate. Braz. J. Food Technol. 2018, 21, No. e2017145.

[8] Behravan, M.; Panahi, A. H.; Naghizadeh, A.; Ziaee, M.; Mahdavi, R.; Mirzapour, A. Facile green synthesis of silver nanoparticles using Berberis vulgaris leaf and root aqueous extract and its antibacterial activity. Int. J. Biol. Macromol. 2019, 124, 148-154.

[9] Femi-Adepoju, A. G.; Dada, A. O.; Otum, K. O.; Adepoju, A. O.; Fatoba, O. P. Green synthesis of silver nanoparticles using terrestrial fern [Gleichenia pectinata [Willd.] C. Presl.]: characterization and antimicrobial studies. Heliyon 2019, 5, No. e01543.

[10] Mallmann, E. J. J.; Cunha, F. A.; Castro, B. N. F.; Maciel, A. M.; Menezes, E. A.; Fechine, P. B. A. Antifungal activity of silver nanoparticles obtained by green synthesis. Rev. Inst. Med. Trop. Sao Paulo 2015, 57, 165-167.

[11] Cunha, F. A.; Maia, K. R.; Mallman, E. J. J.; Cunha, M. C. S. O.; Maciel, A. A. M.; Sousa, I. P.; Menezes, E. A.; Fechine, P. B. A. Silver nanoparticles-disk diffusion test against Escherichia coli isolates. Rev. Inst. Med. Trop. Sao Paulo 2016, 58, 73.

[12] Sousa, F. A.; Noronha, V. T.; Machado, T. F.; Silveira, J. V.; Cunha, F. A.; Fechine, P. B. A.; Paula, A. J. Silver nanocoatings at large length scales: Influence of the AgNPs morphology and capping agents on the coating chemical stability and antimicrobial effect. J. Braz. Chem. Soc. 2017, 28, 1639-1649.

[13] Noronha, V. T.; Sousa, F. A.; Souza Filho, A. G.; Silva, C. A.; Cunha, F. A.; Koo, H.; Fechine, P. B. A.; Paula, A. J. Influence of Surface Silanization on the Physicochemical Stability of Silver Nanocoatings: A Large Length Scale Assessment. J. Phys. Chem. C 2017, 121, 11300-11311.

[14] Cunha, F. A.; Cunha, M. C. S. O.; Frota, S. M.; Mallman, E. J. J.; Freire, T. M.; Costa, Ls.; Paula, A. J.; Menezes, E. A.; Fechine, P. B. A. Biogenic synthesis of multifunctional silver nanoparticles from Rhodotorula glutinis and Rhodotorula mucilaginosa: antifungal, catalytic and cytotoxicity activities. World J. Microbiol. Biotechnol. 2018, 34, 127.

[15] Ishida, k.; Cipriano, T. F.; Rocha, G. M.; Weissmuller, G.; Gomes, F.; Miranda, K.; Rozental, S. Silver nanoparticle production by the fungus Fusarium oxysporum: Nanoparticle characterisation and analysis of antifungal activity against pathogenic yeasts. Mem. Inst. Oswaldo Cruz 2014, 109, 220-228.

[16] Amit Kessel and Nir Ben-Tal. Introduction to proteins structure, function, and motion-CRC Press [2011].

[17] Katherine A.Willets and Richard P. Van Duyne; Localized Surface Plasmon Resonance Spectroscopy and Sensing. Reviews in Advance 2006,308.

[18] https://nanocomposix.eu/pages/silver-nanoparticles-optical-properties

[19] Zachary D. Schultz, James M. Marr and Hao Wang. Tip enhanced Raman scattering: plasmonic enhancements for nanoscale chemical analysis. Nanophotonics 2014; 3(1-2): 91–104.

[20] Eleonora Petryayeva, Ulrich J. Krull. Localized surface plasmon resonance: Nanostructures, bioassays and biosensing—A review. Analytica Chimica Acta 706 (2011) 8– 24.

[21] Mehdi Asghari-Khiavi, Bayden R. Wood, Pejman Hojati-Talemi, Andrew Downes, Don McNaughton and Adam Mechler. Exploring the origin of tip-enhanced Raman scattering; preparation of efficient TERS probes with high yield. J. Raman Spectrosc. 2012, 43, 173–180.

[22] Sebastian Thomas, Georg Wachter, Christoph Lemell, Joachim Burgdörfer and Peter Hommelhoff. Large optical field enhancement for nanotips with large opening angles. New J. Phys. 17 (2015) 063010.

[23] Suljo Linic, Phillip Christopher and David B. Ingram. Plasmonic-metal nanostructures for efficient conversion of solar to chemical energy. NATURE MATERIALS | VOL 10 | DECEMBER 2011.

[24] Jia Wang, Xiaobin Wu, Rui Wang and Mingqian Zhang. Detection of Carbon Nanotubes Using Tip- Enhanced Raman Spectroscopy. DOI: 10.5772/17325 · Source: InTech.

[25] Zayats A., Richards D. Nano-Optics and Near-Field Optical Microscopy-Artech House (2008).

[26] Satoshi Kawata, Vladimir M. Shalaev-Tip Enhancement (Advances in Nano-Optics and Nano-Photonics)-Elsevier Science (2007).

[27] Hongxing Xu – Nanophotonics Manipulating Light with Plasmons-Pan Stanford Publishing (2018).

[28] Marc Lamy de la Chapelle and Annemarie Pucci - Nanoantenna-Plasmon-Enhanced Spectroscopies for Biotechnological Applications.

[29] Eric Le Ru, Pablo Etchegoin-Principles of Surface-Enhanced Raman Spectroscopy and related plasmonic effects-Elsevier (2009).

[30] Lukas Novotny, Bert Hecht-Principles of Nano-Optics-Cambridge University Press (2012).

[31] Shun-Lin Zhang - Raman Spectroscopy and its Application in Nanostructures.

[32] Marek Procházka - Surface-Enhanced Raman Spectroscopy Bioanalytical, Biomolecular and Medical Applications. Springer (2016).

[33] Marc Lamy de la Chapelle and Nathalie Lidgi-Guigui - Handbook of Enhanced Spectroscopy.

[34] Stefan Alexander Maier - Plasmonics Fundamentals and Applications (2007).

[35] Hans Frauenfelder, Shirley S. Chan, Winnie S. Chan - The Physics of Proteins.

[36] Anthony T. Tu - Raman spectroscopy in biology, principles and applications.

[37] Sebastian Schluecker - Surface Enhanced Raman Spectroscopy.

[38] Hartschuh, A - Tip-Enhanced Near-Field Optical Microscopy. Angew. Chem. Int. Ed. 2008, 47, 8178 – 8191.

[39] S. Challa, S. R. Kumar-Raman spectroscopy for nanomaterials characterization-Springer (2012).

[40] Chang RK, Furtak TE (eds) (1981) Surface enhanced Raman scattering. Plenum, New York.

[41] Nie S, Emory SR (1997) Probing single molecules and single nanoparticles by surface-enhanced Raman scattering. Science 275:1102.

[42] Kneipp K, Wang Y, Kneipp H, Perelman LT, Itzkan I, Dasari RR, Feld MS (1997) Single molecule detection using surface-enhanced Raman scattering (SERS). Phys Rev Lett 78:1667.

[43] De Fornel F (2001) Evanescent waves from Newtonian optics to atomic optics. Springer, Berlin.

[44] Inouye Y, Kawata S (1994) Near-field scanning optical microscope with a metallic probe tip. Opt Lett 19:159

[45] Bachelot R, Gleyzes P, Boccara AC (1995) Near-field optical microscope based on local perturbation of a diffraction spot. Opt Lett 20:1924.

[46] E. Abbe, "Beitrage zur Theorie der Microscopie und der Microscopischen Wahrnehmung". Arch. Mikrosk. Anat. 9, 413-468 (1873).

[47] Lord Rayleigh, "On the theory of optical images with special reference to the microscope". Philos. Mag. 5, 167-195 (1896).

[48] Born M, Wolf E. (1999) Principles of optics, 7th edn. Cambridge University Press, Cambridge.

[49] Goodman JW (1996) Introduction to Fourier optics. McGraw-Hill, New York.

[50] Wessel J,. Surface-enhanced optical microscopy. J Opt Soc Am B 2:1538. 1985.

[51] Inouye Y, Hayazawa N, Hayashi K, Sekkat Z, Kawata S (1999) Near-field scanning optical microscope using a metallized cantilever tip for nanospectroscopy. Proc SPIE 3791:40.

[52] Zhang W, Yeo BS, Schmid T, Zenobi R (2007) Single molecule tip-enhanced Raman spectroscopy with silver tips. J Phys Chem C 111:1733.

[53] Hartschuh A, Sánchez EJ, Xie XS, Novotny L (2003) High-resolution near-field Raman microscopy of single-walled carbon nanotubes. Phys Rev Lett 90:095503.

[54] CANÇADO, L. G.; HARTSCHUH, A.; NOVOTNY, L. Tip-enhanced Raman spectroscopy of carbon nanotubes. *Journal of Raman Spectroscopy*, Wiley Online Library, v. 40, n. 10, p. 1420–1426, 2009.

[55] Alexandre R. Paschoal. A microscopia Raman de alta resolução e suas aplicações na ciencia dos materiais. Phd thesis, 2011.

[56] Samuel Berweger and Prof. Markus Raschke – Department of Physics, Department of Chemistry, and JILA, University of Colorado at Boulder. Princeton Instruments, Inc. All rights reserved.

[57] Friedrich Siebert, Peter Hildebrandt - Vibrational Spectroscopy in Life Science-Wiley-VCH, 2007.

[58] Amerasan, D.; Nataraj, T.; Murugan, K.; Panneerselvam, C.; Madhiyazhagan, P.; Nicoletti, M.; Benelli, G. Myco-synthesis of silver nanoparticles using Metarhizium anisopliae against the rural malaria vector Anopheles culicifacies Giles (Diptera: Culicidae). J. Pest Sci. 2016, 89, 249−256.

[59] Apte, M.; Girme, G.; Bankar, A.; Ravikumar, A.; Zinjarde, S. 3, 4-dihydroxy-L-phenylalanine-derived melanin from Yarrowia lipolytica mediates the synthesis of silver and gold nanostructures. J. Nanobiotechnol. 2013, 11, 2.

[60] Banu, A.; Rathod, V.; Ranganath, E. Silver nanoparticle production by Rhizopus stolonifer and its antibacterial activity against extended spectrum-lactamase producing (ESBL) strains of Enterobacteriaceae. Mater. Res. Bull. 2011, 46, 1417−1423.

[61] Shameli, K.; Bin Ahmad, M.; Zamanian, A.; Sangpour, P.; Shabanzadeh, P.; Abdollahi, Y.; Zargar, M. Green biosynthesis of silver nanoparticles using Curcuma longa tuber powder. Int. J. Nanomed. 2012, 7, 5603−5610.

[62] Navin Jain, Arpit Bhargava, Sonali Majumdar, J. C. Tarafdar and Jitendra Panwar. Extracellular biosynthesis and characterization of silver nanoparticles usingAspergillus flavusNJP08: A mechanism perspective. Nanoscale, 2011,3, 635–641 | 635.

[63] Varahalarao Vadlapudi, Ramars Amanchy. Phytofabrication of silver nanoparticles using Myriostachya wightiana as a novel bioresource, and evaluation of their biological activities. Braz. Arch. Biol. Technol. v.60: e17160295 Jan/Dec 2017.

[64] Lomelí-Marroquín, D.; Medina Cruz, D.; Nieto-Argüello, A.; Crua Vernet, A.; Chen, J.; Torres-Castro, A.; Webster, T. J.; CholulaDíaz, J. L. Starch-mediated synthesis of mono- and bimetallic silver/gold nanoparticles as antimicrobial and anticancer agents. Int. J. Nanomed. 2019, 14, 2171-2190.

[65] Vigneshwaran, N.; Ashtaputre, N. M.; Varadarajan, V. P.; Nachane, R. P.; Paralikar, K. M.; Balasubramanya, R. H. Biological synthesis of silver nanoparticles using the fungus Aspergillus flavus. Mater. Lett. 2007, 61, 1413-1418.

[66] Zhang, A.; Zhang, J.; Fang, Y. Photoluminescence from colloidal silver nanoparticles. J. Lumin. 2008, 128, 1635-1640.

[67] Zhao, Y.; Jiang, Y.; Fang, Y. Spectroscopy property of Ag nanoparticles. Spectrochim. Acta, Part A 2006, 65, 1003-1006.

[68] Feliu, N.; Hassan, M.; Garcia Rico, E.; Cui, D.; Parak, W.; Alvarez-Puebla, R. SERS quantification and characterization of proteins and other biomolecules. Langmuir 2017, 33, 9711-9730.

[69] Rygula, A.; Majzner, K.; Marzec, K. M.; Kaczor, A.; Pilarczyk, M.; Baranska, M. Raman spectroscopy of proteins: A review. J. Raman Spectrosc. 2013, 44, 1061-1076 2013.

[70] Liu-Bin, Z.; Huang, R.; Mu-Xing, B.; De-Yin, W.; Zhong-Qun, T. Effect of Aromatic Amine-Metal Interaction on Surface Vibrational Raman Spectroscopy of Adsorbed Molecules Investigated by Density functional Theory. J. Phys. Chem. C 2011, 115, 4174-4183.

[71] Sanghi, R.; Verma, P. Biomimetic synthesis and characterisation of protein capped silver nanoparticles. Bioresour. Technol. 2009, 100, 501-504.

[72] Naik, R. R.; Stringer, S. J.; Agarwal, G.; Jones, S. E.; Stone, M. O. Biomimetic synthesis and patterning of silver nanoparticles. Nat. Mater. 2002, 1, 169-172.

[73] Otto, A.; Futamata, M. Surface-Enhanced Raman Scattering Physics and Applications, 1st ed.; Kneipp, K.; Moskovits, M.; Kneipp, H., Eds.; Springer-Verlag: Berlin, 2006; pp 148-184.

[74] Schulz, H.; Baranska, M. Identification and quantification of valuable plant substances by IR and Raman spectroscopy. Vib. Spectrosc. 2007, 43, 13-25.

[75] Kitagawa, T.; Hirota, S. Raman Spectroscopy of Proteins. Handbook of Vibrational Spectroscopy, 1st ed.; Chalmers, J. M.; Griffiths, P. R., Eds.; John Wiley & Sons, Ltd, 2006; Vol. 5, pp 3426-3446.

[76] Tu, A. T. Raman Spectroscopy in Biology: Principles and Applications, 1st ed.; John Wiley & Sons, Ltd, 1982; pp 65-109.

[77] Kurouski, D.; Postiglione, T.; Deckert-Gaudig, T.; Deckert, V.; Lednev, I. K. Amide I vibrational mode suppression in surface [SERS] and tip [TERS] enhanced Raman spectra of protein specimens. Analyst 2013, 138, 1665-1673.

[78] Li-Jia, X.; Zong, C.; Xiao-Shan, Z.; Hu, P.; Jia-Min, F.; Ren, B. Label-free detection of native proteins by surface-enhanced Raman spectroscopy using iodide-modified nanoparticles. Anal. Chem. 2014, 86, 2238-2245.

[79] Prochazka, M.; Stepanek, J. Applications of Raman Spectroscopy to Biology: From Basic Studies to Disease Diagnosis [Advances in Biomedical Spectroscopy], 1st ed.; Ghomi, M., Ed.; IOS Press, 2012; pp 1-30.

[80] Hu, M.; Novo, C.; Funston, A.; Wang, H.; Staleva, H.; Zou, S.; Mulvaney, P.; Xia, Y.; Hartland, G. V. Dark-field microscopy studies of single metal nanoparticles: Understanding the factors that influence the linewidth of the localized surface plasmon resonance. J. Mater. Chem. 2008, 18, 1949-1960.

[81] Schultz, S.; Smith, D. R.; Mock, J. J.; Schultz, D. A. Single-target molecule detection with nonbleaching multicolor optical immunolabels. Proc. Natl. Acad. Sci. U.S.A. 2000, 97, 996-1001.

[83] César Rodrigues Fernandes. Espectroscopias Raman E Infravermelho Em Cristais De Aminoácidos: Os Casos Da L-Valina E Do Ácido L-Glutâmico. Ph.D. 2015.

[84] Cristiano Balbino Da Silva. Propriedades Estruturais E Vibracionais Dos Dipeptídeos. L-Alanil-L-Fenilalanina E L,L-Dileucina. Ph.D. 2019.

[85] Victoria L. Brewster, Lorna Ashton, and Royston Goodacre. Monitoring the Glycosylation Status of Proteins Using Raman Spectroscopy. Anal. Chem. 2011, 83, 6074–6081.

[86] David P. Cowcher, Tanja Deckert-Gaudig, Victoria L. Brewster, Lorna Ashton, Volker Deckert and Royston Goodacre. Detection of Protein Glycosylation Using Tip-Enhanced Raman Scattering. Anal. Chem. 2016, 88, 2105−2112.

[87] Dmitry Kurouski, Richard P. Van Duynea and Igor K. Lednevb. Exploring the structure and formation mechanism of amyloid fibrils by Raman spectroscopy: a review. DOI: 10.1039/c5an00342c.

[88] Stacey L. Carrier, Corey M. Kownacki, and Zachary D. Schultza. Protein-Ligand Binding Investigated by a Single Nanoparticle
TERS Approach. Chem Commun (Camb). 2011 February 21; 47(7): 2065–2067.

[89] Lifu Xiao and Zachary D Schultz. Spectroscopic Imaging at the Nanoscale: Technologies and Recent Applications. Anal Chem. 2018 January 02; 90(1): 440–458.

[90] Dmitry Kurouski, Thomas Postiglione, Tanja Deckert-Gaudig, Volker Deckert and Igor K. Lednev. Amide I vibrational mode suppression in surface (SERS) and tip (TERS) enhanced Raman spectra of protein specimens.

[91] Lizhen Gao, Huiling Zhao, Tianfeng Li, Peipei Huo, Dong Chen and Bo Liu. Atomic Force Microscopy Based Tip-Enhanced Raman Spectroscopy in Biology. Int. J. Mol. Sci. 2018, 19, 1193.

[92] C. FAGNANO, A. TORREGGIANI, and G. FINI. Raman Spectroscopic Studies of the Anhydrous Complexes of Avidin and Streptavidin With Biotin. Riospectroscopy, Vol. 2,225- 232, 1996.

[93] Tanja Deckert-Gaudig, Atsushi Taguchi, Satoshi Kawata and Volker Deckert. Tip-enhanced Raman spectroscopy – from early developments to recent advances. Chem. Soc. Rev., 2017, 46, 4077.

[94] J. L. Lippert, D. Tyminski, and P. J. Desmeules. Determination of the Secondary Structure of Proteins by Laser Raman Spectroscopy. Journal of the American Chemical Society / 98:22 / October 27, 1976.

[95] MAXIMIANO, R. V. *Espectroscopia de Campo-Próximo em Sistemas Bidimensionais*. Dissertação [Mestrado] — Departamento de Física da Universidade Federal de Minas Gerais, Belo Horizonte, Brasil, 2012.

[96] Zenhausern F, O'Boyle MP, Wickramasinghe HK [1994] Apertureless near-field optical microscope. Appl Phys Lett 65:1623.

[97] Tsai DP, Othonos A, Moskovits M, Uttamchandani D [1994] Raman spectroscopy using a fiber optic probe with subwavelength aperture. Appl Phys Lett 64:1768.

[98] Webster S, Bachelder DN, Smith DA [1998] Submicron resolution measurement of stress in silicon by near-field Raman spectroscopy. Appl Phys Lett 72:1478.

[99] 11. Raether H [1988] Surface plasmon polaritons on smooth and rough surfaces and on gratings. Springer, Berlin.

[100] Kawata S. [2001] Near-field optics and surface plasmon polaritons. Springer, New York.

[101] Challa S. S. R. Kumar Editor [2012] Raman Spectroscopy for Nanomaterials Characterization. Springer, New York.

[102] LAPSHIN, D. et al. Direct measurement of the absolute value of the interaction force between the fiber probe and the sample in a scanning near-field optical microscope. *Applied physics letters*, AIP Publishing, v. 81, n. 8, p. 1503–1505, 2002.

[103] KARRAI, K.; GROBER, R. D. Piezoelectric tip-sample distance control for near field optical microscopes. *Applied physics letters*, AIP Publishing, v. 66, n. 14, p. 1842–1844, 1995.

[104] SCHMIDT, J.; BERGANDER, H.; ENG, L. Experimental and theoretical analysis of shear–force interaction in the non-contact regime with 100 pn force resolution. *Applied surface science*, Elsevier, v. 157, n. 4, p. 295–301, 2000.

[105] Vasconcelos e Lorenço T. Desenvolvimento e estudo de sondas para microscopia óptica de campo próximo. Dissertação [Doutorado), Departamento de Física da Universidade Federal de Minas Gerais, Belo Horizonte, Brasil, 2016.

[106] Araújo Trinidade P. A. Study of the Electrostatic Shielding and Environmental Interactions in Carbon Nanotubes by Resonance Raman Spectroscopy. Dissertação [Doutorado) Departamento de Física da Universidade Federal de Minas Gerais, Belo Horizonte, Brasil, 2010. 8.

[107] Carstem Georgi S. Exciton Mobility and Localized Defects in Single Carbon Nanotubes Studied with Tip-Enhanced Near-Field Optical Microscopy. Dissertação [Doutorado) der Ludwig-Maximilians-Universität München, 2010.

[108] Huihong Qian. Tip-enhanced Near-Field Optical Spectroscopy on Single-Walled Carbon Nanotubes. Dissertação [Doutorado) der Ludwig-Maximilians-Universität München, 2008.

9. ANNEXED.
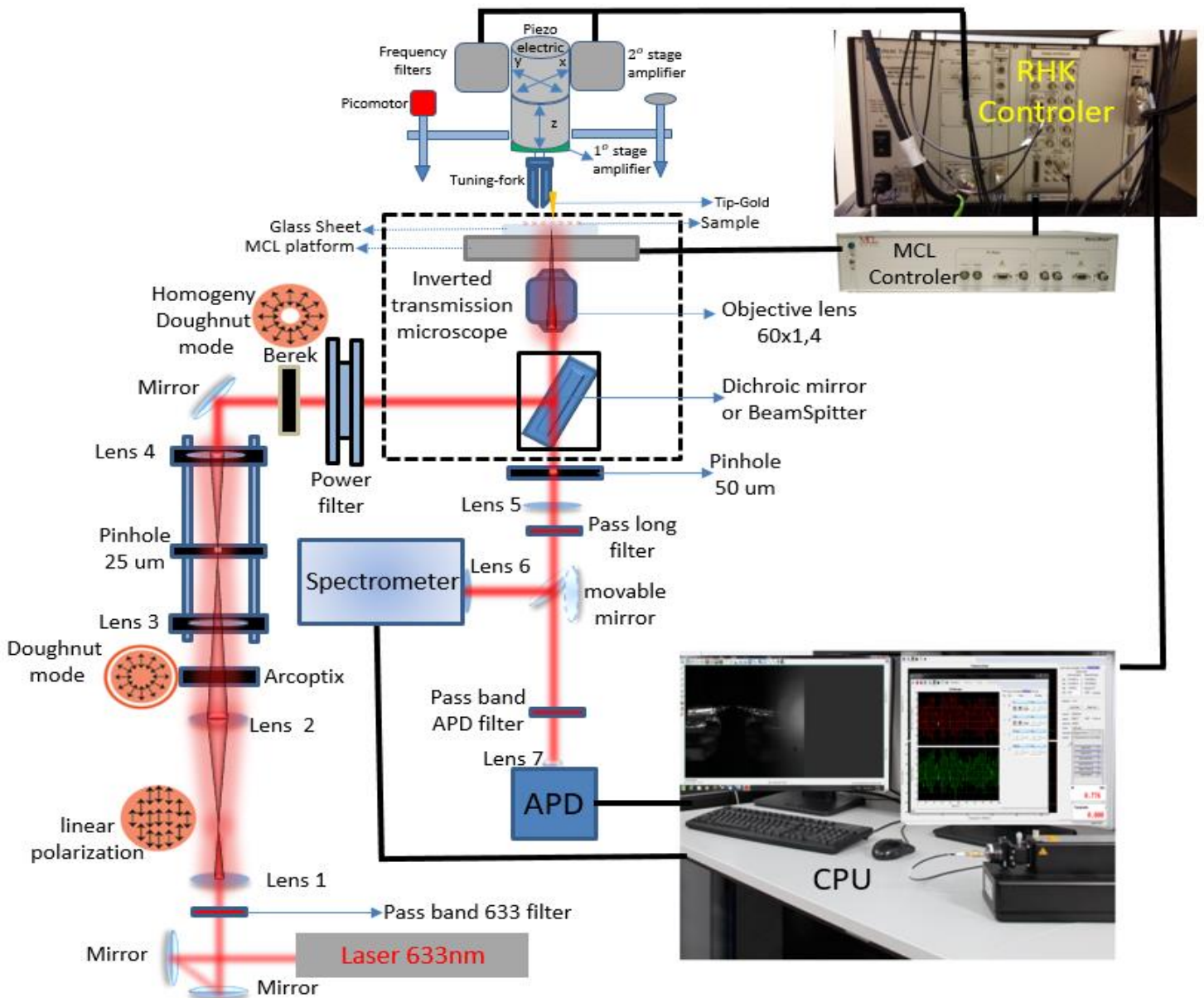
Support figure 1. TERS optical path system.

A) Non-Gap System Mode TERS.

A general schematic representation of the TERS experimental equipment used in the Physics Department of the Federal University of Ceará is illustrated in support Fig. 1. Below is a summary of the assembly. Basically, consists of an inverted microscope to which an atomic force microscopy scanning head is attached (more precisely an AFM shear-force mode) in which the light scattered from the microscope is directed to a

spectrometer coupled with a CCD or a photodetector (APD, Avalanche Photo-Diode type), with the option of use depending on the position of a moving mirror in the optical path at the exit of the microscope. At the beginning of the optical path, after emission by the laser, there is a bandpass filter and a set of lenses and mirrors that focus and direct the light beam to the entrance of the microscope, in addition to the ARCoptix devices and a Berek, which are responsible for controlling the polarization of the beam. Then, the beam enters the microscope, hits a dichroic mirror and is directed towards the objective lens. This same objective lens collects the light scattered by the sample and, immediately outside the microscope, there is a lens that collimates the beam again. Finally, there is a folding mirror whose function is to redirect the beam to the spectrometer or to the APD. The entire system discussed is controlled by the RHK R9 controller.

The equipment is completely insulated by means of a black MDF wooden box with internal metal plates and acoustic isolation sponges, outside of the box only the data cables, the power sources and the step head picomotor system AFM scan. The power supplies network of the laboratory equipment is very independent from the Physics Department power supplies network through a no-brake connected to an isolating transformer as safety devices and independent grounding. Finally, there is a dehumidifier and air conditioning working at all times to keep the laboratory at a stable temperature and free from moisture and dust that may affect the equipment's lenses, mirrors or electronic components.

The design and assembly of the equipment and all TERS components are as follows. Basically is a Raman spectroscopy system operating simultaneously with the AFM technique based on the lateral force feedback

system (shear-force feedback) through the use of a tuning fork to which an Au-tip is attached to one of its bottom legs.

One of the main lighting concepts of the TERS optical system is based on a Raman Confocal Micro-spectroscopy system, where the sample is illuminated with the use of an inverted microscope in transmission illumination mode, using a Nikon microscope model ECLIPSE- Ti-U. All optical components, microscope, spectrometer, CCD, APD, picomotor and the scanning head are on a pneumatic table with high stability. It is an optical table model 780 SeriesTop, developed by the company TMC Vibration Control with stainless steel precision plates under insulating pistons coupled to a gas system that keeps the table in constant vibration damping system.

Most of the TERS optical components and accessories were purchased from ThorLabs. The laser used is a HeNe with emission at a wavelength of $\lambda = 632.8$ nm, linearly polarized, Gaussian field profile and with 22 mW output power at the optical beginning path, In the laser begin beam emission, two mirrors are used to perfectly align the laser beam, just after that a line filter (632.8 nm, MaxLine R laser cleanup filter, Thorlabs) is introduced followed by the pair of lenses 1 and 2, (AC254-040-A and AC254-250-A, Thorlabs, see support Fig. 1) positioned one in the focus of the other next in order to expand the light beam. The first lens should have a shorter focal length, in such a way that it results in an increase in the diameter of the laser beam, given by the ratio between the focal distances, sufficient to obtain a diameter of approximately 10 mm after the beam expansion. The beam must always be well collimated after expansion. Continuing, the beam must pass through a polarization converter, manufactured by ARCoptix, which will convert linear

polarization into radial polarization, donut mode, support Fig. 2. Using the ARCoptix LC Driver software provided by the manufacturer, the parameters Output 1, fine adjustment 8.800 and in the item Output 2, fine adjustment, 1.860 are entered. Such parameters were found particularly for this TERS system described here according to the instructions in the ARCoptix manual.
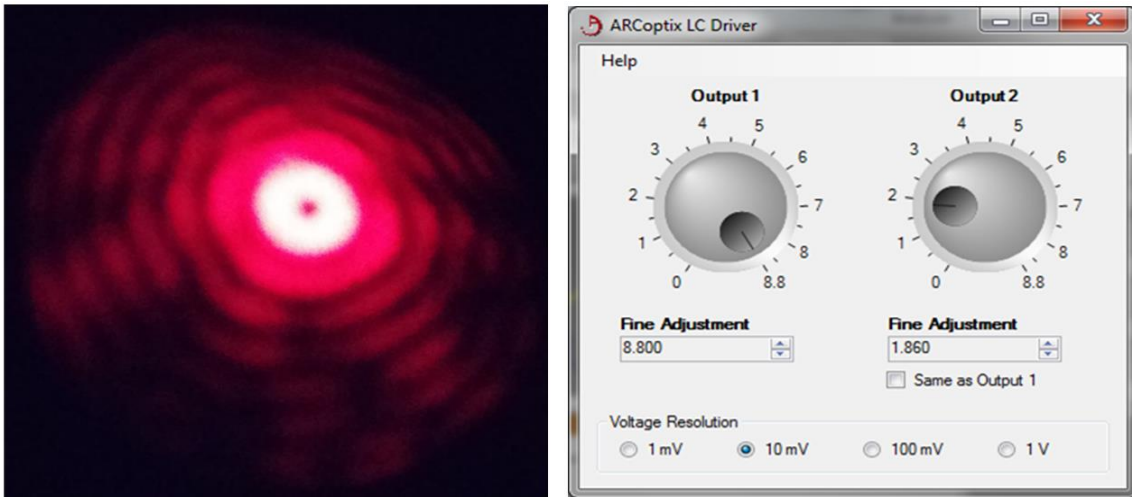
Support Figure 2. a) Photo showing the beam in donut mode, b) parameters for obtaining donut mode in the software.

Then, the beam must pass through a grid that is composed of a lens system (lens 3 (AC254-050-A, Thorlabs) and lens 4 (AC254-125-A, Thorlabs, see support Fig. 1)) similar to used in the first expansion of the beam, but now between them there is a small opening, a pinhole with a 25 µm hole at the focal point of both lenses. The pinhole has a spatial filter function, eliminating peaks of higher laser orders and undesirable patterns produced particles on lenses and mirrors.

Subsequently, the beam hits a mirror that directs you to a polarization compensator of the type Soleil-Babinet, or Berek, changing the beam distribution at the entrance of the microscope in order to obtain a radial and homogeneous polarization beam in the sample plane. . In the

focal plane, the horizontal components of the beam with radial polarization cancel each other out while the vertical components add up, resulting in intense z polarization. Therefore, it is necessary that the beam have a homogeneous intensity distribution. Otherwise, the resulting beam will have an oblique, non-vertical electric field polarization direction as desired. Note that even when the beam enters the microscope with radial and homogeneous polarization, the beam dividing mirror (the Dichroic) and the objective itself can break its homogeneity. The Berek must be aligned to act in the polarization corrections of the beam. It is important to mention that the laser beam must be expanded to fill the rear opening of the lens, 10 mm. For said expansion, it is necessary to combine two pairs of lenses with different focal lengths, as previously discussed. In this experiment, the Nikon objective oil immersion lens was used with a magnification of 60x and NA=1.39. It is worth mentioning that the laser emission power is constant, as a result, power filters neutral density are introduced into the optical path.

Just after the beam leaves the microscope there is another 50 um pinhole to clean the beam coming out of the microscope and then go through by lens 5 (AC254-125-A, Thorlabs, see support Fig. 1) that collimates the beam to pass after through the long-pass filter that eliminates the Rayleigh scattering part and then reaches the folding mirror to direct you to either the spectrometer or the APD photodetector. The spectrometer used is an Andor Shamrock model 303i-A; lens 6 (AC254-0501-A, Thorlabs, see support Fig. 1), with a short focal length, 10 mm, is used in the opening slot of the spectrometer, so that the image in the focal plane of the microscope is well defined in the plane of the Spectrometer CCD. The second possible option for the folding mirror is APD, used here to quickly analyze the intensity of a single energy band, making it possible to make

Raman images of the order of 100×faster. The APD used here is manufactured by PerkinElmer model SPCM-AQRH-14. It detects photons in the 400 to 1060 nm wavelength range. At the entrance of the APD the lens 7 (AC127-019-A, Thorlabs, see support Fig. 1) of 10 mm focal length is inserted in order to focus the laser beam on the photosensitive electronics of the APD. In order to select a desired Raman vibrational mode to observe in the APD, an optical bandpass filter is introduced before the entry of the APD.

To obtain information about the sample, it is necessary to move it using an XY scanning platform. The microscope has a stainless steel piece attached to the top specially designed to ensure the XY platform is stable. The XY scanning system used in the TERS system was manufactured by Mad City Labs, Inc, model H50, equipped with a piezoelectric PZT platform of linear phase of nanopositioning.

APD is based on the phenomenon of impact ionization. When light strikes a photo sensor, an electron (and hole) is generated by absorbing photons with sufficient kinetic energy that can generate new electron-hole pairs, so they give part of their energy to other electrons and so on generating an avalanche. It works similarly to a photomultiplier that has a range and sensitivity that often exceeds that of a photomultiplier tube. It has an active circular area that achieve maximum photon detection efficiency of more than 65% at 650 nm in a diameter of 180 um. It has an autonomous module that detects individual photons of light over the range of 400 nm wavelength up to 1060 nm. The APD device used here is an SPCM-AQRH-14 manufactured by Perkin Elmer. The photodiode is thermally cooled and controlled by temperature, ensuring a stabilized performance despite changes in ambient temperature. As each photon is

detected, a TTL pulse of 2.5 Volts minimum of a 50 and 15 ns wide high load on the BNC connector. The signal from this BNC output is processed by the RHK controller.

APD requires a 5 V power supply. To align the APD, it must first be positioned on an L-shaped support in order to have freedom of movement in the x, y and z directions using micrometric screws. Then, a lens is inserted (lens 7 AC127-019-A, Thorlabs, see support Fig. 1) in order to focus the light beam on the photosensitive region of the APD. Initially, a coarse adjustment is carried out by positioning the lens together with the micrometric screws so that the luminous point resulting from focusing is in the middle of the sensitive area of the APD. The APD is very sensitive to light, so it should be placed in a black box on all sides to keep it isolated from any other light that does not come from the microscope.

To map a desired wavelength range or range (or, equivalently, frequency), the user must introduce a set of bandpass or longpass filters. APD has the advantage of obtaining images much faster when working with times on the order of hundreds of milliseconds per pixel. Such images can serve as a basis for the analysis with spectroscopic maps. Fine alignment adjustment is done with the RH9 R9 controller Rev9 software as follows: the APD is moved with the micrometer screws in order to maximize the reading of the R9 on input C1 software.

The spectroscopic system used here comprises an iDus DU401A-BR-DD CCD connected to a Shamrock RS-303i Spectrometer, both manufactured by Andor Technology. Light enters the spectrometer cavity and is reflected by a flat mirror. Through a convenient position in the GDR, selected from the software provided by Andor technology, it is possible to

select each wavelength range. The spectrometer works with three diffraction grids that provide different spectral resolutions. This is a spectrometer with a focal length of 303 mm, a wavelength resolution of 0.1 nm (<0.2 nm with 26 µm of pixel in the CCD detector) and an accuracy of ± 0.2 nm. The iDus DU401A-BR-DD contains pixels with dimensions 26x26 µm arranged in a matrix of 1024x128 pixels. Its image area is 26.6×3.3 mm^2. It has a thermoelectric cooling device that reaches up to -75C^0 (it is installed inside a refrigerator CCD box), allowing the negligible dark current.

To align the spectrometer in the optical path; first, the folding mirror is very well aligned in such a way that the beam is between 90 degrees and in the middle of the spectrometer entry slot (this part is crucial). This ready, the lens 6 (AC254-0501-A, Thorlabs, see support Fig. 1) of 10 mm focal length is placed on the cavity road to keep the beam coming from the microscope well focused. To fine tune; the base of the lens has two micrometric screws, one that brings the lens away from the slit and the other that moves it from right to left. The lens is placed on a support that also has two micrometric screws that move it to the right and left and up and down. All previous fine-tuning is done using the Andor Solis software previously installed on the user's computer to calibrate the right alignment and intensity. In support Fig. 3, a screenshot is shown showing how the alignment should look in the software incorporated with the spectrometer. In order to verify the correct alignment, Raman measurements were made on samples of standard silicon and skinned graphene.
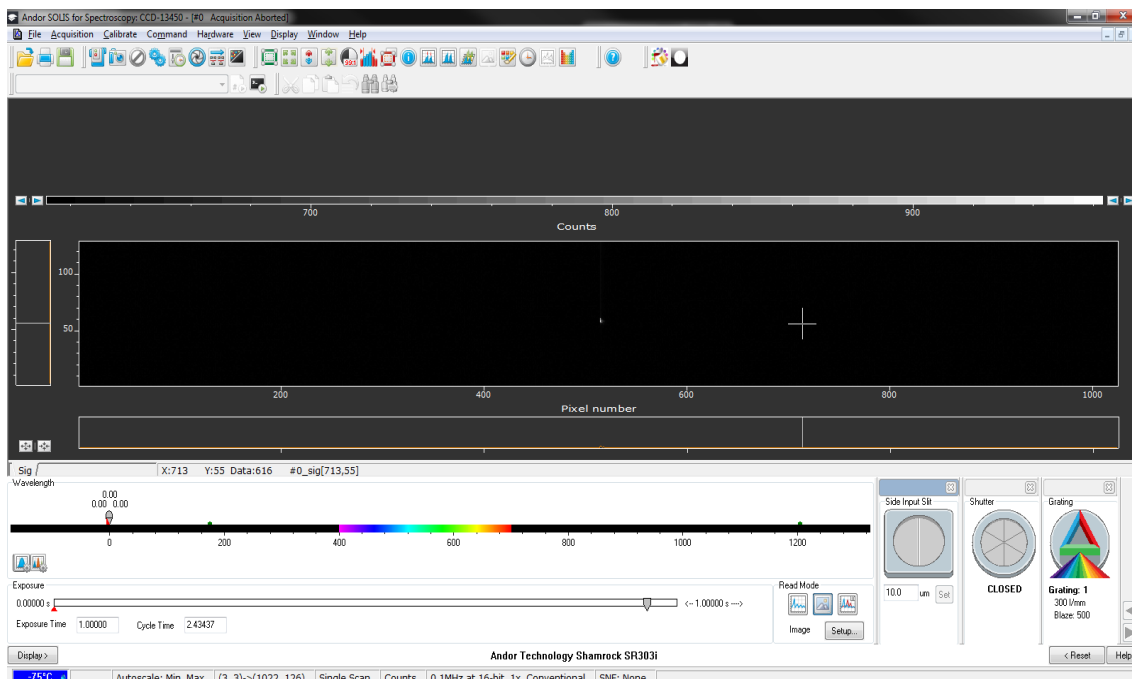
Support figure 3. Screen capture of RHK's Andor Solis software showing the spectrophotometer alignment values.

B) The SPM System.

The SPM system generally used for a TERS system is based on an SNOM, with a solid metallic tip in transmission mode, which is responsible for positioning the probe tip up to approximately 10 nm from the sample surface and in the position of the focus of the sample laser. The scanning head used is based on the shear-force AFM system, which is a shear-force AFM, where a small tuning fork is used instead of the cantilevers for sensing the probe's interaction with the sample surface. This choice is due to two main advantages, related to the type of sensor. First, the probe used is made of gold; its manufacture will be discussed in another chapter. This metal is very soft and therefore the force of interaction between the tip and the sample must be weak so as not to damage it. In an AFM system in contact mode, the interaction forces are in the range of 10−100 nN, while in the AFM shear-force the interaction forces are less than 0.10 nN. Second, commercial AFMs use the reflection of a laser in the lever arm to measure the deflection caused by the probe-sample interaction. This optical system

for sensing probe-sample interaction can interfere with the TERS optical system. In a different way, the AFM shear-force is based on the conversion of mechanical oscillations of a tuning fork into an electrical signal, thus being suitable for the desired TERS system **[101-104]**.

An efficient method for detection in AFM shear-force is to use a quartz tuning fork, which is a piezoelectric crystal. This micro is manufactured for commercial use, as a timekeeping element in electronic watch circuits. It is a millimetric quartz crystal in the form of a tuning fork with two electrodes deposited on its faces, see support Fig. 4 a). The resonance frequency is generally 32.768 kHz in the air, where the tuning fork vibrates with greater amplitude, leading to a greater potential difference in the electrodes. For reasons of fragility, the tuning fork arrives encapsulated with a metallic protection when it is sent by the manufacturer, see support Fig. 4 b).
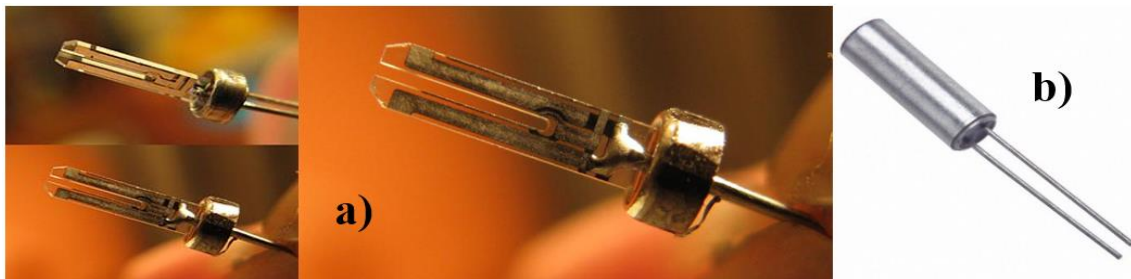
Support figure 4. a) Tuning-fork photos without capsule, b) tuning fork encapsulated.

The scanning head is placed on a solid, well-polished steel base, see support Fig. 5. This is divided into three parts: the first is a central cylinder containing the piezoelectric for the movements x, y, z, Dither and the lower part of the cylinder is the first amplification stage, where the tuning fork is welded; the second part is divided into two sections, one containing the frequency filters and the other containing the second amplification stage.

In an AFM shear-force system, the tuning fork is set to vibrate in its resonant frequency by means of another piezo, called Dither, fixed on the support base of the first stage. The resonance frequency of the Dither is tuned to that of the tuning fork, where the greatest amplitude of the electrical signal is observed. While the Dither resonance frequency remains constant during the experiment, the tuning-fork resonance frequency is changed when the probe interacts with the sample surface. In this condition, the tip movement corresponds to a harmonic damped forced oscillator, where the damping increases with decreasing the distance between the probe and the sample. As a consequence, a shift in the pitch frequency of the tuning fork is observed. The origin of this interaction is still a matter of debate, but in ambient conditions and at distances less than 20 nm it is accepted that it is attributed mainly to the confinement of a thin layer of water from the humidity between the apex of the probe and the sample, and by force Van Der Waals **[95-106]**.

Changes in amplitude and phase of the signal generated by the tuning fork are monitored by a digital lock-in amplifier system or phase looked loop system (Easy-PLL). Easy-PLL, incorporated into RHK Technology's R9 converts changes in the resonance frequency into DC voltages. This information is analyzed by the general system controller that at the same time applies voltages to the piezo-Z, which controls the vertical position of the probe. This process is understood as a feedback loop, for sensing the probe-sample interaction. For this purpose, a picomotor is used in conjunction with the piezo-Z for the fine approximation between the probe and the sample. This approximation occurs as follows: the piezo-Z slowly stretches to its full extent or until probe-sample interaction is observed. If the interaction does not occur, the piezo-Z is contracted and the controller sends PTL signals to the picomotor to lower the base of the scanning head

by a difference in height less than the total length of the piezo-Z. Thus, the piezo-Z and the picomotor act in a synchronized manner until a change in the resonance frequency of the tuning fork is observed close to the established threshold (set-point) **[95-105]**.
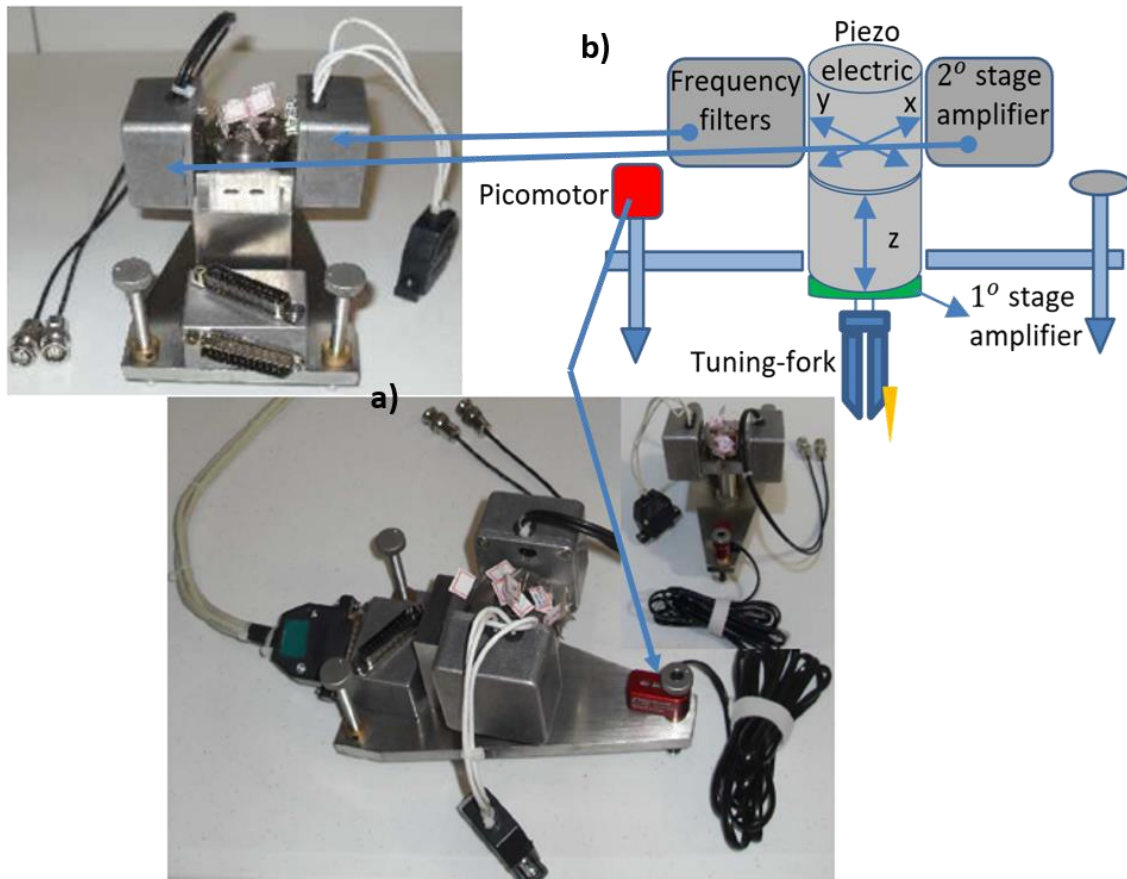

Support figure 5. a) Scan head AFM shear-force system, b) drawing indicating the parts of the head **[106]**.

C) Distance Control System.

Support Fig. 6 a) shows a commercial tuning-fork, which is composed of a micro mechanized quartz element with electrodes deposited on the surface of the device, as previously mentioned. At the base of the tuning fork, the arm can be seen being supported by an assembly epoxy resin. The total length of the element without assembly is approximately 5.87 mm, the width is 1.38 mm and the thickness of the element is 220 µm. Having two electrical connections that are put in contact with the electrodes

of the arms. The most common frequencies are 2^{15}Hz $= 32.768$ kHz and 100 kHz [65-106].

The mechanical oscillation of the arms of a tuning fork induces surface charges that are collected by electrodes and measured by an external electronic circuit. The electric field being formed acts as a mechanical-electrical converter similar to a piezo ceramic actuator. The reverse also occurs, an alternating voltage applied to the electrodes of the adjusting forks as a result of mechanical oscillation of the arms. The particular arrangement of the electrode in the arm ensures that only the movements of the arms between them can be excited and detected electronically. This is because expansion and contraction occur perpendicular to the described field lines of the tuning-fork loads; see Support Fig. 6 b).
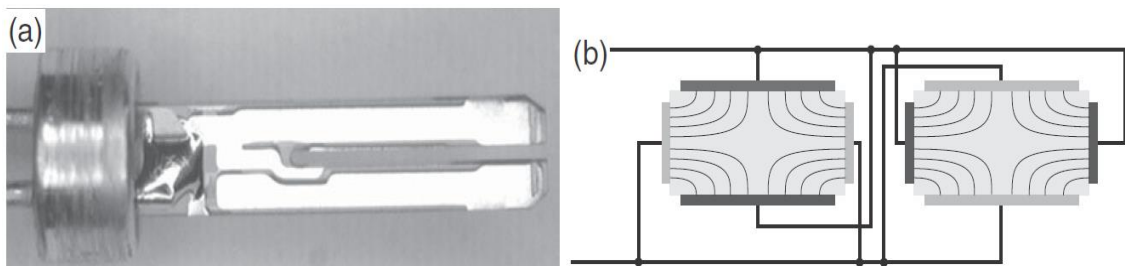

Support figure 6. a) Element dimensions of a quartz tuning fork, 5870μm×1380μm×220μm. b) Connection scheme of an arm of the quartz tuning fork for a cut perpendicular to the tips [95].

If the oscillation of an arm is excited by means of a mechanical coupling with a separate oscillator (a piezo oscillation, a Dicter), it is necessary to ensure the right mode of excitation, because otherwise it is not possible to detect any signals. The advantages of quartz tuning forks compared to other piezoelectric elements, in addition to their small size, which are their standardized and low price due to the large-scale production properties. The small size allows a probe (a tip) to be attached to one of the tuning-fork arms, so that it interacts weakly with the tuning fork resonance,

thus allowing a coupling that does not have influenza in its oscillation. Support Fig. 7 shows a tip glued to a tuning fork. In this, the shear force is the detection scheme, the tuning fork arms act as oscillating beams and not the probe itself.

It is important that the probe itself does not oscillate in the tuning fork frequency to avoid a type of operation of the coupled oscillator. Therefore, the length of the probe that protrudes from the end of the tuning fork must be kept as short as possible. For the tuning fork to be operational at $\approx \mathbf{32}$ kHz with a tip it implies that the length of the protruding probe must be less than $\sim \mathbf{2.3}$ mm **[95]**.
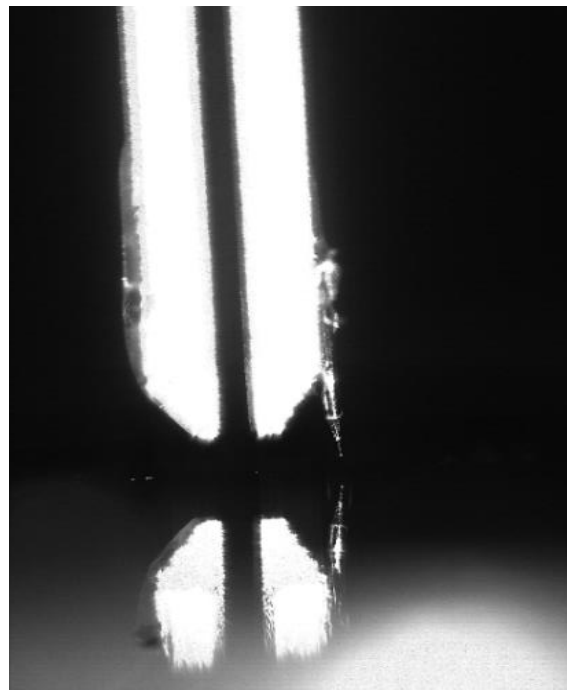
Support figure 7. Tuning fork photo with a gold tip glued to one of its arms, coming close to a surface **[95]**.

The sharp gold tips that are used in the TERS experiment are very smooth and cannot withstand strong forces. The feedback mechanism that controls the distance between the tip and the sample and to keep it within a few nanometers of the sample surface must be very sensitive and apply

only the small forces you need. As a result, the contact mode and the tapping mode of the AFM techniques are not applicable. The detection of distance-dependent shear forces resulting from lateral tip vibration parallel to the sample surface is established as the preferred method for working with tuning forks and very smooth for distance control **[107]**.

Measuring very small forces in the pN range (Pico Newtons) is a major challenge. A very practical solution is to convert this small force into a frequency variation of an electrical signal, which can be measured with excellent accuracy. The common approach for the distance control of near field tips is with the use of tuning fork sensors (TFS). The tips of the tuning fork arms are covered by electrodes that are used to connect them to an external electronic circuit. Mechanical oscillation generates an oscillating output voltage due to the piezoelectric effect. Oscillation with very small $x(t)$ amplitudes can be described by a harmonic oscillator model, where the complex amplitude dependent on time and frequency is given by:

$$m\ddot{x}(d,t) + m\gamma(d)\dot{x}(d,t) + m\omega_0^2(d)x(d,t) = Fe^{-i\omega t}$$

Where γ is the damping constant, $f_0 = \left(\frac{\omega_0}{2\pi}\right)$ the resonance frequency, and F the driving force constant; that for example, provided by an external piezoelectric Dither by shaking the tuning fork. The d parameter indicates the dependence of the sample distance and the probe. The steady state solution is:

$$x(t) = \frac{e^{-i2\pi t}}{f_0^2 - f^2 - \left(\frac{iff_0}{\sqrt{3}Q}\right)}$$

Where f and f_0 are the normal oscillation and the resonant frequency, respectively. The quality factor Q reflects damping and is defined as:

$$Q = \frac{f_0}{\Delta f} = \frac{\omega_0}{\gamma \sqrt{3}}$$

Where Δf is the total width at half the maximum of the resonance peak $|A(f)|$ who is a Lorentzian curve. The real part of the amplitude has the form:

$$A(t) = |A[f]| \cdot sin[2\pi f t + \varphi[f]]$$

Where $\varphi(f)$ is the phase shift in relation to the harmonic transmission force, 0^0 is for resonances far below 90^0 and 180^0 for resonance far above [106-108]. The frequency-dependent amplitude and phase are shown in support Fig. 7 (cp).

A gold tip is attached to one of the tuning fork arms. This additional mass in the system changes the resonance frequency to values of 30, 500-31.5 Hz and the quality factor is in the range of 1000. When the tip approaches the sample surface, the cutting forces will result from lateral vibration of the tip in relation to the surface. These forces are strongly dependent on distance and become significant at nanometer distances. They lead to a slight damping of the pitch of the tuning trolley, resulting in a smaller amplitude and a change in the resonance frequency from f_0 to f_1. This is also shown in support Fig. 8 (cv). To detect shear forces, the amplitude can be monitored at a constant direction frequency using a blocking detector. The tuning fork is excited slightly outside the resonance where $dA(f)/df$ is large. Shifting the resonance frequency due to the shear force will then lead to changes in amplitude. This approach has the

major disadvantage of a reasonably long response time. It takes approximately 2 oscillation cycles for the system to respond to an interaction and reach the new steady state. This time it is in the 100 ms interval and too long for the purpose of feedback [106-108].
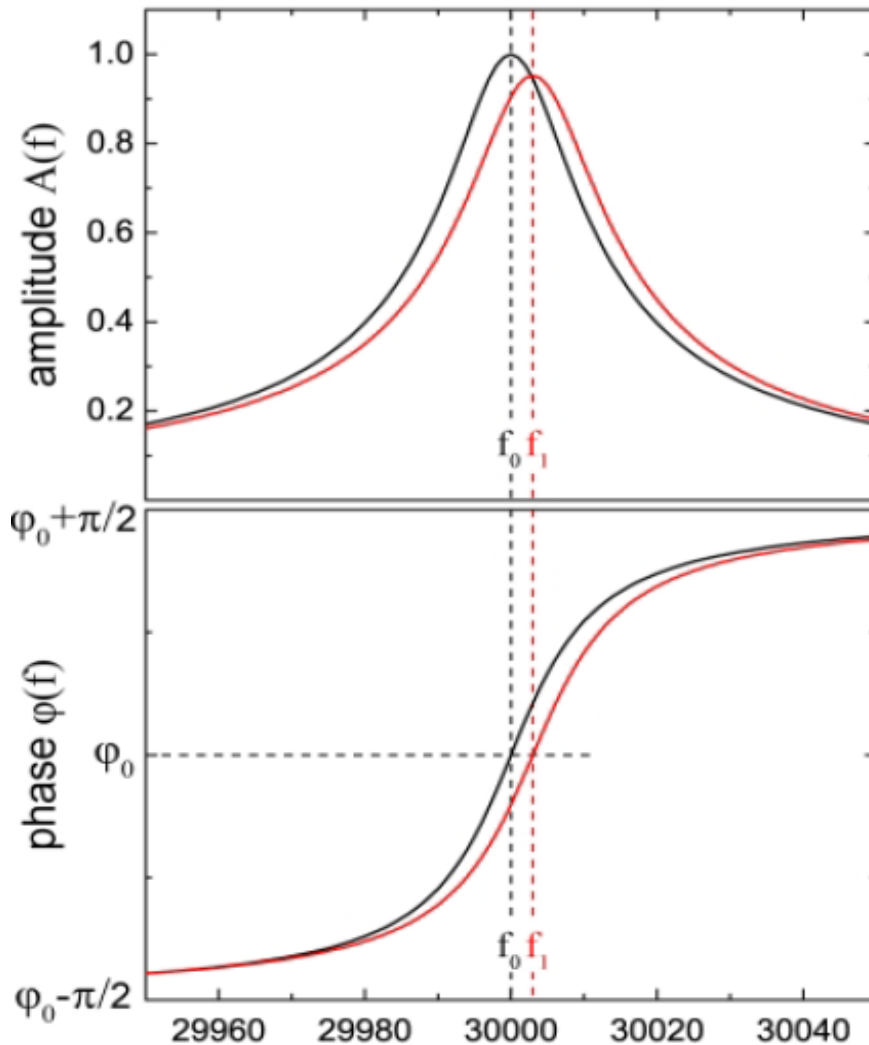

Support figure 8. Oscillation amplitude curves depending on the frequency and phase of the tuning fork. The black (cp) and red (cv) curves represent the free space oscillation and the case with sample-tip interaction, respectively. The shear forces between the tip and the surface slightly shift the resonance frequency to f_1 and slightly reduce the quality factor and, therefore, the amplitude. The φ_0 phase at the respective resonance frequency remains the same and is used to determine this frequency. The f value is constantly monitored by the SPM controller, which varies the distance from the sample to the tip to keep the frequency change constant $(f - f_0)$ [106-108].

A faster and more sensitive approach is to detect the change in resonance frequency directly. In a first approximation, the resonance frequency responds instantly and takes only several cycles to determine. It is monitored using a phase-locked loop (PLL), similar to the frequency modulators used in radios. As shown in support Fig. 8, it is evident that the phase curve is just shifting at f and the phase value at the new resonance frequency f_1.

The PLL system (easyPLL, Nanosurf) controls the tuning fork at a variable frequency f, using an extra piezoelectric (Dither) that is mechanically coupled to the tuning fork. The tuning fork output voltage is amplified by a JFET preamplifier circuit (impedance conversion) and an operational amplifier (OPA, 1000x voltage gain). The PLL measures the phase of this output in relation to the conduction and keeps its value at φ_0, varying the conduction frequency f. So, f always corresponds to the actual resonance frequency f_1 and is delivered to the surface tip microscopy (SPM) controller. This is the phase feedback that is illustrated in support Fig. 9. The amplitude of oscillation of the tip parallel to the surface is in the range of the picometer, due to the high stiffness of the tuning fork. The force acting on the tip is a few dozen pN, which is low enough to scan with a gold tip.

The SPM controller is generating the stresses that are applied to the piezoelectric tubes with which the position of the tip can be controlled in the x, y and z directions, see support Fig. 9. The z voltage that determines the distance from the sample to the tip is varied so to keep the frequency change $(f_1 - f_0)$. This is the feedback in z (z-feedback). Typically, a change of about 1.5 Hz is used, corresponding to a sample distance of a few nanometers. The x and y voltages are used for the precise positioning

of the tip within the laser focus. The SPM controller further controls the scanning stage and records APD's photon counting rates. Optical images are generated by plotting these rates against the position of the scan step. The topography of the surface, that is, the height modulations, are reflected by the z-stress in each sample position **[106-108]**.
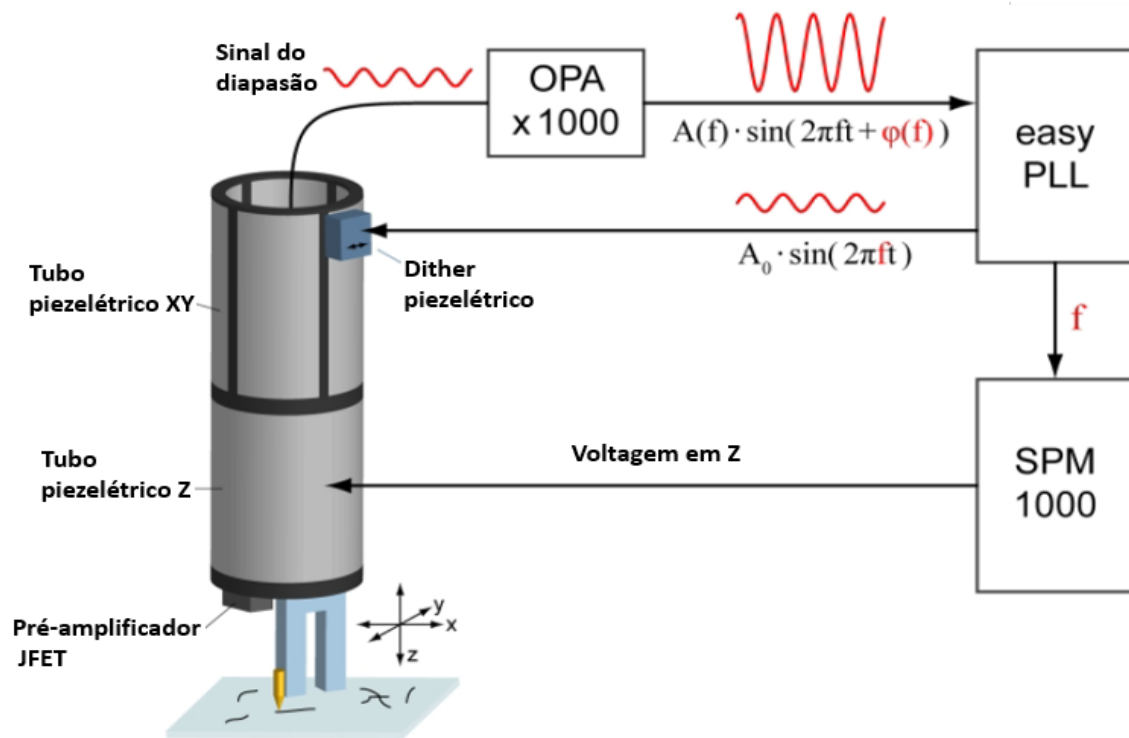
Support figure 9. The tuning fork is driven mechanically at a frequency f by a piezoelectric, Dither. The output signal is amplified and then detected by a phase lock loop (PLL). The output phase is kept constant at φ_0 by varying f, which then corresponds to the resonance frequency. The f value is constantly monitored by the SPM controller, which varies the distance from the sample to the tip to keep the frequency change constant $(f - f_0)$ **[106-108]**.

For the particular case of the TERS equipment used in the laboratory and using the software incorporated with the RHK, the obtained amplitude curve for the distance control is shown in support Fig. 10.
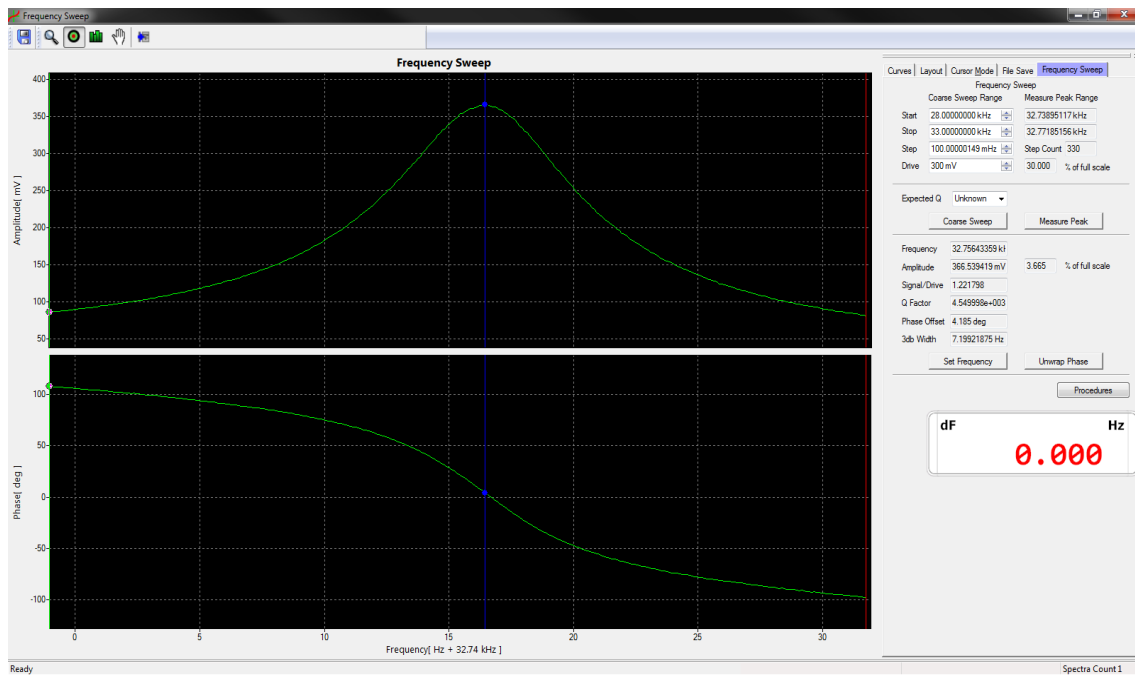
Support figure 10. Amplitude curve obtained by the tuning-fork system.

D) Papers Accepted.

Vibrational Spectroscopy and Morphological Studies on Protein-Capped Biosynthesized Silver Nanoparticles

Enzo Victorino Hemandez Agressott,[†] Dominic Blätte,[‡] Francisco Afrânio Cunha,[§,∥] Victor T. Noronha,[†] Richard Ciesielski,[‡] Achim Hartschuh,[‡] Amauri Jardim de Paula,[†] Pierre Basílio Almeida Fechine,[§] Antônio Gomes Souza Filho,[†] and Alexandre Rocha Paschoal*,[†]

[†]Departamento de Física, Universidade Federal do Ceará, Campus do Pici, P.O. Box 6030, 65455-900 Fortaleza, CE, Brazil

[‡]Department of Chemistry and Center for NanoScience (CeNS), LMU Munich, Butenandtstr. 5-13, 81377 Munich, Germany

[§]Grupo de Química de Materiais Avançados (GQMat), Departamento de Química Analítica e Físico-Química, Universidade Federal do Ceara (UFC), Campus do Pici, CEP 60451-970 Fortaleza, CE, Brazil

[∥]Laboratório de Microbiologia de Leveduras da Faculdade de Farmácia da Universidade Federal do Ceara (UFC), Campus do Pici, CEP 60451-970 Fortaleza, CE, Brazil

Ⓢ *Supporting Information*

ABSTRACT: Silver nanoparticles (AgNPs) have a large number of applications in technology and physical and biological sciences. These nanomaterials can be synthesized by chemical and biological methods. The biological synthesis using fungi represents a green approach for nanomaterial production that has the advantage of biocompatibility. This work studies silver nanoparticles (AgNPs) produced by fungi *Rhodotorula glutinis* and *Rhodotorula mucilaginosa* found in ordinary soil of the Universidade Federal do Ceará campus (Brazil). The biosynthesized AgNPs have a protein-capping layer involving a metallic Ag core. The focus of this paper is to investigate the size and structure of the capping layer, how it interacts with the Ag core, and how sensitive the system (core + protein) is to visible light illumination. For this, we employed SEM, AFM, photoluminescence spectroscopy, SERS, and dark-field spectroscopy. The AgNPs were isolated, and SEM measurements showed the average size diameter between 58 nm for *R. glutinis* and 30 nm for *R. mucilaginosa*. These values are in agreement with the AFM measurements, which also provided the average size diameter of 85 nm for *R. glutinis* and 56 nm for *R. mucilaginosa* as well as additional information about the average size of the protein-capping layers, whose found values were 24 and 21 nm for *R. mucilaginosa* and *R. glutinis* nanoparticles, respectively. The protein-capping layer structure seemed to be easily disturbed, and the SERS spectra were unstable. It was possible to identify Raman peaks that might be related to α-helix, β-sheet, and protein mixed structures. Finally, dark-field microscopy showed that the silver cores are very stable, but some are affected by the laser energy due to heating or melting.
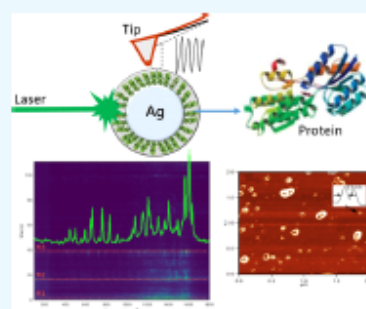
1. INTRODUCTION

Nanoparticles are systems commonly considered to have a size of approximately 1–100 nm; the design, synthesis, and manipulation of this type of system are made through nanotechnology. The small size of these materials makes them attractive for applications in a wide range of areas. Nanoparticles, based on metals, such as Au, Pt, Pd, and Ag, are used in health care products, cosmetics, and food, as well as in environmental and biomedical sciences, chemical industries, space industries, and catalysis.[1,2]

Several routes and chemical methods are used for the synthesis of nanoparticles (NPs) from metal salts. However, most of them include the use of toxic solvents that generate waste harmful to the health and environment and result in high energy consumption in routes that are generally complex and multistep. A promising approach to achieve this goal is to explore the wide range of natural resources available through

the so-called green synthesis. In this context, the use of fungi and bacteria for the synthesis of silver nanoparticles (AgNPs) has been achieving rising interest over the last years. Among the biogenic processes for the production of metallic NPs, those mediated by fungi present high efficiency, besides simplicity and low cost.[3,4] Fungi cultures, when compared to bacteria, require simpler nutrients, produce a large amount of biomass, and are easily handled. In addition, most of the fungi used to produce AgNPs are nonpathogenic to humans and the presence of a capping protein layer involving the metallic core makes these particles potentially biocompatible.[5,6]

The production of silver nanoparticles by fungi *Rhodotorula mucilaginosa* (Rm) and *Rhodotorula glutinis* (Rg) was

E) Papers for Submission.

Raman study of Ag nanoparticles coated with proteins synthesized by fungi using Tip-Enhanced Raman Spectroscopy

Enzo V. H. Agressott[1, 2], Thiago Alves de Moura[1, 2], Nathália Leal Marinho[1], Francisco Afrânio Cunha[3,4], P. B. Fechine[3], Alexandre R. Paschoal[1] and Antônio Gomes de Souza Filho[1]

EnBraER
VI Encontro Brasileiro de Espectroscopia Raman 2019

UNIVERSIDADE FEDERAL DO CEARÁ

[1]Departamento de Física, Universidade Federal do Ceará, Fortaleza.
[2]Instituto Federal de Educação, Ciência e Tecnologia do Ceará, Campus Acopiara.
[3]Grupo de Química de Materiais Avançados, Departamento de Química Analítica e Físico-Química, Universidade Federal do Ceará, Fortaleza.
[4]Laboratório de Microbiologia de Leveduras da Faculdade de Farmácia da Universidade Federal do Ceará, Fortaleza.
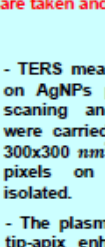
INTRODUCTION

- Proteins perform vital functional and structural tasks in living systems. Therefore, it is of great interest to study the behavior and functions of proteins at the molecular level. The detection and characterization of proteins on this scale is key to understanding the mechanisms involved in the development of new drugs and in the early diagnosis of diseases [1, 2].

- Two types of Ag nanoparticles (AgNPs) coated with biogenic proteins were synthesized by the fungal *Rhodotorula Glutinis* (RG-AgNPs) and *Rhodotorula Mucilaginosa* (RM-AgNPs) in the so-called green synthesis method [3, 4]. AgNPs applications we can highlight the delivery and release of drugs; development of sensors to diagnose diseases [1, 5].

- The Tip-Enhanced Raman Scattering (TERS) is an emerging and versatile tool for the chemical analysis of biomolecules (proteins), which provides molecular information on a nanometric scale. This combines atomic force microscopy (AFM) with conventional Raman spectroscopy, resulting in a strong improvement of the Raman signal with a lateral resolution similar to the dimensions of the AFM tip [6, 7].

METHODS

R. mucilaginosa

Fungi

R. glutinis

AgNPs coated with proteins production by fungi RG and RM was previously done by Cunha et al. [8].

3- With a micropipette, one drop is deposited on a 0.2 mm glass coverslip and left to dry for 48 hours at room temperature.

2- then 50 ml of deionized water are added and sonicated for 20 min.

1- 10 mL of the stored AgNPs in suspension are taken and sonicated for 30 min.

Figure 1. RG-AgNPs sample characterization. TERS image for the 1600 cm^{-1} peak and the associated AFM are show on a) and b) respectively; for better visualizations the 3D-AFM image and SEM image are shown on the c) and d); e) Raman Spectra on the point 1, 2, 3; and f) 4, 5, 6.

Figure 2. RM-AgNPs sample characterization. TERS image for the 1600 cm^{-1} peak and the associated AFM are show on a) and b) respectively; for better visualizations the 3D-AFM image and SEM image are show on the c) and d); e) Raman Spectra on the point 1, 2, 3; and f) 4, 5, 6.

RESULT AND DISCUSSION

- TERS measurements were performed on AgNPs proteins coated and AFM scaning and Raman hyperspectrum were carried out simultaneously on a 300x300 nm^2 region covered by 32x32 pixels on small agglomerates or isolated.

- The plasmons resonance on the Au-tip-apix enhanced the Raman signal, Fig. 1 and 2. The Raman scattering vibrational modes of the proteins were observed; also the spectroscopic image has a good correspondence with the AFM image.

- Well defined peaks at about 1187cm^{-1} (C-S Stretching), 1255cm^{-1} (C-H flexion), 1346cm^{-1} (C-H flexion+C-C stretch), 1505cm^{-1} (C-H flexion+C-C stretching) and 1618cm^{-1} (C-C stretching) were observed for each sample on individual AgNPs [9]. Peak identifications is shows on the table 1.
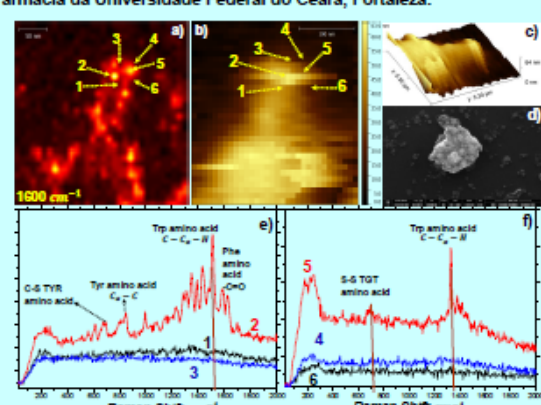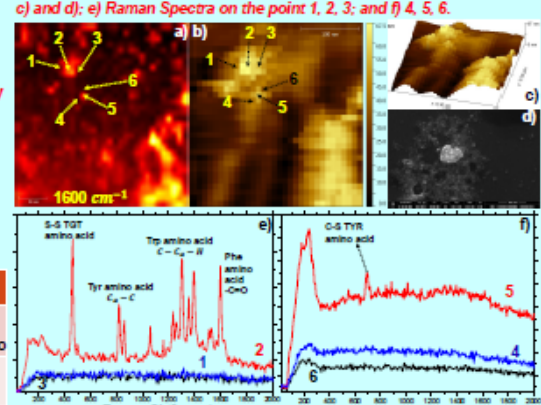
Table 1

R. Glutinis	R. Mucilaginosa	Assignment [9]
[1600-1690] cm^{-1}		Amide I, -C=O stretching/hydrogen bonding coupled with COO
[1480-1580] cm^{-1}		Amide II, N-H groups bending vibrations, C-N stretch
[1230-1300] cm^{-1}		Amide III, C-N stretch, 30% N-H bend, C-C stretching, C-H flexion
[625-770] cm^{-1}		Amide IV, OCN bending
[640-800] cm^{-1}		Amide V, out-of-plane NH bending
[540-600] cm^{-1}		Amide VI, out-of-plane C=O bending
200 cm^{-1}		Skeletal mode

CONCLUSIONS

The Tip-Enhanced Raman Scattering has been successfully applied to study isolated and small bundles of AgNPs synthesized by fungi. The enhanced Raman spectra obtained were stable, indicating that the structural conformations of the protein involving the silver core just is affected by plasmons on the Au-tip and not by the Ag-nucleus. The results presented here allowed the identification of alpha-helix, beta-sheet and protein mixed structures. The protein Au-tip interaction seems to happen through the amine group.

REFERENCES

[1] Ahluwalia V. et al. Green synthesis of silver nanoparticles by Trichoderma harzianum and their bio-efficacy evaluation against Staphylococcus aureus and Klebsiella pneumonia. Ind. Crops Prod., 2014, 55, 202–206.
[2] Regina Treffer, R. et al. Advances in TERS (tip-enhanced Raman scattering) for biochemical applications. Biochem. Soc. Trans. 2012, 40, 609–614.
[3] Hulkoti, N. I. et al. Biosynthesis of nanoparticles using microbes-A review. Colloids Surf., B. 2014, 121, 474–483.
[4] Gour, A. et al. Advances in green synthesis of nanoparticles. Artif. Cells, Nanomed., Biotechnol. 2019, 47, 844-851.
[5] Erdogan, O. et al Green synthesis of silver nanoparticles via Cynara scolymus leaf extracts: The characterization, anticancer potential with photodynamic therapy in MCF7 cells. PLoS ONE 2019, 14, No. e0216496.
[6] Bruno Pettinger. Single-molecule surface- and tip-enhanced raman spectroscopy. Molecular Physics Vol. 108, No. 16, 20 August 2010, 2039–2059.
[7] Neugebauer, U. Et al. On the Way to Nanometer-Sized Information of the Bacterial Surface by Tip-Enhanced Raman Spectroscopy. ChemPhysChem 2006, 7, 1428 – 1430.
[8] Cunha et al. Biogenic synthesis of multifunctional silver nanoparticles from Rhodotorula glutinis and Rhodotorula mucilaginosa: antifungal, catalytic and cytotoxicity activities. World J. Microbiol. Biotechnol. 2018, 34, 127.
[9] Rygula, A. et al Raman spectroscopy of proteins: A review. J. Raman Spectrosc. 2013, 44, 1061–1076, 2013.